Solution Processing of Hybrid Perovskite by Scalable and Sustainable Techniques for Solar Cell Application

Zur Erlangung des akademischen Grades eines

DOKTORS DER INGENIEURWISSENSCHAFTEN
(Dr.-Ing.)

von der KIT-Fakultät für
Elektrotechnik und Informationstechnik des
Karlsruher Instituts für Technologie (KIT)

angenommene

DISSERTATION

von

M.Sc. Johannes Michael Küffner
geb. in Bad Windsheim

Tag der mündlichen Prüfung: 21.01.2022

Hauptreferent: Prof. Dr.-Ing. Michael Powalla
Korreferent: Prof. Dr. techn. Christoph J. Brabec

Abstract

After only a few years of research, hybrid organic-inorganic metal-halide perovskite solar cells (PSCs) achieve a record power conversion efficiency (PCE) of >25 %, which makes them one of the most efficient photovoltaic technologies. Due to the outstanding optoelectronic properties of the perovskite semiconductor and its low-cost fabrication by solution processing, the absorber material is a promising candidate for next-generation photovoltaic applications and industrial mass production. Nevertheless, the majority of PSCs reported in literature only exhibits small lab scale (~0.1 cm^2) and is mainly fabricated by hardly scalable deposition techniques. Thus, besides some other bottlenecks such as stability and toxicity, one of the major challenges of the technology is upscaling the deposition of homogeneous perovskite layers to large areas (≥100 cm^2) and via industry-relevant processes to enable the commercialization of PSCs. On this account, this thesis deals with the subject of solution processing of hybrid perovskite layers by scalable and sustainable techniques in order to be applied in solar cells.

In solution processing of perovskite thin films, four main conversion methods are well known to remove the solvent from the wet film, thereby converting it to a dry crystallized layer. In this thesis, a focus is set on the two methods of heat- and gas-assisted conversion since they are identified as the methods exhibiting the largest upscaling potential. As starting point, the heat-assisted conversion for $MAPbI_3$ (MAPI) based solar cells processed via blade coating is analyzed. This conversion method was found to be less suitable for upscaling perovskite deposition due to wet film fluid dynamics and poor process controllability. Moreover, it is shown that utilizing a surfactant improves the perovskite morphology but also results in detrimental procedural effects.
However, gas-assisted conversion after blade coating via a static low-pressure gas system is indicated as superior to control the MAPI perovskite morphology and for upscaling. In addition, the perovskite morphology is optimized through a blade coated nanoparticle wetting agent and composition engineering of the perovskite precursor solution. It is pointed out that a further increase in PSC champion efficiency to up to ~18 % on a standard device area (~0.25 cm^2) can be achieved by layer thickness optimizations. By combining all engineering steps, the author proves scalability to a substrate area of ~80 cm^2 and presents perovskite solar modules (PSMs) with an aperture area of up to ~50 cm^2 reaching a PCE of ~9 %.
Aside from that, the author investigates gas-assisted conversion for the scalable deposition of suitable solvent systems to fabricate multi-cation (MC) perovskite layers, which are as per literature more stable. Thereby, this thesis shows the requirement of a moving high-pressure gas system. Furthermore, the implementation of the green and sustainable perovskite precursor solvent dimethyl sulfoxide is evaluated resulting in comparable PSC performances to the toxic counterpart of ~17 % on blade coated standard device area. Thus, it is highlighted that the use of toxic solvents can be avoided. Additionally, gas-assisted conversion in combination with slot-die coating is optimized which represents an even more industry-relevant deposition technique than blade coating. By additive engineering and defect passivation strategies, PSCs with slot-die coated perovskite and with PCEs of >17 % on standard device area are shown.
This thesis indicates that gas-assisted conversion is a promising method for upscaling solution processing of hybrid perovskite by scalable and sustainable techniques for solar cell application.

Kurzfassung

Nach nur wenigen Jahren Forschung erzielen Organisch-Inorganische Hybrid-Metallhalogenid Perowskit-Solarzellen einen Rekordwirkungsgrad von >25 %, was sie zu einer der effizientesten Photovoltaik-Technologien macht. Aufgrund der herausragenden optoelektronischen Eigenschaften des Perowskit-Halbleiters und dessen kostengünstigen Herstellung durch lösungsbasierte Verfahren verspricht das Absorbermaterial ein aussichtsreicher Kandidat für Photovoltaik-Anwendungen der nächsten Generation und die großtechnische Massenproduktion zu sein. Nichtsdestotrotz weist die Überzahl von den in der Literatur berichteten Perowskit-Solarzellen nur kleinen Labormaßstab ($\sim$0.1 cm^2) auf und ist hauptsächlich mit Abscheidetechniken hergestellt, die kaum skalierbar sind. Daher ist die Aufskalierung der Abscheidung von homogenen Perowskit-Schichten auf große Flächen ($\geq$100 cm^2) und mittels industrierelevanten Prozessen, neben anderen Hindernissen wie Stabilität und Toxizität, einer der größten Herausforderungen der Technologie, um die Kommerzialisierung von Perowskit-Solarzellen zu ermöglichen. Aus diesem Grund befasst sich diese Dissertation mit dem Thema der lösungsbasierten Fertigung von Hybrid-Perowskitschichten mithilfe skalierbarer und umweltverträglicher Verfahren für den Einsatz in Solarzellen.

In der lösungsbasierten Fertigung von Perowskit-Dünnschichten sind vor allem vier Trocknungsmethoden bekannt, um das Lösemittel aus dem Nassfilm zu entfernen, was dessen Konvertierung zu einer trockenen kristallinen Schicht gleichkommt. In dieser Dissertation liegt der Fokus auf zwei Konvertierungsmethoden, der hitze- und der gasgestützten Methode, da diese als die mit dem größten Aufskalierungspotenzial identifiziert werden. Als Ausgangspunkt wird die hitzegestützte Konvertierung für Solarzellen basierend auf gerakeltem $MAPbI_3$ (MAPI) untersucht. Es lies sich feststellen, dass aufgrund des dynamischen Flüssigkeitsverhaltens im Nassfilm und schlechter Prozessbeherrschbarkeit diese Konvertierungsmethode für die Aufskalierung der Perowskit-Abscheidung weniger geeignet ist. Zudem wird gezeigt, dass die Nutzung eines Netzmittels die Perowskit-Morphologie verbessert, aber auch zu nachteiligen prozesstechnischen Auswirkungen führt.
Die gasgestützte Konvertierungsmethode mittels eines stationären Niederdruck-Gassystems im Anschluss an die Rakelbeschichtung stellt sich hingegen, für die Aufskalierung und um die MAPI Perowskit-Morphologie zu kontrollieren, als überlegen dar. Darüber hinaus wird die Perowskit-Morphologie mithilfe eines gerakelten Nanopartikel-Benetzungsmittels und der Anpassung der Komponenten in der Perowskit-Präkursorlösung optimiert. Es wird gezeigt, dass mittels Schichtdickenoptimierungen eine weitere Verbesserung der Champion-Effizienz der Perowskit-Solarzelle mit Standard-Bauteilfläche ($\sim$0.25 cm^2) bis $\sim$18 % erreicht werden kann. Durch Kombination aller Entwicklungsschritte weist der Autor die Skalierbarkeit bis zu einer Substratfläche von $\sim$80 cm^2 nach und präsentiert Perowskit-Solarmodule mit einer Aperturfläche von bis zu $\sim$50 cm^2 und einem erzielten Wirkungsgrad von $\sim$9 %.
Außerdem untersucht der Autor die gasgestützte Konvertierung für die skalierbare Abscheidung von geeigneten Lösemittelsystemen, um Multi-Kationen-Perowskitschichten herzustellen, die laut Literatur stabiler sind. Dabei zeigt diese Dissertation die Notwendigkeit eines sich bewegenden Hochdruck-Gassystems auf. Des Weiteren wird die Implementierung des grünen und um-

weltverträglichen Perowskit-Präkursorlösemittels Dimethylsulfoxid evaluiert, welches auf gerakelter Standard-Bauteilfläche zum giftigen Pendant vergleichbare Perowskit-Solarzelleffizienzen von ∼17 % liefert. Auf diese Weise wird deutlich gemacht, dass die Verwendung von giftigen Lösemitteln vermeidbar ist. Zusätzlich wird die gasgestützte Konvertierung in Kombination mit der Schlitzdüsenbeschichtung optimiert, die gegenüber der Rakelbeschichtung einer noch industrierelevanteren Abscheidetechnik entspricht. Mittels Additiv-Entwicklung und Strategien zur Defektpassivierung werden Perowskit-Solarzellen mit per Schlitzdüse beschichtetem Perowskit und Wirkungsgraden von >17 % auf Standard-Bauteilfläche gezeigt.
Diese Dissertation zeigt auf, dass die gasgestützte Konvertierung eine erfolgversprechende Methode für die Aufskalierung der lösungsbasierten Fertigung von Hybrid-Perowskit mithilfe skalierbarer und umweltverträglicher Verfahren ist, um in Solarzellen Anwendung zu finden.

Table of contents

Abbreviations and symbols

Abbreviations

2-BE	2-butoxyethanol
2-ME	2-methoxyethanol
2-MP	2-methylpyrazine
2T	two-terminal
4T	four-terminal
ACN	acetonitrile
Ag	silver
Al_2O_3	aluminium oxide
Al_2O_3 NP	aluminium oxide nanoparticle
AM1.5G	AM1.5 global standard solar spectrum
Ar	argon
Au	gold
BC	blade coating
BCP	bathocuproine (2,9-Dimethyl-4,7-diphenyl-1,10-phenanthroline)
Br^-	bromide
Br	bromine
$CaTiO_3$	calcium titanate
CB	chlorobenzene
CIGS	copper indium gallium diselenide ($CuIn_xGa_{1-x}Se_2$)
Cl^-	chloride
Cl	chlorine
CLSM	confocal laser scanning microscopy
CO_2	carbon dioxide
Cs^+	cesium
CsI	cesium iodide
$CsPbI_3$	cesium lead triiodide ($CsPbI_3$)
CTL	charge transport layer
Cu	copper
DALY	disability-adjusted life year
DCB	dichlorobenzene (1,2-Dichlorobenzene)

DEF	diethylformamide (*N*,*N*-Diethylformamide)
DMAC	dimethylacetamide (*N*,*N*-Dimethylacetamide)
DMF	dimethylformamide (*N*,*N*-Dimethylformamide)
DMI	dimethylimidazolidinone (1,3-Dimethyl-2-imidazolidinone)
DMPU	dimethylpropyleneurea (1,3-Dimethyl-3,4,5,6-tetrahydro-2(1H)pyrimidinone)
DMSO	dimethyl sulfoxide
EPBT	energy payback time
EQE	external quantum efficiency
ETL	electron transport layer
ETM	electron transport material
FA^+	formamidinium ($(NH_2-CH=NH_2)^+$)
FACl	formamidinium chloride
FACsPbIBr	double-cation perovskite ($FA_{0.83}Cs_{0.17}Pb(I_{0.87}Br_{0.13})_3$)
FAI	formamidinium iodide
$FAPbI_3$	formamidinium lead triiodide ($CH(NH_2)_2PbI_3$)
FF	fill factor
FTO	fluorine-doped tin oxide (SnO_2:F)
fwd	forward
GBL	γ–butyrolactone
GFF	geometric fill factor
GIXRD	grazing incidence x-ray diffraction
H_2O	water
HCl	hydrochloric acid
HTL	hole transport layer
HTM	hole transport material
I^-	iodide
I	iodine
In	indium
IO:H	hydrogen-doped indium oxide (In_2O_3:H)
IPA	isopropanol
ITO	indium tin oxide (typically $In_{0.74}Sn_{0.08}O_{0.18}$)
IV	current–voltage dependency
JV	current density–voltage dependency

KIT	Karlsruher Institut für Technologie
KSOP	Karlsruhe School of Optics and Photonics
LCA	life cycle assessment
LCOE	levelized cost of electricity
LED	light-emitting diode
LP	amphiphilic surfactant (L – α-phosphatidylcholine)
MA^+	methylammonium ($(CH_3NH_3)^+$)
MAAc	methylammonium acetate ($CH_3NH_2 \cdot CH_3COOH$)
MACl	methylammonium chloride
MAI	methylammonium iodide
$MAPbBr_3$	methylammonium lead tribromide ($CH_3NH_3PbBr_3$)
$MAPbI_3$	methylammonium lead triiodide ($CH_3NH_3PbI_3$)
MAPI	$MAPbI_3$
$MASnI_3$	methylammonium tin triiodide ($CH_3NH_3SnI_3$)
MC	multi-cation
Mg	magnesium
m-MTDATA	triphenyl amine (4,4',4"-tris[phenyl(m-tolyl)amino]triphenylamine)
MPP	maximum power point
N_2	nitrogen
NH_4Cl	ammonium chloride
NiO	nickel oxide
n-i-p	n-type–intrinsic–p-type
NIR	near-infrared
NMP	*N*-Methylpyrrolidone (*N*-methyl-2-pyrrolidone)
NP	nanoparticle
O_2	oxygen
OPV	organic photovoltaic
P1	patterning 1
P2	patterning 2
P3	patterning 3
Pb	lead
$PbAc_2$	lead acetate ($Pb(CH_3COO)_2$)
$PbAc_2$ trihydrate	lead acetate trihydrate ($Pb(CH_3COO)_2 \cdot 3\,H_2O$)
$PbBr_2$	lead bromide

$PbCl_2$	lead chloride
PbI_2	lead iodide
PbO_2	lead oxide
PCBM	C_{61} fullerene derivate ([6,6]-phenyl-C_{61}-butyric acid methyl ester)
PCE	power conversion efficiency at standard test conditions
PEAI	phenethylammonium iodide ($C_8H_{12}NI$)
PEDOT:PSS	conductive polymer (poly(3,4-ethylenedioxythiophene)-poly(styrenesulfonate))
p-i-n	p-type–intrinsic–n-type
PL	photoluminescence
p-n	p-type–n-type
PSC	perovskite solar cell
PSM	perovskite solar module
PTAA	poly(triaryl amine) (poly[bis(4-phenyl)(2,4,6-trimethylphenyl)amine])
PV	photovoltaic
PVD	physical vapor deposition
R2R	roll-to-roll
RH	relative humidity
RMS	root-mean-square
RT	room temperature
rvs	reverse
S2S	sheet-to-sheet
SC	spin coating
SDC	slot-die coating
SEM	scanning electron microscopy
Si	silicon
SiO_2	silicon oxide
SiO_2 NP	silicon oxide nanoparticle
Sn	tin
SnO_2	tin oxide
SPC	spray coating
SQL	Shockley–Queisser limit
TCO	transparent conductive oxide
TEOS	tetraethyl orthosilicate
THF	tetrahydrofuran
TiO_2	titanium oxide
TOF-SIMS	time-of-flight secondary ion mass spectroscopy
US	ultrasonic
UV/Vis	ultraviolet to visible
UV	ultraviolet

UVO	ultraviolet–ozone
XPS	x-ray photoelectron spectroscopy
XRD	x-ray diffraction
ZSW	Zentrum für Sonnenenergie- und Wasserstoff-Forschung Baden-Württemberg

Symbols

2θ	diffraction angle	°
α	absorption coefficient	cm^{-1}
A	absorptance	%
A_{act}	active area	cm^2
A_{ap}	aperture area	cm^2
A_d	dead area	cm^2
β_i	mass transfer coefficient	$m\,s^{-1}$
BP	boiling point	°C
C^*_{max}	maximum supersaturation limit	$mol\,L^{-1}$
C^*_{min}	minimum supersaturation limit	$mol\,L^{-1}$
C_s	solute solubility limit	$mol\,L^{-1}$
d	film thickness	nm
d_{wet}	wet film thickness	µm
D_N	donor number	$kcal\,mol^{-1}$
η	dynamic viscosity	cP
E_b	exciton binding energy	meV
E_g	band gap energy	eV
ϑ	kinematic viscosity	cP
FF	fill factor	%
GFF	geometric fill factor	%
I	current	mA
I_d	dark current of a diode	mA
I_{ph}	photocurrent	mA
I_{SC}	short circuit current	mA
I_{sh}	shunt current	mA
J_{EQE}	photocurrent density obtained by EQE measurement	$mA\,cm^{-2}$
J_{SC}	short circuit current density	$mA\,cm^{-2}$
k_B	Boltzmann constant	$1.380\,649 \times 10^{-23}\,J\,K^{-1}$
λ	wavelength	nm
L_c	charge carrier diffusion length	nm
μ	octahedral factor	
μ_c	charge carrier mobility	$cm^2\,V^{-1}\,s^{-1}$
Ma	Marangoni number	
p	pressure	bar

p_{oi}	vapor pressure	bar or atm
PCE	power conversion efficiency	%
Q	gas flow rate	L min^{-1}
Q_{ink}	ink pump rate	mL min^{-1}
ρ	density	g mL^{-1}
R	reflectance	%
R_q	root-mean-square roughness	nm
R_s	series resistance	Ω
R_{sh}	shunt resistance	kΩ
R_{sq}	sheet resistance	$\Omega_{\square}$
Ra	Rayleigh number	
σ	surface tension	mN m^{-1}
σ_S	degree of supersaturation	
τ_c	charge carrier lifetime	μs
t	tolerance factor	
T	transmittance	%
T_a	absolute temperature	K
v	gas flow velocity	m s^{-1}
v_{BC}	blade coating velocity	mm s^{-1}
v_{GK}	gas knife velocity	mm s^{-1}
v_{SD}	slot-die coating velocity	mm s^{-1}
V	voltage	V
V_{OC}	open circuit voltage	mV
ω	angle of incidence	°

1 Introduction and objective

1.1 Motivation

The global energy demand is expected to grow by ~20 % to 25 % till 2040, not leveling off before the mid-century [1] due to a population growth and economic development in developing countries, while demand of developed countries will remain fairly unaltered [1,2]. Carbon based fossil fuels such as coal, oil, and natural gas are covering the majority of humanity's energy demand today [1].

Disregarding from an inevitably depleting supply, burning these natural resources for generating electricity and heating releases large quantities of carbon dioxide (CO_2) and other greenhouse gases into the atmosphere. These emissions lead to heat trapping in the atmosphere and consequently to an increase of the overall average surface temperature of the earth [3], which already has drastic and will increasingly have devastating consequences on wildlife, biodiversity, ecosystems, habitats and, hence, humankind due to weather and climate extremes, rising sea levels and environmental changes [4, 5]. Since pre-industrial times, earth's surface temperature has already increased by ~1.0 °C [3]. Without ambitious climate policies for decarbonization and against global warming earth's temperature would increase by 3 °C to 5 °C above the pre-industrial baseline by the end of the current century [4, 5]. Therefore, mankind must take steps to reduce our carbon footprint and in the long term reach carbon neutrality.

Regarding Germany, in 2021 the First Senate of the Federal Constitutional Court held that the provisions of the Federal Climate Change Act of the year 2019, governing national climate targets and the annual emission amounts allowed until 2030, are incompatible with fundamental rights insofar as they lack sufficient specifications for further emission reductions from 2031 onwards [6]. In all respects, this judgment represents a novelty.
In the 2015 Paris Climate Agreement, under the United Nations Framework Convention on Climate Change, virtual all existing countries agreed to take action to limit global average temperature rise to "well below 2 °C above pre-industrial levels" and that nations will pursue "efforts to limit the temperature increase to 1.5 °C", "recognizing that this would significantly reduce the risks and impacts of climate change" [7]. To accomplish this, a resolute focus on the reduction of fossil fuel consumption is required imperatively like never before. For the decarbonization of the world's energy system, upscaling electricity from clean energy sources will be crucial. Thus, renewable energy sources need to play a key role in the future to conserve the planet and at the same time fulfill rising energy demands [3, 8].

Renewable energies such as wind energy, photovoltaic (PV), hydropower, geothermal energy and biomass [3, 8] are expected to surpass both coal and gas as global electricity generation capacity in the 2030s [3]. Among the renewable energies, solar energy as the most abundantly available and clean energy form will dominate the generation of electricity by 2050 [3, 9, 10] due to the enormous amount of green and sustainable energy constantly striking planet earth without any side effects such as the emission of greenhouse gases, and its continuously decreasing costs [11].

Nowadays, (single- or polycrystalline) silicon (Si) based PV is with a share of ~95 % of the global annual PV production market-dominant, still outplaying thin film technologies [11]. Nevertheless, Si based PV is close to reach its theoretical efficiency limit under laboratory conditions [12]. Furthermore, manufacturing Si based PV requires material- and energy-intensive high-temperature processes, which shows their limited potential for further cost reduction [11].

Hybrid organic-inorganic metal-halide thin film perovskite solar cells (PSCs) with perovskite crystals as the semiconducting absorber material [13] are expected to play a key role in the future of PV. PSCs achieved major breakthroughs in somewhat more than 10 years [14, 15]. They reach a record power conversion efficiency (PCE) for opaque devices of 25.5 % fabricated by nonscalable deposition techniques such as spin coating (SC) with small lab-scale active area (A_{act}) values (~0.1 cm^2) [12, 16–18] as indicated in Figure 1.1a from originally 2.2 % in 2006 [19] and 3.8 % in 2009 [20] presented by Kojima et al. This makes perovskite PV to the fastest-advancing solar technology to date.

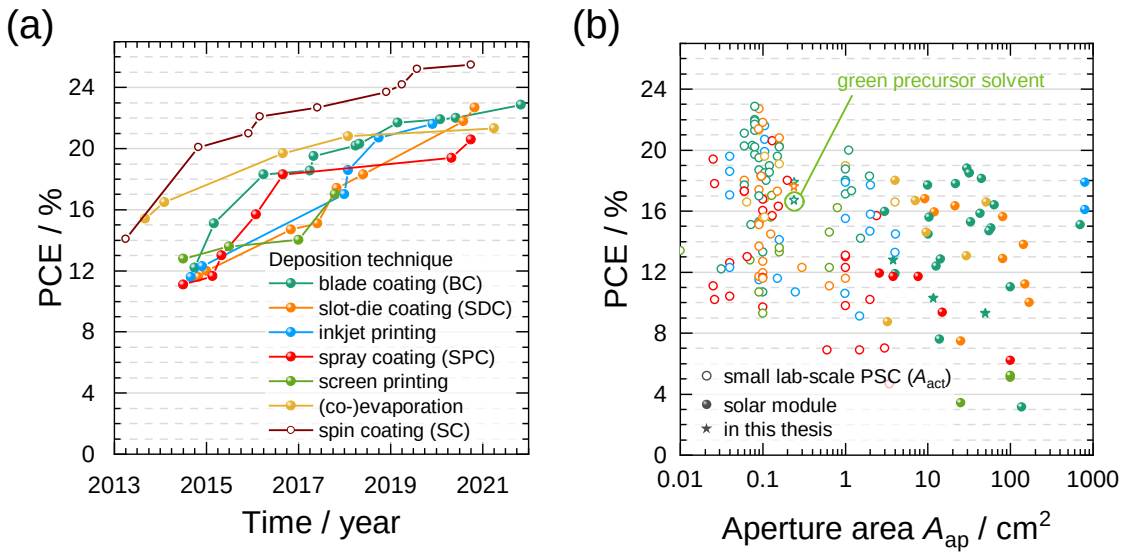

Figure 1.1: Evolution of the PCEs of solar cells with perovskite absorbers fabricated by different main deposition techniques: (a) Chronologically evolution of scalable deposition techniques in comparison to record efficiencies fabricated by SC. (b) Overview of scalable deposition techniques over device aperture area (A_{ap}). Data from [16, 21–28]. Adapted with permission from [21, 23]. © John Wiley and Sons.

Additional advantages of perovskite absorbers include the processing feasibility via solution, which will lead to a most likely strong cost reduction of manufacturing [21]. Due to the fact that they are more cost-efficient, PSCs might become a potential alternative to Si based PV. Furthermore, the low processing temperatures of <150 °C during thin-film fabrication allow the deposition on a multitude of various substrates such as flexible foils [29] via roll-to-roll (R2R) coating [30, 31]. Moreover, PSCs are especially suitable for the use in tandem PV cells [32], where a perovskite based cell is stacked for instance on top of a Si bottom cell [33], on a PSC [34] or on other large-area deposited thin-film technologies such as copper indium gallium diselenide (CIGS) in a two-terminal (2T) or four-terminal (4T) multi-junction configuration, because the band gap of perovskite is naturally relatively wide and can be easily tuned by variation of its compositions [35]. Thus, efficient harvesting of different shares of the sun spectrum is enabled, surpassing the theoretical limits of a single-junction cell and outperforming its PCE [16]. Hence, tandem technologies are expected to accelerate the transition of the PV

technology into the generation of leading electricity source in the future [36].
Nevertheless, efficiencies of perovskite photovoltaic devices fabricated by scalable printing techniques, for example blade coating (BC) or slot-die coating (SDC), via solution processing still lag behind compared to cell performances prepared by nonscalable coating methods like SC (Figure 1.1a) [37]. In addition, Figure 1.1b illustrates the fact that with increasing device aperture area (A_{ap}) of record solar cells from small lab scale of areas between 1 mm^2 and 1 cm^2 to areas of perovskite solar modules (PSMs) of a few 100 cm^2 PCE drops dramatically [38–43]. However, for long-term success of the perovskite technology a high-throughput deposition especially on these industry-relevant areas is imperatively necessary, which makes upscaling one of the main current research focuses of the technology.

In particular due to the impressive rise in PCE of PSCs and the potential low carbon footprint, production costs as well as levelized cost of electricity (LCOE) [44], which is a measure of the average net present cost of electricity generation by a technology over its lifetime [45], industry already shows an lively and increasing interest in the perovskite technology. Worldwide more and more established and start-up companies are working on upscaling and commercialization of perovskite based PV or tandem PV, light-emitting diodes (LEDs) and displays, quantum dots, sensors, photodetectors and other perovskite applications (Table 1.1) [46].

The continuously increasing number of companies of currently ~25 shows the high potential of a market entry of a perovskite product in the near future [48, 49]. Therefore, the United States Department of Energy recently announced the Solar Energy Technologies Office Fiscal Year 2020 Perovskite Funding Program to support research and development in order to advance perovskite PV devices, manufacturing and performance validation and selected 22 projects to receive $40 million [50]. The author believes that it is desirable, if the European Union would initiate a similar program.

Despite rapid progress of the PCE of solution processed PSCs, various scientific and technological challenges still exist to this day. This fact furthermore motivates and justifies additional intense research efforts on the subject of solution processing perovskite absorbers. Here, one needs to name for instance the ongoing discussion on which perovskite conversion method exhibits the highest potential for upscaling, the acquirement of an improved procedural understanding about controlling the perovskite morphology or the technological demonstration of upscaling the superior conversion method. The novel realization of fully green solvent systems especially for the more stable multi-cation (MC) perovskite compounds and the implementation and optimization of SDC as a scalable solution deposition technique, which is even closer to a future industrial process than BC, are important proximate steps. Some of these challenges are examined in more detail within this thesis.

1.2 Aim of this thesis

As demonstrated in the introductory comments, one of the main challenges of the perovskite based PV is the currently still in general lower performance on large and application relevant device areas, respectively. In this work a suitable perovskite conversion method is developed and investigated via solution processing which allows the long-term transfer from unscalable to scalable printing techniques in order to upscale the perovskite technology with its excellent efficiencies on solar cell active areas of a few mm^2 to relevant areas of several m^2 without loss of performance. Besides the independent application of large-area PSCs, the latter is

Table 1.1: Overview of key companies worldwide in 2021 working on the commercialization of perovskite based applications.

Company name	Application	Location
Oxford PV Ltd.	Tandem PV	UK/Germany
Helio Display Materials Ltd.	LEDs/Displays	UK
PeroLED Ltd.	LEDs/Displays	UK
Power Roll Ltd.	Flexible PV	UK
TubeSolar AG (with Ascent Solar Technologies Inc.)	Flexible Tandem PV	Germany
Saule SA	Inkjet PV	Poland
PEROVSKIA SA	Printed PV	Switzerland
Valais Perovskite Solar (VPS) SA	Flexible PV	Switzerland
Evolar AB	Tandem PV	Sweden
PeroSolar AG	Flexible PV	Turkey
BlueDot Photonics Inc.	PV modules	USA
Tandem PV Inc.	Tandem PV	USA
Solar-Tectic LLC	Tandem PV	USA
Swift Solar Inc.	Flexible Tandem PV	USA
CubicPV Inc. (fmr. Hunt Perovskite Technologies LLC)	Tandem PV	USA
Energy Materials Corp. (EMC)	Flexible R2R PV	USA
Microquanta Semiconductor Ltd.	PV modules	China
Wonder Solar Ltd.	PV modules	China
Wuxi Utmost Light Technology (UtmoLight) Ltd.	PV modules	China
PEROLED Ltd. Korea	LEDs/Displays	South Korea
Panasonic Corp.	Printed PV	Japan
Toshiba Corp.	Flexible PV	Japan
EneCoat Technologies Ltd.	Flexible R2R PV	Japan
Nanolumi Pte. Ltd.	LEDs/Displays	Singapore
P3C Technology and Solutions Ltd.	Printed PV	India
Greatcell Energy Ltd.	PV modules	Australia

Data from [46, 47].

central primarily with regard to modules or tandem modules. The majority of scalable solution deposition techniques utilized for thin film PV have already been established for instance in longtime research on organic photovoltaic (OPV) [51]. Moreover, solution processing enables, especially in the case of well-known R2R coating, the cost-efficient fabrication of thin films with higher throughput [52] compared to vapor phase deposition techniques without the need for expensive and complex vacuum systems [53]. Furthermore, for upscaling to mass production and commercialization, stable perovskite compositions and appropriate handling of toxic precursor solvents during perovskite solution processing are additional tasks that have to be tackled already

during the initial development phase of PSCs. Consequently, the author focuses on these tasks in this thesis.

In order to overcome the aforementioned challenges, the scientific aims of this thesis are formulated as follows:

Aim 1: Identifying the most promising perovskite conversion methods for upscaling.

Aim 2: Understanding the heat-assisted perovskite conversion for $MAPbI_3$ (MAPI) based solar cells processed by scalable techniques.

Aim 3: Investigation of methods for controlling and optimizing MAPI perovskite morphology (via gas-assisted conversion).

Aim 4: Demonstration of large-area perovskite solution processing and module fabrication.

Aim 5: Evaluation of scalable multi-cation (MC) perovskite deposition from a standard and a green solvent system (via gas-assisted conversion).

Aim 6: Implementation and optimization of slot-die coating (SDC) for processing MC perovskite (via gas-assisted conversion).

This thesis focuses on solution processing of hybrid perovskite by blade coating (BC) as an example for a scalable printing technique and further down by SDC as more industry relevant scalable deposition technique. Thereby, two perovskite conversion methods are investigated, the heat- and the gas-assisted conversion. Furthermore, the focus lies on two perovskite types, the standard MAPI and a multi-cation composition. Besides the scientific aims, a technological implementation for a static low-pressure and a moving high-pressure gas system had to be established for this thesis to enable the deposition of both perovskite types, respectively. The utilized fabrication recipes are consecutively analyzed and optimized in the course of this thesis.

This thesis was realized at the Zentrum für Sonnenenergie- und Wasserstoff-Forschung Baden-Württemberg (ZSW) in Stuttgart, Germany.

1.3 Outline of this thesis

This thesis is structured into seven chapters.

Firstly, Chapter 1 introduces the reader to the topic of the thesis and specifies objectives. The chapter includes the motivation of this thesis (Section 1.1) and the definition of its scientific aims (Section 1.2).

Chapter 2 describes the theoretical fundamentals of perovskite solar cells and modules which are essential for understanding the investigations carried out in this thesis. Thereby, an overview of the state of art is given. The subjects discussed in this chapter comprise the properties and working principle of perovskite solar cells (Section 2.1) including photovoltaic device architectures and current research challenges. Furthermore, the fundamentals of upscaling perovskite solution processing are discussed (Section 2.2). This section implies an overview of scalable deposition techniques, the basics in nucleation and crystal growth kinetics, and a discussion of conversion methods of perovskite wet films and their potential for upscaling (Aim 1), followed

by the illustration of fluid dynamics in heated wet films. Additionally, the theoretical background of PSMs is presented (Section 2.3).

The experimental methods for preparation and characterization utilized for this thesis are described in Chapter 3 including all preparation steps of perovskite solar cells and modules (Section 3.1) and characterization methods (Section 3.2).

The first main result part of this thesis Chapter 4 highlights the scientific Aim 2 of understanding the heat-assisted perovskite conversion for MAPI based solar cells processed by scalable techniques. For this purpose, the principles of heat-assisted perovskite conversion are investigated without the use of a surfactant (Section 4.1). Subsequently, a study on the utilization of a surfactant via heat-assisted conversion follows (Section 4.2). As a conclusion of these studies, a different conversion method is suggested (Section 4.3).

In the following Chapter 5, methods for controlling and optimizing the MAPI perovskite morphology are investigated via gas-assisted conversion (Aim 3) in order to scale up blade coated MAPI based solar cells and modules. In doing so, this conversion method is developed at first (Section 5.1) including the technological establishment of a static low-pressure gas system. Afterward, the perovskite morphology processed with gas-assisted conversion is further optimized (Section 5.2) with the aid of a blade coated nanoparticle wetting agent and precursor solution composition engineering. In Section 5.3, the efficiency of solar cells is increased by layer thickness optimizations of the absorber and the hole transport layer. Furthermore, large-area perovskite solution processing and module fabrication is demonstrated (Aim 4) in the subsequent Section 5.4. Section 5.5 concludes Chapter 5.

By means of the findings of the prior chapter, gas-assisted conversion can be transferred from its use for depositing MAPI films to processing a different perovskite composition in Chapter 6. The chapter depicts the evaluation of scalable perovskite deposition from suitable solvent systems for multi-cation perovskite solar cells via blade coating (Section 6.1), firstly from a standard toxic and secondly from a green solvent system (Aim 5) in Section 6.2. This evaluation is enabled by the previous technological establishment of a moving high-pressure gas system. Subsequently, results on the implementation and optimization of slot-die coating of multi-cation perovskite via gas-assisted conversion are described (Aim 6) in Section 6.3. Finally, the potential for further optimizations is discussed (Section 6.4). Section 6.5 concludes Chapter 6.

Chapter 7 concludes this thesis by summarizing the most relevant results (Section 7.1) and by giving an outlook (Section 7.2).

2 Fundamentals of perovskite solar cells and modules

This chapter gives an overview on the specific fundamentals, theories, and recent research progress related to the topics which regards this thesis. The chapter is divided into three sections covering the properties of perovskite solar cells, discussing perovskite upscaling by solution processing and introducing perovskite solar modules.

The first Section 2.1 explains the properties and working principle of perovskite solar cells. After introducing hybrid perovskite as photovoltaic absorber and its properties (Subsection 2.1.1) a brief introduction on the working principle and characteristics of perovskite solar cells is given (Subsection 2.1.2). Subsequently, device architectures of planar perovskite solar cells are illustrated (Subsection 2.1.3). The section is finalized by a short overview on the current research focus and challenges of the perovskite technology (Subsection 2.1.4).

The subsequent Section 2.2 focuses on the upscaling of perovskite solution processing. Thereby, the first subsection summarizes scalable deposition techniques (Subsection 2.2.1), whereas the second comments on the basics of nucleation and crystal growth kinetics (Subsection 2.2.2). Furthermore, conversion methods of perovskite wet films are defined and their potential for upscaling are discussed (Subsection 2.2.3). Finally, fluid dynamics in heated wet films are shortly explained (Subsection 2.2.4).

Section 2.3 briefly introduces perovskite solar modules. Thereby, mainly the serial interconnection design is presented (Subsection 2.3.1). Additionally, a few details on the optimization of the cell width of modules are given (Subsection 2.3.2).

2.1 Properties and working principle of perovskite solar cells

This section refers to the properties and working principle of perovskite solar cells. The following subsections explain the crystallographic and optoelectronic properties of hybrid perovskite utilized as photovoltaic absorber (Subsection 2.1.1), describe the working principle and current-voltage characteristics (Subsection 2.1.2) and the architectural concept of planar perovskite solar cells (Subsection 2.1.3), and present an overview on the current research focus and challenges of perovskites, such as hysteresis, stability, toxicity or upscaling (Subsection 2.1.4).

2.1.1 Properties of hybrid perovskite as photovoltaic absorber

Perovskites are a material class with the crystal structure of the inorganic compound calcium titanate ($CaTiO_3$) which was discovered by the German mineralogist Gustav Rose in 1839 [54] and named after the Russian mineralogist Lev Perovski. As a mineral it is called perovskite.

Crystallographic properties

Perovskites are described by the formula ABX_3. In case of organic-inorganic hybrid perovskites, A denotes a monovalent organic cation, B a divalent metal cation, and X a halide anion. The B cations are coordinated with X anions forming BX_6 octahedrons which are connected with each other. Figure 2.1 visualizes the cubic perovskite crystal structure [55].

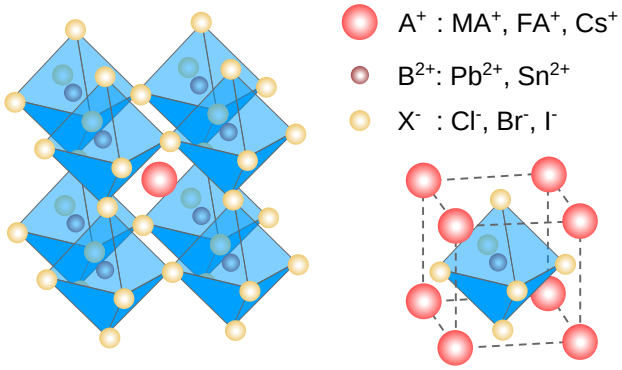

Figure 2.1: Schematic illustration of the unit cell of cubic perovskite crystal structure with a formula of ABX_3.

In an organometal halide perovskite crystal, A is for instance a methylammonium (MA^+), formamidinium (FA^+) or cesium (Cs^+) ion, B a lead (Pb) or tin (Sn) cation and X a chloride (Cl^-), bromide (Br^-) or iodide (I^-) ion as listed in Figure 2.1. The best known organic-inorganic halide perovskite is methylammonium lead triiodide ($MAPbI_3$), so-called MAPI [56]. Moreover, perovskites with multiple anions, metals, and cations also referred to as multi-cation (MC) perovskites are gaining increasing attention in the research community [57, 58].

One of the major advantages of perovskites is the possibility to integrate different cations and anions in the ABX_3 crystal structure which opens up the field of tunable semiconductor properties such as the band gap energy (E_g) as mentioned further down.
The size and interaction of the A-site and BX_6 octahedrons determine the structure of an ABX_3 compound [59]. The empirical so-called tolerance factor (t) introduced by Victor Goldschmidt in 1926 [60] describes expectable crystal structure and contortion [59] of potential compounds:

$$t = \frac{R_A + R_X}{\sqrt{2}\,(R_B + R_X)} \tag{2.1}$$

where R_A, R_B, and R_X are the effective ionic radii of the A, B, and X ion, respectively. An ideal cubic perovskite structure is formed for $t = 1$ [61]. The tolerance factor describes to what extent the cation A can be integrated in the interstitial. For $0.81 < t < 1.11$, the formation of a perovskite compound is expectable [61, 62]. For $0.9 < t < 1.0$, it presumably crystallizes in a cubic structure. However, for $0.81 < t < 0.9$ the cubic structure might be distorted due to tilting of the BX_6 octahedrons leading to less symmetric tetragonal and orthorhombic phases [61, 62]. If the cation A is too large ($t \gg 1$), lower-dimensional 2D perovskite phases are formed instead of a bulk 3D structure [61].
For more precise predictions, the additional octahedral factor (μ), which is a measure of BX_6 octahedral stability, can be utilized which is described as

$$\mu = \frac{R_B}{R_X} \tag{2.2}$$

and needs to fulfill the condition $0.44 < \mu < 0.90$ for the formation of a symmetrical octahedron and of perovskite [61, 62].

The concept of t and μ can be extended for perovskite materials with more complex compositions. For instance, for a multi-cation perovskite with a composition $A_yA'_{1-y}BX_3$ [63], the tolerance factor can be determined as:

$$t = \frac{yR_A + (1-y)R_{A'} + R_X}{\sqrt{2}\,(R_B + R_X)}. \tag{2.3}$$

The formation of the three photoactive perovskite (black) phases, such as the cubic (α-), tetragonal (β-) or orthorhombic (γ-) phase, as well as of photoinactive non-perovskite (yellow) phases, like the hexagonal (δ-) phase, highly depends on the temperature. Phase transition temperatures are contingent on the perovskite composition. The archetypal $MAPbI_3$ composition shows phase transitions at 165 K and 327 K. It generally crystallizes in a tetragonal crystal structure at room temperature (RT) and the cubic phase is formed at a temperature of >327 K, while the orthorhombic crystal phase is preferred at a temperature of <165 K [34, 64–67].

Optoelectronic properties

Besides the reason of easy processability, the metal organic perovskite compounds are utilized in optoelectronic devices such as photovoltaic cells due to their outstanding optoelectronic properties. The main features of a perovskite semiconductor such as MAPI are:

- A high absorption coefficient (α) in the order of 10^4 to 10^5 cm^{-1} [68–71] which implicates that an absorber thickness of 300 to 600 nm is enough to entirely absorb sun light with a higher energy than E_g [72].
- A low exciton binding energy (E_b) of <25 meV [73–76] which is smaller than the thermal energy at RT and results in an instantaneous dissociation of the excitons in free charge carriers.
- A long charge carrier lifetime (τ_c) of >1 µs [77] which arise from a low perovskite recombination rate and defect density.
- A high charge carrier mobility (μ_c) of 10 to 40 $cm^2\,V^{-1}\,s^{-1}$ [78, 79].
- A long charge carrier diffusion length (L_c) of >1 µm [80, 81], which is clearly longer than the thin film absorption length. Similar charge carrier diffusion lengths for electrons and holes indicate an ambipolar transport of charge carriers inside the absorber [80, 82–84].
- A tunable band gap energy E_g [85, 86].

The band gap energy E_g plays a central role in all optoelectronic applications. However, there is an ongoing discussion in literature if metal organic perovskites are classified as direct or indirect semiconductors. Generally, the majority of reports agree on the fact that a direct optical

transition dominates the optical properties of the compound [70, 87–91]. Nevertheless, there are also reports discussing a second indirect band transition [87, 89, 92–95].

The band structure and, thus, the band gap primarily results from the properties of the BX_6 octahedron whereas the band structure is only slightly altered by the A cation. Consequently, the band gap of metal halide perovskites can be mainly adjusted by varying the B cation and X anion [66, 96–98].
In order to increase E_g, normally iodine (I) is partly or fully substituted by bromine (Br). Thus, MAPI and methylammonium lead tribromide ($MAPbBr_3$) exhibit a E_g of ~1.55 eV [70] and a considerably higher 2.28 eV [99, 100], respectively. Consequently, a partly substitution allows the variation of E_g between the two values and thereby over the whole visible range of the sun spectrum [85, 100–102]. This fact is essential for any tandem application [34, 35, 103].
To reduce E_g, typically the Pb is replaced by Sn reaching a E_g of 1.3 eV for methylammonium tin triiodide ($MASnI_3$) perovskite [104].
Although the A cation has no direct influence on the band structure, it alters the band gap indirectly. For instance, replacing MA^+ by Cs^+ ions leads to a change in lattice constant and, hence, to a E_g of 1.73 eV for cesium lead triiodide ($CsPbI_3$) perovskite [105].

2.1.2 Working principle and characteristics of perovskite solar cells

In this subsection the working principle and characteristics of perovskite solar cells are discussed. However, primary knowledge on the physics of a solar cell are presupposed. For further details, the author recommends reference [106].

Working principle

Solar cells convert the energy of the incident light via chemical energy into electrical energy [106]. The fundamental processes in solar cells which occur during this conversion are:

(i) Absorption of incident photons by the active absorber,

(ii) creation of a bonded electron–hole pair (exciton),

(iii) dissociation of the exciton into free charge carriers,

(iv) spatial separation of the two types of charge carriers, and

(v) extraction of the two types of charge carriers via the selective contacts.

In contrast to a p-type–n-type (p-n) junction of Si solar cells [107, 108], PSCs are normally produced in a p-type–intrinsic–n-type (p-i-n) heterojunction due to the excellent optoelectronic properties of perovskite as explained in the previous Subsection 2.1.1. Figure 2.2 demonstrates the band diagram and working principle of a PSC with selective contacts.

Compared to p-n solar cells, here, there is no doping of the absorber needed. For charge carrier separation, the intrinsic undoped absorber is placed between an electron and a hole selective charge transport layer (CTL) [109], respectively.

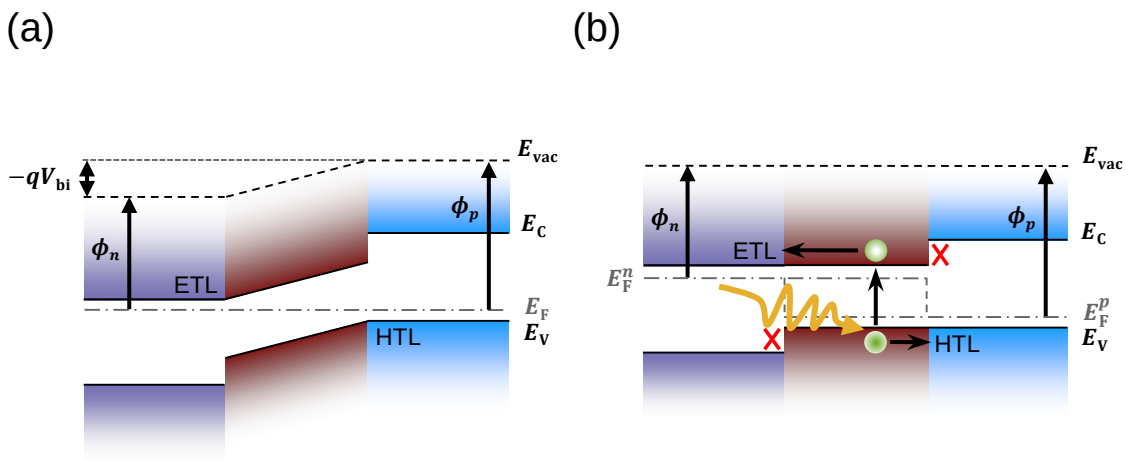

Figure 2.2: Schematic illustration of a band diagram of p-i-n solar cells (a) in equilibrium in the absence of light and bias voltage and (b) under illumination and at open circuit condition.

Transmission and thermalization together with radiative recombination losses of a solar cell lead to a significantly decreased PCE compared to the thermodynamic limit of the conversion process from radiation to electrical energy, the so-called Shockley–Queisser limit (SQL) [110]. Besides the incident spectrum, the maximum possible PCE is apparently primarily defined by E_g of the absorber. For a Si or CIGS solar cell with a E_g of ~1.1 eV, which is the range of an ideal E_g of 1.1 to 1.4 eV, the theoretical efficiency limit under the AM1.5 global standard solar spectrum (AM1.5G) is ~32 %. For a PSC with a E_g of 1.6 eV, it is ~30 % [111].

Electrical equivalent circuit

In its simplest way, a solar cell is modeled by an electrical equivalent circuit composed of a single-diode in parallel with a direct current (I) source, which is the photogenerated current, in short photocurrent (I_{ph}), under sunlight illumination. Moreover, a shunt resistance (R_{sh}) and a series resistance (R_s) are added (Figure 2.3). They represent any leakage current due to imperfections caused by pinholes in the absorber leading to direct contact between the two electrodes, and the electrical resistance of the solar cell due to charge transport and injection, respectively [112, 113].

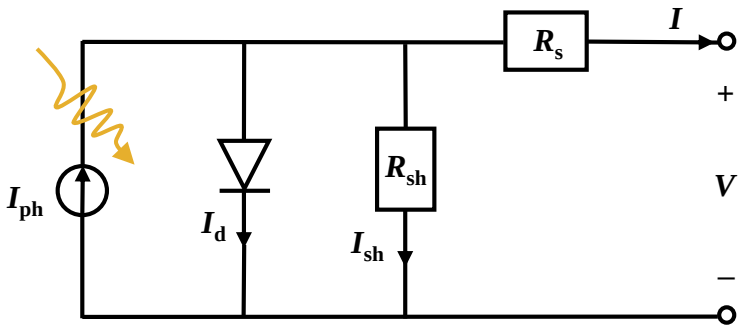

Figure 2.3: Electrical equivalent circuit of a solar cell based on a single-diode model.

The current I produced by this circuit, which is equivalent to the current produced by the solar cell, is estimated by means of I_{ph}, the dark current of a diode (I_d), which is calculated by the Shockley diode equation, and the shunt current (I_{sh}) determined by Ohm's law [113, 114]. Thus, the relation between the current I and the voltage (V) is given by

$$I(V) = -I_{ph} + I_d + I_{sh} = -I_{ph} + I_0 \left[\exp\left(\frac{q(V - I(V)R_s)}{nk_B T_a} \right) - 1 \right] + \frac{V - I(V)R_s}{R_{sh}} \tag{2.4}$$

where I_0 is the dark saturation current, n is the diode ideality factor, q is the electron charge, k_B is the Boltzmann constant and T_a is the absolute temperature of the solar cell.

The two-diode model can result in a more accurate description of experimental data as it includes the recombination mechanisms of the charge carriers as well [106, 115].

Current-voltage characteristic

The performance of a solar cell is determined from its current–voltage dependency (IV) characteristics. The power conversion efficiency (PCE), the most important characteristic to describe the performance of a solar cell, can be represented as

$$\text{PCE} = \frac{P_{max}}{P_{in}} = \frac{I_{MPP} \cdot V_{MPP}}{P_{in}} = \frac{I_{SC} \cdot V_{OC} \cdot \text{FF}}{P_{in}} \tag{2.5}$$

where P_{max} is the maximum generated electrical power output and P_{in} is the incident radiative power [114]. Under standard test conditions, an irradiation of power of $1000\,\text{W}\,\text{m}^{-2}$ with an AM1.5G spectrum at 25 °C [116] is considered as the incident power.

Both R_{sh} and R_s significantly influence the FF of a solar cell. To maximize FF, R_{sh} and R_s should be high and low, respectively.

2.1.3 Device architectures of planar perovskite solar cells

In a planar perovskite photovoltaic device architecture, the perovskite absorber can be placed in two configurations between the two CTLs, the electron selective CTL also called electron

transport layer (ETL) and the hole selective CTL also called hole transport layer (HTL), as illustrated in Figure 2.4.

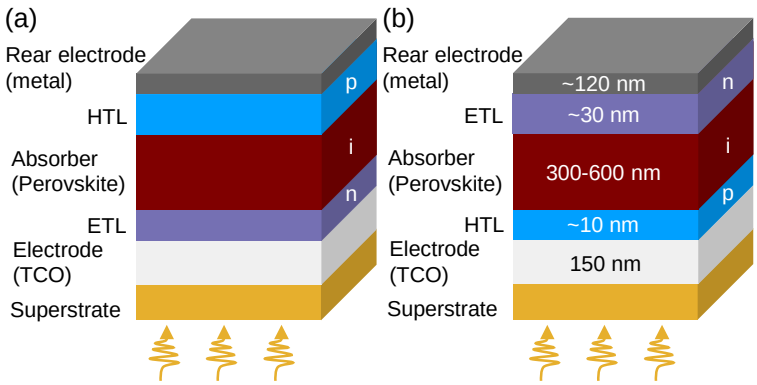

Figure 2.4: Schematic illustration of different device architectures of planar perovskite solar cells in (a) standard or n-i-p and (b) inverted or p-i-n configuration with light incident from the glass side.

To enable light transport into the solar cell a transparent front electrode also called transparent conductive oxide (TCO), for instance indium tin oxide (ITO) or fluorine-doped tin oxide (FTO), is utilized.
Depending on the polarity of the selective CTL facing the incident light, one refers to the standard (n-type–intrinsic–p-type (n-i-p)) or the inverted (p-i-n) configuration as displayed in Figure 2.4a and Figure 2.4b, respectively. This thesis focuses on the p-i-n configuration.

Figure 2.5 gives an overview of materials [117–121], namely perovskite compositions, electron transport materials (ETMs), hole transport materials (HTMs), TCOs and metals which are commonly utilized in PSCs as absorber, ETLs, HTLs, front and rear electrodes, respectively. In addition, their energy levels are indicated.

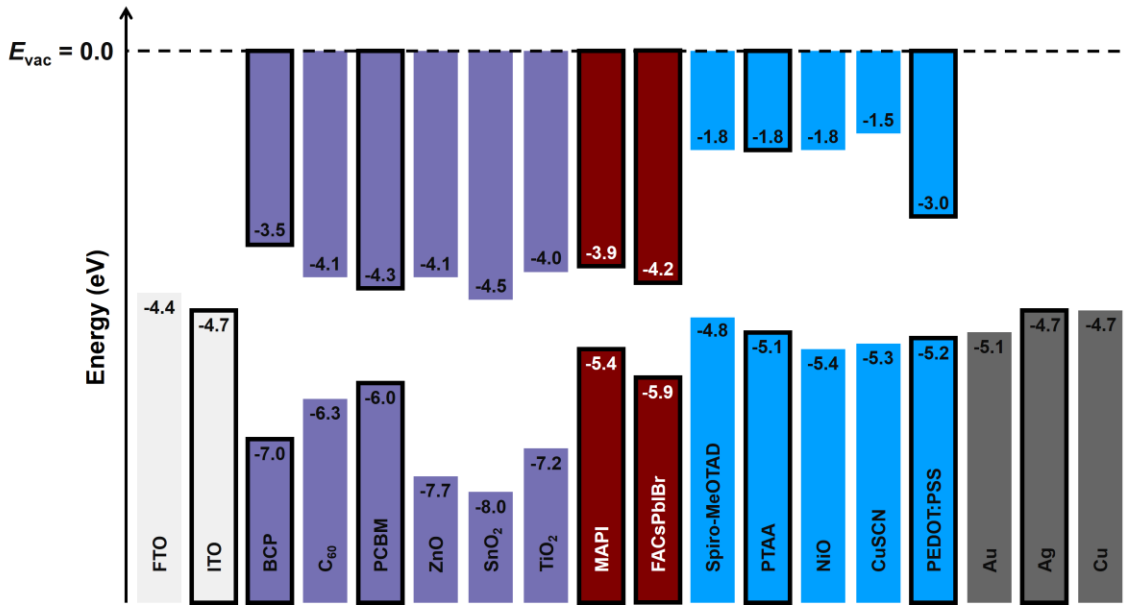

Figure 2.5: Schematic energy level diagram with valence band maxima and conduction band minima of typical ETMs (purple) and HTMs (blue) for PSCs as well as transparent front electrodes (light gray), such as FTO and ITO, and metal rear electrodes (gray), like gold (Au), silver (Ag) and copper (Cu), compared to the absorber, the archetypal MAPI and double-cation perovskite (FACsPbIBr) (brown). Materials framed in black are utilized in this thesis. Data from [39, 117, 118, 120, 122–125].

The function of the selective CTLs is mainly the charge carrier separation via spatial selectivity as mentioned in Subsection 2.1.2. According to that, the energy levels have to be selected in such a way that one type of charge carrier passes the material and is transported to the particular electrode. Hence for ETLs, the energy of the conduction band minimum needs to be lower than the one of the perovskite absorber. Furthermore, the energy of the valence band maximum should be also lower than the one of the perovskite to effectively inhibit the transport of holes. For HTLs, the opposite is valid.

In addition to the electrical properties of the selective CTLs, the optical transmittance (T) of the CTL facing the incident light is critical for solar cell performance and should be as high as possible in order to hinder parasitic absorption since PSCs are normally based on a superstrate concept where the transparent substrate is responsible for light incoupling.

2.1.4 Current research focus and challenges

As for every new technology, there are challenges of perovskite solar cells [38, 126–130] as well which have to be addressed before a commercial application. Thus, to the four biggest challenges is shortly responded below.

Hysteresis

One challenge with regard to the comparability and reproducibility of perovskite solar cells is the so-called hysteresis behavior of the current density–voltage dependency (*JV*) scan. Already in early stages of PSC research, it was reported that measurement parameters have a tremendous impact on the determination of the *JV* curve and therefore on the extracted characteristic photovoltaic device parameters [131,132]. In doing so, scan direction and scan speed [133–137], or preconditioning by voltage bias or illumination [133,138] as well as device temperature [139] influence the resulting shape of the *JV* curve. The forward (*fwd*) scan direction indicates the $V = 0\,\mathrm{V} \rightarrow V = V_{\mathrm{OC}}$ scan (referred to as "up" measurement) and reverse (*rvs*) scan direction the one in opposite direction (referred to as "down" measurement).
Since the discovery of the effect, there is a continuing tremendous effort to explain the origin of the hysteresis but it is not fully clarified till this day. Several studies show that the underlying mechanism causing hysteresis is mainly the migration of ions, such as MA^+ and I^- ions, and their vacancies in the perovskite crystal structure [140–143]. The ion movement caused by the built-in electrical field at the interfaces of the perovskite absorber and the charge selective contacts, the HTL and ETL, results in an accumulation of ionic charges at the interface. Therefore, an internal electric field is created which is reverse to the built-in electrical field [143, 144] reducing the photocurrent extractable from the solar cell [134]. In the extreme case, this can lead to a complete compensation of the built-in field [145, 146]. By changing the applied voltage (*V*), the built-in electrical field and the accumulation of charge carriers can be increased or compensated. Since ion migration occurs in larger timescales than the electron and hole transport of milliseconds to seconds due to their relatively large masses which are similar timescales than the *JV* measurements [134, 147], scan speed and bias preconditioning have an influence on the *JV* characteristics.

Strategies to reduce hysteresis are primarily based on the optimization of the charge carrier extraction at the interfaces of the absorber. The accurate choice of the CTLs has a significant influence on reducing hysteresis [133, 148–151]. Furthermore, perovskite morphology might have an impact as well [152–154].

For better comparability, continuous load of the solar cell at its maximum power point (MPP) also called MPP tracking is typically performed to determine a meaningful value for the PCE.

For more details on hysteresis, the author recommends references [140, 155, 156].

Stability

Clearly, the major challenge for commercialization of PSCs is their long-term stability [120, 157–159] in order to reach a lifetime guarantee of at least 20 years and thereby to be able to compete with Si solar cells. Besides degradation due to thermal stress [160–163] and thermal cycling [164], PSCs can degrade in the presence of light, in particular ultraviolet (UV) radiation [71, 165–169], oxygen (O_2) especially in combination with UV radiation [170–173], water (H_2O) and thereby moisture as well [174–177]. These degradation mechanisms can be mainly ascribed to the intrinsic absorber material instability but also to the instability of CTLs [178–180] and device contacts [181, 182].

Thermal instability at elevated temperatures is associated with the low crystallization temperatures of metal organic perovskites. In order to increase thermal stability of the perovskite, the

organic cation, normally MA^+, is partly or fully replaced by Cs^+ and/or FA^+ ions [162, 183–185] which in addition hinders light-induced halide segregation [186, 187].

The UV degradation is mostly prominent in PSCs with photocatalytic metal oxides such as titanium oxide (TiO_2) [169,188,189] and arises from the light-induced desorption of O_2 adsorbed at the surface [158, 167, 188]. Replacing TiO_2 by other oxides such as tin oxide (SnO_2) or nickel oxide (NiO) can help to improve device stability [169, 188, 190, 191].

The main reason for degradation in presence of O_2 in conjunction with light are the small chemical reaction kinetics of the decomposition reaction [167, 171]. Under the same conditions, perovskites with FA^+ degrade less compared to MA^+ due to a lower deprotonation probability of the FA^+ cations [171].

Moisture sensitivity of perovskite is mainly due to the intrinsic properties of the metal organic perovskite material such as good solubility in H_2O as well as the hygroscopic nature of the amine group of the organic salt [159]. In addition to encapsulation of devices which also prevents O_2 contact [192–195], the development of 2D perovskite layers on top of a 3D perovskite [196–201] or utilizing hydrophobic layers in the device architecture [202, 203] are successful strategies to reduce moisture sensitivity.

Despite all degradation pathways, standardized industrial certification tests [204] for thin film solar modules, including damp heat tests, have been already passed by PSCs [193, 205–207]. To reach long-term PSC stability and elongated application periods, not only the perovskite absorber but all layers in the device stack need to fulfill the stability requirements.

Toxicity

Another challenge of PSCs is their toxicity. At this point, one can divide between the toxic Pb [208, 209], which is the integral component of most hybrid perovskites in the case of highly efficient PSCs, and the perovskite solution processing via toxic solvents [210–212] such as the most commonly used dimethylformamide (DMF).

Concerning the former challenge, there are contradictory assumptions on the hazard of Pb containing PSCs [209, 213–215]. While some studies emphasize the toxicity of Pb [208, 216], the expected processed amount of Pb during manufacturing and the amount which might be released from a PSC even for a complete failure of an encapsulation ending up in the soil is relatively small [213, 214]. Nevertheless, the use of heavy metal fractions in electronic devices is critical due to their confirmed toxicity and is restricted by the European Union since 2011, however the PV sector is excluded so far [217]. The toxicity is intensified by the excellent aqueous solubility of the utilized lead salts as mentioned above. Various approaches to fabricate Pb-free alternatives have been pursued [218–221] such as Sn-based perovskite compounds [222–224] but generally with a clear reduction in PCE of solar cells [225, 226] and as well implicating chemical instabilities [227] and health risks [209]. Besides replacing Pb, research further concentrates on concepts to hinder the elution of Pb during application via suitable encapsulation strategies [28, 228, 229].
Despite the use of Pb, life cycle assessments (LCAs) show that PSCs represent the potentially most environmentally friendly technology compared to established PV technologies [210, 212] in case their lifetime can be significantly enhanced, and Pb only plays a minor role [230, 231]. In addition, potential recycling of Pb has been demonstrated [232, 233]. Moreover, the technology promises energy payback times (EPBTs) of clearly <1 year [212, 234].

In the author's opinion, the second concern of toxic solvents is the larger issue which hinders paving the way for commercialization. Furthermore, low toxicity solvent systems could end up in a remarkably more cost-effective option in the intermediate and longer term as potential alternate solvent production routes develop [235] due to less required safety precautions. Alternative industry-friendly solvent systems for processing the perovskite absorber are investigated [236–238] but reach lower maximum PCE compared to their toxic counterparts [236, 239, 240]. Section 6.2 deals with the subject of replacing toxic solvent systems by a green alternative for a multi-cation perovskite composition.
Solution-free fabrication processes such as vacuum deposition via for instance thermal evaporation might be an option as alternative to solution processing [241].

Upscaling

Despite the astonishing achievements in depositing perovskite on small lab scale, large-scale PSCs to date still lag behind the established photovoltaic technologies [16, 242]. As mentioned in Section 1.1, for practical applicability and industrial relevance of perovskite based materials in solar cells upscalability of the technology is particularly required concerning on the one hand upscaling of areas and on the other hand of operational throughput. Currently, all presented PCEs >23 % are based on perovskite absorber layers deposited by SC as illustrated in Figure 1.1a. However, by means of SC homogeneous perovskite film areas of only a few cm^2 can be deposited. Especially the antisolvent-assisted perovskite conversion method typically utilized with SC is hardly scalable (see Subsection 2.2.3). Another challenge is the fabrication of perovskite under ambient conditions due to the above described instability against H_2O and O_2. The main focus in upscaling the perovskite technology lies generally on solution processing due to the in principle perspectively low manufacturing and LCOE [243]. Thereby, promising results on areas >50 cm^2 have already been reported in particular with the scalable deposition techniques of BC and SDC [21] as presented in Figure 1.1b. Thereby, R2R production is the goal aimed for in the long run [244–247]. The to date highest PCE of 17.9 % on the largest designated illumination area of a rigid PSM of ~800 cm^2 has been achieved in 2020 by the Japanese company Panasonic via inkjet printing [12, 242]. Furthermore in 2021, the Japanese company Toshiba claimed a PCE of 15.1 % on a flexible PSM active area (A_{act}) of ~700 cm^2 through one-step meniscus coating [248] as illustrated in Figure 1.1b. However, solution processing are linked to certain hurdles such as the high complexity of a homogeneous drying, nucleation and crystallization of the wet film on large areas [21] which is the major aim of this thesis. Besides solution processing, scalable vapor phase deposition techniques are currently starting to prosper [53, 191, 241, 249].

2.2 Upscaling of perovskite solution processing

The following section refers to the fundamentals of upscaling perovskite solution processing by scalable deposition techniques, which are presented firstly (Subsection 2.2.1). After covering the basics on nucleation and crystal growth kinetics (Subsection 2.2.2), the four typical conversion methods of perovskite wet films, namely antisolvent-, vacuum-, heat-, and gas-assisted conversion, are specified and their potential for upscaling is briefly discussed (Subsection 2.2.3). Additionally, fluid dynamics in heated wet films including the Rayleigh–Bénard and Marangoni convection are noted (Subsection 2.2.4).

2.2.1 Scalable deposition techniques

The for this thesis main scalable deposition techniques for solution processing of perovskite, blade coating [250, 251] and slot-die coating [252], are presented in the following. Further solution processing techniques for perovskite [21, 22, 24, 40, 58, 253–256] are spray coating (SPC) [257–259], inkjet [260–262], and for PSCs unusual gravure printing [263, 264]. Screen printing is typically not used to deposit perovskite but to fabricate charge transport or contact layers in PSCs [265–270].

Besides solution processing of perovskite, vapor phase deposition techniques under vacuum conditions, which are scalable as well, such as sequential evaporation [22] or co-evaporation [241] are by now well-established to deposit perovskite films. Furthermore, a combination of vapor phase deposition and solution processing has been reported [271].

Blade coating

Blade coating (BC), also called knife coating or doctor blading, is a robust single directional meniscus coating technique with low investment cost, is highly adjustable and suitable not only for rigid substrates but also for flexible ones. In order to deposit a wet thin film, a fixed quantity of ink, here of the perovskite precursor solution, is applied in front of the blade forming a liquid meniscus between the blade and the substrate. The blade is then moved forward relative to the substrate to spread a homogeneous wet thin film on the substrate as illustrated in Figure 2.6. For this purpose, either the blade or the substrate is moved. D-bar coating is similar to blade coating at which a cylindrical bar is utilized instead of the blade where the liquid solution is directly loaded onto [21, 40, 51].

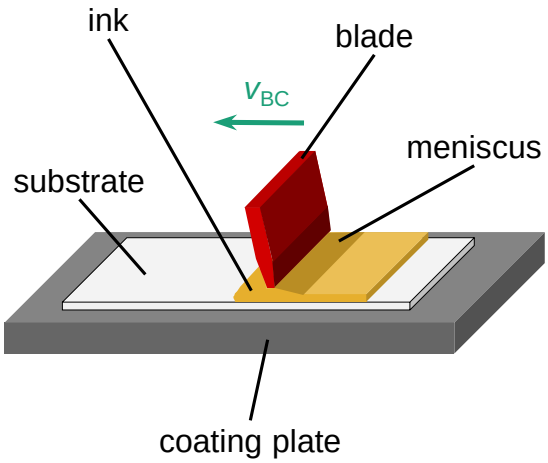

Figure 2.6: Schematic illustration of blade coating (BC).

The wet film thickness (d_{wet}) of the deposited thin film depends, besides the meniscus itself, generally on several factors including the concentration of the precursor ink, the gap height between blade and substrate, and the blade coating velocity (v_{BC}) at which the blade moves relative the substrate [272]. Further factors influencing d_{wet} are the quantity of the applied ink

volume, the dynamic viscosity (η) of the ink, the blade geometry, and the substrate wettability. For blade coating, the ink waste is substantially reduced compared to the lab-scale spin coating. The coating technique can not only been used in a sheet-to-sheet (S2S) but also in a R2R setup, in which the blade is stationary and a flexible substrate on a roller is in motion [40, 51].

For blade coating of wet films with the heat-assisted perovskite conversion (see Subsection 2.2.3) at a processing temperature of 145 °C and utilizing MAPI precursors in DMF, Deng et al. derived a relationship of the perovskite dry film thickness (d) as a function of blade coating velocity v_{BC}. The relationship is presented in Figure 2.7a. It describes an evaporation (Figure 2.7b) and the Landau–Levich regime [273] (Figure 2.7c) during processing with the aid of experimental observations and measurements [274].

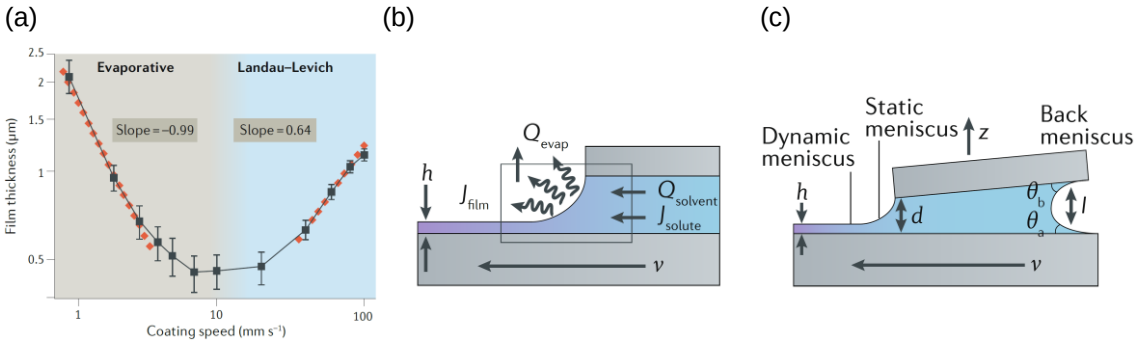

Figure 2.7: (a) Thickness of a MAPI film as a function of coating speed when the substrate is heated at 145 °C. Linear fitting determines the evaporation and the Landau–Levich regimes. (b) Evaporation regime and (c) Landau–Levich regime in more detail. Adapted with permission from [253]. © Springer Nature.

When coating speed or v_{BC} is low, coating falls in the evaporation regime where solution coating and crystallization occur simultaneously. At a high coating speed, d_{wet} increases in the Landau–Levich regime where crystallization occurs after the wet thin film formation [253,275,276]. This increase is caused by the fact that the liquid film is being dragged out by viscous forces and then by drying [277]. By contrast, d_{wet} decreases with an increase in v_{BC} in the evaporation regime because of mass-transport effects due to convection at the moving contact line and Marangoni effect (see Subsection 2.2.4) [273,277]. Solids concentrate near the contact line owing to solvent evaporation at the meniscus surface [253, 275].

Slot-die coating

Slot-die coating (SDC) is similar to blade coating but is a pre-metered scalable meniscus deposition technique in particular for R2R processes as it offers continuous ink supply. The microfluidic slot-die head, which are two metal plates forming a thin slit on the bottom side, is placed at a fixed gap height over the substrate. In the slot-die head, an ink reservoir is integrated which is connected to a solution pumping system that supplies ink at a certain rate as illustrated in Figure 2.8. Consequently, the setup requires larger quantities of ink compared to blade coating in order to fill the ink reservoir and the supply pipe but the deposition technique itself induces low ink waste [21, 40, 51, 253].

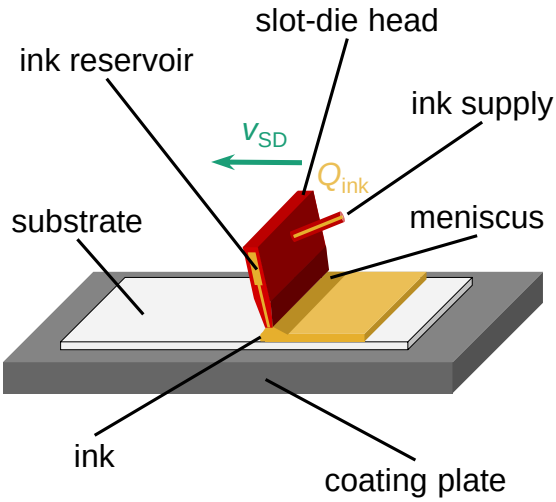

Figure 2.8: Schematic illustration of slot-die coating (SDC).

During deposition, the solution forms an up- and downstream meniscus between the dies of the head and the substrate. For a defect-free thin film, it is necessary to generate a stable coating bead [278]. Parameters defining d_{wet} are the gap height between the slot-die head and the substrate, the slot-die coating velocity (v_{SD}) and the ink pump rate (Q_{ink}) of the solution [21,40,51,253]. In addition, the coating bead, meniscus and the thickness and uniformity of the resulting film are dependent on the layout and geometry of the slot-die head [279]. Furthermore, the slot-die head can be held at elevated temperatures to alter the dynamic viscosity of the ink and solute solubility in the solution [21]. For R2R application, the head is usually positioned horizontally on a roller, whereas for S2S systems the head is commonly positioned vertically over the substrate [22].

2.2.2 Nucleation and crystal growth kinetics

For solution processing of hybrid perovskite thin films, the perovskite formation is a transition from the precursor solution state to a solid film state. During this transition process, the drying kinetics significantly influence the nucleation, intermediate (solvate) state, and crystal growth [280] which consequently affects the resulting perovskite solid film morphology.

In general, the crystal growth is dependent on two mechanisms:

i) Diffusion controlled growth, when the concentration of growth species decreases below the minimum critical concentration necessary for nucleation, crystal growth continues but nucleation stops, and

ii) surface reaction controlled growth, when growth species diffusion from the bulk to the growth surface is sufficiently rapid.

Hybrid perovskite precursor solutions exhibit intrinsically low heterogeneous nucleation rates [281]. The nanocrystal nucleation and growth kinetics of perovskite and its intermediate agrees with the classical diffusion controlled or so-called self-seeding crystal growth model [275,280–

284], the LaMer model [285], which describes the precursor solution concentration change as a function of time and is illustrated in Figure 2.9a.

It divides the crystal growth into three distinct regions or phases:

i) initial increase in solution concentration due to solvent evaporation,

ii) formation of nuclei in the solution as the growth species concentration exceeds the minimum supersaturation limit (C^*_{min}), and

iii) subsequent crystal growth by the control of growth species diffusion and a reduction in solution concentration.

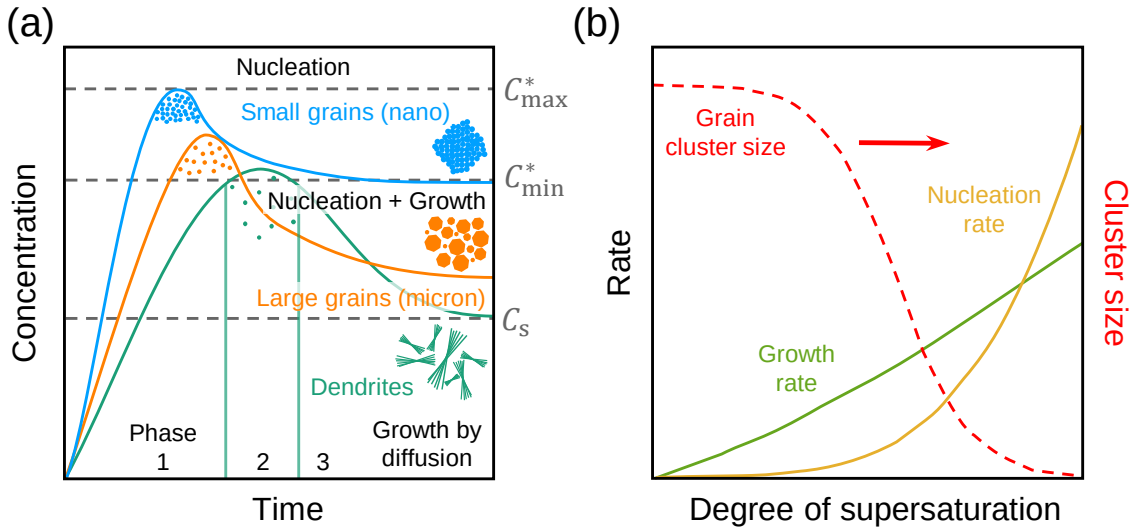

Figure 2.9: Nucleation and growth models describing the correlation between precursor solution concentration and nucleation density: (a) Classical LaMer curve for homogeneous nucleation and (b) nucleation and growth rates as a function of the supersaturation degree [247, 280–282, 286].

Each phase is indicated with the help of the two green lines in Figure 2.9a. In the first phase (i), as solvent evaporates, the curve of concentration C crosses the solute solubility limit (C_s) and approaches supersaturation. In the second phase (ii), the solution reaches C^*_{min} overcoming the energy barrier for nucleation and nucleation begins to precipitate. The ensuing nucleation density is proportional to the area under the curve enclosed between C^*_{min} and the maximum supersaturation limit (C^*_{max}). The formed nuclei grow with continuous supply of solute by diffusion. As the crystal nucleation and growth proceed, the solute is continuously consumed, which in turn suppresses the nucleation rate. In the third phase (iii), the concentration curve moves below the supersaturation minimum and the precipitation of solute material brings about a further decrease in the solution concentration. Since the solution is still supersaturated but below C^*_{min} ($C^*_{\text{min}} > C > C_s$), only crystal growth occurs [247, 275, 281, 286, 287].

Based on the Weimarn theory [288], the competition between both nucleation and growth kinetics is a function of the degree of supersaturation in the solution and broadly dictates the density of nucleation sites formed. Consequently, it largely determines the resulting average dimensions of crystal clusters. The rates of nucleation and crystal growth are polynomial functions of the supersaturation degree [289].

The crystal cluster nucleation rate is described as

$$V_1 = kA \exp\left(\frac{-\Delta G^*}{k_B T_a}\right) \tag{2.6}$$

where k_B is the Boltzmann constant, k is a constant, A is a complicated function of the molecular-level diffusion-kinetics parameters, T_a is the absolute temperature, and ΔG^* is the critical free energy of nucleation. For a crystal cluster with spherical shape, ΔG^* can be expressed as

$$\Delta G^* = \frac{16\pi\gamma^2\Omega^3}{3{k_B}^2{T_a}^2{\sigma_S}^2} \tag{2.7}$$

where γ is the surface free energy of the critical crystal cluster, Ω is the molecular volume of the perovskite crystal, and σ_S is the degree of supersaturation of the perovskite precursor solution. Based on Equation 2.6 and 2.7, the nucleation rate V_1 exhibits an exponential growth rate as the degree of supersaturation increases, that is

$$V_1 \propto \exp\left(-\frac{1}{{\sigma_S}^2}\right).$$

According to Burton–Cabrera–Frank theory [290], the crystal growth rate V_2 can also be correlated with the degree of supersaturation σ_S as follows

$$V_2 = A_1{\sigma_S}^2 \tanh\left(\frac{B_1}{\sigma_S}\right) \tag{2.8}$$

where A_1 and B_1 are complex temperature-dependent constants. V_2 as a function of σ_S can be described as parabolic growth ($V_2 \propto {\sigma_S}^2$) when σ_S is low and as linear growth ($V_2 \propto \sigma_S$) when σ_S is high [291]. In comparison with crystal growth rate V_2, the nucleation rate V_1 is relatively more sensitive to σ_S owing to the exponential relationship. The number of crystal clusters per unit area N can be expressed as

$$N = 1.1\left(\frac{V_1}{V_2}\right)^{\frac{1}{2}} \tag{2.9}$$

which is inversely proportional to the average cluster size. The dependence of nucleation rate V_1, growth rate V_2, and cluster size on the degree of supersaturation is schematically illustrated in Figure 2.9b.

Hence, the time span of the second phase of the LaMer model can be adjusted by controlling the dynamic process of wet film drying, largely determining the final perovskite film morphology [275,286,292]. For heat- (see Subsection 2.2.3 and Chapter 4) but primarily for gas-assisted perovskite conversion (see Subsection 2.2.3 and Chapter 5 and 6), an acceleration of the evaporation rate of the solvent molecules and higher degree of supersaturation occurs compared to a diffusion controlled growth, for instance in the case of natural drying, leading to a higher nucleation rate (Equation 2.6 and 2.7). Eventually, this leads to an increased density of nucleation sites (Equation 2.9) and therefore results in a dense and compact perovskite film morphology

consisting of crystal grains with relatively small size in comparison to heat-assisted conversion as illustrated in Figure 2.9a.
In summary, with increasing perovskite supersaturation of the wet film the size of crystal grains will decrease as well as grain growth time will be shortened [280, 283, 286, 291].

The author emphasizes that with the same precursor solution formulation the solvent removal rate is in general faster in the case of spin coating (nucleation in seconds) contrary to the ones of scalable meniscus coating (solvent removal in a few tens of seconds), for instance when using blade or SDC, because generated d_{wet} is normally smaller for SC. Consequently, the lateral diffusion of the solute has sufficient time to occur for BC or SDC [275, 280, 286].

For more information on the classical theories of nanocrystal nucleation and growth, the author recommends reference [293].

2.2.3 Conversion methods of perovskite wet films and their potential

In order to increase solution concentration and reach supersaturation, the solution solvent needs to be evaporated and removed from the wet film, respectively. The kinetics of this drying process of the perovskite precursor wet film, which is in principle independent of the coating method, affect nucleation and crystal growth as explained in the previous Subsection 2.2.2. Therefore, the choice of the method to evaporate the perovskite precursor solution solvent is of great importance. Literature specifies four main methods to generate supersaturation state [40, 58, 283, 286, 294], also called quenching methods, which are illustrated in Figure 2.10. They are hereinafter referred to as perovskite conversion methods: (i) antisolvent- (Figure 2.10a), (ii) vacuum- (Figure 2.10b), (iii) heat- (Figure 2.10c), and (iv) gas-assisted (Figure 2.10d) conversion method.

In the following, the four perovskite conversion methods are shortly explained and their potential for upscaling is discussed.

Antisolvent-assisted conversion

In the case of antisolvent-assisted conversion (Figure 2.10a) or also called solvent extraction introduced in 2014 [295], an orthogonal solvent with a low perovskite solubility, which is miscible with the precursor solvent, is applied on the wet film [296, 297]. This solvent extracts the perovskite precursor solvent of the wet film enabling the state of supersaturation in the remaining film. Thereby, nucleation and crystal growth are decoupled with the formation of an intermediate phase. The method is implemented primarily in spin coating by dripping the antisolvent onto a spinning substrate covered with the wet film in order to remove the antisolvent together with the extracted precursor solvent molecules [40, 286]. The antisolvent has been also applied by spray coating (SPC) [298].

Antisolvent quantity, type, dripping point, and its application rate have to be taken in consideration in order to control the quality of the perovskite morphology. In fact, solubility of the organic precursors in the antisolvent and its miscibility with the host perovskite solution solvents are the two key factors to control crystallization and therefore the resulting perovskite morphology [296].

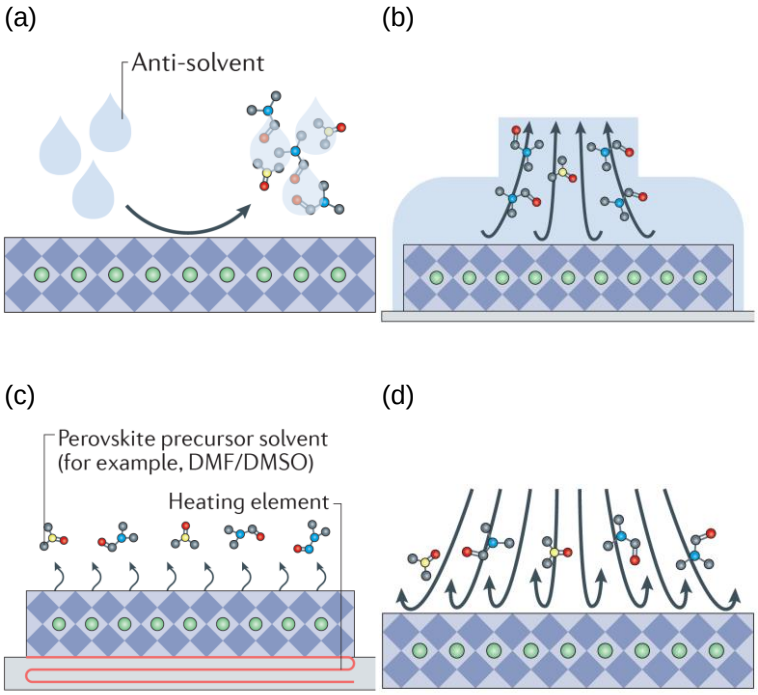

Figure 2.10: Schematic illustration of typical perovskite conversion methods: (a) antisolvent-, (b) vacuum-, (c) heat-, and (d) gas-assisted perovskite conversion. Adapted with permission from [40]. © Springer Nature.

Antisolvent dripping combined with spin coating is easy to use and is a RT process but is neither scalable nor can it be readily transferred to scalable printing techniques since as the size of the substrate increases the centrifugal force increases, inducing that the antisolvent might evaporate before reaching the edge of the large-area substrate or spread heterogeneously [299]. Thus, it is limited with respect to the film area for practical applications [286]. To tackle this limitation, antisolvent immersion has been developed [300–304]. To avoid drying of the printed wet film before immersing it into the antisolvent bath, either ultrafast transfer or a wide processing window is important. Antisolvent immersion has been combined with blade coating [303, 305, 306], while blade coating the antisolvent on top of the wet film has only been presented in one single case [307]. Furthermore, antisolvent immersion has also been implemented together with SDC [308, 309] and gravure printing the perovskite precursor wet films [264].

Antisolvent immersion imposes no limit to substrate size and could be combined with scalable R2R printing techniques [264] but the major technical concern imposed by the recirculation of a large antisolvent bath for continuous high-throughput production hindered the author from utilization of this conversion method in this thesis.

Vacuum-assisted conversion

Vacuum-assisted conversion (Figure 2.10b) is based on changes in pressure (p) to remove the perovskite precursor solvent out of the wet film and reach supersaturation initiating nucleation [286]. The vacuum degree and its duration are the two determinative parameters that should be taken

into account [310]. From 2015 on, a vacuum-assisted thermal annealing process via spin coating [311, 312] and later via inkjet printing [313] was reported. Thenceforward, several more studies on true vacuum quenching in early stages primarily for perovskite deposition by spin coating followed [310, 314–317]. Furthermore, vacuum-assisted conversion is by now applied in a one- or two-step process together with scalable printing techniques such as blade [318–328], slot-die [329, 330] and spray coating [331], and inkjet printing [332–334].

Similar to antisolvent immersion, one advantage of the method is that precursor solution deposition and crystallization can be effectively decoupled [286].

Vacuum-assisted conversion is feasible with flexible substrates [323, 335, 336] and is a RT process but requires normally expensive equipment such as the vacuum chamber and pumps. Furthermore, the possibility of a fast and abrupt quenching to reach the state of supersaturation in the wet film via vacuum in a R2R system is hardly imaginable since different pressure conditions in contiguous sectors of the vacuum chamber need to be accomplished. This is in the author's opinion difficult to realize. Consequently, the method is rather advanced and unfortunately complicated to scale. For that reasons, the author decided to omit this perovskite conversion method in this thesis.

Heat-assisted conversion

The heat-assisted conversion (Figure 2.10c), also called hot-casting [337, 338], is a straightforward method to promote solvent removal from a wet film and induce rapid supersaturation, thus, simultaneously with solution deposition. It can be easily carried out by coating the precursor solution on a substrate preheated to temperatures of ~80 to 150 °C. The strategy has been applied to deposit perovskite thin films by various printing techniques such as spin coating [339] and scalable deposition methods like blade [274, 340–352] or meniscus [353–355], slot-die [240, 356–361], spray [362–365], and dip coating [366], and inkjet printing [367].

Comprehensive in-situ investigations on the structural evolution and crystal growth mechanism have been conducted [348, 349, 357]. It was found that the participation of intermediate phases plays a key role in heat-assisted conversion. In case of a slow solvent removal at RT, indirect crystallization occurs from the precursor solution to perovskite via intermediate phases resulting in an inferior perovskite layer with a dendritic crystal morphology. In contrast, high substrate temperatures ensure fast solvent removal resulting in direct crystallization by skipping the formation of intermediate phases. As a result, dense perovskite films are obtained [286].

Controlling the crystallization dynamics during heat-assisted conversion at high deposition temperatures approaching or exceeding the boiling point (BP) of the precursor solvent might be challenging due the fact that solute migration and aggregation associated with solution convection is extremely sensitive to the coating temperature [286]. This is presented in Subsection 2.2.4 in more detail. Consequently, experienced operation are commonly required to reach reproducible perovskite layers with dense and uniform morphology over large areas. Furthermore, drying and nucleation or crystal growth take place simultaneously with solution deposition which might represent a further challenge complicating the film morphology control [286].

The heat-assisted conversion method is easy to implement and to use and is highly scalable. It normally requires no additional processing equipment. Nevertheless, the method is limited to rigid substrates if high temperatures >140 °C are necessary which might be most likely not

compatible with flexible substrates. Due to the advantages of this conversion method, the author studied the principle in detail in this thesis (see Chapter 4).

Gas-assisted conversion

Gas-assisted conversion (Figure 2.10d) relies on convection forces to quickly drive out the precursor solution solvent from the wet film [338, 368]. In this process, the gas flow rate (Q) and its temperature are two crucial parameters. In addition, the solvent composition has to be considered as well [286]. Since early 2014, the gas-assisted conversion method has been utilized via spin coating [369–372]. Similar to antisolvent-assisted conversion, the timing of applying the gas should be carefully optimized depending on the material composition and solvent systems [286]. Later, gas quenching was developed for depositing perovskite films in a one- or two-step process by scalable printing techniques such as blade [272, 373–380], slot-die [25, 245, 357, 381–383], D-bar coating [384–387] and so-called air-blading [388]. Moreover, first results on applying gas quenching to fabricate flexible PSCs and PSMs by blade coating have been presented as well [375, 389, 390].

The decoupling of the precursor solution coating, the drying inducing the nucleation, and the crystallization, respectively, is central for this conversion method which might ensure high controllability and reproducibility [286].

Gas-assisted conversion requires merely inexpensive additional equipment, is fully scalable and can be utilized at RT and for rigid as well as flexible substrates [391]. Consequently, from the author's point of view, gas-assisted conversion offers the highest potential of the four concepts for upscaling PSCs (see Chapter 5 and 6).

The author notes that combinations of two perovskite conversion methods are possible such as gas- together with heat-assisted conversion [392] or gas- together with vacuum-assisted conversion [310, 393]. For more information on all perovskite conversion methods, the author recommends reference [286].

Based on the discussions in the Subsection 2.2.3, the author identified heat- and gas-assisted conversion as the most promising perovskite conversion methods for upscaling PSCs, hence, these are utilized in this thesis.

2.2.4 Fluid dynamics in heated wet films

Since heat-assisted perovskite conversion is utilized in Chapter 4 of this thesis, a short introduction to fluid dynamics in heated wet films is given in the following. The solute dissolved in solution is redistributed during the drying process in the form of self-diffusion and solution flows, which impacts on the final film uniformity [275]. In general, cellular motion in a fluid may occur due to two distinct effects, the Rayleigh–Bénard and the Marangoni convection, which are central for this thesis. Here, the author briefly introduces the two types of convection.

Rayleigh–Bénard convection

If the substrate is heated from below, which is the case for heat-assisted perovskite conversion, the liquid density (ρ) near the heated substrate decreases and an upward buoyancy force emerges.

This leads to the initiation of a circulating flow, if the buoyancy can overcome the damping liquid viscous force. To evaluate the flow stability, the dimensionless Rayleigh number (Ra), the ratio of buoyancy force to viscous force, is utilized [347, 394] as follows

$$Ra = \frac{g\beta\Delta T {d_{\mathrm{wet}}}^3}{\vartheta\alpha_{\mathrm{T}}} \tag{2.10}$$

where g is the gravitation acceleration, β is the liquid thermal expansion coefficient, ϑ is the kinematic viscosity, α_{T} is the thermal diffusivity, d_{wet} is the wet film thickness, and ΔT is the temperature difference between the heated plate and the film surface [347, 394].

In the Rayleigh–Bénard convection [395, 396], the density generally changes in the direction of g, if the film experiences a temperature gradient in the same direction [394]. If Ra is larger than a critical value, so that the fluid becomes unstable, so-called Bénard convection cells such as circulating rolls [396] may form.

Marangoni convection

In addition, such Bénard cells may form in an evaporating liquid film, independently of the buoyancy-driven convection described above. In an evaporating film, the local surface temperature and solution concentration may change giving rise to a so-called Marangoni convection which is the flow due to a gradient of surface tension induced by a temperature gradient [275, 276, 347, 351, 394, 397]. The dimensionless Marangoni number (Ma), comparing the surface tension forces to the viscous forces, is used to determine the possibility of occurrence of Marangoni motion described as

$$Ma = -\frac{\partial\sigma}{\partial T_{\mathrm{S}}}\left(\frac{d_{\mathrm{wet}}\Delta T}{\eta\alpha_{\mathrm{T}}}\right) \tag{2.11}$$

where σ is the surface tension, T_{S} is the local surface temperature, and η is the dynamic viscosity of the liquid solution. If the critical Ra for a thin film of 1108 is exceeded, the Bénard cells are driven by density gradients or Rayleigh–Bénard convection, whereas exceeding the critical Ma of 80 indicates that the cells are formed by surface tension effects [398, 399].
The simultaneous and reinforcing action of both driving forces is possible.

However, for thin films encountered in layers of solar cells, Ra, calculated based on the physical properties of perovskite precursor solutions [400] and typical d_{wet} of microns, is <1 and thus very small [347, 351, 394]. However, Ma is much larger. Therefore, the large perovskite domains or islands observed in this thesis (see Section 4.1) and in other studies [340, 342, 344, 401] might be due to the formation of Bénard cells induced by Marangoni motion [347] in contrast to assumptions of some reports [342, 401].

Surfactant have an important role in overcoming the Landau–Levich problem [402] which prevents the formation of a homogeneous film [253] described in Subsection 2.2.1. Figure 2.11 illustrates the process.

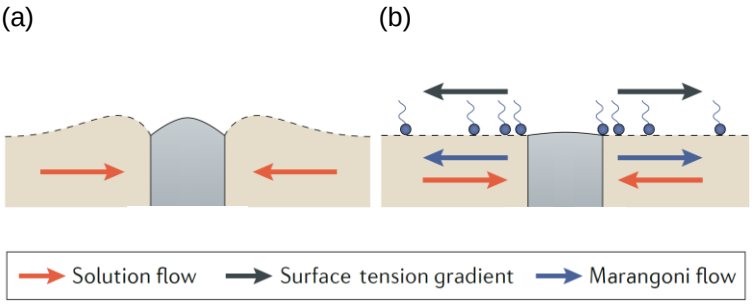

Figure 2.11: Schematic illustration of fluid dynamics during drying of a heated perovskite precursor solution wet film (a) without and (b) with a surfactant. Adapted with permission from [253]. © Springer Nature. See also [274, 275, 357].

During drying, microscale fluid flows toward perovskite islands and the surface tension increases owing to evaporation of the solvent. When using a surfactant [274, 403] in the perovskite precursor solution (see Section 4.2), surface tension can be decreased and thereby the original flow is counteracted by a Marangoni flow driven by a surfactant-induced surface tension gradient diminishing the possibility of occurrence of Bénard cells and suppressing the island pattern [253, 274].

For further information on Marangoni convection the author recommends reference [404].

2.3 Perovskite solar modules

Besides small-scale PSCs, first prototype perovskite solar modules (PSMs) are demonstrated as well in this thesis. This section shortly explains the fundamentals of PSMs. The section comprises two main topics, the serial interconnection design (Subsection 2.3.1) and the optimization of the cell width of modules (Subsection 2.3.2).

2.3.1 Serial interconnection design

The PSMs fabricated in this thesis base upon the monolithic serial interconnection [299,405,406] which is well-known from other thin film solar modules [407]. For the purpose of realizing a serial interconnection of individual subcells, specific patterning lines are inserted in the solar cell architecture already during deposition of the individual functional layers of the solar cell. Figure 2.12 illustrates the concept of the monolithic serial interconnection.

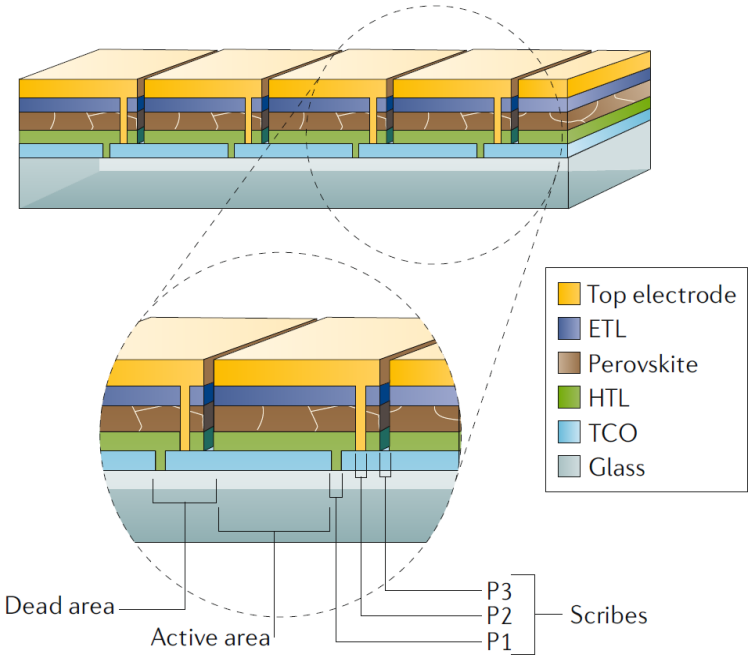

Figure 2.12: Schematic illustration of the monolithic serial interconnection of PSMs. Adapted with permission from [253]. © Springer Nature.

By means of patterning 1 (P1) lines, the front electrode is separated into subcells. Afterward, all functional layers are deposited except for the back electrode. Via patterning 2 (P2) lines to remove all layers except for the front electrode, and the deposition of the back electrode, the serial interconnection between the subcells is established. To prevent short-circuiting of the subcells, finally patterning 3 (P3) lines are applied after depositing the back electrode. By this means, the active area A_{act} of a subcell in the module is defined in one direction by the sector between the P3 and P1 line, whereas the area between P1 and P3 is not contributing to I_{ph} generation and specifies consequently the so-called dead area (A_{d}) [40, 55, 253].

With regard to thin film solar cells, the described concept is required because of the relatively low conductivity of the TCOs which hinders an efficient charge carrier transport and therefore make large-area subcells less reasonable [408]. For the fabrication of PSMs in this thesis, P1 and P2 lines were produced by laser ablation, whereas P3 lines were mechanically scribed. More details are given in Subsection 3.1.6.

2.3.2 Optimization of cell width

By optimizing the cell and patterning width, the geometric fill factor (GFF) of a subcell and thereby of a module can be increased. The GFF is defined by the ratio of the active area A_{act} and the total aperture area A_{ap} of a subcell and a module [253], respectively, expressed as

$$\mathrm{GFF} = \frac{A_{\mathrm{act}}}{A_{\mathrm{ap}}} = \frac{A_{\mathrm{act}}}{A_{\mathrm{act}} + A_{\mathrm{d}}} \tag{2.12}$$

where A_{ap} is defined as the sum of A_{act} and the dead area A_d.

However, this concept apparently works only if one can assume, disregarding the front and back electrode, a negligible lateral conductivity of the functional layers which is, however, the case for PSCs.

3 Experimental methods for preparation and characterization

This chapter describes the experimental methods for preparation and characterization utilized in this thesis.

The first Section 3.1 of this chapter describes the preparation methods which are utilized to fabricate the PSCs and PSMs including each layer. It is divided into several subsections that cover the general solar cell layout (Subsection 3.1.1), the preparation of the substrates (Subsection 3.1.2), the deposition of the charge selective layers (Subsection 3.1.3) and the deposition of the perovskite absorber (Subsection 3.1.4) and the opaque contact (Subsection 3.1.5). Furthermore, the preparation of the monolithic interconnection of the PSMs is described (Subsection 3.1.6).

The second Section 3.2 introduces the analytical methods that are utilized for the evaluation of the electrical performance of the solar cells (Subsection 3.2.1) and for the optical and crystallographic (Subsection 3.2.2), the morphological (Subsection 3.2.3) and the surface characterization (Subsection 3.2.4) of thin films.

3.1 Preparation of perovskite solar cells and modules

This section covers the preparation methods to fabricate efficient PSCs and PSMs via scalable solution processing by blade coating (BC) or slot-die coating (SDC), spin coating (SC) and physical vapor deposition (PVD). Moreover, laser and mechanical patterning of the PSMs are described.

All chemicals were used as received without further purification.

3.1.1 General solar cell layout

Figure 3.1 illustrates the preparation sequence and deposition methods for the PSCs.

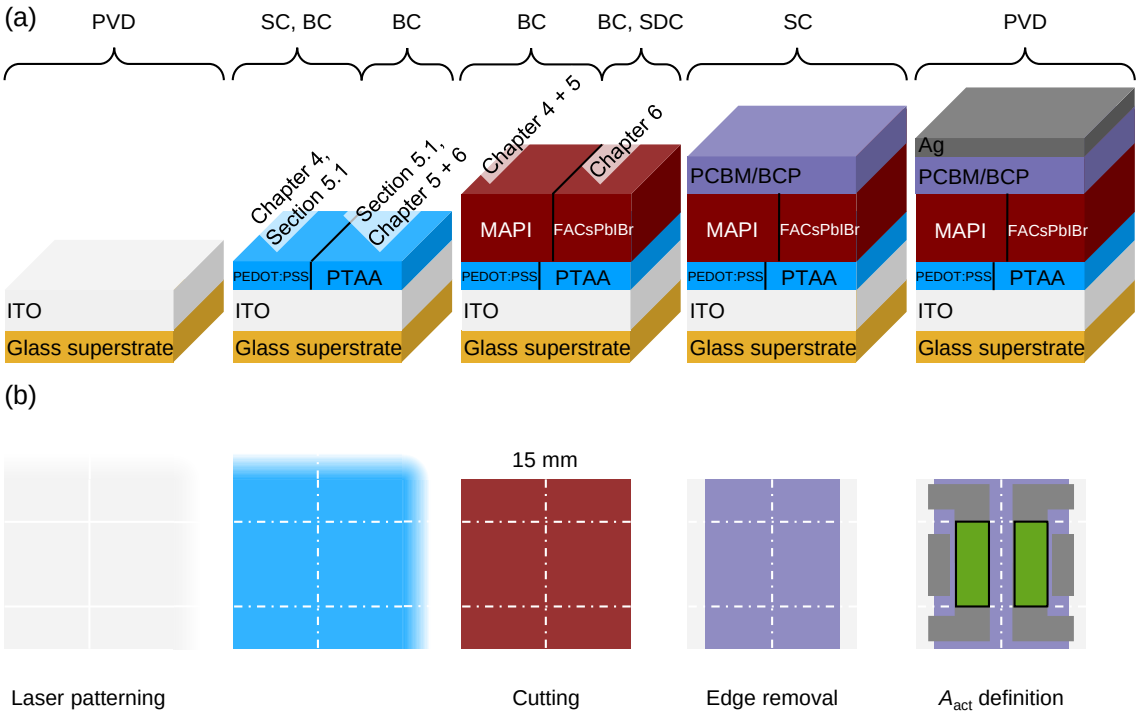

Figure 3.1: Preparation sequence and deposition methods for fabrication of PSCs (physical vapor deposition (PVD), spin coating (SC), blade coating (BC), slot-die coating (SDC)) in (a) cross-sectional and (b) top-view configuration.

3.1.2 Preparation of substrates

Cells

For the case of heat-assisted and its combination with gas-assisted perovskite conversion (Figure 5.4), substrates with dimensions of $3 \times 3\,\mathrm{cm}^2$ were utilized.

Typically, soda lime float glass substrates coated with ITO[1] as TCO with dimensions of $3 \times 6\,\mathrm{cm}^2$ (Figure 3.2) were patterned by pulsed laser (wavelength (λ)=1064 nm) ablation to define the cell area in one direction. The substrates were cleaned by blowing with nitrogen (N_2). The substrates were treated with argon (Ar) plasma for 120 s at 30 W (0.38 mbar)[2] for the case of MAPI perovskite and at 100 W for the case of multi-cation perovskite.

[1] 150 nm, sheet resistance (R_{sq}) <15 $\Omega_{\square}$, VisionTek Systems
[2] Pico Plasma Cleaner, Diener electronic

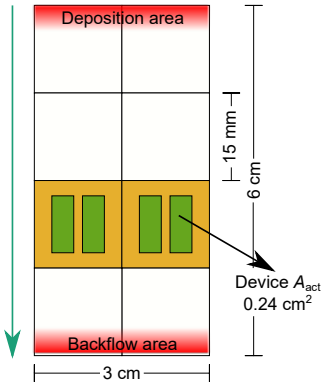

Figure 3.2: Schematic top-view illustration of substrate dimensions typically used in this thesis. A dummy glass is placed behind the substrate in BC direction (dark green). Usually, the two further down located $15 \times 15\,\text{mm}^2$ substrates (yellow) are selected and utilized for measuring the corresponding PSCs due to the fact of an undesirable solution deposition and backflow region (red) at the beginning and end of the substrate, respectively. Two PSCs (light green) are located on each $15 \times 15\,\text{mm}^2$ substrate (see Figure 3.1b).

For the case of slot-die coating perovskite substrates with dimensions of $3 \times 9\,\text{cm}^2$ were utilized.

Modules

Soda lime float glass substrates coated with ITO[3] (3×6, 5×8 and $9 \times 9\,\text{cm}^2$) were P1 patterned (see Subsection 3.1.6) and subsequently etched with hydrochloric acid (HCl). Thereby, 19 mm, 29 mm and 62 mm long cells of the modules with 3×3, 5×5 and $9 \times 9\,\text{cm}^2$ substrates, respectively, were accomplished. After etching, the substrates were sequentially cleaned in an ultrasonic (US) bath of acetone, isopropanol (IPA), H_2O[4] and IPA for 10 min each.

3.1.3 Deposition of charge carrier selective layers

Hole transport layers (HTLs)

The conductive polymer (PEDOT:PSS) layer was deposited either via spin or via blade coating. For spin coating in a spin coater[5] in a flowbox in a cleanroom under ambient conditions[6] by static droplet deposition on the ITO substrates via a three-step recipe comprising 500 rpm for 3 s, 4000 rpm for 55 s, and 1000 rpm for 3 s, a solution of PEDOT:PSS[7] was utilized. A volume of 400 to 500 µL was applied for each substrate.
For blade coating on the ITO substrates a solution of PEDOT:PSS[8] was utilized. The substrate and blade coater plate temperatures were 70 °C ($3 \times 3\,\text{cm}^2$: 60 to 70 °C). A solution volume of 10 µL ($3 \times 3\,\text{cm}^2$: 15 to 60 µL) was utilized. The blade coating velocity (v_{BC}) was $5\,\text{mm}\,\text{s}^{-1}$ ($3 \times 3\,\text{cm}^2$: 5 to $15\,\text{mm}\,\text{s}^{-1}$), and the gap height was adjusted to 80 µm ($3 \times 3\,\text{cm}^2$: 80

[3] 150 nm, R_{sq} <15 $\Omega_{\square}$, VisionTek Systems
[4] deionized
[5] WS-650-23B, Laurell
[6] 19 °C to 22 °C, 30 % to 50 % relative humidity (RH)
[7] CLEVIOS P VP.Al 4083, Heraeus
[8] CLEVIOS P VP.Al 4083, Heraeus ($3 \times 3\,\text{cm}^2$: 4083 or 1:1 (vol:vol) 4083:H_2O or 1:3 (vol:vol) 4083:IPA)

to 400 µm). Subsequently, the PEDOT:PSS layer was annealed at 120 °C ($3 \times 3\,cm^2$: 120 to 140 °C) for 10 min ($3 \times 3\,cm^2$: 5 to 10 min).

Poly(triaryl amine) (PTAA) was deposited on the ITO substrates by blade coating a solution of PTAA[9] in dichlorobenzene (DCB)[10] with a concentration of normally $5\,mg\,mL^{-1}$. The substrate and blade coater plate temperatures were 50 °C. A solution volume of 15 µL (17 µL: SDC) was utilized. The blade coating velocity v_{BC} was $15\,mm\,s^{-1}$, and the gap height was adjusted to 80 µm. Subsequently, the PTAA layer was annealed at 100 °C for 10 min.

Subsequently to the PTAA layer, a NP wetting agent was deposited on top [409] by blade coating 10 µL (12 µL: SDC) of a normally 0.9 wt% dispersion of silicon oxide nanoparticles (SiO_2 NPs) in ethanol at a v_{BC} of $5\,mm\,s^{-1}$, 80 µm gap, and at RT. The SiO_2 NPs were dried at 100 °C for 10 min.

The SiO_2 NPs were synthesized following Bogush et al. [410] using fixed amounts of 2.717 mL of ethanol[11], 101 µL of ammonia[12], 114 µL of tetraethyl orthosilicate (TEOS)[13], and 27 µL of H_2O[14] [411]. After stirring at 30 °C for 3 h, the weight concentration of the stock dispersion was 1.2 wt% in ethanol with an approximate NP diameter of 20 nm to 30 nm. For a desired concentration, the NP stock dispersion was freshly diluted with ethanol. The stock solution was renewed regularly due to possible agglomeration of NPs forming clusters during storage, which might impair the wetting properties. For more details see Subsection 5.2.1.

For blade coating PEDOT:PSS, PTAA and the SiO_2 NPs, a commercial height adjustable blade[15] on a blade coater[16] was utilized in a flowbox in a cleanroom under ambient conditions[17] (inside a N_2-filled glovebox: SDC study, Section 6.3).

After the deposition of the NPs, the substrates were transferred into a N_2-filled glovebox (already in glovebox: SDC study, Section 6.3).

Electron transport layers (ETLs)

After depositing the perovskite layer, the $3 \times 6\,cm^2$ ($3 \times 9\,cm^2$: SDC) substrates were transferred out of the glovebox and were cut in pieces of $15 \times 15\,mm^2$.

Spin coating the ETLs consisting of C_{61} fullerene derivate (PCBM) and bathocuproine (BCP) was performed in a spin coater[18] inside a N_2-filled glovebox.

A $40\,mg\,mL^{-1}$ concentrated PCBM[19] solution in DCB[20] was spin coated by static droplet deposition with a two-step recipe compromising 1000 rpm for 35 s (30 s: MC) and 4000 rpm (2000 rpm: MC) for 5 s. The solution was kept stirring at 60 °C during processing and was applied hot. A

[9] $17\,800\,g\,mol^{-1}$, EM Index
[10] anhydrous, 99 %, Sigma-Aldrich
[11] 99.5 %, Sigma-Aldrich or anhydrous, VWR
[12] 99.9 %, Roth
[13] 98 %, Sigma-Aldrich
[14] deionized
[15] ZUA 2000 Universal Film Applicator, Zehntner Testing Instruments
[16] ZAA 2300 Automatic Film Applicator, Zehntner Testing Instruments
[17] 19 °C to 22 °C, 30 % to 50 % relative humidity (RH)
[18] WS-650-23B, Laurell: MAPI; MB-SC-200, MBraun: Multi-cation
[19] 99 %, Solenne BV; >99 %, Sigma-Aldrich or >99 %, Ossila: SDC study (Section 6.3)
[20] anhydrous, 99 %, Sigma-Aldrich

volume of 30 µL (50 µL: SDC study, Section 6.3) was utilized for each substrate.
For the SDC study (Section 6.3), the solution was filtered before use.

Afterward, 40 µL of a 1 mg mL^{-1} concentrated BCP[21] solution in ethanol[22] was spin coated by static droplet deposition (dynamically: MC) on top of PCBM at 3000 rpm for 34 s.

3.1.4 Deposition of perovskite absorber

Two different perovskite absorber were utilized in this thesis, namely the $MAPbI_3$ (MAPI) and the multi-cation (MC) perovskite absorber. Both, heat- and gas-assisted perovskite conversion were performed in the case of the MAPI absorber, whereas for the MC absorber only a gas-assisted recipe was applied.

$MAPbI_3$ (MAPI) perovskite

For blade coating via heat-assisted conversion, a normally 46 wt% perovskite precursor solution with lead acetate trihydrate ($PbAc_2$ trihydrate)[23] mixed with methylammonium iodide (MAI)[24] in a molar ratio of 1:3 was utilized. The precursor mixture was dissolved in dimethylformamide (DMF)[25]. The solution was stirred at 60 °C to 80 °C for 15 min to 240 min. Normally, the solution was not filtered.

Blade coating was conducted via a blade coater[26] and a commercial height adjustable blade[27] inside a N_2-filled glovebox. The substrate and blade coater plate temperature were varied between 25 °C and 145 °C (processing temperature). The gap height was fixed at 60 µm, v_{BC} between 10 mm s^{-1} and 50 mm s^{-1}, and a volume of 20 µL of the precursor solution (RT or 60 °C) was applied. Afterward, the substrates were transferred to a hot plate and were annealed at 90 °C to 100 °C for 10 min inside the glovebox [412].

For more details see Section 4.1.

For utilization of the amphiphilic surfactant L−α-phosphatidylcholine (LP), LP[28] of a concentration of 0.2 mg mL^{-1} to 0.8 mg mL^{-1} was added in the preliminary prepared perovskite precursor solution. LP can also be dissolved in DMF at first by stirring the solution at RT for 50 min [412].

For more details see Section 4.2.

In the case of gas stream-assisted blade coating, a normally 44 wt% perovskite precursor solution with lead acetate ($PbAc_2$)[29] mixed with methylammonium iodide (MAI)[30] in a molar ratio of 1:3 was utilized. Usually, 5 % molar ratio of the lead (Pb) source in the precursor materials was

[21] 99.99 %, sublimed grade, Sigma-Aldrich
[22] anhydrous, VWR
[23] 99.999 % trace metals basis, Sigma-Aldrich
[24] >99.99 %, Dyesol
[25] anhydrous, 99.8 %, Sigma-Aldrich
[26] TFC200 Thin Film Coater, Automatic Research
[27] ZUA 2000 Universal Film Applicator, Zehntner Testing Instruments
[28] egg yolk, ≥99 %, Sigma-Aldrich
[29] dry, >98.0 %, TCI
[30] >99.99 %, Dyesol or >99 %, Greatcell Solar Materials

replaced by lead chloride ($PbCl_2$)[31] to avoid void formation in the resulting perovskite layer (see Subsection 5.2.2). The precursor mixture was dissolved in dimethylformamide (DMF)[32]. After stirring the solution at 60 °C for 90 min, the solution was cooled to RT and was utilized after ~3 h.

Blade coating was conducted via a blade coater[33] and a commercial height adjustable blade[34] inside a N_2-filled glovebox. The substrate and blade coater plate temperature were kept at 40 ± 5 °C. The gap height was fixed at 100 µm, v_{BC} between 10 mm s^{-1} and 20 mm s^{-1}, and the volume between 15 µL and 20 µL of the precursor solution (RT) was applied. After the deposition and a delay time of 20 s, the wet film was dried on the blade coater plate by a laminar N_2 gas stream changing its color to brown in less than 1 min. The gas stream (p=4.5 bar, Q=20 L min^{-1}) was generated by a slot-die[35] with a width of 88 mm and a slit width of 150 µm. The distance from the outlet of the slot-die to the blade coater plate was 1.2 cm and ~4 cm to 5 cm to the substrate. The resulting N_2 gas flow velocity (v) over the substrate was 3 m s^{-1} to 4 m s^{-1} measured by a flow meter. Afterward, the substrates were transferred to a hot plate and were annealed at 100 °C for 10 min inside the glovebox [409].

For more details see Subsection 5.1.1.

Multi-cation (MC) perovskite

A multi-cation (double-cation) $FA_{0.83}Cs_{0.17}Pb(I_{0.87}Br_{0.13})_3$ perovskite was utilized in a concentration of 0.93 mol L^{-1}. The precursor materials lead iodide (PbI_2)[36], cesium iodide (CsI)[37], lead bromide ($PbBr_2$)[38] and formamidinium iodide (FAI)[39] were dissolved in a DMF[40] and dimethyl sulfoxide (DMSO)[41] mixture of 4:1 (vol:vol) ratio or solely in DMSO. After stirring at 70 °C for 15 min, the solutions were cooled down to RT, filtered and utilized after ~2 to 3 h.

The multi-cation perovskite recipe is based on the gas-assisted perovskite conversion. Depositing the perovskite layer was performed via a blade coater[42] and a commercial height adjustable blade[43] inside a N_2-filled glovebox equipped with a pressure relief valve. The substrates are taped on the blade coater plate at the shorter edges during gas stream-assisted drying. The substrate and plate temperatures were kept at 40 ± 5 °C. The gap height was fixed at 100 µm and v_{BC} values were fixed at 18 mm s^{-1} and 7.5 mm s^{-1} for the DMF:DMSO and DMSO recipe, respectively. A volume of 15 µL of each precursor solution (RT) was applied. After a delay time until the first color change and of ~35 s for the DMF:DMSO and DMSO recipe, respectively, the wet film was dried by a laminar N_2 gas stream changing its color to brown. During the delay time, the blade was removed from the blade coater plate and a gas knife was installed.

[31] 98 %, Sigma-Aldrich
[32] anhydrous, 99.8 %, Sigma-Aldrich
[33] TFC200 Thin Film Coater, Automatic Research
[34] ZUA 2000 Universal Film Applicator, Zehntner Testing Instruments
[35] SC 80, Automatic Research
[36] >99.99 %, TCI
[37] >99.9995 %, Sigma-Aldrich
[38] for perovskite precursor, TCI
[39] anhydrous, >99 %, Sigma-Aldrich
[40] anhydrous, 99.8 %, Sigma-Aldrich
[41] anhydrous, ≥99.9 %, Sigma-Aldrich
[42] TFC200 Thin Film Coater, Automatic Research
[43] ZUA 2000 Universal Film Applicator, Zehntner Testing Instruments

The gas stream (p=2.0 bar, Q=100 L min^{-1}, single inlet) was generated by a stainless steel air knife[44] with a width of 152 mm and a slit width of 50 µm mounted to a sled moving over the substrate at gas knife velocity (v_{GK}) values of 9 mm s^{-1} and 3.5 mm s^{-1} for the DMF:DMSO and DMSO recipe, respectively. The stream direction was 45° to the substrate surface in the blade coating direction and contrary to it for the DMF:DMSO and DMSO recipe, respectively. The distance from the gas knife outlet to the blade coater plate was ~4 mm. The resulting N_2 gas flow velocity v was 30 m s^{-1} to 35 m s^{-1} measured by a flow meter. Subsequently, the substrates were transferred to a hot plate and were annealed at 100 °C or 150 °C for 10 min inside the glovebox [413].

For more details see Subsection 6.1.1.

For slot-die coating the multi-cation (double-cation) $FA_{0.83}Cs_{0.17}Pb(I_{0.87}Br_{0.13})_3$ perovskite with gas-assisted conversion, a precursor solution with a concentration of 0.93 mol L^{-1} was utilized. The four precursor materials PbI_2[45], CsI[46], $PbBr_2$[47], FAI[48] were dissolved in a mixture of DMF[49] and DMSO[50] in 4:1 (vol:vol) ratio. After stirring at 70 °C for 15 min, the solution was cooled down to RT and filtered.

Depositing the perovskite wet film was performed via a slot-die head[51] mounted to a sled on a blade coater[52] inside a N_2-filled glovebox equipped with a pressure relief valve. The slot-die included only one shim without a meniscus guide, with a thickness of 100 µm and a coating width of 3 cm. The substrates are taped on the blade coater plate at the shorter edges during gas stream-assisted drying.
For the SDC reference process, the following process parameters are utilized: The substrate and plate temperatures were kept at 40 ± 5 °C. The gap height was fixed at 101.6 µm and v_{SD} at 20 mm s^{-1}. The precursor solution (RT) was applied with a Q_{ink} of 0.20 mL min^{-1}. After a delay time of ~35 s, the wet film was dried by a laminar N_2 gas stream changing its color to brown. During the delay time, the sled with the slot-die was removed from the blade coater plate and a gas knife was installed. The gas stream (p=2.0 bar, Q=100 L min^{-1}, single inlet) was generated by a stainless steel air knife[53] with a width of 152 mm and a slit width of 50 µm mounted to a sled moving over the substrate at v_{GK} of 5 mm s^{-1}. The stream direction was 45° to the substrate surface in the slot-die coating direction. The distance from the gas knife outlet to the blade coater plate was ~4 mm. The resulting N_2 gas flow velocity v was 30 m s^{-1} to 35 m s^{-1} measured by a flow meter. Subsequently, the substrates were transferred to a hot plate and were normally annealed at 130 °C for 30 min inside the glovebox [414].

For additive engineering with formamidinium chloride (FACl) (Section 6.3), firstly the precursor solution concentration was changed to 1.10 mol L^{-1} in a DMF:DMSO mixture in 4:1 (vol:vol) ratio. Secondly, FACl[54] was dissolved in a DMF:DMSO mixture in 4:1 (vol:vol) ratio and in a concentration of 50 mg mL^{-1}. Each solution was stirred at 70 °C for 15 min. Thirdly, the

[44] Exair Super Air Knife, Eputec Drucklufttechnik
[45] >99.99 %, TCI
[46] 99.999 % trace metals basis, Sigma-Aldrich
[47] for perovskite precursor, TCI
[48] anhydrous, >98 %, Sigma-Aldrich (product from Greatcell Solar)
[49] anhydrous, 99.8 %, Sigma-Aldrich
[50] anhydrous, ≥99.9 %, Sigma-Aldrich
[51] SC 80, Automatic Research
[52] ZAA 2300 Automatic Film Applicator, Zehntner Testing Instruments
[53] Exair Super Air Knife, Eputec Drucklufttechnik
[54] >97 %, Sigma-Aldrich

FACl solution was added to the perovskite precursor solution resulting in a final concentration of 0.93 mol L^{-1} and in different FACl concentrations (3, 5 and 8 mol %) in the final solution. Furthermore, the solution was filtered before use.
For blade coating FACl containing precursor solutions (see Figure 6.13), a blade coater[55] was utilized (inside a N_2-filled glovebox). The values of delay time, v_{BC} and v_{GK} were fixed at ~35 s, 15 mm s^{-1} and 5 mm s^{-1}, respectively. The substrates were annealed at 100 °C for 30 min [415]. All other parameters for blade coating multi-cation perovskite DMF:DMSO mixtures are described above.

In the case of the additional defect passivation layer (Section 6.3), the stream direction after slot-die coating was 90° to the substrate surface.
Spin coating phenethylammonium iodide (PEAI) was performed in a spin coater[56] inside a N_2-filled glovebox. A 1 mg mL^{-1} concentrated PEAI[57] in IPA[58] was spin coated dynamically on top of the double-cation perovskite at 5000 rpm for 35 s. A volume of 50 µL was utilized for each substrate [414].

For more details see Section 6.3 and reference [414].

3.1.5 Deposition of opaque contact

To finalize the PSCs, a ~120 nm thick Ag electrode was thermally evaporated by PVD under high vacuum conditions ($<10 \times 10^{-6}$ mbar) through a metal aperture mask defining a device A_{act} of 0.24 cm^2 of two cells on each 15 × 15 mm^2 sample.

In the case of the PSMs, a ~120 nm thick Ag electrode was deposited by PVD exclusive of the cleaned exposed ITO areas, thereby filling the P2 trenches and thus connecting the module subcells (see Subsection 3.1.6).

3.1.6 Monolithic interconnection of solar modules

To fabricate PSMs with monolithic interconnected cells three patterning steps, namely P1, P2 and P3, were performed.

Patterning 1 (P1)

The ITO substrates were laser (λ=1064 nm) patterned with parallel P1 lines with 5 mm spacing. The P1 line is ~140 µm wide.

Patterning 2 (P2)

After the deposition of all solution-processed layers, P2 lines were laser (λ=1064 nm) patterned to expose the ITO layer next to the P1 line in a distance of ~100 µm. The P2 line is ~50 µm wide. Afterwards, Ag was evaporated (see Subsection 3.1.5).

[55] ZAA 2300 Automatic Film Applicator, Zehntner Testing Instruments
[56] MB-SC-200, MBraun
[57] 98 %, Sigma-Aldrich
[58] anhydrous, 99.5 %, Sigma-Aldrich

Patterning 3 (P3)

After the Ag evaporation, the monolithic interconnection was finalized by the P3 line which was mechanically scribed in a distance of ~100 µm next to the P2 line removing all layers except the ITO layer. The P3 line is ~60 µm wide.

The lateral extension of the dead area width from the P1 to P3 line is ~425 µm resulting in a module geometric fill factor (GFF) of approximately 92 %. A_{ap} of the modules with $3 \times 3\,cm^2$, $5 \times 5\,cm^2$ and $9 \times 9\,cm^2$ substrate size is $3.80\,cm^2$, $11.60\,cm^2$ and $49.60\,cm^2$, respectively. Figure 3.3 illustrates the module dimensions on a $5 \times 5\,cm^2$ substrate.

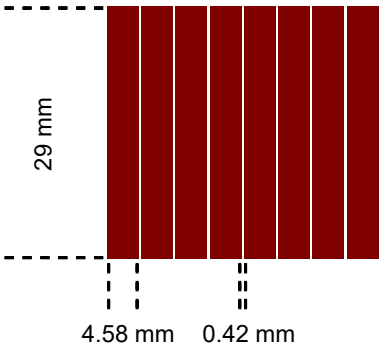

Figure 3.3: Schematic top-view illustration of module dimensions on a $5 \times 5\,cm^2$ substrate.

3.2 Characterization methods

This study comprises a variety of analytical methods for characterization of the electrical, optical and crystallographic, morphological and surface properties of thin films and complete PSCs and PSMs. The corresponding experimental setups and measurement parameters are described in the following subsections.

3.2.1 Electrical characterization

For the characterization of the photovoltaic device performance and the spectral response of the solar cells and modules, *IV* measurements and EQE analysis, respectively, were conducted.

Current density–voltage dependency

Current density–voltage dependency (*JV*) measurements to determine the performance of photovoltaic devices including modules (Subsection 2.1.2) were performed with a source meter[59] at a scan speed of $0.28\,V\,s^{-1}$ in ambient air under illumination of standard test conditions by a class AAA solar simulator[60], which was calibrated by means of a Si cell to $1000\,W\,m^{-2}$ (AM1.5G). In the case of single cells, devices were measured from −0.2 V to 1.5 V (*fwd*) and vice versa (*rvs*). The devices were annealed at 90 °C for 10 s to 20 s (30 s to 60 s: MC) and cooled to RT right

[59] 2400, Keithley
[60] WXS-90S-L2 Super Solar Simulator, Wacom

before measuring. No light soaking or biasing was applied to the devices before recording the *IV* characteristics. The PSCs were kept at 25.0 °C during the measurements.

For the SDC study (Section 6.3), *IV* characteristics were recorded by an automated measurement system with four source measure units[61] including an in-house LabView program implemented by Moritz Schultes where eight cells can be analyzed simultaneously. The devices were annealed at 90 °C for 30 s to 60 s and cooled to RT right before measuring.

External quantum efficiency (EQE)

External quantum efficiency (EQE) data was determined with an EQE system[62] without voltage- and with or without light-bias (corresponding to ~0.25 sun) in the spectral range from 300 nm to ~900 nm. The setup was calibrated with a standardized Si photodiode (300 nm to 1100 nm) prior to the measurements. The measurement spot size was 0.05 cm^2.

The EQE is the ratio of the photogenerated electrons in a solar cell at short circuit condition to the number of incident photons at a specific wavelength.
Therefore, the integration of EQE is utilized to calculate the short circuit current density (J_{SC}), as follows

$$J_{SC} = q \int_0^\infty \mathrm{EQE}(\lambda)\, \Phi_{AM1.5G}(\lambda)\, d\lambda \tag{3.1}$$

where q is the electron charge, $\Phi_{AM1.5G}$ is the wavelength-dependent photon flux of the solar spectrum (AM1.5G) per unit area at wavelength λ.

E_g was estimated from EQE spectra to be ~1.59 eV in the case of gas stream-assisted blade coated MAPI (5 % $PbCl_2$) and ~1.62 eV in the case of multi-cation perovskite.

3.2.2 Optical and crystallographic characterization

This subsection covers the experimental techniques for optical and crystallographic characterization of thin films, such as UV/Vis spectroscopy to determine transmittance and XRD, respectively.

UV/Vis spectroscopy

Ultraviolet to visible (UV/Vis) spectroscopy data including transmittance (T) spectra were measured with a spectrophotometer[63]. The incidence of light was normally from the glass side.

The absorptance (A) spectra were calculated by using determined signals as follows

$$A = 1 - T - R \tag{3.2}$$

[61] X200, Ossila
[62] PVE300, Bentham
[63] Lambda 900, PerkinElmer

where T and R are the measured transmittance and reflectance signals, respectively. Signals were measured without integrating sphere, thus scattering was neglected. The incidence of light was from the sample side.

X-ray diffraction (XRD) and Grazing incidence x-ray diffraction (GIXRD)

X-ray diffraction (XRD) data (2θ scan, typically 5° to 70°) was collected via a diffractometer[64] in Bragg-Brentano geometry with a Cu K-α radiation source (λ=1.5406 Å). The acceleration voltage and current were set to 40 V and 40 µA, respectively.
Grazing incidence x-ray diffraction (GIXRD) data (2° to 31°) was collected at an angle of incidence (ω) of 0.15° with the same voltage and current parameters. Measurements were carried out by Julia Zillner.

3.2.3 Morphological characterization

This subsection covers the experimental techniques for the characterization of thin film morphology. Herein the most important analysis techniques are scanning electron microscopy (SEM) and confocal laser scanning microscopy (CLSM).

Scanning electron microscopy (SEM)

A scanning electron microscope[65] was used at normally 5 kV to obtain top-view and cross-section scanning electron microscopy (SEM) images utilizing an in-lens detector. Measurements were carried out by Tina Wahl, Daniela Müller and Jonas Hanisch.

Confocal laser scanning microscopy (CLSM)

Confocal laser scanning microscopy (CLSM) images were taken with a color 3D confocal laser scanning microscope[66]. The software for image and root-mean-square (RMS) roughness (R_q) data processing of the surface of thin films and their thicknesses was VK Analyzer from Keyence. R_q indicates the root mean square of the height of each point in the range of image and is described as

$$R_q = \sqrt{\frac{1}{N}\sum_{n=1}^{N} {Z_n}^2} \tag{3.3}$$

where Z_n is the height of each point on the height of the reference surface and n is the number of pixels in the range of image. The entire image file was set as specified measurement range.

The thickness of perovskite thin films was determined via step height line scan measurements.

[64] Empyrean, Panalytical
[65] XL30 Sirion FEG, FEI or Gemini 2 Crossbeam 550, Zeiss
[66] VK-9710, Keyence

3.2.4 Surface characterization

To characterize the thin film surface amongst others TOF-SIMS and XPS measurements were carried out.

Time-of-flight secondary ion mass spectroscopy (TOF-SIMS)

The time-of-flight secondary ion mass spectroscopy (TOF-SIMS) depth profiles were measured with a TOF-SIMS setup[67]. Pulsed primary ions from a 30 keV Bi^+ liquid-metal ion gun were used as an analytical source, and a 1 keV Cs^+ source was utilized as a sputtering ion source. TOF-SIMS depth analysis was performed on a $50 \times 50\,\mu m^2$ area in the so-called spectrometry mode inside a $200 \times 200\,\mu m^2$ sputtering crater.

For the 2D surface images, the Bi^+ liquid-metal ion gun was used in the so-called fast imaging mode on a $20 \times 20\,\mu m^2$ area.

3D tomography was performed on a $20 \times 20\,\mu m^2$ analysis area in the so-called delayed extraction mode but additionally with the Cs^+ sputter source (1 keV, $200 \times 200\,\mu m^2$). The depth of the 3D cube is approximately 360 nm. Measurements were carried out by Jonas Hanisch.

X-ray photoelectron spectroscopy (XPS)

The samples were fixed by two Cu clamps on a rotatable sample holder and were brought into a vacuum chamber[68]. A magnesium (Mg) source[69] generates x-ray with an energy of 1253.6 eV. A detector[70] selects the emitted electrons. Single spectra were recorded in Fixed Analyzer Transmission mode. All measured curves were fitted by the program Unifit to determine exact binding of each single component. Measurements were carried out by Wolfram Hempel.

Crystal grain size measurements

The evaluation of the SEM images and measurement of the crystal grain size distribution were performed via the program ImageJ [416]. The area of each crystal grain was manually marked (see Figure C.2) and was determined by means of the program. The crystal grain diameter was estimated by assuming circular grains as follows

$$d_{\text{grain}} = \sqrt{\frac{4A_{\text{grain}}}{\pi}} \tag{3.4}$$

where A_{grain} is the crystal grain area.

[67] TOF-SIMS 5, IONTOF
[68] LHS-10, Leybold Heraeus
[69] PS XR-20, SPECS
[70] PHOIBOS100 MCD5, SPECS

4 Understanding the heat-assisted perovskite conversion for MAPI based solar cells processed by blade coating

The first main chapter of this study describes the development and understanding of the heat-assisted perovskite conversion for blade coated MAPI based perovskite solar cells (PSCs). The chapter is divided into two result sections, which discuss principle investigations on heat-assisted perovskite conversion without and with the utilization of a surfactant in the precursor solution, respectively. The chapter is finalized with a short conclusion.

The first Section 4.1 discusses the principle investigations on heat-assisted perovskite conversion. Thereby, it focuses on the conversion without the use of a surfactant. A morphological study on perovskite films via altering the perovskite processing temperature is presented (Subsection 4.1.1). Subsequently, the effects of perovskite processing temperatures on PCE of PSCs are shortly discussed (Subsection 4.1.2).

Secondly in Section 4.2, heat-assisted perovskite conversion with the use of a surfactant in the perovskite precursor solution is evaluated. The first subsection describes the improvement of the perovskite morphology by surfactant utilization (Subsection 4.2.1). The second subsection includes the description of detrimental consequences of the surfactant (Subsection 4.2.2).

The subsequent Section 4.3 concludes Chapter 4 on understanding the heat-assisted perovskite conversion for blade coated MAPI based perovskite solar cells. It summarizes main disadvantages of the heat-assisted perovskite conversion with or without the use of a surfactant and gives reasons for changing the conversion method in the two subsequent main Chapters 5 and 6 of this thesis.

4.1 Principle investigations on heat-assisted perovskite conversion

The following section includes the principle investigations on heat-assisted perovskite conversion from a $PbAc_2$ based precursor solution in inert N_2 atmosphere. The aim of the section is to study the influence of processing temperature on the perovskite morphology (Subsection 4.1.1) and its consequent effect on the PCE of PSCs (Subsection 4.1.2). Thereby, no surfactant was utilized in the precursor solution, which is in contrast to Section 4.2, where a surfactant is used.

4.1.1 Morphological study of perovskite processing temperature

At first, the author investigated heat-assisted perovskite conversion, since it represents the most easily realizable conversion method and might be scalable as discussed in Subsection 2.2.3. Furthermore, blade coating (BC) (Subsection 2.2.1) was utilized as scalable deposition technique.

SEM top-view images of annealed MAPI perovskite layers blade coated on top of PEDOT:PSS at different substrate and blade coater plate temperatures during wet film deposition, respectively, which are referred to as the processing temperature hereinafter, are presented in Figure 4.1.

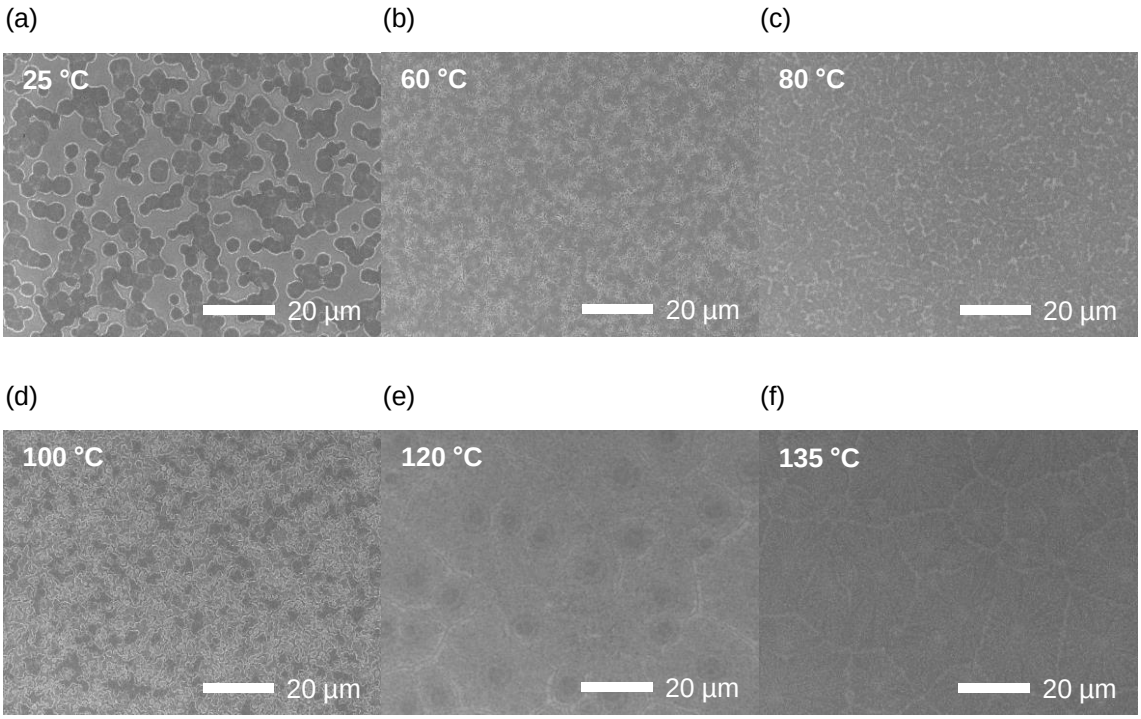

Figure 4.1: SEM top-view images of annealed perovskite layer blade coated on top of PEDOT:PSS at different processing temperature: (a) 25 °C, (b) 60 °C, (c) 80 °C, (d) 100 °C, (e) 120 °C, (f) 135 °C.

Figure 4.1a-c reveal inhomogeneous perovskite layers with distance between the perovskite grain clusters especially for the case of 25 °C (Figure 4.1a). This fact is coherent with nucleation and crystal growth kinetics introduced in Subsection 2.2.2: After blade coating at 25 °C, the deposited film is still wet when starting the annealing step at 90 °C. Therefore, the degree of supersaturation σ_S is too low in this case to reach a high density of nucleation sites. A diffusion controlled growth is predominant which leads to inhomogeneous films. With increasing processing temperature the density of nucleation sites can be increased (Figure 4.1a-c). At a processing temperature of ≥80 °C (Figure 4.1c-f), the wet film already fully nucleates on the blade coater plate. This fact might be caused by the BP of 153 °C of pure DMF (see Section 6.2) used here drastically increasing σ_S when the processing temperature is ≥80 °C.
However, the images in Figure 4.1d-f clearly indicate different perovskite morphology with varying sizes of Bénard convection cells. These convection cells are based on the Rayleigh–Bénard convection introduced in Subsection 2.2.4. The convection cell size increases with higher processing temperatures [412]. Literature reports similar investigations [344, 347, 397, 401].

Since the convection cells are large enough, they are not only observed in SEM images but can be also investigated in simple CLSM measurements as illustrated in Figure 4.2 for annealed perovskite layer blade coated on top of PEDOT:PSS at processing temperatures of 100 °C, 120 °C and 135 °C.

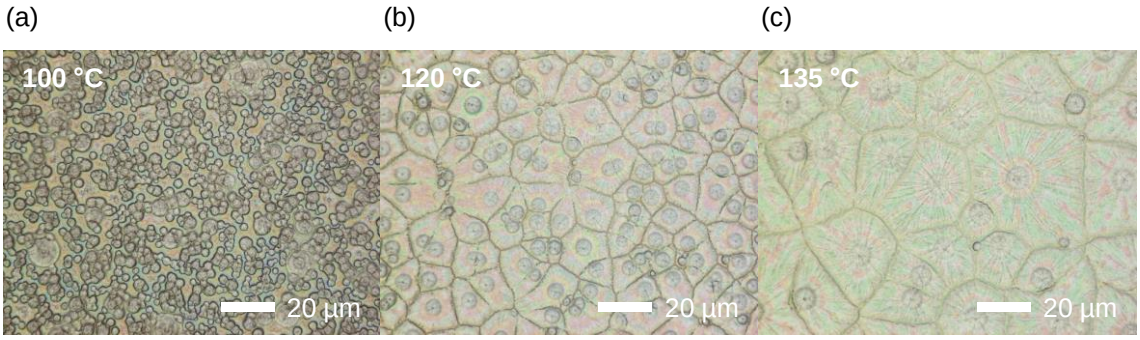

Figure 4.2: CLSM top-view images of annealed perovskite layer blade coated on top of PEDOT:PSS at different processing temperature: (a) 100 °C, (b) 120 °C, (c) 135 °C.

Here, roughness differences are exhibited more clearly than in SEM images (Figure 4.1). Thereby, nucleation sites in the center of the perovskite crystal grain clusters and trenches between adjacent clusters, in the following referred to as islands, are visible. Furthermore, the size of convection cells and perovskite islands, respectively, increases with processing temperature as already illustrated in Figure 4.1.

To investigate the root-mean-square (RMS) roughness (R_q) of the resulting perovskite layer, the author conducted CLSM top-view height images on the samples in Figure 4.2 and measured R_q as shown in Figure 4.3.

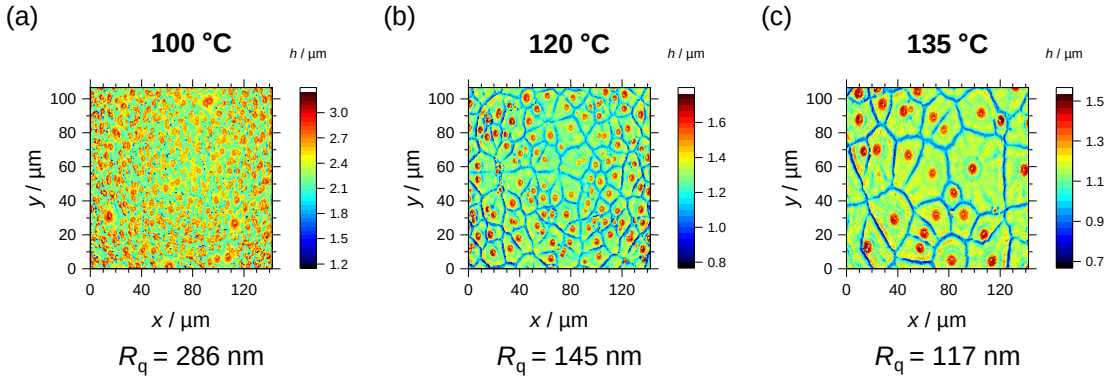

Figure 4.3: CLSM top-view height images and R_q analysis of annealed perovskite layer blade coated on top of PEDOT:PSS at different processing temperature: (a) 100 °C, (b) 120 °C, (c) 135 °C.

The R_q analysis reveals a decrease in R_q from 286 nm to 145 nm and 117 nm with increasing the processing temperature from 100 °C to 120 °C and 135 °C, respectively. However, Figure 4.3c illustrates that the height difference between a nucleation site in the center of the convection cell (red) and a trench surrounding the island (blue) is ~800 nm even in the case of 135 °C. It seems that the trenches are as deep as reaching the subjacent PEDOT:PSS layer. The roughness difference is caused by the circulating convection rolls of the fluid [396] as mentioned in Subsection 2.2.4. Via heat-assisted perovskite conversion it is challenging to achieve smooth perovskite surfaces but normally no formation of voids towards the HTL is involved (see Subsection 5.2.2) due to a bottom-up wet film drying [377]. The mentioned drawbacks represent intrinsic challenges of the heat-assisted perovskite conversion leading to detrimental consequences for device performance as shortly discussed in the following Subsection 4.1.2.

The author emphasizes that, besides the morphological study of the perovskite processing temperature which was the focus of Subsection 4.1.1, the perovskite crystal structure of the presented absorber films has been confirmed via XRD measurements, but are omitted here.

4.1.2 Effect of perovskite processing temperature on PCE

To investigate the effect of the perovskite processing temperature and the resulting perovskite morphology described in Subsection 4.1.1 on device performance the author utilized blade coated perovskite layers processed by heat-assisted conversion at different temperatures in PSCs. The *JV* curves of these MAPI based solar cells with PEDOT:PSS as HTM measured in *fwd* scan direction are illustrated in Figure 4.4.

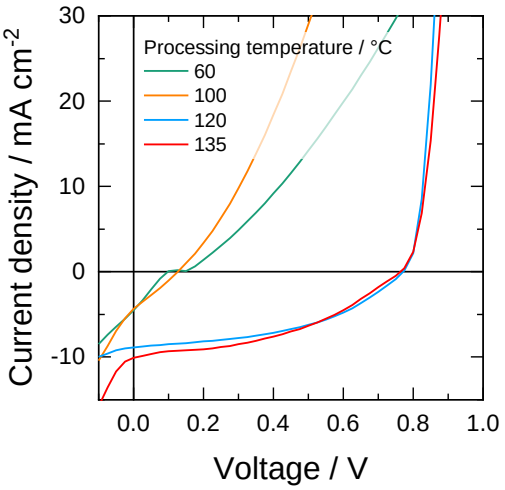

Figure 4.4: *JV* curves of MAPI based PSCs (without BCP) blade coated on top of PEDOT:PSS at different processing temperatures without surfactant measured in *fwd* scan direction.

From Figure 4.4, one can clearly see that photovoltaic devices processed at low processing temperatures, such as 60 °C and 100 °C are short-circuited and deliver almost no I_{ph} due to an inhomogeneous absorber layer as illustrated in Figure 4.1. However, solar cells with a higher processing temperature like 120 °C and 135 °C disclose a diode behavior generating I_{ph}. Nevertheless, devices still exhibit low R_{sh} values for a device blade coated at a processing temperature of 120 °C or 135 °C which is highly likely caused by the shunt pathways through the perovskite layer via the trenches surrounding the perovskite islands indicated in Figure 4.3b, d. These PCE dependencies are completely consistent with corresponding perovskite morphology depending on the processing temperature discussed in Subsection 4.1.1.
Consequently, the author decided to choose processing temperatures ≥120 °C for heat-assisted perovskite conversion. This fact is accordant to reports in literature choosing temperatures of 120 °C to 150 °C [274, 340, 342, 344–352].

4.2 Heat-assisted perovskite conversion with surfactant

This section is devoted to the heat-assisted perovskite conversion with the utilization of a surfactant in the precursor solution to improve the perovskite morphology (Subsection 4.2.1), which is in contrast to Section 4.1, where a surfactant was omitted. Furthermore, the detrimental consequences of the surfactant are discussed (Subsection 4.2.2).

4.2.1 Improved perovskite morphology by surfactant utilization

Deng et al. introduced the utilization of very small amounts of amphiphilic surfactants such as L – α-phosphatidylcholine (LP) in the perovskite precursor solution altering fluid drying dynamics and wetting behavior on the subjacent layer to improve the perovskite layer morphology originally for heat-assisted conversion [274]. The molecular structure of LP is illustrated in Figure 4.5.

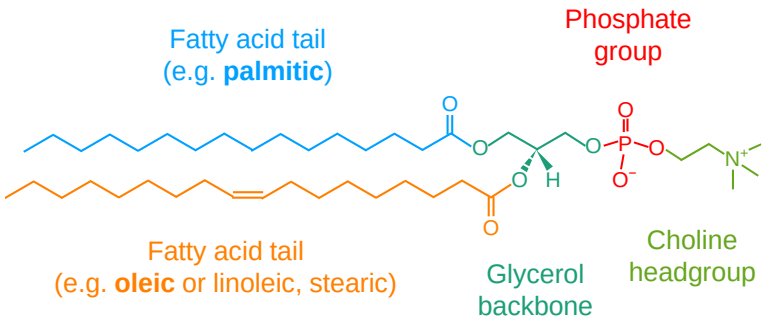

Figure 4.5: Molecular structure of the amphiphilic surfactant L – α-phosphatidylcholine (LP) utilized in this work. The composition of palmitic, oleic, linoleic and stearic acid will vary due to the natural nature [274].

The molecule structure exhibits a polar phosphate group with a choline headgroup and two non-polar long fatty acid tails. Consequently, the molecule exhibits a hydrophilic and lipophilic (hydrophobic) functional groups, thus, is amphiphilic. Therefore, the phospholipid can act as a surfactant due to its self-assembling on the surface of a solution with the hydrophobic group pointing to air to reduce the surface tension σ of the solution as mentioned in Subsection 2.2.4 [274]. Furthermore, the molecule is capable of passivating charge traps or ionic defects due to its amphoteric (zwitterionic) character which implies the existence of negatively charged and positively charged components, the phosphate and quaternary ammonium component in the choline group [417], respectively, as illustrated in Figure 4.5.

Figure 4.6 presents SEM 30° tilted cross-section images of annealed perovskite layer blade coated on top of PEDOT:PSS without and with 0.2 mg mL^{-1} LP surfactant in the perovskite precursor solution.

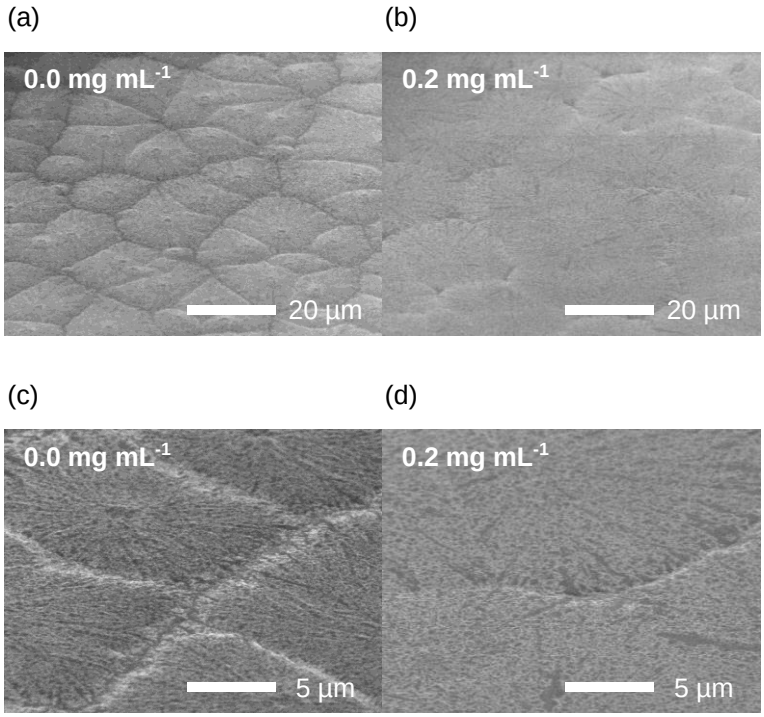

Figure 4.6: SEM 30° tilted cross-section images of annealed perovskite layer blade coated on top of PEDOT:PSS at a processing temperature of 135 °C (a, c) without and (b, d) with 0.2 mg mL^{-1} surfactant.

Without the surfactant, clear trenches are observed as indicated by Figure 4.6a and c. However, when utilizing 0.2 mg mL^{-1} LP surfactant the appearance of trenches is dramatically reduced. Furthermore, the nucleation sites (Figure 4.6c) indicated by the already discussed height differences (Figure 4.3) are not visible in the case of the sample including the surfactant (Figure 4.6b, d). Additionally, with the surfactant the mean crystal grain cluster diameter seems to increase although the processing temperature of both samples is the same, namely 135 °C. The morphological study of perovskite processing temperature has already been discussed in Subsection 4.1.1. Moreover, the images indicate that one island is not one single perovskite crystal grain but a cluster of many grains [412]. The findings when utilizing the LP surfactant observed by the author are similar to the ones reported by Deng et al. [274].

To further investigate the perovskite surface roughness of absorber layers with the addition of LP, the author conducted CLSM top-view height images and measured R_q of annealed perovskite layers blade coated on top of PEDOT:PSS at a processing temperature of 135 °C of two samples one with LP and one without the surfactant. Figure 4.7 presents the corresponding analysis.

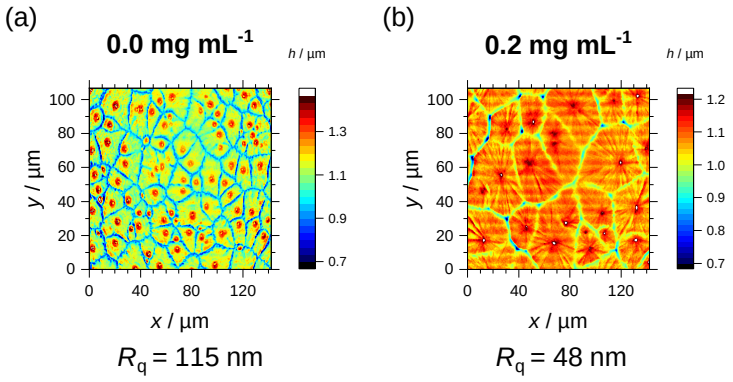

Figure 4.7: CLSM top-view height images and R_q analysis of annealed perovskite layer blade coated on top of PEDOT:PSS at a processing temperature of 135 °C (a) without and (b) with 0.2 mg mL^{-1} surfactant.

Figure 4.7 indicates a dramatic decrease in R_q from 115 nm to 48 nm of the perovskite surface when utilizing the surfactant. Furthermore, the depth of trenches surrounding the perovskite crystal clusters or convection cells are decreased as well as assumed from SEM images in Figure 4.6. Moreover, utilization of surfactant increases the island diameter and therefore decreases the total area of trenches as mentioned before. Nevertheless, the trenches are not fully avoided as illustrated in Figure 4.7b.

The author studied the effect of LP surfactant utilization in the precursor solution not only by a morphological SEM study which has been already presented in literature [274] and roughness analysis but also, for the first time, by elemental analysis via TOF-SIMS measurements. Figure 4.8 presents TOF-SIMS top-view images for MA^+ and Pb of annealed perovskite layer blade coated on top of PEDOT:PSS without and with 0.2 mg mL^{-1} LP surfactant in the perovskite precursor solution.

As illustrated in Figure 4.8a and c, the islands or perovskite grain clusters are clearly visible in the measurements of MA^+ and Pb. Consequently, that means that the elemental contribution is not homogeneous in the first nanometers of the perovskite surface and the components Pb (Figure 4.8c) but especially MA^+ (Figure 4.8a) are reduced at the trenches. The width of trenches of MA^+ of ~1 µm is larger than for Pb (<1 µm). Furthermore, Pb is slightly accumulated at the nucleation site while MA^+ is depleted.
However, when using the LP surfactant in the precursor solution, not only the perovskite morphology is improved as indicated in Figure 4.6 and 4.7 but also the elemental components of the absorber layer MA^+ and Pb are more homogeneously distributed in the perovskite surface (Figure 4.8b, d). No elemental accumulation or depletion are observed at potential trenches and nucleation cites in this case [412].
The findings from the morphological study indicate that they are directly linked to the elemental study due to the intrinsic mechanism of the Rayleigh–Bénard convection (Subsection 2.2.4). Due to the convection and its facile removal, the volatile MA^+ leaves the wet film during heat-assisted perovskite conversion predominantly at the area where a trench stays behind after annealing. Furthermore, it might pull some Pb with it out of the wet film during drying explaining the depletion of Pb at the trenches. In conclusion, the LP surfactant hinders the Rayleigh–Bénard convection leading to a more homogeneous elemental distribution of the perovskite absorber layer.

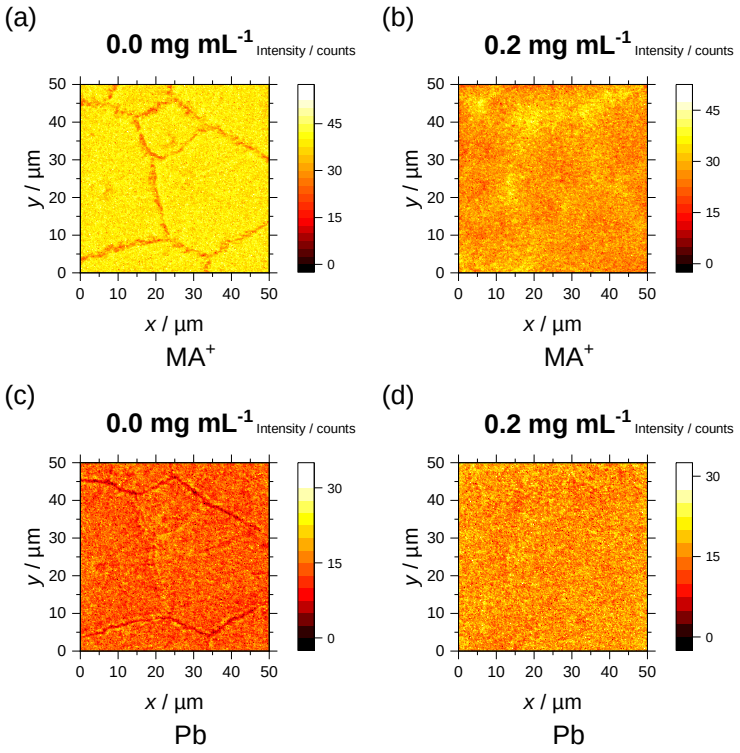

Figure 4.8: TOF-SIMS top-view images of annealed perovskite layer blade coated on top of PEDOT:PSS at a processing temperature of 135 °C (a, c) without and (b, d) with 0.2 mg mL^{-1} surfactant: (a-b) MA^+ and (c-d) Pb signals.

4.2.2 Detrimental consequences of surfactant

As the author presents in this subsection, the surfactant LP not only improves the perovskite morphology, surface roughness and elemental distribution as shown before, however, it causes detrimental consequences as well. The findings on these consequences are, to the best of the author's knowledge, not yet reported in literature. It should be noted that the layers subsequent to the absorber in literature reports are typically deposited via vacuum deposition, when utilizing LP as a surfactant in the perovskite precursor solution [274, 344, 350, 352, 375, 389, 418, 419]. Hence, the option of full solution processing of the device stack is excluded.

However, since the thesis focuses on solution processing the goal was to deposit the ETL layer on top of perovskite from solution as well. The SEM 30° tilted cross-section images in Figure 4.9 indicate the challenge with depositing the ETL, such as PCBM in a nonpolar solvent like CB or DCB, hindering an unproblematic continuation of the device stack by solution processing as discovered by the author.

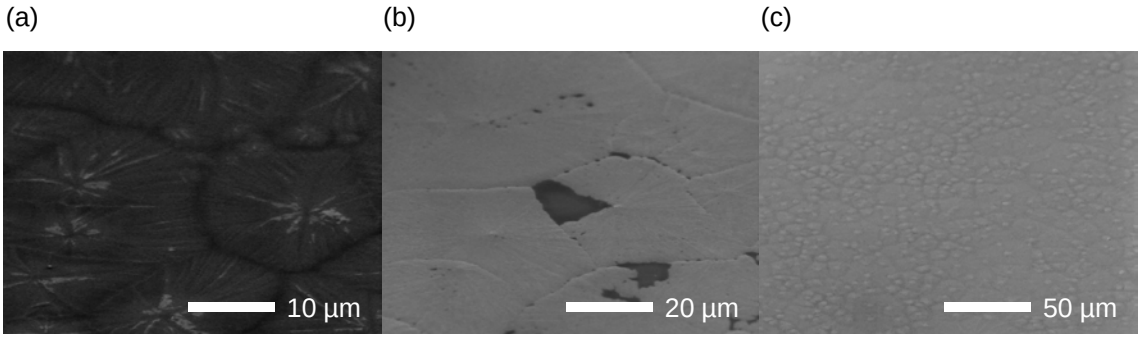

Figure 4.9: SEM 30° tilted cross-section images of PCBM spin coated on annealed perovskite layer blade coated on top of PEDOT:PSS at a processing temperature of (a) 120 °C and (b-c) 135 °C (a) without and (b-c) with 0.2 mg mL^{-1} surfactant and (c) with 4 s plasma (Ar, 20 W) treatment on perovskite.

When utilizing no surfactant in the precursor solution, the deposition of the ETM PCBM on the annealed perovskite is accomplished without any issue as illustrated in Figure 4.9a. Despite the fact that the PCBM layer in this case is slightly too thin in order to completely cover the perovskite surface roughness with a R_q of ~150 nm (Figure 4.3b), the PCBM solution is wetting the absorber perfectly. However, when using 0.2 mg mL^{-1} LP surfactant in the precursor solution this not the case as illustrated in Figure 4.9b. The PCBM solution is drastically dewetting on the absorber surface leading to an completely uncontinuous or inhomogeneous layer. The author assumes that the reason for that is the irregular adsorption of the surfactant predominantly at the perovskite surface, as discussed further down, due to Rayleigh–Bénard convection (Subsection 2.2.4) right before complete drying of the wet film. Due to its amphiphilic nature and the polar phosphate and choline groups in the molecular structure (Figure 4.5) the surfactant prevents sufficient wetting of the PCBM solution based on a nonpolar solvent.

To address and overcome this challenge, the author investigated a short, low-energy and precisely adjusted additional Ar plasma treatment of the perovskite absorber surface as explained in more detail further down in order to fragment the LP molecules at the surface after finalizing the perovskite layer, which hinder excellent wetting. Figure 4.9c illustrates that after the additional plasma treatment on the perovskite fabricated by a precursor solution including the surfactant the PCBM layer is, however, fully wetting the surface and a homogeneously covered ETL is accomplished [412].

In order to verify the existence of the surfactant molecules in the perovskite layer after annealing, the author conducted TOF-SIMS measurements of the distribution of the PO_3^- fragment, since it corresponds to a functional group of the LP molecule structure as illustrated in Figure 4.5. The top-view images of annealed perovskite layer blade coated on top of PEDOT:PSS at a processing temperature of 135 °C with different amounts of LP surfactant in the perovskite precursor solution are presented in Figure 4.10.

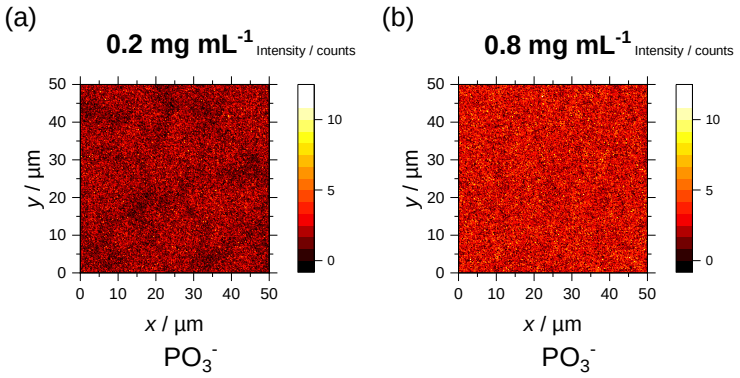

Figure 4.10: TOF-SIMS top-view images of annealed perovskite layer blade coated on top of PEDOT:PSS at a processing temperature of 135 °C with (a) 0.2 mg mL^{-1} and (b) 0.8 mg mL^{-1} surfactant: PO_3^- fragment signal, which correspond to the functional group (phosphate) of the LP molecule (Figure 4.5).

The sample with four times higher surfactant content (Figure 4.10b) compared to the reference sample indicated in Figure 4.10a exhibits a slightly brighter appearance which means that a higher intensity of PO_3^- is quantified at the perovskite surface.

Figure A.1 illustrates corresponding TOF-SIMS top-view images of spin coated perovskite layer with different concentrations of LP surfactant of 0.0 mg mL^{-1}, 0.2 mg mL^{-1} and 0.8 mg mL^{-1} in the precursor solution on top of PEDOT:PSS similarly proving again that the surfactant molecule can be detected by the identification of PO_3^- [412]. It seems, that the PO_3^- signal and, thus, the surfactant molecule is slightly more homogeneously distributed on a spin coated (Figure A.1b) than on a blade coated perovskite surface (Figure 4.10a).

Additionally, to verify the exact location of the surfactant molecules in the perovskite layer after annealing and to investigate the influence of the short plasma treatment on the perovskite film, TOF-SIMS depth profiles through samples of annealed perovskite layer blade coated on top of Glass/ITO/PEDOT:PSS at a processing temperature of 135 °C with surfactant in the precursor solution are analyzed. Furthermore, the author investigated a 10 s plasma treatment on the perovskite to possibly remove the surfactant molecules (Figure 4.11) as mentioned before.

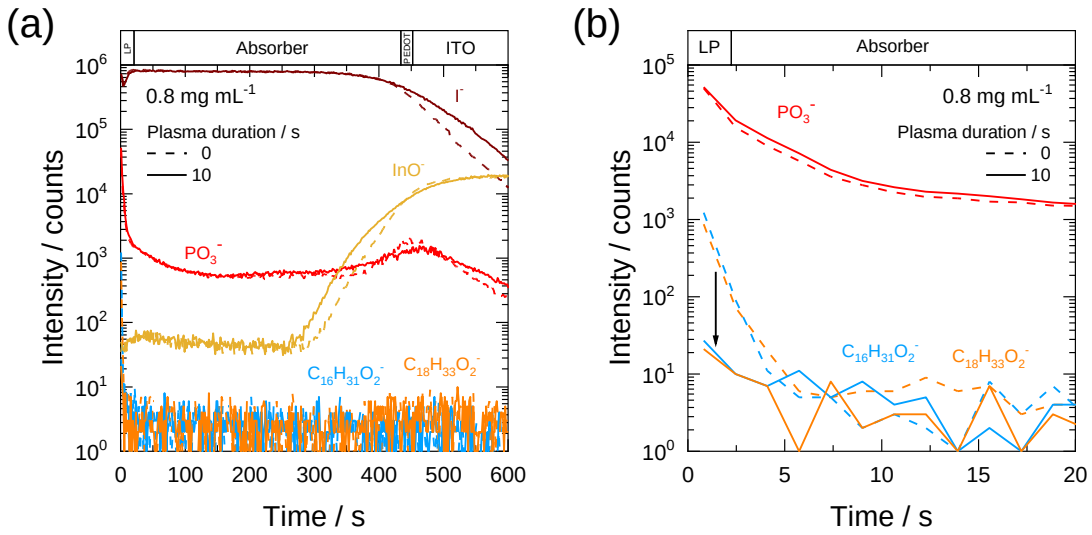

Figure 4.11: TOF-SIMS depth profiles through samples of annealed perovskite layer blade coated on top of Glass/ITO/PEDOT:PSS at a processing temperature of 135 °C with and without 10 s plasma (Ar, 20 W) on perovskite with 0.8 mg mL^{-1} surfactant. All components in (b) correspond to the functional groups (phosphate, fatty acid tails) of the LP molecule (Figure 4.5).

Figure 4.11 indicates where the surfactant or rather three main functional groups of the LP surfactant (Figure 4.5) are located in the perovskite layer after annealing. In Figure 4.11a, no difference in intensity of the signals of samples without and with 10 s plasma treatment on perovskite are found. Furthermore, the slight intensity increase of PO_3^- at the ITO/PEDOT:PSS interface is caused by the PEDOT:PSS layer itself which is most likely caused by impurities in the PEDOT:PSS remaining in the material and aqueous solution, respectively, after its chemical synthesis [420, 421]. Moreover, the intensity of I^- is constant through the perovskite absorber layer.

When zooming in on the first 20 s sputter time (Figure 4.11b), one can see that, interestingly, the surfactant is predominately located at the very top surface of the perovskite layer as indicated by the decreasing signal over sputtering time of $C_{16}H_{31}O_2^-$ and $C_{18}H_{33}O_2^-$ which corresponds to the palmitic and oleic fatty acid tails (Figure 4.5) and PO_3^-, respectively, which was already used as surfactant indication in TOF-SIMS top-view measurements presented in Figure 4.10. The application of the short plasma treatment on the perovskite leads to a fragmentation mainly of the fatty acid tails as illustrated by the black arrow, however, PO_3^- is not fragmented (Figure 4.11b). This fact is consistent because the fatty acid groups exhibit long, hydrophobic carbon chains which can be more easily fragmented via the plasma treatment than the small phosphate group.

The fragmentation of the irregularly arranged LP molecules and the activation of the perovskite surface by the plasma leads to the improved wetting properties of the PCBM in a nonpolar solvent on the perovskite layer comprising the LP surfactant in the precursor solution as mentioned before (Figure 4.9c) [412].

It should be noted that the location of the LP surfactant in the annealed perovskite thin film might be dependent on the perovskite conversion method utilized for wet film drying. Since fluid dynamics in heated wet films (Subsection 2.2.4) play a key role mainly in heat-assisted perovskite conversion, it is highly likely that the LP molecules do not adsorb at the perovskite surface but at a different location in the perovskite absorber layer in the case of gas-assisted

perovskite conversion which is applied in Chapter 5 and 6. Thus, the detrimental procedural effects of the surfactant mentioned before might be avoided by using the gas-assisted instead of the heat-assisted perovskite conversion.

TOF-SIMS depth profiles in Figure A.2 verify the existence of surfactant in corresponding spin coated perovskite layer on top of Glass/ITO/PEDOT:PSS by investigating samples with and without surfactant in the precursor solution and without plasma treatment on the perovskite. As mentioned before, the PO_3^- increase at the interface toward the ITO for the sample without the LP surfactant (Figure A.2a) is caused by residuals in the PEDOT:PSS after synthesis. The increase of PO_3^- mainly at the perovskite surface in the sample with surfactant (Figure A.2a) is directly related to the surfactant itself. In Figure A.2b, this increase is depicted more clearly via the black arrow. A similar increase is visible for the fatty acid tails when utilizing the surfactant (Figure A.2b) as indicated by the second black arrow [412].

To study the effect of the surfactant and the plasma treatment on photovoltaic device performance, the author utilized perovskite layers with different concentrations of LP surfactant in the perovskite precursor solution (0.0 mg mL^{-1}, 0.2 mg mL^{-1} and 0.8 mg mL^{-1}), plasma duration (0 s, 2 s and 10 s) and different perovskite deposition technique (SC, BC) as illustrated by *JV* curves measured in *fwd* scan direction in Figure 4.12.

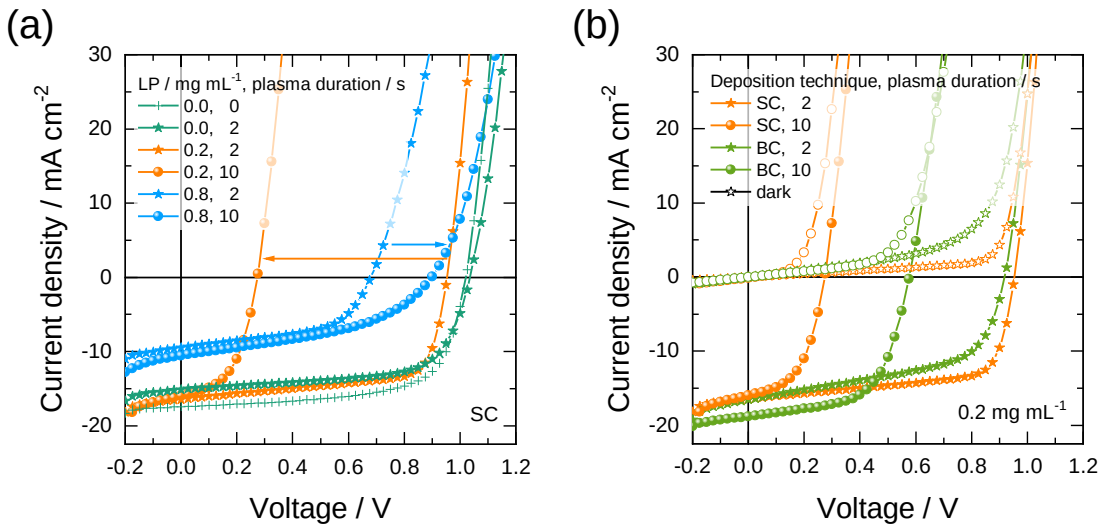

Figure 4.12: *JV* curves of MAPI based PSCs measured in *fwd* scan direction (a) spin coated (solvent vapor annealing) with different concentrations of surfactant and plasma (Ar, 20 W) duration and (b) spin or blade coated (processing temperature of 135 °C) on top of PEDOT:PSS with 0.2 mg mL^{-1} surfactant with different plasma duration on perovskite.

Figure 4.12a illustrates the dependency of plasma treatment and device performance of spin coated PSCs. The green, orange and blue *JV* curves represent the LP surfactant concentration in the precursor solution of 0.0 mg mL^{-1}, 0.2 mg mL^{-1} and 0.8 mg mL^{-1}, respectively. The reference device without surfactant and plasma treatment showed the highest performance. When treating the reference perovskite by a plasma over a period of 2 s, the J_{SC} drops by merely ~2.5 mA cm^{-2} and V_{OC} values stay constant at ~1.0 V. This implies that a plasma treatment on the perovskite surface can detrimentally affect the interface to the ETL and therefore device efficiency. This can be explained by volatile MA^+ ions leaving the film via the plasma treatment as presented by XPS measurements further down (Figure 4.13a).

When comparing to the reference sample, a surfactant content of 0.2 mg mL^{-1} is only slightly detrimental for the J_{SC}. However, using a high surfactant content (0.8 mg mL^{-1}) leads to a huge decrease of J_{SC} of >5 mA cm^{-2}.
While 10 s of plasma treatment decreases the V_{OC} dramatically in the case of 0.2 mg mL^{-1} surfactant, the same treatment, however, increases the V_{OC} in the case of the higher surfactant content (0.8 mg mL^{-1}) as indicated by the blue and orange arrows. Nevertheless, this is consistent with the degree of fragmentation of surfactant molecules measured by TOF-SIMS depth profiles as already mentioned before (Figure 4.11).
Summing up, the plasma treatment duration and surfactant concentration are mainly related to the resulting V_{OC} and J_{SC}, respectively. A high surfactant content and a too long plasma treatment, especially for the case of low surfactant concentration, is detrimental for solar cell device performance. In addition, the optimum plasma treatment duration is closely correlated to the surfactant concentration [412].

As presented in Figure 4.12b (0.2 mg mL^{-1} LP surfactant), in general lower R_{sh} values are observed for PSCs with blade coated perovskite compared to ones with spin coated films due to the shunt pathways intrinsically generated by the heat-assisted perovskite conversion as mentioned before. Furthermore, a 10 s plasma treatment of the perovskite surface reduces the V_{OC} less drastically in the case of BC compared to the spin coated counterpart.
The reason for that might be the higher resulting concentration of surfactant located at the perovskite surface for a blade coated sample as revealed by comparing the PO_3^- fragment signal intensity in Figure 4.10a (BC) with the one in Figure A.1b (SC), although the same surfactant content in the perovskite precursor solution of 0.2 mg mL^{-1} was utilized in both cases. This higher resulting concentration protects the blade coated perovskite surface against the plasma more effectively [412].

Via heat-assisted perovskite conversion, a maximum PCE of 10.9 % and 10.8 % in *fwd* and *rvs* scan direction, respectively, on an A_{act} of 0.24 cm^2 of blade coated MAPI PSCs with a processing temperature of 135 °C, 0.2 mg mL^{-1} LP surfactant in the perovskite precursor solution and 2 s plasma treatment on perovskite was reached (not shown), which is comparable to results of their spin coated counterparts. The reasons for the in general low performance are (i) mainly the low V_{OC} and partly the J_{SC} values caused by the HTM PEDOT:PSS (see Subsection 5.1.2), (ii) the V_{OC} decrease due to the use of the surfactant and the plasma treatment on the perovskite surface (Figure 4.12a) and (iii) a low FF caused by the discussed decreased R_{sh} (Figure 4.4) which results from the blade coating deposition technique in combination with the heat-assisted conversion method itself (Figure 4.12b).

To gain a deeper insight into the effects of the surfactant at the perovskite surface, XPS measurements are conducted. The main XPS spectra with photoelectrons of N 1s and Pb 4f are illustrated in Figure 4.13.

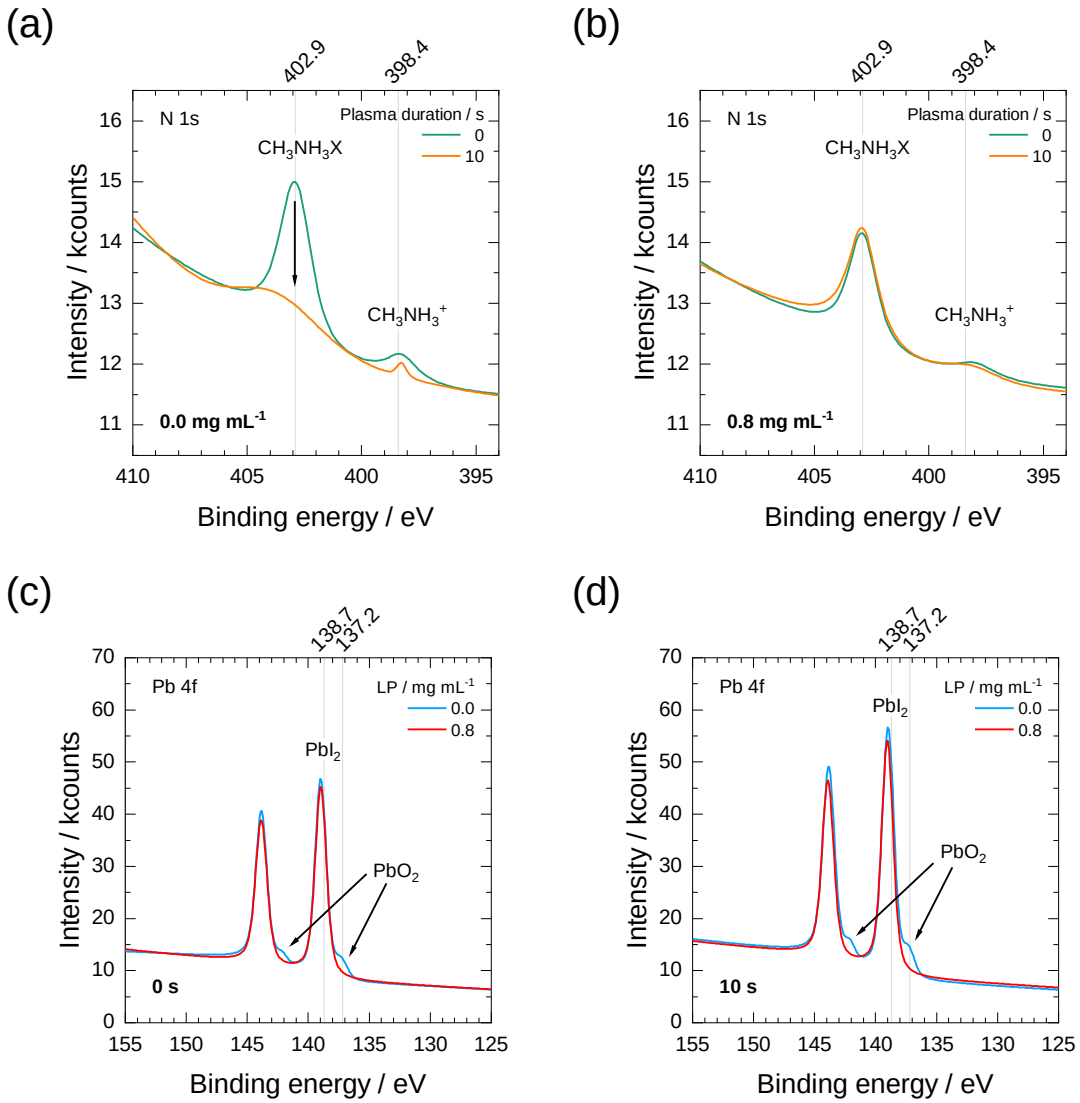

Figure 4.13: XPS spectra of annealed perovskite layer spin coated on top of Glass/ITO/PEDOT:PSS (a) without and (b) with 0.8 mg mL^{-1} surfactant and (c) without and (d) with 10 s plasma (Ar, 20 W) treatment on the perovskite: Photoelectrons of (a-b) N 1s and (c-d) Pb 4f. Figure A.3 shows corresponding photoelectrons of I 3d.

Figure 4.13 illustrates two main findings:

(i) Especially for the case with surfactant a decrease of a methylammonium compound through the plasma treatment, here labeled as CH_3NH_3X, implied by the nitrogen N peak at a binding energy of 402.9 eV (Figure 4.13b) is reduced in contrast to the sample without surfactant (Figure 4.13a). This indicates that the surfactant can protect the release of methylammonium from the perovskite surface during a too long plasma treatment [412] which was already assumed in the paragraph discussing Figure 4.12.

(ii) The portion of lead oxide (PbO_2) at a binding energy of 137.2 eV is missing in the case of perovskite including the surfactant (Figure 4.13c, d) which might imply that the surfactant can protect the PbI_3 group against oxidation to PbO. Furthermore, the PbO_2

peak intensity is increased by a negligible absolute value of 1.3 % after a plasma treatment of 10 s (Figure 4.13d).

The theory of bullet point (ii) is corroborated by the author through storing samples without and with surfactant in the perovskite precursor solution under ambient conditions (19 °C to 22 °C, 30 % to 50 % RH) over a period of 3 days (not shown). The samples without surfactant turned yellow indicating a decomposition of MAPI, however, the samples with LP did not. This stabilization ability is an interesting and promising feature of the surfactant which has been proven for the first time after it has been only assumed in literature [417]. Since stability of PSCs is not the main focus of this thesis, this feature was not investigated further but it should be studied in more detail in future.

Figure A.3 shows corresponding photoelectrons of I 3d without and with surfactant for the cases without (Figure A.3a) and with plasma (Figure A.3b). Since the binding energy in the case of I 3d is in general relatively higher compared to N 1s (Figure 4.13a, b) or Pb 4f (Figure 4.13c, d), the kinetic energy of the photoelectrons must be lower which means that the I_2 results relate to the very top surface of the perovskite layer. The measurements indicate no major shift of the elemental iodine I_2 peak at a binding energy of 619.9 eV between the samples without and with surfactant which implies that the I content is not influenced by the addition of the surfactant. When comparing the intensities and areas of the peaks of samples without and with plasma treatment, one cannot make a statement about the theory, if some I might leave the film due to the plasma treatment.

Additionally, the author tested the scalability of the heat-assisted perovskite conversion as illustrated by the photographical image of annealed MAPI fabricated by blade coating on PEDOT:PSS on $9 \times 9\,\mathrm{cm}^2$ substrates (Figure A.4). The author notes that drying features of the perovskite surface are visible which might be caused by a not perfectly homogeneous temperature distribution of the blade coater plate and consequently above the wet film during the quenching process. Moreover, it was found that it is not trivial to reach smooth perovskite surfaces via heat-assisted perovskite conversion due to a bottom-up wet film drying [377]. Due to the same reason, normally no formation of voids towards the HTL is observed for this perovskite conversion method [377] which typically would be indicated by a gray and milky appearance of the samples when observed from their backside through glass (see Subsection 5.2.2).

Due to the mentioned challenges complicating the solution processing and its upscaling by scalable techniques the heat-assisted perovskite conversion is not further utilized in this thesis.

4.3 Conclusion

Chapter 4 depicted the development and understanding of the heat-assisted perovskite conversion for MAPI ($PbAc_2$) based solar cells processed by blade coating.

The results of the morphological study disclosed that the most continuous and homogeneous perovskite thin films are achieved by choosing high processing temperatures ≥120 °C. PCE values of PSCs directly correlate to the perovskite morphology.
The author observed that the perovskite morphology is hardly controllable via heat-assisted conversion since wet film deposition, drying and nucleation plus even crystallization occur nearly simultaneously due to the high processing temperature which is on the other hand required to achieve the most continuous and homogeneous perovskite layers. Consequently due to their

temporally coupling, it is challenging to control each of the processes by itself. However, the ability for controlling each process is the key to manipulate and optimize the resulting perovskite morphology.
Additionally, the high processing temperatures result in fluid dynamics in the heated wet film such as Rayleigh–Bénard convection leading to convection cells which generate trenches in the annealed perovskite films encircling these cells. Hence, R_{sh} of PSCs is decreased and the risk of short-circuited devices is tremendously increased [412].
To address this problem, the author utilized the surfactant LP presented in literature [274] to hinder the solution convection. Applying the surfactant helps to improve the perovskite morphology, however, the trenches in the annealed thin film could not be completely avoided which leads to decreased device performance.
Furthermore, detrimental consequences of the surfactant were observed such as its adsorption at the perovskite surface which was verified by TOF-SIMS investigations hindering a continuation of the device stack by solution processing due to dewetting of the ETL solution. Thus, the author developed an additional plasma treatment on the annealed perovskite surface to remove the surfactant in order to enable wetting during the subsequent PCBM deposition via solution processing. This plasma step, however, detrimentally influences device performance as well.
Nevertheless, XPS measurements indicated that the surfactant added in the precursor solution and adsorbing at the surface of the annealed perovskite layer hinders the formation of PbO_2. This fact might be an indication for a possibly increased perovskite stability when adding the surfactant [412]. The author suggests to investigate this feature of the surfactant and its hydrophobic behavior [417] in more detail in future.
A test of upscaling substrate sizes to $9 \times 9\,cm^2$ revealed inhomogeneous perovskite layers with drying features and increased surface roughness caused intrinsically by the process of heat-assisted perovskite conversion.
In addition, the studies in Chapter 4 indicated that it is challenging to achieve smooth perovskite surfaces via heat-assisted perovskite conversion but normally involving no formation of voids towards the HTL due to a bottom-up wet film drying [377]. In contrast, Subsection 5.2.2 discusses the contrary observation for gas-assisted perovskite conversion since the wet film dries top-down leading to highly smooth perovskite surfaces, however, void formation at the HTL/perovskite is highly likely and needs to be addressed.

In summary, Chapter 4 highlighted that solely heat-assisted perovskite conversion seems less suitable for solution processing of hybrid perovskite thin films with well defined morphology and appears to be strongly limited for upscaling MAPI based PSCs by scalable techniques. Consequently, a different conversion method is required to control the perovskite morphology and in order to upscale solution processing of hybrid perovskite by scalable techniques.

Therefore, the following Chapter 5 focuses on controlling the perovskite morphology for upscaling blade coated MAPI based solar cells and modules applying gas-assisted perovskite conversion whereby perovskite morphology can be controlled via decoupling of wet film deposition, drying and nucleation or crystallization, respectively. Hence, this will require the establishment of a static low-pressure gas system.

5 Controlling perovskite morphology for upscaling blade coated MAPI based solar cells and modules

The second main chapter of this study depicts the control of the perovskite morphology for upscaling blade coated MAPI based solar cells and modules by gas-assisted perovskite conversion. It comprises four result sections, which discuss the development of gas-assisted perovskite conversion, further optimizations of the perovskite morphology, layer thickness optimization to improve device efficiency, and large-area deposition for module fabrication. The chapter is finalized with a short conclusion.

The first Section 5.1 covers the general development of gas-assisted perovskite conversion. Thereby, the establishment of a static low-pressure gas system is presented (Subsection 5.1.1). Furthermore, the hole transport material (HTM) is replaced to improve V_{OC} of PSCs (Subsection 5.1.2).

Secondly, the perovskite morphology is optimized with gas-assisted conversion in Section 5.2. Herein, one subsection describes blade coated nanoparticles (NPs) to achieve efficient wetting on the new hydrophobic hole transport layer (Subsection 5.2.1). For controlling the perovskite layer formation, composition engineering of the precursor solution is investigated (Subsection 5.2.2).

The subsequent Section 5.3 evaluates layer thickness optimization to increase device efficiency. Here, improvements in J_{SC} by modifying the absorber thickness (Subsection 5.3.1) and in FF by optimizing the HTL thickness (Subsection 5.3.2), respectively, are presented.

To test the upscalability of blade coated MAPI perovskite films, large-area deposition (Subsection 5.4.1) and their utilization in solar modules (Subsection 5.4.2) are examined in Section 5.4.

Section 5.5 concludes Chapter 5. It summarizes the quintessences of using a static low-pressure gas system in this chapter and discusses the needs of a moving high-pressure gas system in Chapter 6.

5.1 Development of gas-assisted perovskite conversion

This section is devoted to the development of gas-assisted perovskite conversion. The aim of the section is a successive advancement of the MAPI ($PbAc_2$) based solar cells by changing the conversion method of heat- (Chapter 4) to the here established gas-assisted perovskite conversion (Subsection 5.1.1) and by replacement of the hole transport material (HTM) (Subsection 5.1.2).

5.1.1 Establishment of static low-pressure gas system

For deposition of the $PbAc_2$ based MAPI perovskite layers, the author established and utilized a static low-pressure gas system in this thesis which enabled gas stream-assisted blade coating in a N_2-filled glovebox [409]. This procedure can be divided in three steps:

Step 1: Ink deposition via blade coating,

Step 2: gas stream-assisted drying of the wet film, and

Step 3: thermal annealing of the dry film.

Figure 5.1 displays a schematic illustration of the drying process (Step 2) representing the quenching inducing crystal nucleation.

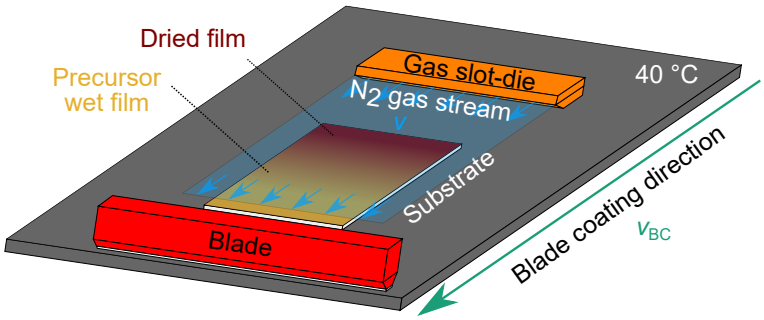

Figure 5.1: Schematic illustration of low-pressure N_2 gas stream-assisted drying with a static gas system utilized for fabrication of MAPI based perovskite layers.

The applied v_{BC} is in the Landau–Levich regime (Figure 2.7) where a wet film forms after the blade has passed [274, 276, 389]. After blade coating (Step 1), the wet film is dried by a laminar N_2 gas stream similarly to examples reported in literature [280, 374, 388]. The wet film is dried for a period of 3 min (Step 2) to guarantee that it is completely dry before being subsequently converted to the perovskite crystal structure by thermal annealing (Step 3), even though no in-situ drying measurements [280, 349, 422–424] are used here to confirm this.

The gas system is installed statically and a substrate temperature normally close to RT (40 °C) is applied as described further down, which is tremendously lower compared to the substrate temperatures utilized in the case of heat-assisted conversion in Chapter 4. Details on the procedure are given in Subsection 3.1.4.

To investigate the differences on perovskite layer morphology for both methods, heat- and gas-assisted conversion, the author compared top-view CLSM images of annealed absorber films with and without applying a gas stream and at different processing temperatures as illustrated in Figure 5.2.

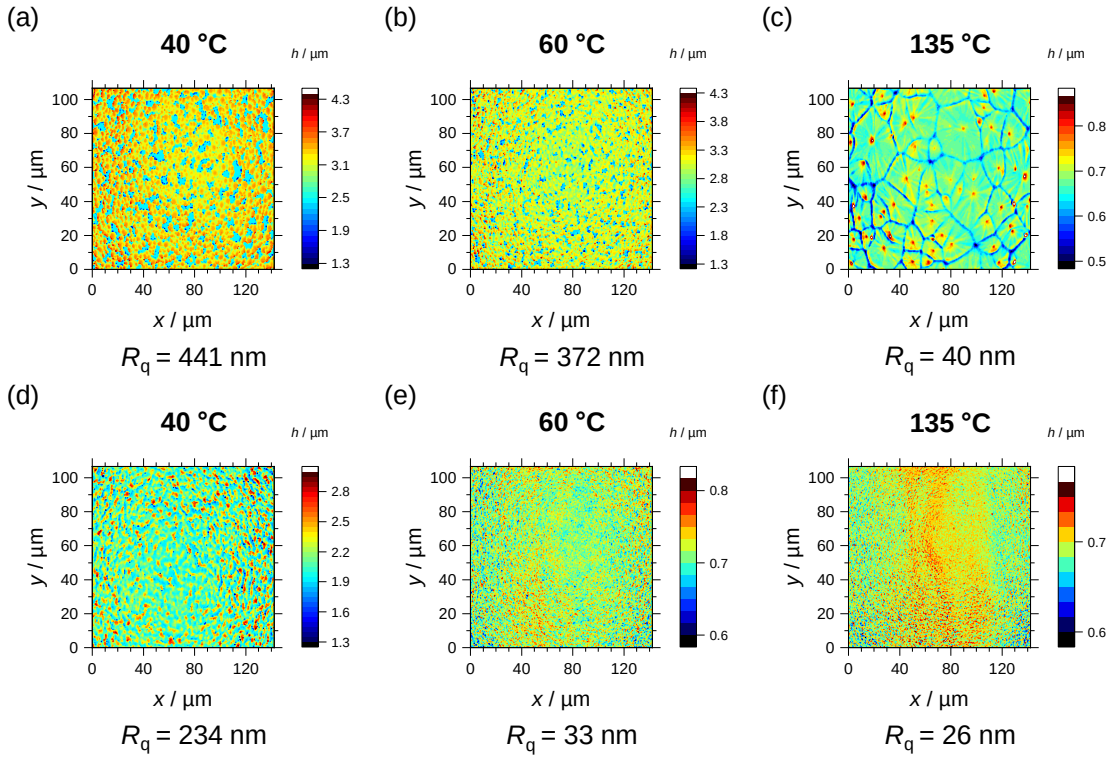

Figure 5.2: CLSM top-view height images and R_q analysis of annealed perovskite layer blade coated on top of PEDOT:PSS (a-c) without and (d-f) with Q=40 L min^{-1} N_2 stream at different processing temperature with 0.2 mg mL^{-1} surfactant: (a, d) 40 °C, (b, e) 60 °C, (c, f) 135 °C.

The additional gas stream enables a more homogeneous perovskite layer morphology and tremendously decreased RMS roughness R_q (Figure 5.3) of the film surface compared to the utilization of pure heat for conversion (Chapter 4). Furthermore, the formation of convection cells via fluid dynamics in heated wet films (Subsection 2.2.4) is completely avoided here (Figure 5.2f).

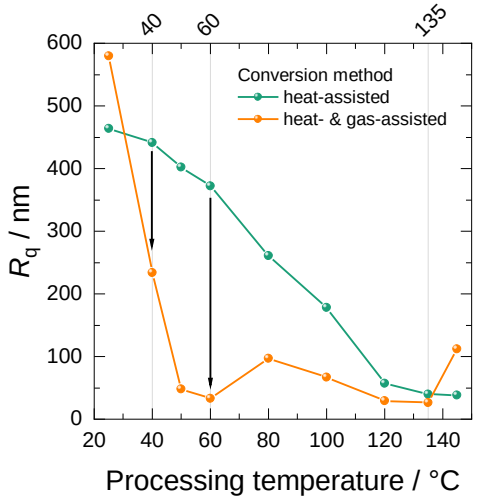

Figure 5.3: R_q analysis of CLSM top-view height images (Figure 5.2 and Figure B.1) of annealed perovskite layer blade coated on top of PEDOT:PSS without and with Q=40 L min^{-1} N_2 stream as a function of processing temperature with 0.2 mg mL^{-1} surfactant.

Figure 5.4 presents box charts of PCE, FF, V_{OC} and corresponding *JV* curves of PSCs for the case of 50 °C processing temperature, as example for a low-temperature fabrication, without and with N_2 stream with Q of 40 L min^{-1}.

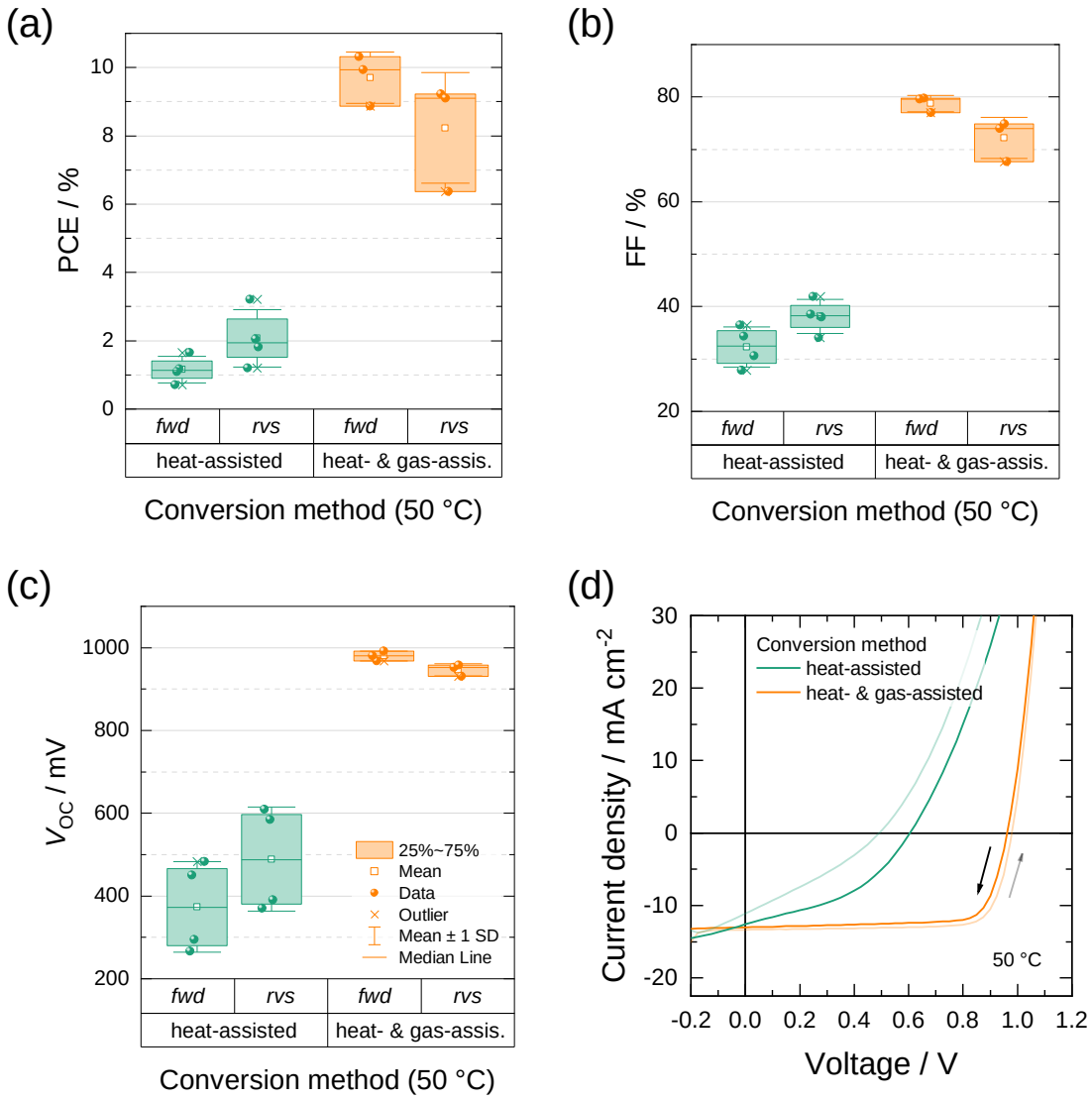

Figure 5.4: Box chart of (a) PCE, (b) FF and (c) V_{OC} of MAPI perovskite based PSCs blade coated on top of PEDOT:PSS without and with Q=40 L min^{-1} N_2 stream at a processing temperature of 50 °C with 0.2 mg mL^{-1} surfactant. (d) *JV* curves of corresponding representative devices measured in *fwd* and *rvs* scan directions.

The perovskite morphology (Figure 4.1) and R_q (Figure 5.3) resulting from the corresponding conversion method is directly related to device performance.
In general, utilizing the N_2 stream enables four matters of fact compared to the heat-assisted perovskite conversion (Chapter 4): (i) dramatic decrease of the perovskite surface roughness, (ii) drastic decrease of the processing temperature as illustrated in Figure 5.3, (iii) avoiding the formation of drying features (see Figure 5.21) and (iv) smaller mean perovskite crystal grain sizes.

For the case of heat-assisted perovskite conversion, solution deposition, drying with nucleation and crystallization happens at the same time and in less than seconds. Thus, controlling the perovskite conversion and the resulting layer morphology is tremendously challenging [422] as discussed in Chapter 4.
However, gas-assisted conversion allows the decoupling of the three processes which makes this method an extremely appropriate one to control each individual step and therefore the resulting perovskite morphology [286].

The different stages of fabrication of the perovskite film after each step of perovskite precursor solution blade coating, gas stream-assisted drying, and thermal annealing are displayed in Figure 5.5 [409].

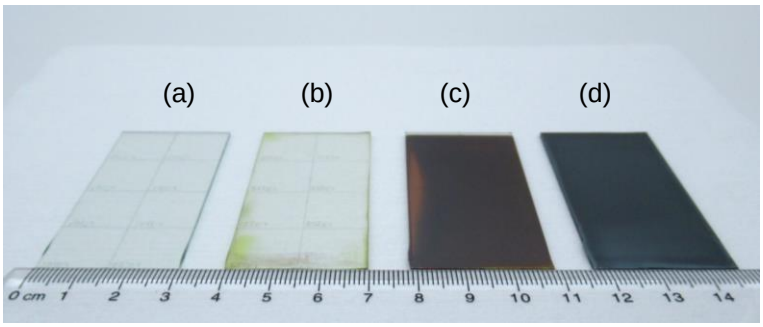

Figure 5.5: Photographical image of perovskite film on scarified and engraved $3 \times 6\,\mathrm{cm}^2$ substrates at different stages of fabrication viewed from top side: (a) Glass/ITO/HTL substrate, (b) perovskite precursor wet film after blade coating on named stack, (c) solid dried perovskite precursor film after gas stream-assisted drying (Q=20 L/min), and (d) fully annealed and converted perovskite film after thermal annealing.

The author emphasizes that the processing temperature during perovskite conversion was strongly decreased from >120 °C in the case of heat-assisted conversion (Chapter 4) to near RT in case of the ecologically friendly and low-energy gas-assisted conversion.

Consequently for the mentioned results of investigation, gas-assisted conversion at low temperatures, where drying and crystallization are decoupled, has in the author's opinion the higher potential to be utilized for upscaling solution processing of PSCs compared to heat-assisted conversion.

In Chapter 5, a pure DMF precursor solution is chosen due to the fact that a lower mass transfer coefficient (β_i) of the gas and slower gas flow velocity (v) are required to dry the wet film compared to a solvent with an even lower vapor pressure (p_oi) than DMF like DMSO or a solution mixture of both [280, 423]. The value of v of the N_2 gas flow over the substrate was $3\,\mathrm{m\,s^{-1}}$ to $4\,\mathrm{m\,s^{-1}}$ measured by a flow meter. This is by a factor of 10 lower compared to the velocity which is applied in Chapter 6.

Moreover, the author selected a $PbAc_2$-based perovskite precursor solution since nucleation arises faster compared to a PbI_2-based one [423] due to the available extra MA^+ and therefore facile removal of methylammonium acetate (MAAc) (Equation 5.1) [425,426] at low temperature near 60 °C [427] as discussed in further detail in Subsection 5.2.2 [409].

$$\mathrm{PbAc_2} + 3\,\mathrm{MAI} \longrightarrow \mathrm{MAPbI_3} + 2\,\mathrm{MAAc}\uparrow \tag{5.1}$$

Hence, it is unessential that the gas system is moving over the wet film surface during gas stream-assisted drying and therefore exhibits low pressure and can be installed statically. In contrast to that, Chapter 6 deals with the utilization of solvent mixtures and amongst others PbI_2 as Pb source and their consequences on the requirement of a moving high-pressure gas system.

5.1.2 Improvement in V_{OC} by replacement of HTM

Typically, poly(triaryl amine) (PTAA) is replacing the widely used PEDOT:PSS as HTM [428–430] in planar p-i-n PSCs because of its efficient carrier transport properties [431–433]. PSCs with PTAA mostly benefit from boosted V_{OC} [431, 434, 435] because of a proper energy level alignment in contrast to PEDOT:PSS likely due to a work function reduction as a consequence of its chemical reaction with perovskite at the interface [436]. V_{OC} values of PSCs with PTAA and MAPI of up to 1.26 V were reached [435]. Moreover, PSCs with PEDOT:PSS as HTM exhibit poorer stability compared to ones with PTAA [437] which might be attributed to the acidity and hygroscopicity of PEDOT:PSS [436] detrimentally affecting the perovskite film [409].

To increase the V_{OC}, the author examined and compared both HTMs in gas stream-assisted blade coated MAPI based PSCs (Figure 5.6). Corresponding *JV* characteristics are presented in Figure 5.6d.

The results indicate that the V_{OC} is increased by $\sim$100 mV when utilizing PTAA instead of PEDOT:PSS (Figure 5.6b). Additionally, J_{SC} is slightly increased by $\sim$1 mA cm^{-2} (Figure 5.6c). Furthermore, the hysteresis seems to be decreased for the case of PTAA.

However, PTAA is a nonpolar polymer with a low surface energy and thus is highly hydrophobic, which leads to severe dewetting of the subsequently deposited perovskite precursor solutions containing polar solvents, such as DMF or DMF/DMSO mixtures [372, 437–439]. This is the case even on small lab-scale substrates, but especially when upscaling A_{act} of PSCs or their substrate size. This led to a higher number of short-circuited devices with PTAA in the author's experiments because of pinholes in the perovskite layer [409].

Several techniques exist to enhance the PTAA surface energy and improve the perovskite precursor solution wetting, from which the following three are the most established ones:

- Solvent prewetting where the perovskite precursor solution containing solvent is applied prior to perovskite deposition [433, 434],
- oxygen or ultraviolet–ozone (UVO) plasma treatment of the PTAA [440, 441], and
- addition of surfactants to the perovskite precursor solution, such as LP [274], which is utilized in Section 4.2.

Rather than utilizing a surfactant in the precursor solution, another unusual option is adding a second HTM in the PTAA such as m-MTDATA [442, 443].

However, the disadvantages of each method are clear:

Solvent prewetting is mainly applied for spin coating and is hardly applicable for blade coating of larger PTAA-covered substrates ($\geq 30 \times 30$ mm^2) due to solvent shrinking leaving uncovered areas behind after precursor solution deposition [409].

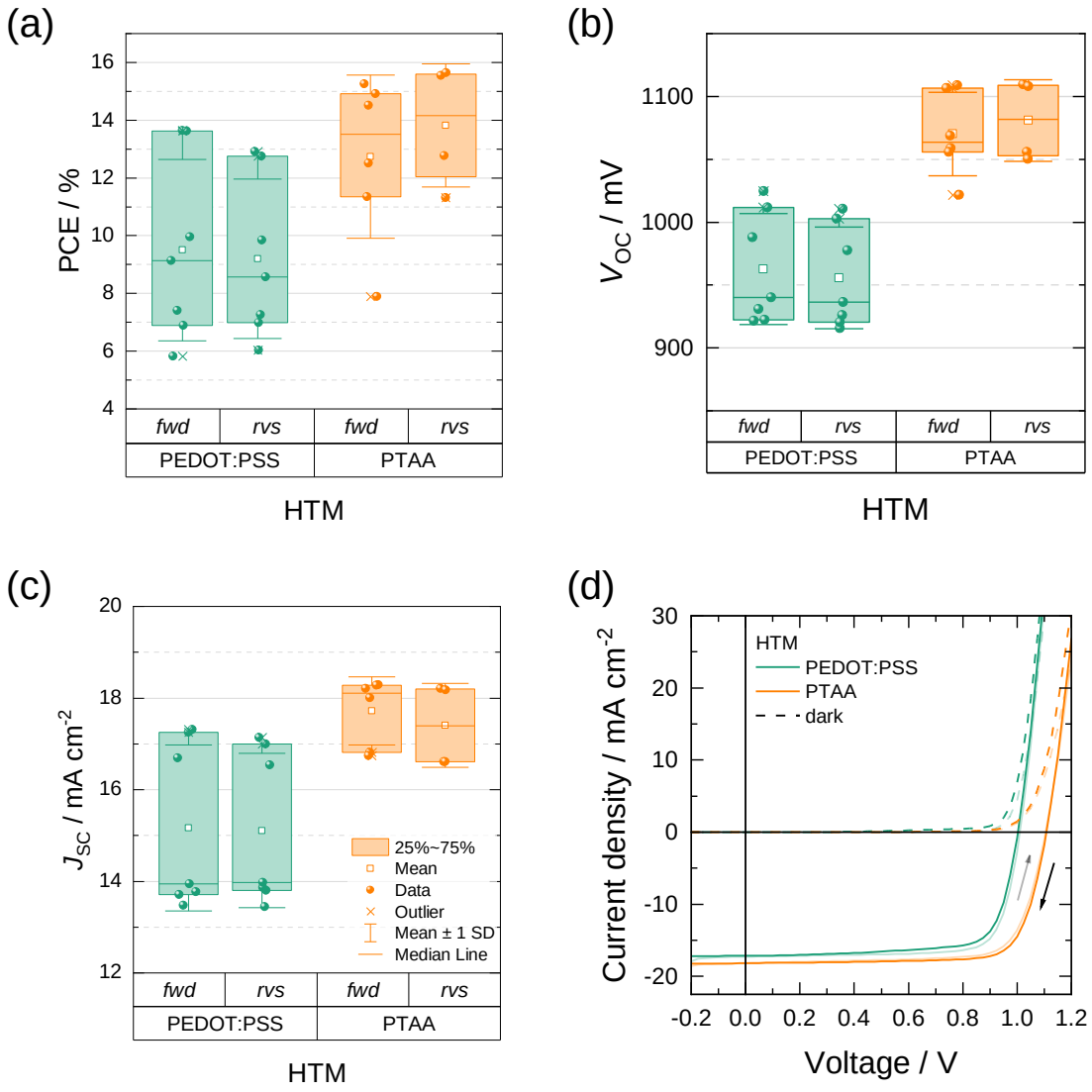

Figure 5.6: Box chart of (a) PCE, (b) V_{OC} and (c) J_{SC} of MAPI perovskite based PSCs (40 wt% precursor solution without LP) blade coated on PEDOT:PSS or PTAA as HTM (without SiO_2 NPs: see Subsection 5.2.1). Short-circuited devices are omitted (see Subsection 5.2.1). (d) *JV* curves of corresponding representative devices measured in *fwd* and *rvs* scan directions.

The effect of the plasma treatment is critically affected by its power and duration, can easily damage the HTL and alter its optoelectronic properties or work functions consequently reducing device performance mainly due to a reduced V_{OC} [440, 441].

Amphiphilic surfactants can passivate defects [417] but might change the perovskite crystallization and adsorb predominantly at the surface of the perovskite layer [412, 417] hindering an unproblematic continuation of the device stack by solution processing since dewetting of the ETM in a nonpolar solvent occurs [412] as presented earlier (Subsection 4.2.2). Therefore, vacuum deposition of the subsequent layers seems to be mandatory [274, 344, 350, 352, 375, 389] and the option of full solution processing is excluded.

These major bottlenecks limit the development of low-temperature inverted planar PSCs and modules and their upscaling via solution-based processing by scalable printing techniques like

blade coating [409]. For this purpose, a different nondestructive surface modification procedure for nonwetting HTLs, such as PTAA, is developed and applied in this thesis.

To enhance the surface energy of PTAA and thus improve the perovskite precursor solution wetting on the nonwetting material, a universal nanoparticle (NP) wetting agent is developed in this thesis [411]. The transfer of this NP wetting agent concept deposited via spin coating to a deposition via a scalable printing technique and the p-i-n configuration with PTAA instead of the n-i-p architecture as presented in this reference is described in the following Subsection 5.2.1.

5.2 Optimizations of perovskite morphology with gas-assisted conversion

This section comprises the morphology optimizations of the MAPI perovskite thin film using the gas-assisted conversion. Thereby, one study addresses the efficient wetting of the precursor solution on the newly used hydrophobic HTL PTAA via blade coated NPs (Subsection 5.2.1). The second study is devoted to the perovskite layer formation control by composition engineering of the precursor solution via lead chloride ($PbCl_2$) (Subsection 5.2.2).

The nanoparticle (NP) wetting agent used in the following sections is based on collaborative findings of M. Schultes (ZSW) and amongst others (N. Giesbrecht, E. Ahlswede, P. Docampo, T. Bein, and M. Powalla) the author of this thesis acting as coauthor in the corresponding peer-reviewed paper [411]. All the following studies on blade coated NPs, optimizations of the perovskite morphology and layer thicknesses together with solar cell and module fabrication represent original work of the author of this thesis. Further information and additional highlights of the research are published in the corresponding first author peer-reviewed paper [409]. T. Wahl, M. Schultes, J. Hanisch, J. Zillner, E. Ahlswede, and M. Powalla act as coauthors of the paper, who conducted SEM images, published the initial NP paper, carried out TOF-SIMS and SEM measurements, performed UV/Vis measurements, supervised the work, and acted as adviser of the work, respectively. All authors discussed the results and commented on the manuscript.

5.2.1 Blade coated NPs for efficient wetting on hydrophobic HTL

In the initial paper, NPs were described as a universal wetting agent for depositing perovskite precursor solution on nonwetting materials [411]. Thereby, nonconductive metal oxide NPs, like aluminium oxide (Al_2O_3) or silicon oxide (SiO_2), were utilized between the perovskite and the hydrophobic layer. The oxide NPs exhibit a high surface energy due to their large surface area to volume ratio. Hence, the NPs increase the surface energy of the interface and act as capillary features leading to a precursor solution wetting angle decline. This allows perovskite precursor solutions to be perfectly spread over various hydrophobic films. In particular, 20 nm-sized SiO_2 NPs showed superb wetting and photovoltaic performance [411, 444].

Following the Young's theory, the liquid droplet contact angle directly relates to the surface energy of the subjacent material [445]. Thus, it indicates the surface wettability by the perovskite precursor solution. Consequently, the degree of NP surface coverage and the particle size have the strongest influence on wettability. Moritz Schultes (ZSW) investigated the contact angle

under three main aspects: (i) The number of NPs distributed at the interface, (ii) the NP size or diameter, and (iii) the type of NP material. For further information on how NPs improve the wetting the author recommends references [35, 411].
Moreover, You et al. presented a similar study applying Al_2O_3 NPs even on PTAA [446]. This study revealed the proof of concept that oxide NPs can improve wetting of the precursor solution on PTAA [446, 447]. Nevertheless, all layers of the presented devices in these studies were deposited mainly in the n-i-p device architecture [411, 444] and merely by hardly scalable spin coating [446, 447] without a full investigation on a scalable printing technique [409].

In order to deposit as many layers in the device stack as possible by a scalable printing technique, our universal NP wetting agent concept [411] is transferred from spin to blade coating and to inverted PSCs with PTAA as HTL in this subsection.

The NPs blade coated between the hydrophobic PTAA and the perovskite layer enhance the PTAA surface energy, similarly to the case when they are spin coated, and thereby improve wetting and homogeneous spreading of the perovskite precursor solution on the HTL [409].

An exemplary schematic illustration and a corresponding SEM cross-section image in Figure 5.7 demonstrate the inverted planar device architecture on glass in principle consisting ITO/ PTAA/SiO_2 NPs/MAPI perovskite/PCBM/BCP/Ag [409].

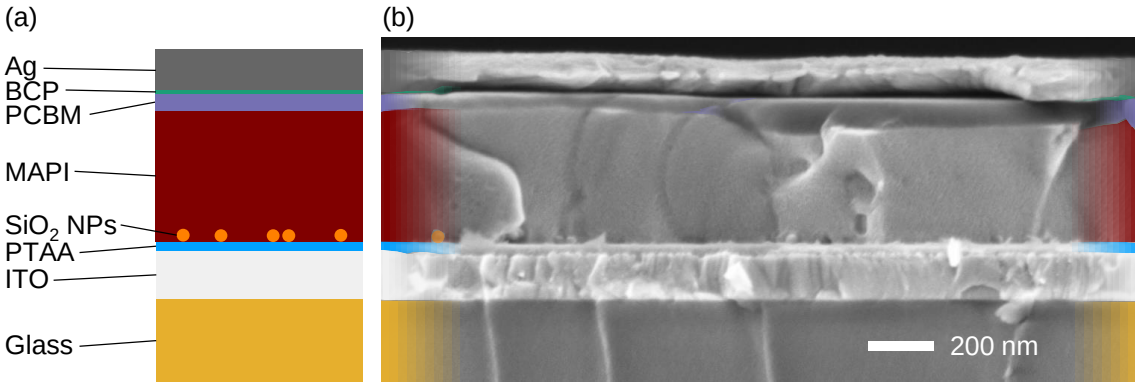

Figure 5.7: (a) Schematic illustration of the inverted device stack with SiO_2 NPs at the PTAA/perovskite interface and (b) SEM cross-section image of a typical opaque PSC with blade coated PTAA, NPs and MAPI perovskite layer (5 % molar ratio $PbCl_2$ of the Pb source in the perovskite precursor solution: see Subsection 5.2.2). The NPs are marked in orange.

Alcohol is utilized for dispersing the nonconductive SiO_2 NPs, since it represents an orthogonal solvent for PTAA and is not damaging the HTL when blade coating the NPs on top. Due to the fact that NP size and material type is left constant here, the wetting of the perovskite precursor solution on PTAA is mainly improved when a critical degree of SiO_2 NP coverage is exceeded. The concentration resulting in optimal wetting properties is identified for the case of blade coating here. The box chart of V_{OC} values of PSCs with SiO_2 NP ethanol dispersions in concentrations ranging from 0.1 wt% to 1.2 wt% blade coated at the PTAA/perovskite are presented in Figure 5.8 [409].

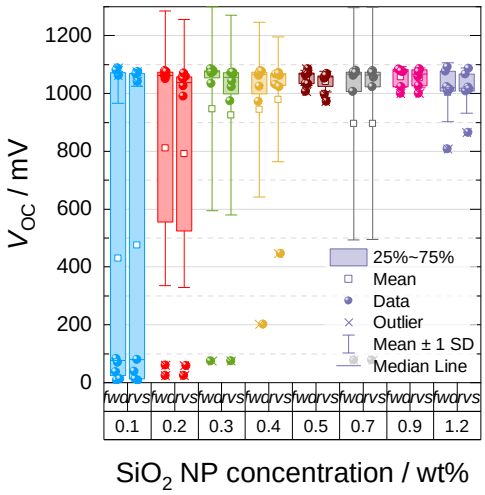

Figure 5.8: Box chart of V_{OC} values of PSCs with blade coated SiO_2 NPs in different concentrated dispersions in ethanol. Shown values were measured in *fwd* and *rvs* scan directions.

With increasing the NP concentration, the number of short-circuited devices decreases. This fact arises from an improved wetting of the perovskite precursor solution on PTAA and therefore avoiding pinholes in the perovskite layer (Figure B.2). When choosing 0.9 wt%, the number of short-circuited devices decreased from over 50 % to <10 % of total devices per batch [409].

SEM top-view images in Figure 5.9 demonstrate the degree of SiO_2 NP coverage on top of PTAA. The NPs exhibit a diameter of 20 nm to 30 nm and do not fully cover the PTAA even for the case of 1.2 wt%. Therefore, no continuous insulating layer is inserted in the device stack [409]. In that case, series resistance (R_s) would drastically increase resulting in decreased device performance as our findings for spin coating the NPs indicate [411].

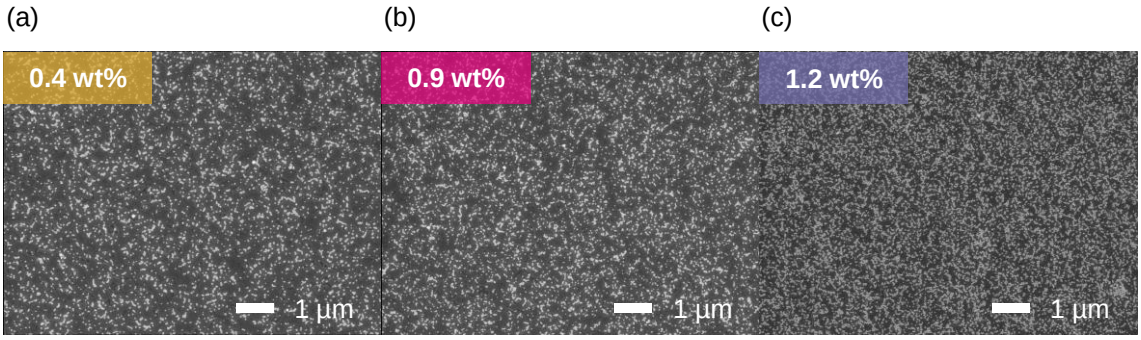

Figure 5.9: SEM top-view images of degrees of SiO_2 NP coverage when blade coating NPs from a (a) 0.4 wt%, (b) 0.9 wt%, and (c) 1.2 wt% solution in ethanol on top of blade coated PTAA.

When using a NP concentration >0.4 wt%, the coverage of NPs is adequate in order to achieve sufficient wetting of the perovskite precursor solution causing no short-circuited devices. In addition, the process window to achieve similar device performance is relatively broad (Figure 5.8). The author decided to continue device fabrication with 0.9 wt% NP dispersions as he observed the most effective wetting and no loss in device performance.

Results of spectral transmittance (T) measurements of pristine ITO, ITO/PTAA, and ITO/PTAA/SiO_2 NPs presented in Figure 5.10 indicate that the SiO_2 NPs cause no parasitic absorption when added in a device stack [409].

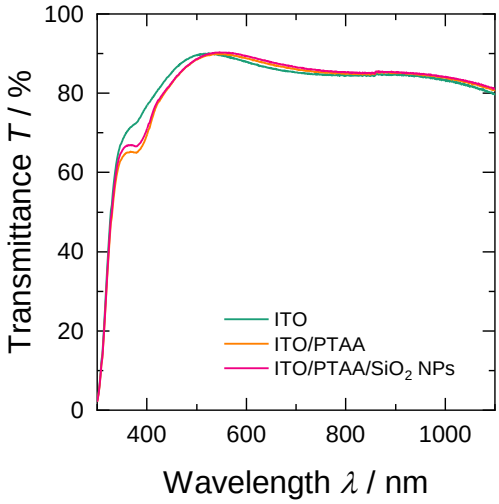

Figure 5.10: Spectral transmittance T of ITO, ITO/PTAA, and ITO/PTAA/SiO_2 NPs (0.9 wt%) as a function of wavelength λ.

Furthermore, the incorporation of the SiO_2 NPs in the device stack results in similar crystallinity and peak position when comparing both XRD pattern of samples with and without NPs as illustrated in Figure 5.11.

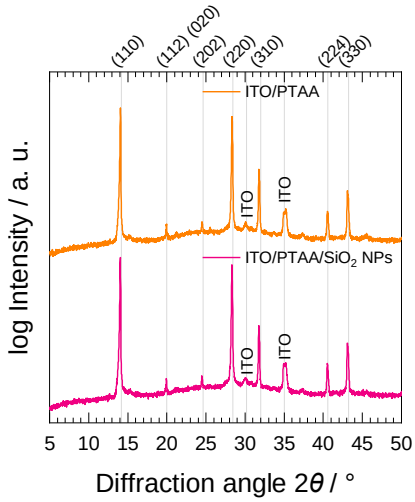

Figure 5.11: XRD patterns of tetragonal crystal structure of annealed perovskite films (5 % molar ratio $PbCl_2$ of the Pb source in the perovskite precursor solution: see Subsection 5.2.2) on top of ITO/PTAA with and without SiO_2 NPs (0.9 wt%).

This confirms no influence of the blade coated NP wetting agent on perovskite crystallization [409]. Consequently, the blade coated NP wetting agent is utilized in all further studies to improve the wetting of the perovskite precursor solution on the hydrophobic HTL PTAA.

Besides improving the wetting on PTAA via blade coated NPs, the perovskite morphology can be optimized by controlling the perovskite layer formation via composition engineering of the perovskite precursor solution [409]. This study is presented in the following Subsection 5.2.2.

5.2.2 Controlling perovskite layer formation by composition engineering of precursor solution

When using a pure $PbAc_2$/MAI precursor solution, the author observed flat surfaces, but there are voids in the perovskite layer toward the HTL interface as illustrated in Figure 5.12a, d, g, if d_{wet} is increased beyond a certain thickness, which correlates to a resulting dry layer thickness of ~250 nm to 300 nm.

Utilizing chlorine (Cl) is known to be beneficial for improving the perovskite morphology [425, 448]. Hence, the author investigated the effect of blending small amounts of $PbCl_2$ in the perovskite precursor solution to control the perovskite layer formation and morphology and to achieve void-free layers by gas stream-assisted blade coating [409].

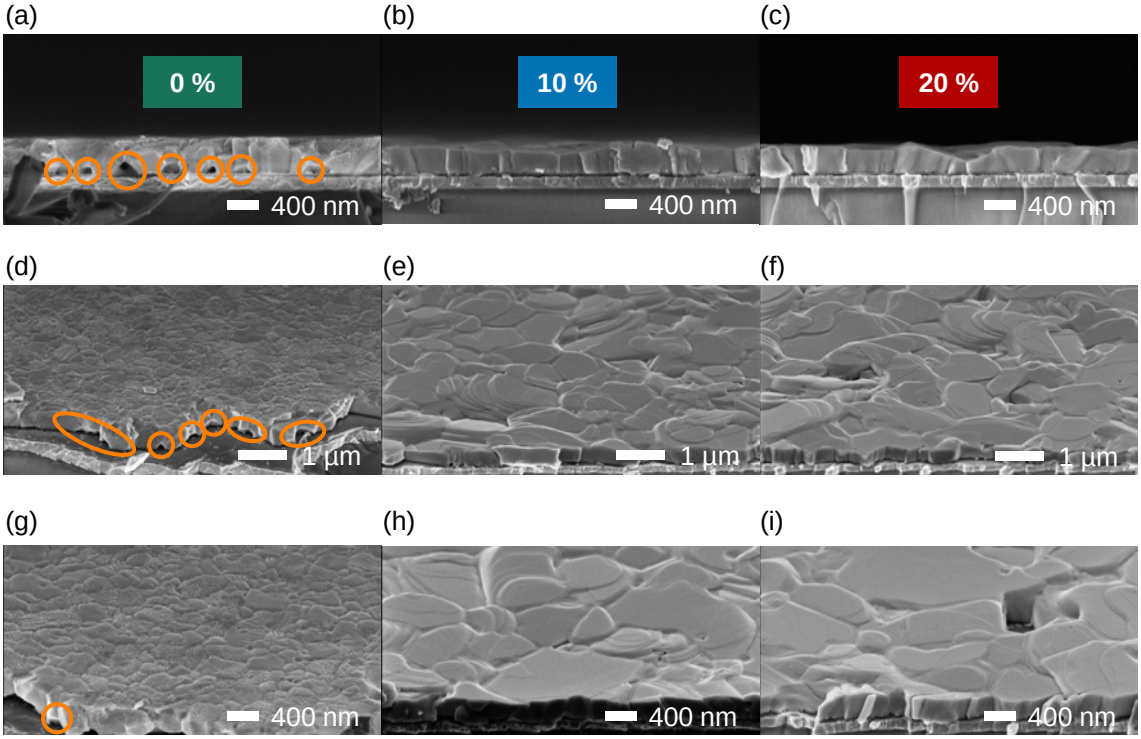

Figure 5.12: SEM cross-section images of annealed perovskite layer on top of blade coated PTAA/SiO_2 NPs with different amounts of $PbCl_2$ in the perovskite precursor solution: (a) 0 %, (b) 10 %, and (c) 20 % molar ratio of the lead source. (d and g, e and h, and f and i) Corresponding 30° tilted images.

By replacing at least 5 % (molar ratio) of the lead source in the precursor solution with $PbCl_2$, the perovskite film morphology is improved by changing the crystallization dynamics, as explained further down, and no voids appear. Consequently, the author accomplished homogeneous,

dense, and compact perovskite layers as presented in Figure 5.12b, e, h. This investigation is also reported by Lee et al. for gas stream-assisted SDC of $PbCl_2$-blended lead acetate trihydrate ($PbAc_2$ trihydrate)-based perovskite solutions [448]. Furthermore, when utilizing $PbCl_2$, the mean perovskite grain size increases from ~300 nm up to 1 μm and >1 μm in the case of 0 %, 10 % and 20 % $PbCl_2$, respectively [409]. This effect is well-known from literature for Cl^- containing precursor additives, such as $PbCl_2$ [425] and methylammonium chloride (MACl) [449].

Using a $PbCl_2$ molar ratio of 10 % or 20 % increases R_q of the perovskite surface from ~30 nm (0 % $PbCl_2$) to ~70 nm and 80 nm, respectively. A rougher perovskite layer is not generally detrimental to device performance as shown later, as long as the subsequent PCBM layer can cover it completely. The appearance of this change in R_q is consistent with literature reports on films deposited from precursor solutions with increased content of $PbCl_2$ or $PbCl_2$ as pure lead source [425, 426]. In contrast to the optimum suggested by Lee et al. for slot-die coating $PbAc_2$ trihydrate-based perovskite solutions [448], 20 % $PbCl_2$ proves to be a too high content for the author's case of blade coating. A molar ratio of already 10 % $PbCl_2$ causes tiny holes in the perovskite layer. When using 20 % $PbCl_2$ the number and dimension of the holes increases even more (Figure 5.12c, f, i) [409], which was reported by Qing et al. as well [425].

This effect of void formation follows a clear mechanism which is illustrated in Figure 5.13 [409].

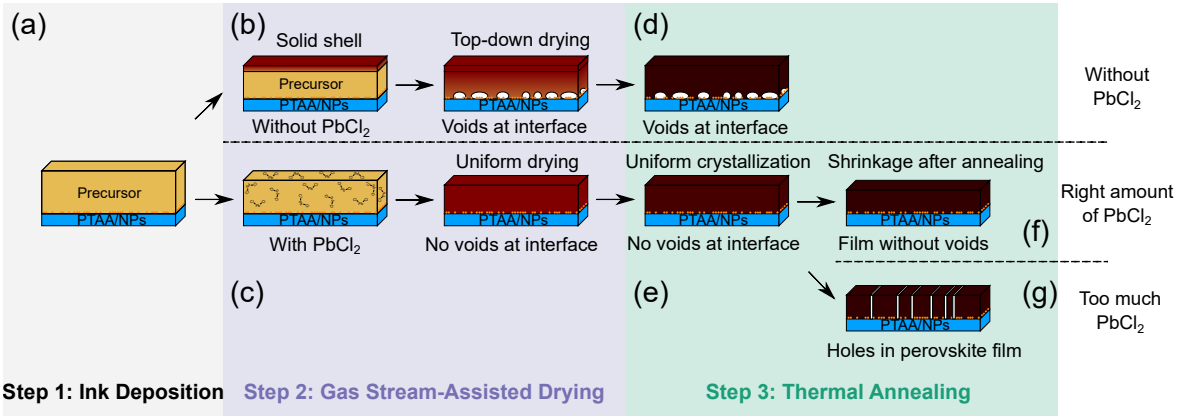

Figure 5.13: Schematic depiction of gas stream-assisted blade coating describing the evolution of a perovskite layer on PTAA/SiO_2 NPs during (a) ink deposition via blade coating (Step 1), gas stream-assisted drying (Step 2) (b) without $PbCl_2$ or (c) with $PbCl_2$, and thermal annealing (Step 3) (d) without $PbCl_2$, with (e-f) the right amount of $PbCl_2$ or (g) too much $PbCl_2$ in the precursor solution. Adapted from Chen et al. [450].

It is described as follows: When blade coating a film (Figure 5.13a) with a d_{wet} exceeding a critical number, a $PbCl_2$-free $PbAc_2$ precursor solution dries by fast removal of the highly volatile byproduct MAAc and solvent molecules via the gas stream primarily at the solution/air interface. This results in a solidification of the film surface. The wet film further dries from top to bottom downward forming a solid shell, which results in trapped residual solvent and byproduct (Figure 5.13b). Consequently, full solvent evaporation during the annealing step results in voids near the subjacent layer [377, 378, 384, 448] (Figure 5.13d) due to shrinking of the drying bottom part of the film beneath the solid shell. Void formation is easily observed by eye indicated by a visible milky or grayish appearance, when viewing the substrates from the glass side (Figure B.3) [409].

An effective way to prevent void formation is to hinder the solid capping layer from building up or removing the solvent before capping formation. When applying $PbCl_2$ in the perovskite precursor solution, the quick solidification at the solution/air interface is prevented (Figure 5.13c) by retarding the nucleation and crystallization rate of the precursor solution due to forming, in the author's case of available extra MA^+ ions, the byproduct MACl in solution [409]. MACl then forms an intermediate complex and solid-state solution with $PbAc_2$ and MAI, respectively, enhancing the solubility of perovskite in the solution [451]. Furthermore, MACl is a less volatile byproduct than MAAc and thereby retards the crystallization process additionally [389,426,448].

Consequently, no solid shell is formed and solvent and byproducts can evaporate from the bottom of the wet film resulting in a compact and homogeneous perovskite layer without voids (Figure 5.13e, f). If there is too much $PbCl_2$ applied, the roughness increases over a decisive limit causing holes in the annealed film [425] (Figure 5.13g) [409].

In addition to $PbCl_2$, DMSO and ammonium chloride (NH_4Cl) can act in a similar way to achieve void-free perovskite coverage by blade coating [389, 450].

The author conducted XRD measurements to investigate the crystal structure of the resulting perovskite with and without $PbCl_2$ in the precursor solution as presented in Figure 5.14 [409].

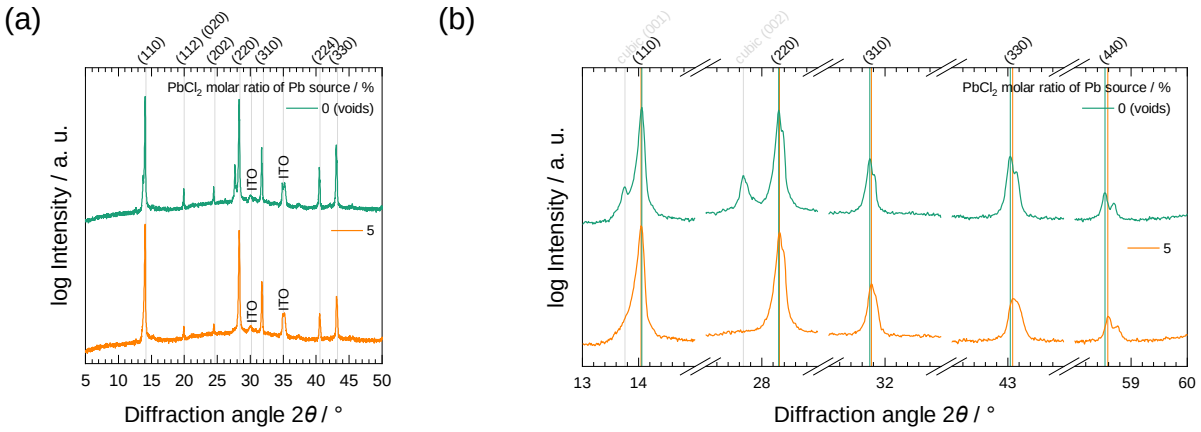

Figure 5.14: (a) XRD patterns of tetragonal crystal structure of annealed perovskite films on top of ITO/PTAA/SiO_2 NPs (0.9 wt%) with and without 5 % molar ratio $PbCl_2$ of the Pb source in the perovskite precursor solution. (b) XRD patterns from (a) with magnification at several main peak positions of the tetragonal crystal structure. Lines indicate the peak positions. Perovskite films without $PbCl_2$ exhibit voids at the PTAA/perovskite interface and additional peaks of the cubic crystal structure.

XRD patterns reveal merely a minimal increasing shift of the main peak positions of the tetragonal perovskite structure toward higher diffraction angles in the diffractogram of the sample including $PbCl_2$ compared to the sample without $PbCl_2$. This would attribute to a smaller crystal lattice. These results indicate that no Cl^- ions or only a minor portion of them seem to be incorporated in the perovskite crystal lattice.

Hence, the author assumes that the Cl^- ions might largely leave the drying film via sublimation of volatile MACl in combination with MAAc [426]. The sample without $PbCl_2$ in the precursor solution exhibits voids at the PTAA/perovskite interface, as mentioned before, resulting in additional peaks right in front of the tetragonal perovskite peaks, mainly the (110) and (220), which can be attributed to the cubic phase of perovskite (Figure 5.14b) [409].

To investigate if and where Cl^- ions remain in the semiconductor film, TOF-SIMS was conducted on annealed perovskite layers with different $PbCl_2$ content in the precursor solution [409].

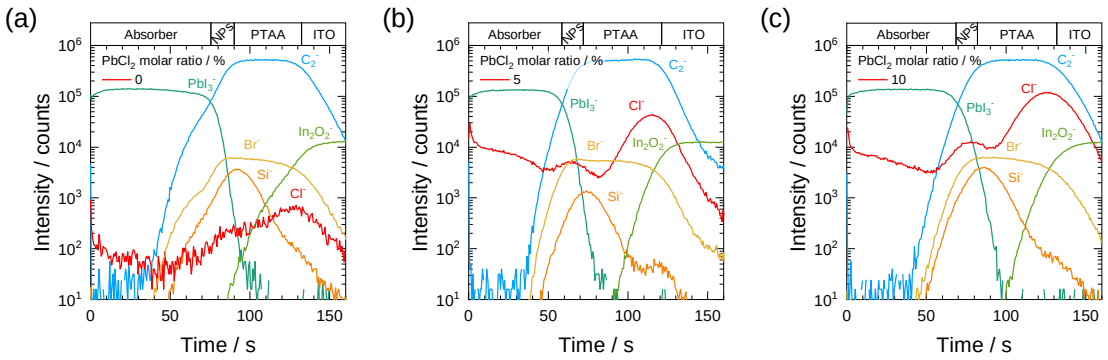

Figure 5.15: TOF-SIMS depth profiles (negative ions) through samples of annealed perovskite thin films blade coated on top of Glass/ITO/PTAA/SiO_2 NPs with different amounts of $PbCl_2$ in the precursor solution: (a) 0 %, (b) 5 % and (c) 10 % molar ratio $PbCl_2$ of the Pb source. Slight shifts of the graphs arise from negligible difference in thickness of perovskite layers.

TOF-SIMS studies reveal that the blended Cl^- is less located in the semiconductor bulk, but accumulates at the surface and mainly near the ITO/PTAA interface as illustrated in Figure 5.15. The Cl^- distribution caused by ion diffusion is conform to reports in literature on spin coated samples independent of substrate and device configuration [452–456].
Additionally, the top-view TOF-SIMS images in Figure 5.16 indicate a continuous increase of grain size (Figure 5.16d-f) in samples with a $PbCl_2$ content from 0 % to 10 % (see Figure 5.16a-c), which was already identified in SEM images (Figure 5.12) [409].

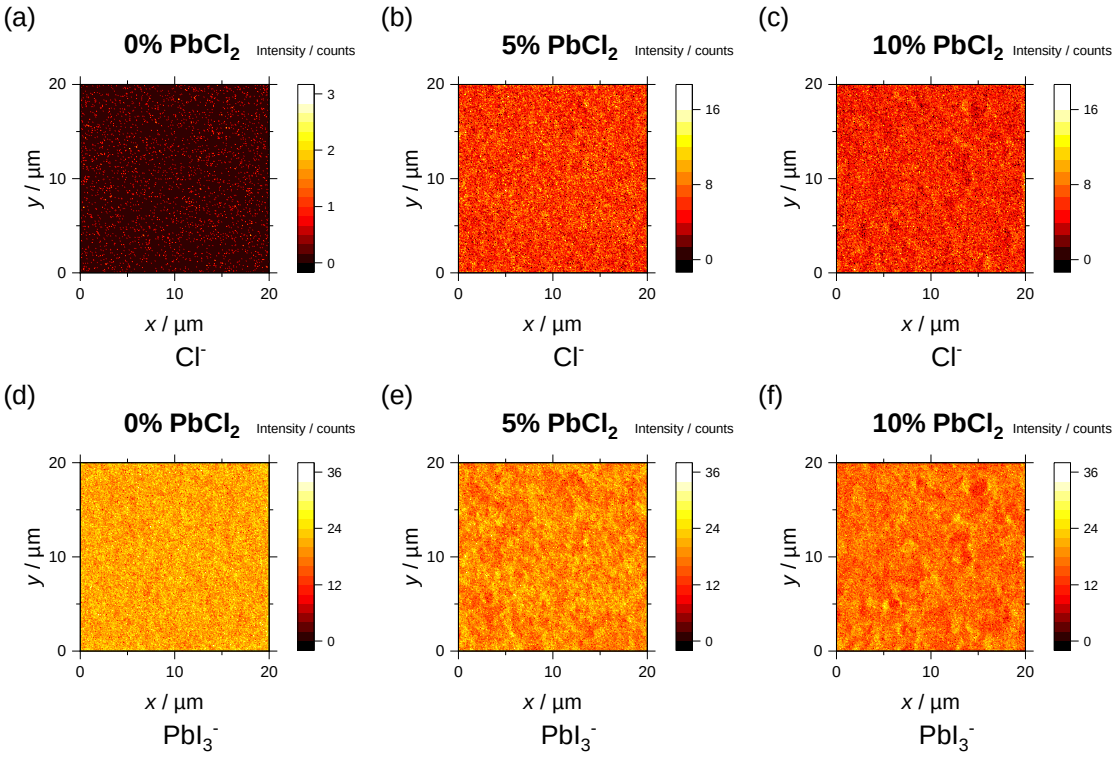

Figure 5.16: TOF-SIMS top-view images of annealed perovskite layer on Glass/ITO/PTAA/SiO_2 NPs with (a, d) 0 %, (b, e) 5 % and (c, f) 10 % molar ratio $PbCl_2$ of the Pb source in the precursor solution: (a-c) Cl^- and (d-f) PbI_3^- ion signals.

It should be noted, that the author investigated only perovskite layers on ITO/PTAA/SiO_2 NPs with TOF-SIMS. When investigating full solar cell device stacks, especially after measuring *JV* characteristics, the location of Cl^- might be different due to electrical field dependent migration of the Cl^- ions. However, as presented further down in Section 6.3, the Cl^- ion location is found to be similar even for a full device architecture with slot-die coated double-cation perovskite absorber (see Figure 6.18).

The less steep increase of the characteristic signals from PTAA and ITO in Figure 5.15a compared to 5.15b and 5.15c is caused by the voids in the perovskite layer, which speed up the premature extraction of sputtered ions locally [409].

Signals of Br^- ions were found in Figure 5.15a, b and c following the graphs of PTAA, although samples were prepared without any Br containing compound. From this fact the author argues, that Br^- impurities in the PTAA remain in the material after its chemical synthesis via Ullmann reaction with aryl halides [457].

Because of the high ionization yield of Cl^- ions in TOF-SIMS and their generally low detection in the author's samples, the TOF-SIMS analysis supports the assumption made from XRD data, that the majority of Cl^- ions leave the absorber film during drying and are not incorporated into the crystal lattice.

The author utilized $PbCl_2$ containing precursor solutions in gas stream-assisted blade coated PSCs and thereby reached PCEs of up to 15 %. An overview of box charts of the characteristic photovoltaic device parameters PCE, FF and V_{OC} of PSCs with different $PbCl_2$ molar ratios of

the Pb source in the precursor solution is presented in Figure 5.17a, b and c, respectively. *JV* data of corresponding record devices is illustrated in Figure 5.17d [409].

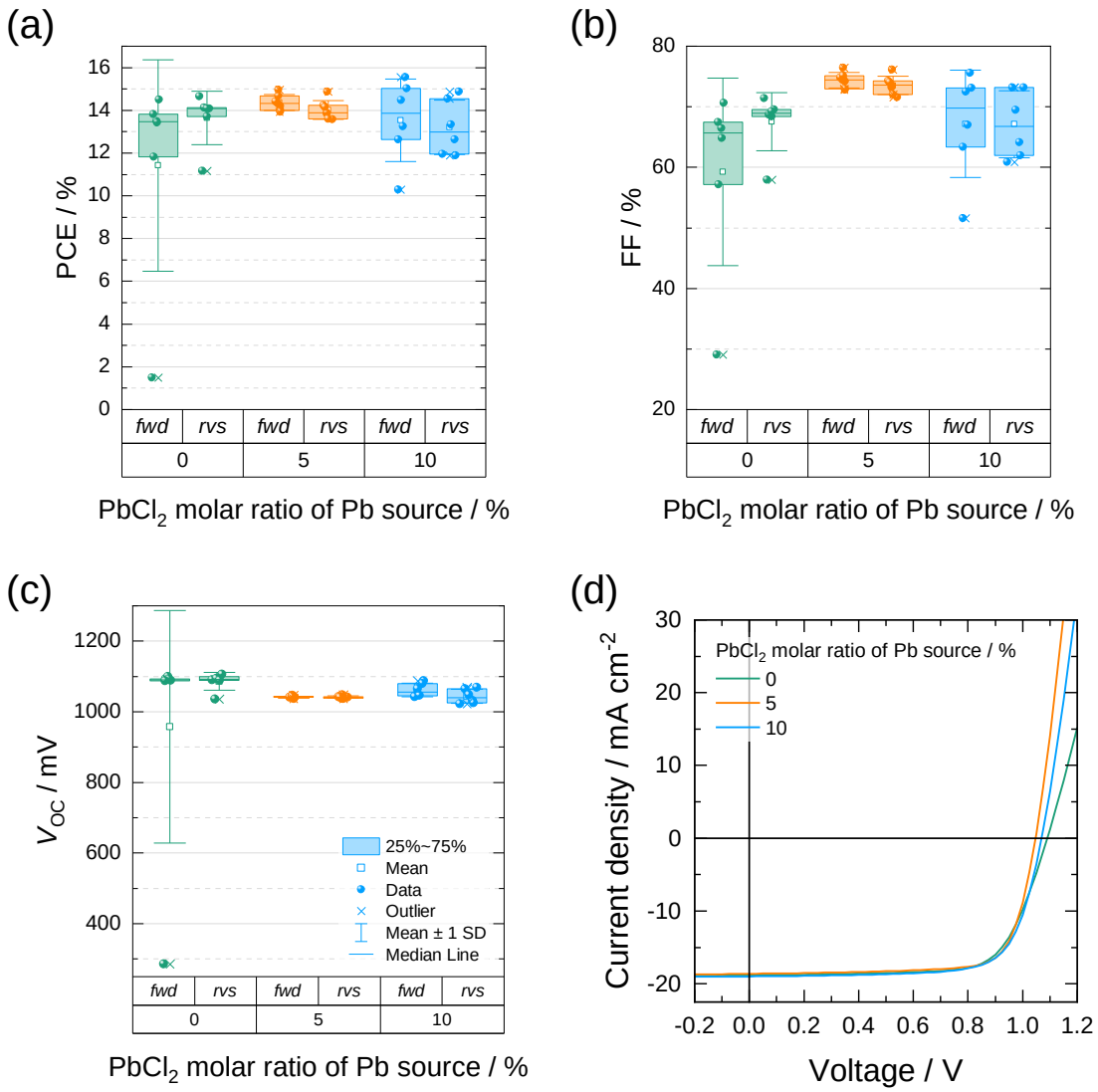

Figure 5.17: Box chart of (a) PCE, (b) FF and (c) V_{OC} of MAPI based PSCs with different $PbCl_2$ molar ratios of the Pb source. (d) *JV* curves of corresponding record devices measured in *rvs* scan direction.

Although the samples with no $PbCl_2$ exhibited voids toward the HTL, surprisingly, such photovoltaic devices showed PCEs of up to 14.7 %. Nevertheless, voids results in decreased coverage, which reduces the device working area and can cause charge recombination and a leakage current increase [448]. PSCs fabricated from precursor solutions containing 5 % $PbCl_2$ exhibit lower R_s of $\sim 1.6\,\Omega\,cm^2$ in contrast to devices excluding $PbCl_2$ ($4.3\,\Omega\,cm^2$) as illustrated in Figure 5.17d. This fact is most likely related to the increased contact area due to avoiding void formation. Figure 5.17c shows that the V_{OC} of devices with $PbCl_2$ slightly drops to 1.05 V from ~1.10 V for devices without $PbCl_2$. However, the median FF is increased from less than 70 % to 75 % as presented in Figure 5.17b. Moreover, when applying 5 % $PbCl_2$, the reproducibility over different experimental batches is increased as well. Randomly distributed tiny holes in the perovskite and increased roughness (Figure 5.12) for the case of 10 % $PbCl_2$ result in a broad

distribution of FF (Figure 5.17b) and V_{OC} (Figure 5.17c), a slight increase in R_s (2.3 Ω cm^2) and hysteresis [409].

5.3 Increased efficiency by layer thickness optimization

The following section deals with layer thickness optimizations in order to further increase device efficiency. Firstly, the absorber thickness is modified to improve the J_{SC} of photovoltaic devices (Subsection 5.3.1). Secondly, the FF of perovskite solar cells is increased by modifying the HTL thickness (Subsection 5.3.2).

5.3.1 Improvement in J_{SC} by modifying absorber thickness

The issue of void formation in Subsection 5.2.2 was solved by utilization of $PbCl_2$ which is in the following used to deposit thicker active layers but without voids.

When using 5 % $PbCl_2$ in the precursor solution, the perovskite film thickness (d) can be increased to over 400 nm without the formation of voids. By adjusting d of void-free perovskite layers, the author increased the J_{SC} of the PSCs and thereby reached PCEs of up to 17 %.

The perovskite thickness d was adjusted by varying the blade coating velocity (v_{BC}) resulting in an increase from ~200 nm to up to 400 nm. An overview of box charts of the characteristic photovoltaic device parameters PCE and J_{SC} of PSCs with four different v_{BC} is presented in Figure 5.18a and b, respectively. The v_{BC} value is was varied from 5 mm s^{-1} to 10, 15 and 20 mm s^{-1} resulting in a mean perovskite layer thickness d of 200, 300, 330 and 390 nm, respectively. JV data of corresponding record devices is illustrated in Figure 5.18c [409].

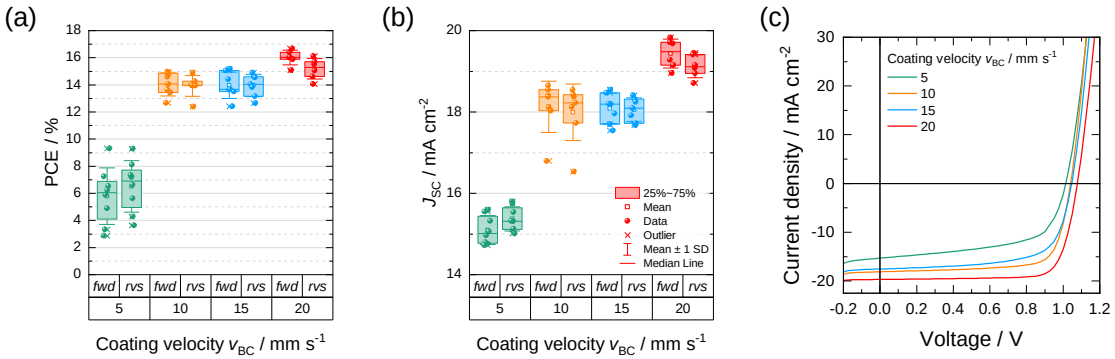

Figure 5.18: Box chart of (a) PCE and (b) J_{SC} of PSCs with active layer blade coated at different coating velocity (v_{BC}) (5 % $PbCl_2$). (c) JV curves of corresponding record devices measured in *fwd* scan direction.

With higher v_{BC} and larger d, J_{SC} values rise from ~15 mA cm^{-2} to 20 mA cm^{-2}. Simultaneously, the V_{OC} of devices is continuously increasing with d from 1.00 V to over 1.05 V. Consequently, the resulting PCEs rise from 7 % to up to 17 %.

Increasing v_{BC} to values greater than 20 mm s^{-1} led to an explicit increase in surface roughness and therefore insufficient PCBM covering [409].

5.3.2 Improvement in FF by modifying HTL thickness

Since earlier tests revealed that more uniform PTAA layers are accomplished when blade coating at higher substrate temperatures instead of the standard RT similarly to a recent report [450], the author reoptimized the PTAA thickness using a substrate temperature of 50 °C. Thereby, a champion PCE of 17.9 % was reached [409].

The concentration of PTAA in DCB was tuned from 5 mg mL^{-1} to 10, 15 and 20 mg mL^{-1} with correlating layer thicknesses of approximately 8, 20, 30 and 75 nm, respectively. Figure B.4 illustrates the appearance in color of the differently thick layers. An overview of box charts of the characteristic photovoltaic device parameters PCE and FF of PSCs with varying PTAA thickness is presented in Figure 5.19a and b, respectively. *JV* data of corresponding record devices is illustrated in Figure 5.19c [409].

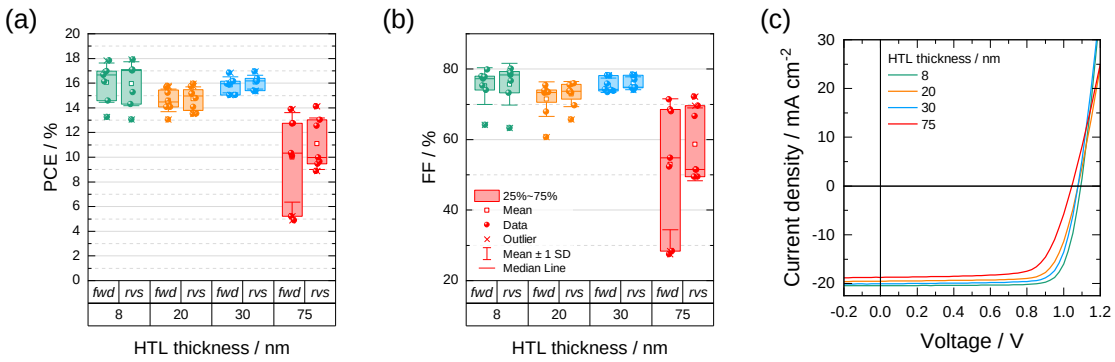

Figure 5.19: Box chart of (a) PCE and (b) FF of PSCs with blade coated PTAA from different concentrated DCB solutions resulting in varying PTAA thicknesses. (c) *JV* curves of corresponding record devices measured in *rvs* scan direction.

Using the lowest PTAA concentration results in highest PCE values mainly due to a boosted FF close to and over 80 %. Furthermore, J_{SC} is dropping from 20.0 mA cm^{-2} to 18.5 mA cm^{-2} with increasing PTAA layer thickness [409]. The results are in excellent agreement with literature [450, 458].

In this study, a champion perovskite solar cell PCE of 17.9 % on an A_{act} of 0.24 cm^2 with no hysteresis was achieved for the PTAA concentration of 5 mg mL^{-1} as illustrated in Figure 5.20 [409].

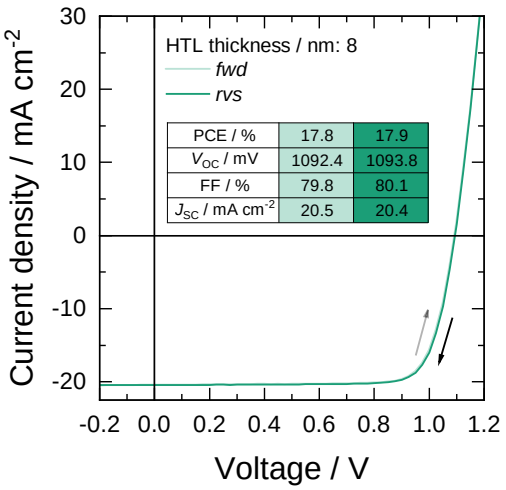

Figure 5.20: *JV* curves in *fwd* and *rvs* scan directions of the champion photovoltaic device in this study.

This fact confirms again the successful transfer of the NP wetting agent concept [411] to scalable gas stream-assisted blade coating and solution-processed PSCs in the p-i-n device architecture with PTAA as HTM [409].

5.4 Large-area perovskite deposition for module fabrication

This section includes the results on upscaling the gas-assisted perovskite conversion process (Subsection 5.4.1), which has been developed and optimized in the previous sections. The aim of the section is the large-area perovskite deposition in order to fabricate PSMs (Subsection 5.4.2).

5.4.1 Upscaling gas-assisted perovskite conversion

To prove the scalability of the before established gas-assisted perovskite conversion and the concept using blade coated NPs as wetting agent, the author produced perovskite layers and PSMs on larger PTAA areas.

Figure 5.21a shows a photographical image of annealed perovskite films deposited via blade coating on Glass/ITO/PTAA/SiO_2 NPs substrates with sizes of 3×6, 5×8 and $9 \times 9\,cm^2$ [409].

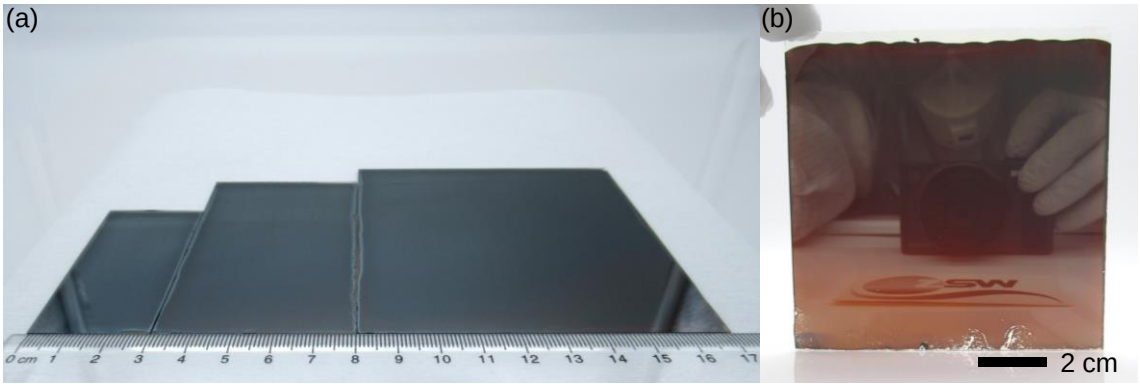

Figure 5.21: (a) Photographical image of annealed perovskite films on Glass/ITO/PTAA/SiO_2 NPs with different substrate sizes viewed from top side. (b) Photographical image of a $9 \times 9\,cm^2$ substrate with reflective appearance viewed from top side.

The perovskite layers indicate no dewetting and pinholes on the hydrophobic PTAA, which clearly proves the scalability of the gas-assisted conversion and the wetting agent concept. By means of the blade coated NPs, upscaling the PTAA substrate size is in principle possible even on larger areas than $9 \times 9\,cm^2$. However, this size represents the technical limit of the author's setup. When coating on $9 \times 9\,cm^2$ substrates, a film thickness and roughness decline in blade coating direction is observed (Figure 5.21b) because of missing continuous solution supply [409].

Since accomplishing thickness homogeneity over larger areas becomes increasingly challenging, blade coating parameters have to be adjusted precisely. When keeping the solution concentration and gap height constant, the thickness over large areas can be mainly adjusted by altering the applied solution volume and coating velocity [409].

To quantify the large-area perovskite homogeneity, the author prepared $9 \times 9\,cm^2$ substrates with four different parameter sets of applied volume (50 µL and 60 µL) and blade coating velocity v_{BC} ($10\,mm\,s^{-1}$ and $20\,mm\,s^{-1}$). After gas stream-assisted blade coating, four $15 \times 15\,mm^2$ substrates with two PSCs each consecutively located in the coating direction are cut out of each $9 \times 9\,cm^2$ sample. A schematic top-view illustration of the selected substrates is displayed in Figure 5.22a.
An overview of the column graphs of all characteristic photovoltaic device parameters of two PSCs at each corresponding position is presented in Figure 5.23.
Furthermore, the author measured and plotted R_q, perovskite film thickness d and the J_{SC} of corresponding PSCs (Figure 5.22)b-d [409].

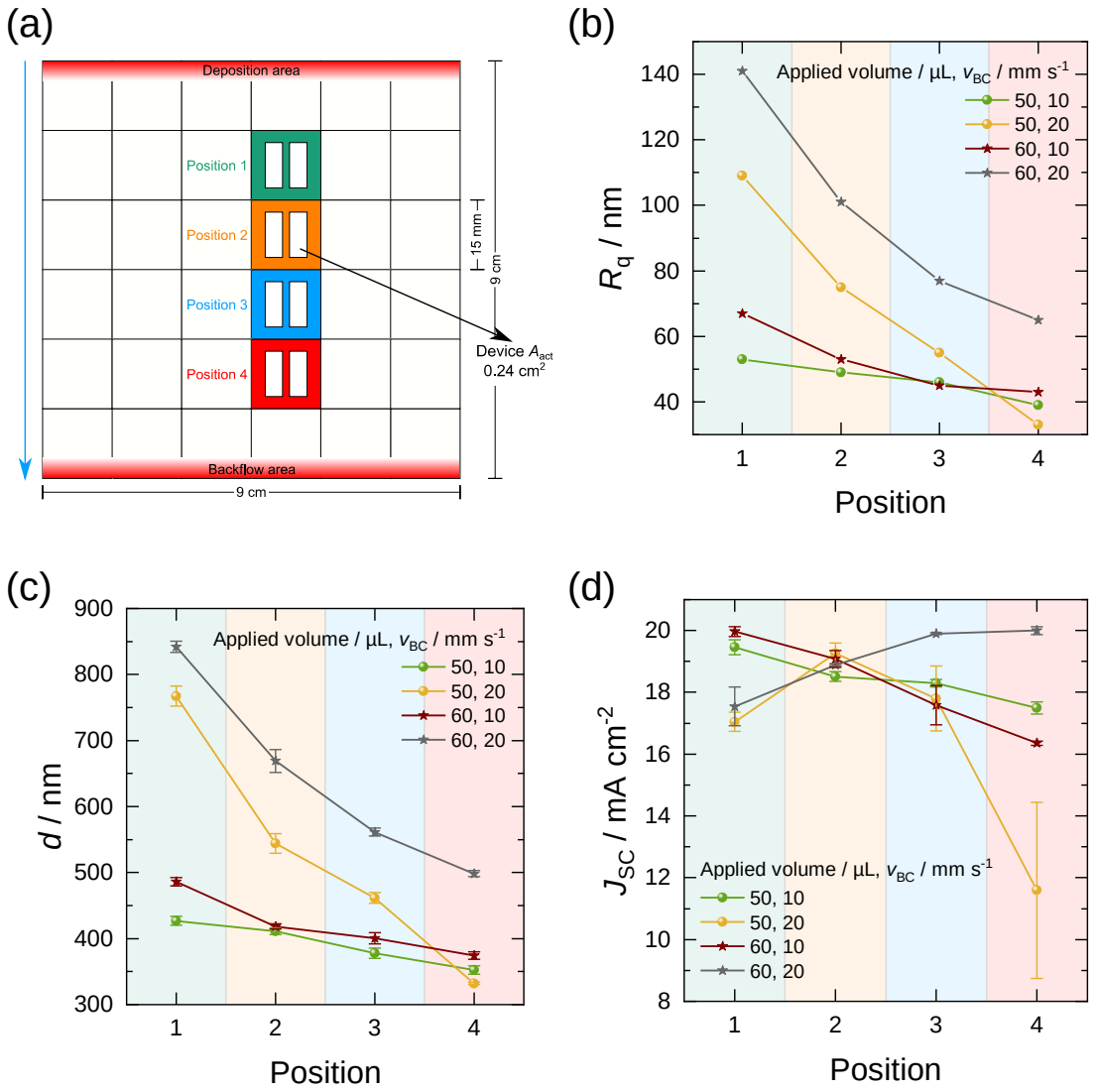

Figure 5.22: Homogeneity study on $9 \times 9\,\mathrm{cm}^2$ substrates with four different perovskite coating parameter sets of applied volume and blade coating velocity v_{BC} as indicated in the legend: (a) Schematic top-view illustration of one substrate. Four $15 \times 15\,\mathrm{mm}^2$ substrates (marked in colors) consecutively located in blade coating direction (blue arrow) are selected and utilized for measuring corresponding *JV* data. (b) R_q, (c) annealed perovskite film thickness (d), and (d) J_{SC} values extracted from *fwd* scans of two PSCs at each corresponding position marked in (a).

The resulting device J_{SC} correlates with both R_q and d. When d is increased, J_{SC} values rise as expected. However, with increasing d, R_q rises as well, which can limit the J_{SC} due to insufficient PCBM covering. Furthermore, V_{OC} and FF values correlate with the J_{SC} (Figure 5.23).

In the case of 60 µL with $20\,\mathrm{mm\,s^{-1}}$, the perovskite precursor wet film is very thick in the beginning of the blade coating process. This results in an annealed layer thickness of 840 nm with a high R_q of 140 nm (position 1). Both values decrease to 670 nm and 100 nm at the next cut substrate in coating direction (position 2), respectively. However, the ETL PCBM is not completely covering the roughness of the perovskite layer (position 1 and 2), which most likely explains the lower J_{SC} of 17.5 and $18.9\,\mathrm{mA\,cm^{-2}}$ compared to 19.9 and $20.0\,\mathrm{mA\,cm^{-2}}$

at position 3 and 4 (Figure 5.22d). This is the case, although d is lower at the latter two positions (Figure 5.22c). When comparing position 3 and 4, d and R_q keeps almost stable in coating direction [409].

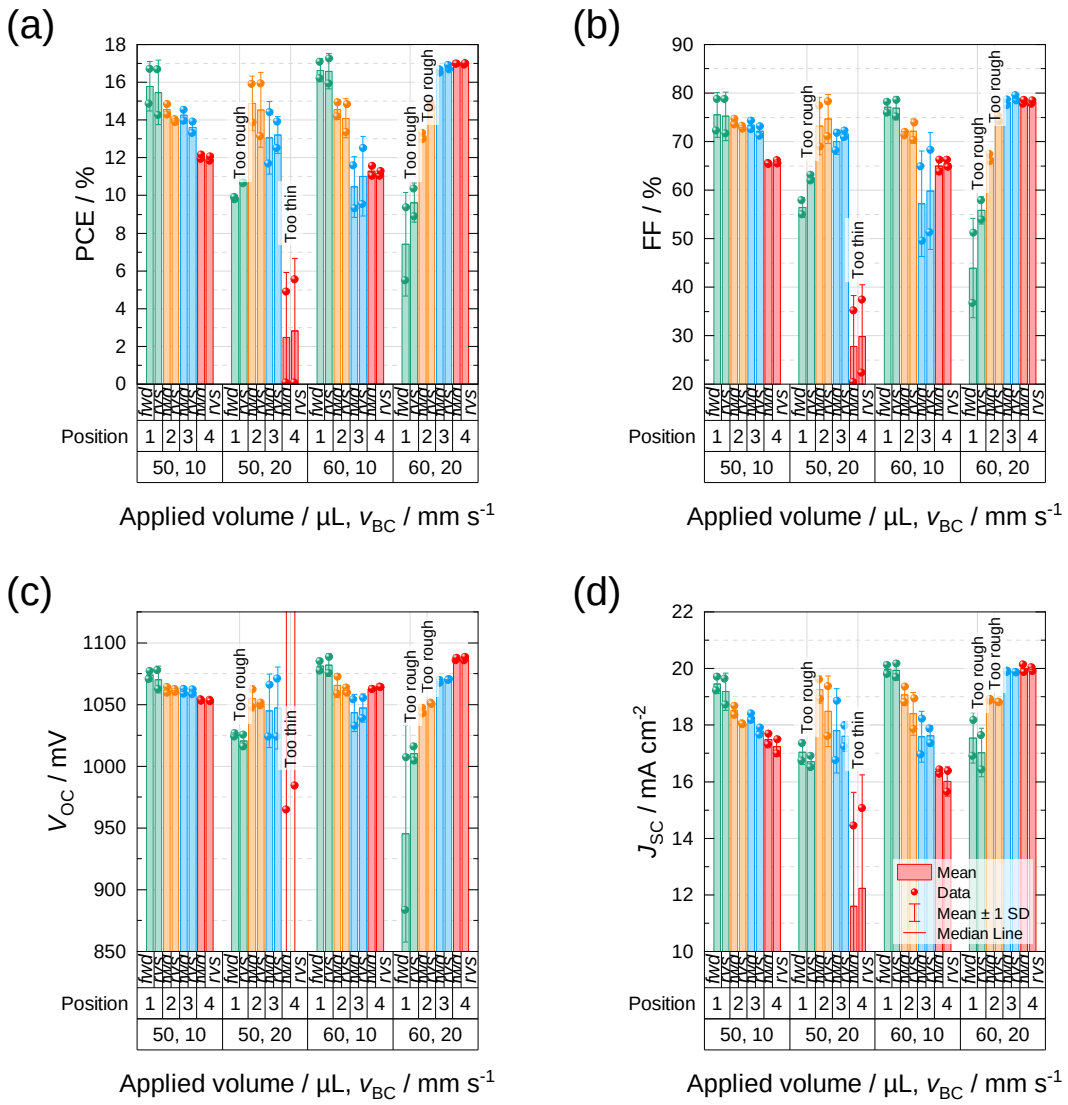

Figure 5.23: Homogeneity study on $9 \times 9\,\mathrm{cm}^2$ substrates with four different perovskite coating parameter sets of applied volume and blade coating velocity v_{BC}: Column graphs of (a) PCE, (b) FF, (c) V_{OC} and (d) J_{SC} of two PSCs at each corresponding position marked in Figure 5.22a. Shown values were measured in *fwd* and *rvs* scan directions.

If using a lower amount of applied volume with a higher v_{BC} (50 µL and 20 mm s^{-1}), the decrease of R_q and d is similar to the first case: R_q is ~110 nm at the beginning of coating, which causes low J_{SC} (position 1), and decreases rapidly with d resulting in a film thickness of 544 nm and 462 nm (position 2 and 3), respectively. Since coating at 20 mm s^{-1} implicates a higher usage of solution compared to 10 mm s^{-1}, thin layers of <335 nm (position 4) follow (Figure 5.22c). This correlates to low J_{SC} values at position 4 (Figure 5.22d) [409].

By using the parameter set of 60 µL with 10 mm s^{-1}, the deviation in R_q, d and J_{SC} over position 1 to 4 is already strongly decreased.

However, the best compromise between constant R_q, d and J_{SC} values over all four positions is given for the fourth parameter set (50 µL and 10 mm s^{-1}). For this case, comparable maximum PCE values of close to 17.0 % with least J_{SC} loss in coating direction of <2 mA cm^{-2}, caused by an absolute reduction in d of only less than 75 nm, are reached. This fact is also demonstrated by each standard deviation of all characteristic photovoltaic device parameters combining position 1 to 4 on one 9×9 cm^2 substrate (Figure B.5). Hence, the author decided to define this parameter set as standard for module fabrication on 9×9 cm^2 substrates [409].

5.4.2 Perovskite solar module fabrication

To test the perovskite homogeneity perpendicular to the coating direction and by implementing the blade coated NP wetting agent introduced in Subsection 5.2.1, the author was able to fabricate large-area PSMs on substrate sizes of 3×3, 5×5 and 9×9 cm^2 (Figure 5.24) [409].

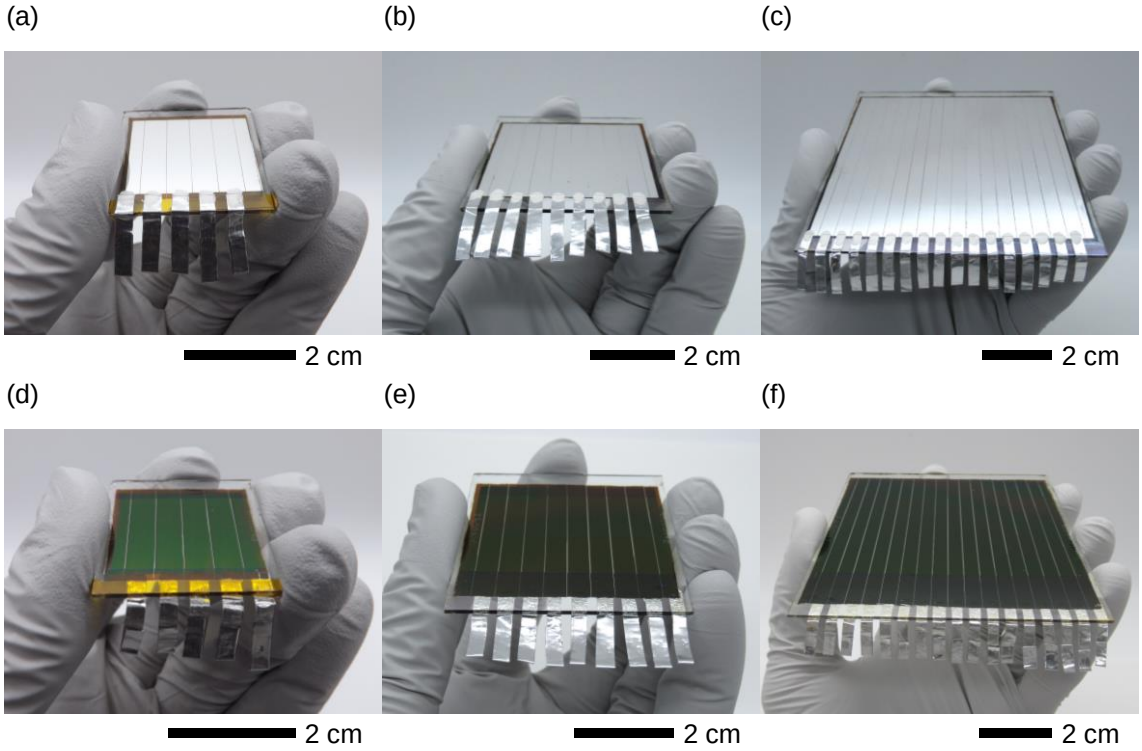

Figure 5.24: Photographical images of modules with different substrate sizes and A_{ap}.

The resulting A_{ap} of the modules are 3.80, 11.60 and 49.60 cm^2, respectively. The geometric fill factor (GFF) of the modules is ~92 %.

The module efficiency and PCE uniformity over all subcells were tested by measuring different numbers of up to 16 subcells connected in series as indicated in Figure 5.25.

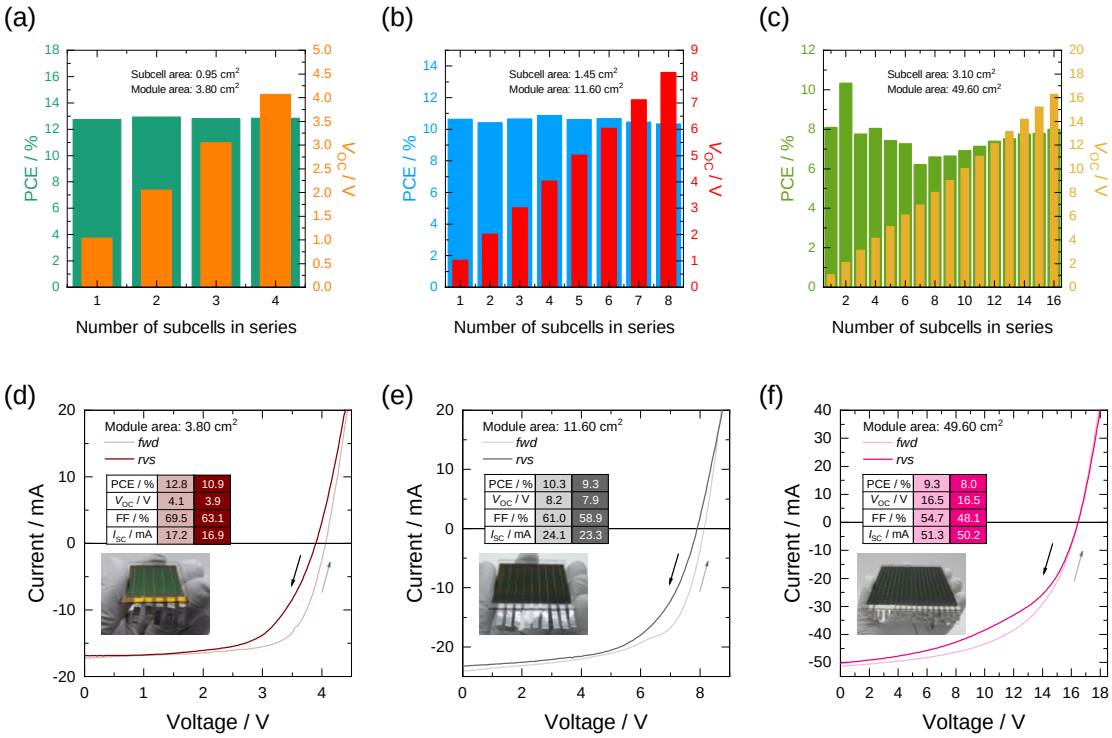

Figure 5.25: (a-c) Column charts of PCE and V_{OC} distribution of different numbers of subcells connected in series. (d-f) *JV* curves measured in *fwd* and *rvs* scan directions of PSMs with different substrate sizes, module A_{ap}, and number of subcells.

The distribution of PCE is relatively homogeneous over all subcells in the modules with different substrate sizes and module A_{ap}. The module V_{OC} is adding up with each additional subcell connected in series to a final V_{OC} of 4.1, 8.2 and 16.3 V on an A_{ap} of 3.80, 11.60 and 49.60 cm^2 (Figure 5.25a-c), respectively, indicating an ideal serial interconnection. These PSMs reach maximum efficiencies of 12.8 %, 10.3 % and 9.3 % in *fwd* scan direction with slight hysteresis [409] as displayed in Figure 5.25d-f.

Although optimizing PSMs is not defined as an aim of this thesis (Section 1.2) and the focus of Chapter 5 lies in the investigation of methods for controlling and optimizing the MAPI perovskite morphology via gas-assisted conversion, the following paragraph, however, highlights some potential options for improvements of PSMs. The in general low performance of the PSMs and the strong decrease in performance when upscaling A_{ap} (Figure 1.1b) are caused by several factors which require further optimizations:

(i) During the etching step of the ITO, which is required for preparing module substrates (Subsection 3.1.2), the A_{ap} of the module needs to be covered with tape. Due to residuals of this tape after etching the risk of inhomogeneous subsequently deposited PTAA/SiO_2 NPs and therefore the perovskite film is drastically increased [409]. The module layout should be altered, so that no etching step is necessary anymore through defining A_{ap} via limitations during Ag electrode evaporation in both directions.

(ii) Moreover, since improving the patterning of PSMs was not the focus of this thesis, the presentation of results on module structuring were omitted. Nevertheless, P2 lines need to be studied in more detail and require optimization to decrease contact resistance at the subcell interconnection [23] in future.

(iii) Additionally, changing the contacting layout of the modules so that one contact is located on the longer side of the first cell would be superior to increase I_{SC} [23].

(iv) In general, the GFF of PSMs needs to be increased (Subsection 2.3.2) to values of >92 % [23] by for instance reducing the P1 width of ~140 µm or replacing the mechanical scribing of the P3 by laser ablation to decrease the P3 width of ~60 µm. Furthermore, the subcell width of 5 mm should be optimized with the help of simulations as a function of the TCO R_{sq}.

(v) The static gas system might have an influence on the perovskite film homogeneity when enlarging the module substrate size, however, a moving gas system (see Subsection 6.1.1) should solve this issue. In addition, blade coating implies a film thickness and roughness decline in coating direction because of missing continuous solution supply which is detrimental to PSM performance as described in detail in Subsection 5.4.1. Slot-die coating (see Section 6.3) will improve layer thickness and roughness homogeneity.

These bullet points show suggestions of the author for potential improvements and to increase device performance of PSMs especially when upscaling A_{ap}.

5.5 Conclusion

Chapter 5 depicted the investigation of controlling the perovskite morphology for upscaling blade coated MAPI based solar cells and modules by gas-assisted perovskite conversion.

The results of the study indicate that the perovskite morphology can be well controlled via the gas-assisted conversion in contrast to the hardly controllable heat-assisted conversion investigated before in Chapter 4. In contrast to heat-assisted conversion, the author identified the temporally decoupling of the drying and nucleation or even crystallization process as main difference. This results in the control of the individual steps leading to homogeneous and smooth perovskite thin film surfaces without undesirable drying features. Additionally, the drying process is feasible at low processing temperatures near RT (40 °C). Beyond that, the gas stream enables tremendously decreased R_q values of the perovskite film surface compared to the heat-assisted conversion and a more homogeneous layer morphology and the formation of convection cells are avoided (Figure 5.2). Furthermore, the author showed that by utilizing $PbAc_2$ as Pb source and DMF as precursor solution solvent a low-pressure and statically installed gas system is sufficient enough to dry the wet film as desired. Since gas-assisted conversion turned out to be the conversion method which is superior to the heat applying counterpart (Chapter 4), the author continued utilizing this method in Chapter 6.
Using PTAA instead of PEDOT:PSS as HTM resulted in a V_{OC} increase of PSCs. However, dewetting of the perovskite precursor solution on the hydrophobic PTAA was identified as main problem.
To solve this problem, the author developed a blade coated NP wetting agent which improves the wetting behavior of the precursor solution on PTAA and helps to optimize the perovskite morphology on macroscopic scale avoiding pinholes. Different analytical methods yielded no detrimental consequence of the NPs such as parasitic absorption or alteration of crystallization. Due to these facts, the wetting agent is as well applied in the following Chapter 6.
By composition engineering of the precursor solution via utilization of $PbCl_2$, the perovskite layer formation and therefore the resulting perovskite morphology can be controlled on microscopic

scale hindering a top down drying and void formation and rather facilitating homogeneous drying. Furthermore, XRD and TOF-SIMS data indicate that the majority of Cl^- ions leave the absorber film during drying and are not incorporated into the crystal lattice.
Moreover, adjusting the PTAA thickness led to an increase in FF and a champion PCE of 17.9 % on an A_{act} of 0.24 cm^2 with a perovskite absorber layer deposited by a scalable printing technique namely blade coating.
In addition by combining all engineering steps, the author scaled up the substrate size and fabricated large-area modules with a PCE of 9.3 % on a maximum A_{ap} of close to 50 cm^2 [409].

In summary, Chapter 5 highlighted that gas-assisted perovskite conversion including the concept of blade coating a NP wetting agent on hydrophobic HTLs, such as PTAA, is suitable for solution processing of hybrid perovskite thin films with well defined morphology and for upscaling MAPI based p-i-n PSCs and modules by scalable techniques.

The following Chapter 6 focuses on the evaluation of scalable perovskite deposition of a more stable multi-cation perovskite composition applying other solvent systems and PbI_2 in contrast to the so far used MAPI absorber based on pure DMF and $PbAc_2$. Hence, this will require a moving high-pressure gas system as presented hereinafter.

6 Evaluation of scalable perovskite deposition from suitable solvent systems for multi-cation perovskite solar cells

The third main chapter specifies the evaluation of scalable perovskite deposition from suitable solvent systems for multi-cation perovskite solar cells. It comprises four result sections, in which blade coating, a green solvent system, slot-die coating by means of gas-assisted perovskite conversion are investigated, and further optimizations are discussed. The chapter is finalized with a short conclusion.

The first Section 6.1 covers blade coating with gas-assisted perovskite conversion. The section comprises the establishment of a moving high-pressure gas system (Subsection 6.1.1) and the discussion on utilizing standard solvent systems, which are normally toxic (Subsection 6.1.2).

The second Section 6.2 comprises the implementation of a green solvent system via blade coating for multi-cation perovskite solar cells.

The subsequent Section 6.3 presents results on the implementation and optimization of slot-die coating in conjunction with gas-assisted perovskite conversion.

The potential for further optimizations is discussed in Section 6.4.

Section 6.5 concludes Chapter 6 on the evaluation of scalable perovskite deposition from suitable solvent systems for multi-cation perovskite solar cells.

6.1 Blade coating with gas-assisted perovskite conversion

This section describes results on blade coating of multi-cation thin films and PSCs with gas-assisted perovskite conversion. Firstly, a moving high-pressure gas system is established for the perovskite conversion (Subsection 6.1.1). Secondly, the utilization of standard toxic solvent systems is shortly discussed (Subsection 6.1.2).

All the following studies on blade coating of suitable solvent systems for multi-cation PSCs with gas-assisted perovskite conversion represent original work of the author of this thesis. Further information and additional highlights of the research are published in the corresponding first author peer-reviewed paper [413]. J. Hanisch, T. Wahl, J. Zillner, E. Ahlswede, and M. Powalla act as coauthors of the paper, who carried out TOF-SIMS measurements, conducted SEM images, analyzed XRD results, supervised the work, and acted as adviser of the work, respectively. All authors discussed the results and commented on the manuscript.

6.1.1 Establishment of moving high-pressure gas system

For deposition of the multi-cation, here double-cation perovskite (FACsPbIBr), absorber layers, the author developed the gas stream-assisted perovskite conversion introduced in Subsection 5.1.1 further and utilized a dynamic high-pressure gas system in this part of the thesis [413]. The reason for choosing FACsPbIBr is its higher stability compared to the MAPI perovskite (Chapter 4 and 5) as shortly explained in the subsequent Subsection 6.1.2. To enable gas stream-assisted blade coating in a N_2-filled glovebox [409], the glovebox was equipped with a pressure relief valve. Figure 6.1 displays a schematic illustration of blade coating and the drying process.

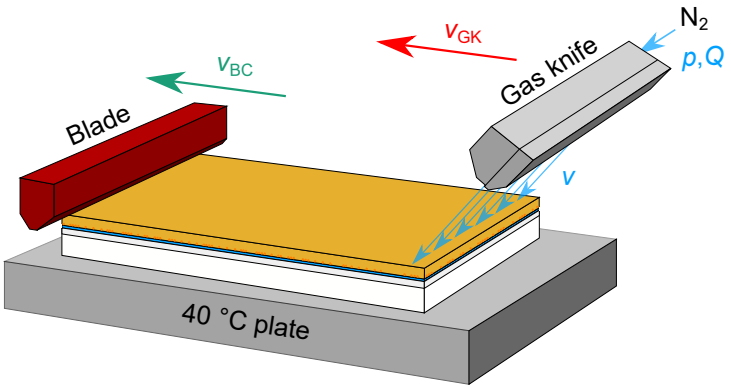

Figure 6.1: Schematic illustration of high-pressure N_2 gas stream-assisted drying with a moving gas system utilized for fabrication of MC based perovskite layers.

The gas system is installed in such way that it can dynamically move over the substrate exhibiting a temperature of normally 40 °C which is considered as low-temperature processing. The movement of the gas knife and its higher N_2 pressure p and flow rate Q are the main differences to Subsection 5.1.1. Details on the procedure are given in Subsection 3.1.4.

The movement and the higher p and Q, respectively, are required here to dry the wet film since two main details changed compared to Chapter 5: (i) the solvent system is now DMF:DMSO (see Subsection 6.1.2) or pure DMSO (see Section 6.2) instead of pure DMF used before and (ii) the Pb source is based on PbI_2 and $PbBr_2$ instead of $PbAc_2$ utilized above. Consequently, β_i has to be higher here due to the lower p_{oi} of DMSO compared to DMF and no formation of volatile MAAc which would be facilely removed from the wet film (Subsection 5.1.1 and Equation 5.1).

The reasons for utilizing the FACsPbIBr, a DMF:DMSO solvent mixture and PbI_2 as Pb source in the perovskite precursor solution in Chapter 6 instead of the MAPI perovskite absorber, pure DMF and $PbAc_2$ (Chapter 5), respectively, are shortly explained in the following Subsection 6.1.2.

6.1.2 Utilization of standard (toxic) solvent systems

MAPI is the most widely used Pb-halide perovskite materials for PSCs as it is a defect tolerant semiconductor with excellent optoelectronic properties [56] as mentioned in Subsection 2.1.1. However, in recent years, MAPI perovskite absorber have been replaced by multi-cation (MC) perovskite precursor mixtures such as triple-cation $FA^+/MA^+/Cs^+$-based perovskite compositions [58] because of their higher resulting device efficiency and intrinsic structural

stability [162, 183, 459]. By now, the research focus lies more on double-cation perovskite materials especially due to their thermal stability, which normally contain FA^+ and/or Cs^+ avoiding the highly volatile MA^+ ions [162, 460].
Admittedly, producing a uniform and high-quality perovskite thin film from such more complex precursor solutions on large area via a scalable printing technique, such as blade coating used here, might be additionally challenging due to their intricate solution chemistry [286, 338].

Furthermore, the approach of a static low-pressure gas system with $PbAc_2$ as Pb source in the perovskite precursor solution (Chapter 5) is not applicable to the case of MC perovskite absorbers due to the formation of nonperovskite phases when mixing $PbAc_2$ with FAI as demonstrated by Luo et al. [461].

MC perovskite precursor solutions usually utilize solvent mixtures of toxic DMF as the main component and only little amount of co-solvents [183, 459, 462], here DMSO, also in order to guarantee the solubility of all precursor materials including CsI [463, 464]. However, for upscaling to mass production and commercialization, appropriate handling of the toxic main constituent of the solvent system must be already considered during the initial development phase [465, 466], which is the focus of the following Section 6.2 [413].

6.2 Implementation of a green solvent system via blade coating

This section includes the implementation of a green solvent system for multi-cation absorber layers via blade coating and gas-assisted perovskite conversion. Furthermore, the results from this implementation are compared to a standard (toxic) solvent system (Subsection 6.1.2).

Harmful and polluting precursor solvents such as DMF hinder the transfer to scalable printing and large-scale production of PSCs by solution processing. For the case of MAPI-based perovskite, several studies have utilized solvents and solvent mixtures that reduce or eliminate the use or generation of substances hazardous to humans, animals, plants and the environment [467], also referred to as green solvents [468], aiming to demonstrate alternatives to DMF [235–237, 239, 469–473]. However, regarding MC perovskite thin films, reports particularly concerning blade coating describe, to the best of the author's knowledge, merely the utilization of toxic solvent systems [272, 280, 282, 342, 344, 418, 422, 474–476]. More nonconventional solvents and co-solvents used for upscaling PSCs are acetonitrile (ACN) [238, 244, 375, 477, 478], 2-methoxyethanol (2-ME) [375, 377, 378, 384, 387, 389, 450, 479–481], or 2-methylpyrazine (2-MP) [482], but it is up for debate if these solvents are sufficiently green [235].

A fully sustainable and green solvent such as pure dimethyl sulfoxide (DMSO) would be more desirable to use for PSC fabrication [211, 483] as recently presented in a comprehensive health and environmental impact analysis including a LCA by Vidal et al. [210] and in Figure 6.2 [413]. For further information the author recommends references [210, 212].

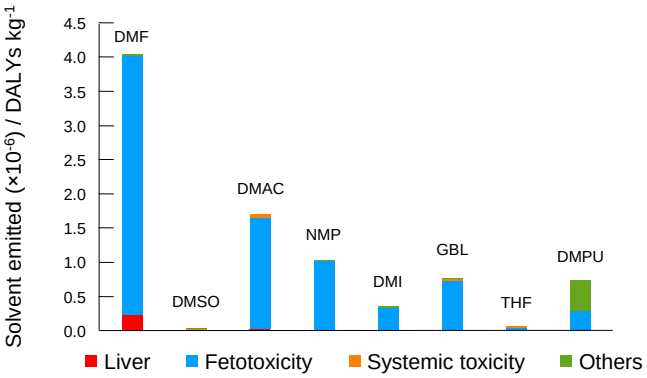

Figure 6.2: Column chart of human health characterization factors by causes expressed in disability-adjusted life years (DALYs) kg^{-1} of substance emitted for the scenario of emission to urban air. Adapted with permission from [210]. © Springer Nature.

An overview of physical characteristics of typical polar precursor solution solvents for PSC production is presented in Table C.1.
Despite its general disadvantage of carrying toxins or dissolved materials with it across skin membranes, the study shows that DMSO offers the least human health and environmental impact compared to all other typical polar aprotic solvents (Figure 6.2) for producing the perovskite layer of PSCs [210, 212], which normally exhibit a strong electronegative polar group in the solvent molecule.
According to the Lewis acid-base theory, an electron pair acceptor is classified as an acid and electron pair donor as a base. The reaction between Lewis acid and base results in either redox reaction or coordinated adducts. Pb halides are known as Lewis acids, while the polar aprotic solvent acts as the Lewis base. In a perovskite precursor solution, the atoms, ions, and solvent molecules coordinate with each other generating a intermediate Lewis acid-base adduct also referred to as complex. A Pb atom or Pb^{2+} ion represents the central object of the complex providing empty orbitals to share the electrons with surrounding solvent molecules [484].
Besides offering the least human health and environmental impact as mentioned before, DMSO has a high donor number (D_N) (Table C.1), which was proposed as a figure of merit to describe the coordination ability of the solvent with perovskite precursors, especially to Pb^{2+} ions [413]. This leads to an excellent solubility of the perovskite precursors in DMSO [375, 485].

However, utilizing pure DMSO implies two main challenges in contrast to DMF or DMF:DMSO mixtures: (i) increased dewetting on the subjacent layer [236, 240], especially on PTAA, due to a high DMSO σ of 42.8 mN m^{-1} [486] and a high η of 2.0 cP [305, 375], resulting in inhomogeneous perovskite films on a large area [375, 439, 487, 488] and a reduced processing velocity [210, 375]; and (ii) complex quenching and longer solvent evaporation periods of the wet film [489, 490] when using low processing temperatures due to its low p_{oi} and higher BP of 189 °C than the one of DMF (153 °C) [210], as summarized in Table C.1 [413].

Since PSCs with perovskite layers fabricated from pure DMSO have normally exhibited poor device performance [236, 239, 240, 488] due to the mentioned challenges, this solvent system has been rarely used except for very few reports. They refer to the fabrication of PbI_2 films in a two-step method [491] or, when utilizing a one-step method, to the deposition of single-cation perovskite layers via a meniscus coating techniques [239, 488] and SC [236, 492–494].

Even fewer studies are reported on double- or multi-cation perovskite produced by solely DMSO solution processing. Meniscus coating of a pure DMSO double-cation precursor solution has

been reported by He et al., but the perovskite composition still contained MA^+ ions [353]. In contrast, Galagan et al. investigated SDC of MA^+-free double-cation perovskite films in merely DMSO which was unfortunately only feasible by adding the hazardous co-solvent 2-butoxyethanol (2-BE) [240]. Furthermore, Zhang et al. recently described a double-cation perovskite solution deposited from pure DMSO but only for hardly scalable SC and antisolvent-assisted conversion [495].

In the following, the author for the first time developed and investigated one-step blade coating of a MA^+-free double-cation perovskite for PSCs from solely green DMSO without co-solvent or additives at low processing temperatures, which is an important step toward environmentally friendly industry-relevant solution processing of PSCs [413].

An exemplary schematic illustration and a corresponding SEM cross-section image in Figure 6.3 demonstrate the inverted planar device architecture on glass in principle consisting ITO/PTAA/SiO_2 NPs/FACsPbIBr/PCBM/BCP/Ag [413].

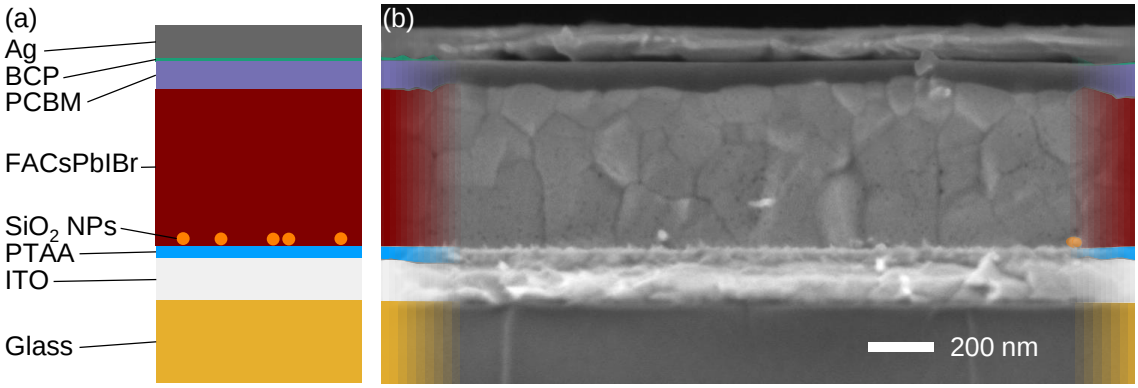

Figure 6.3: (a) Schematic illustration of the inverted device stack with SiO_2 NPs at the PTAA/perovskite interface and (b) SEM cross-section image of a typical opaque PSC with blade coated PTAA, NPs and a FACsPbIBr perovskite layer fabricated from solely DMSO. The NPs are marked in orange.

The chosen chemical composition of the double-cation perovskite of $FA_{0.83}Cs_{0.17}Pb(I_{0.87}Br_{0.13})_3$ allows stable absorber layers avoiding MA^+ ions with E_g >1.60 eV as mentioned in Subsection 2.1.1 and 2.1.4. Consequently, this fact might make the composition as well suitable for tandem applications [460, 496].

The nonpolar polymer PTAA is utilized here again as a HTL because of its efficient carrier transport properties [409] as presented in Subsection 5.1.2. To prevent dewetting of the precursor solution on PTAA, the author again applies the blade coated SiO_2 NP wetting agent at the HTL/perovskite interface developed in Subsection 5.2.1, which enhances the PTAA surface energy [409, 411]. Consequently, there is no need for the in literature widely utilized addition of amphiphilic surfactants to the perovskite precursor solution to lower its σ, such as LP [247, 274, 344, 352, 375, 377, 378, 389, 418, 419, 497] which the author utilized mainly in Section 4.2.

Figure C.1 clearly indicates that without the use of the NP wetting agent on top of PTAA the perovskite precursor solution in pure DMSO is nonwetting on PTAA and does not remain on the substrate after BC, while in the case of PTAA/NPs, fully covered and homogeneous double-cation perovskite layers are obtained after annealing [413].

For comparison, the perovskite precursors are either dissolved in a toxic 4:1 (vol:vol) DMF:DMSO mixture or in merely green DMSO. The author emphasizes that engineering of process parameters, such as Q, direction of the gas stream and delay time after wet film deposition until

quenching as well as v_{BC} and v_{GK}, is critical and leads to different ideal process conditions for both separately optimized recipes of each solvent system [413]. For instance, earlier tests revealed that more uniform perovskite layers are accomplished when choosing larger Q. It results in a higher degree of supersaturation and therefore leading to a boosted nucleation density (see Subsection 2.2.2) with compact perovskite domains [282, 498].

To evaluate the morphology an crystal grains of the resulting perovskite from the toxic and green solvent system, the author compared the SEM top-view images of perovskite layers blade coated on ITO/PTAA/SiO_2 NPs from both solvent systems (Figure 6.4). Both films are annealed at a temperature of either 100 °C or 150 °C for a period of 10 min (Figure 6.4a-d) [413].

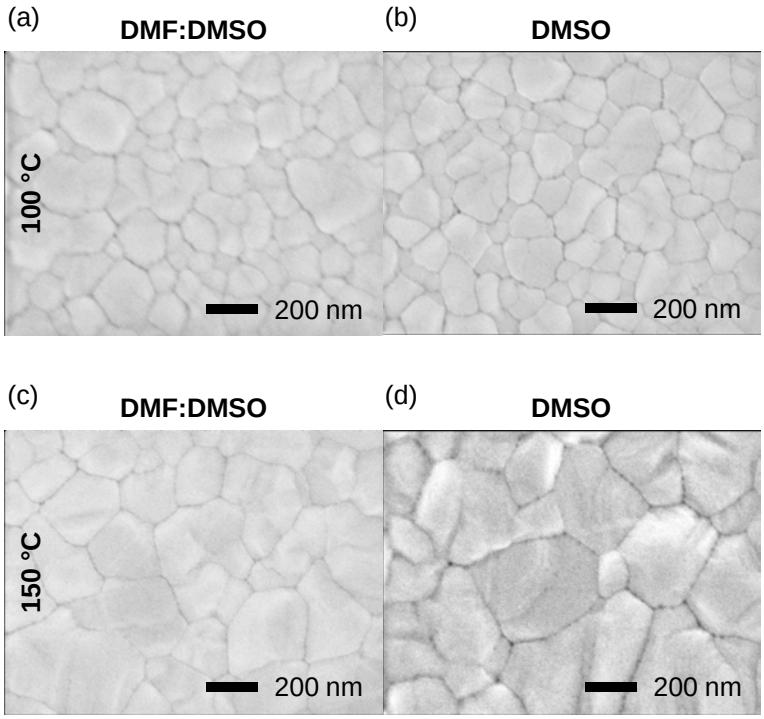

Figure 6.4: SEM top-view images of double-cation perovskite layers blade coated on ITO/PTAA/SiO_2 NPs from a precursor solution in different solvent systems both annealed at temperatures of (a-b) 100 °C or (c-d) 150 °C.

The morphology of the perovskite layer fabricated from DMSO does not significantly differ from the one from the DMF:DMSO mixture for each annealing temperature [413].

Figure 6.5 illustrates the corresponding histograms of crystal grain size distribution determined from SEM images with lower magnification and a larger image section than in Figure 6.4a-d to increase statistics. Figure C.2 presents the analysis of the crystal grain size distribution [413].

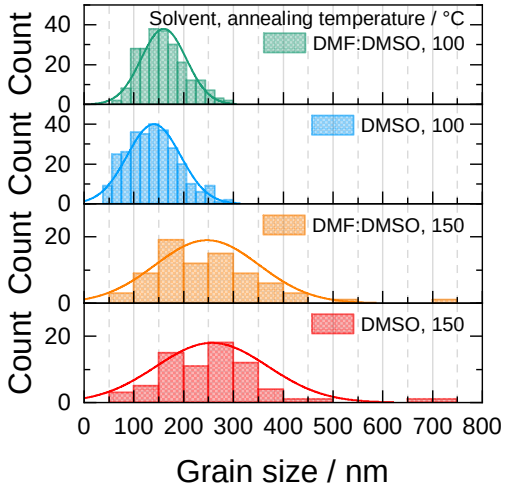

Figure 6.5: To Figure 6.4 corresponding histograms of crystal grain size distribution. For details see Figure C.2.

When identifying the crystal grain size, the samples show an absolute increase in mean crystal grain sizes of ~90 nm (DMF:DMSO) and 110 nm (DMSO) when the annealing temperature is altered from 100 °C to 150 °C, which corresponds to a relative increase of >55 % and 75 %, respectively, as illustrated in Figure 6.4c-d and Figure 6.5. Thus, the increase in growth is nearly similar in both cases. Figure 6.5 discloses a slightly smaller mean crystal grain size of ~140 nm of the perovskite layer fabricated by utilizing DMSO than DMF:DMSO (160 nm) when choosing an annealing temperature of 100 °C. The reason for that might be the different BPs of 153 °C and 189 °C of DMF and DMSO (Table C.1), respectively [413].

In the case of an annealing temperature of 150 °C, the mean grain sizes of ~250 nm of samples deposited from both solvent systems are similar (Figure 6.5) because an annealing temperature of 150 °C is high enough to fully evaporate pure DMSO analogically to a DMF:DMSO mixture. The grain size is larger for a higher annealing temperature of 150 °C due to enhanced grain coarsening as reported in literature [499–501].

Figure C.3 presents the SEM top-view images of the same samples with lower magnification. The images indicate a homogeneous layer with full coverage in the case of the toxic DMF:DMSO solvent systems as well as the green pure DMSO solvent with both annealing temperatures.

To investigate the surface roughness of the FACsPbIBr layers, the author measured the SEM cross-sections of complete solar cell device stacks with a perovskite active layer blade coated from a precursor solution in the two solvent systems (Figure 6.6) [413].

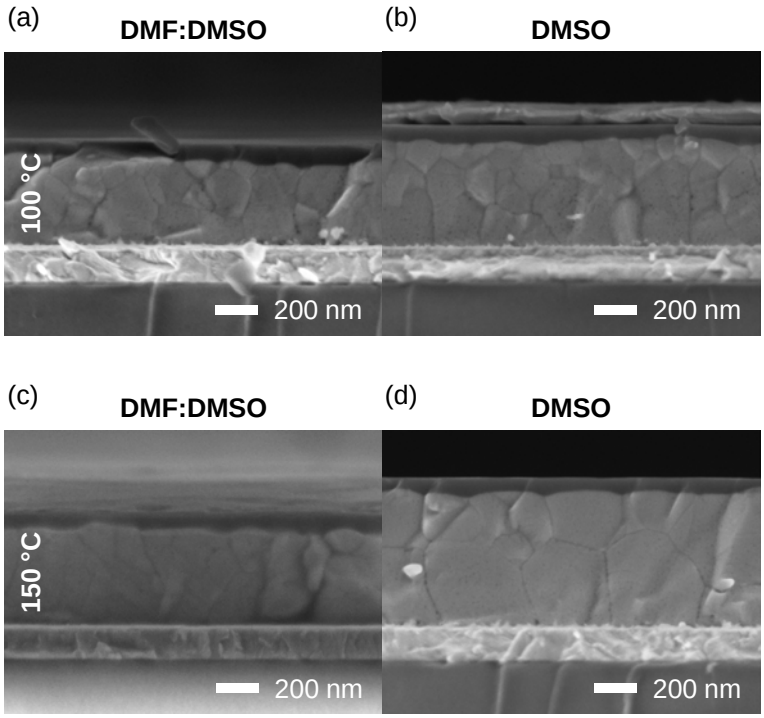

Figure 6.6: SEM cross-section images of complete solar cell device stack with a double-cation perovskite active layer blade coated from a precursor solution in different solvent systems and annealed at different temperatures. (a, c and d) The Ag contact is not visible.

The author observed similar surface roughness independent from the solvent system and the annealing temperature. The ETL of PCBM completely covers the perovskite layer. The author observed larger grains preferentially in the case of the higher annealing temperature (Figure 6.6c-d), as already presented in Figure 6.4c-d. Furthermore, a homogeneous coverage and no voids are found at the HTL/perovskite interface [389,409,448] as described in Subsection 5.2.2. From Figure 6.6, no clear statement can be made on the absorber thicknesses in relation to the four parameter sets since perovskite layers exhibit slight thickness variations over the $3 \times 6\,\mathrm{cm}^2$ substrate caused by the characteristic of the BC process itself [413].

From the SEM studies, the author concluded that the perovskite morphology is homogeneous and the mean grain size, grain size distribution, and surface roughness of samples from toxic and green solvent systems are comparable. This fact is mainly attributed to the sufficient quenching by gas stream-assisted drying further developed in Subsection 6.1.1 and to the improved wetting properties of both perovskite solutions on the nonwetting PTAA layer, especially the one with solely DMSO, with the aid of the NP wetting agent [409, 411, 413] optimized in Subsection 5.2.1.

XRD measurements are conducted on annealed perovskite layers to investigate their crystal structure fabricated from the toxic DMF:DMSO and the green DMSO solvent systems with both annealing temperatures (Figure 6.7) [413].

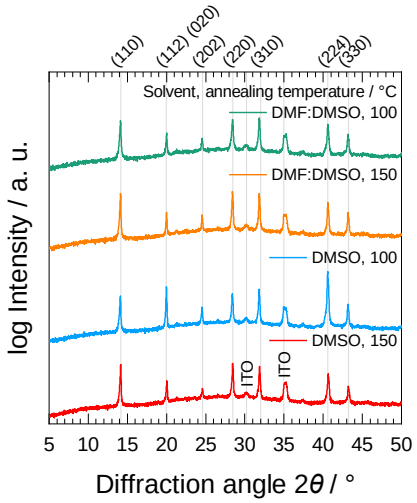

Figure 6.7: XRD patterns of the tetragonal crystal structure of double-cation perovskite layers blade coated on ITO/PTAA/SiO_2 NPs from a precursor solution in different solvent systems and annealed at different temperatures.
The two peaks at ~30° and 35° derive from the ITO. Furthermore, the author did not record any peaks at 2θ of 12.6° and 25.4°, which would indicate undesirable PbI_2.

XRD patterns disclose the formation of the perovskite structure independent of the solvent system and annealing temperature. All peaks from the films can be indexed to the perovskite phase or the subjacent ITO. Hence, this means that the films exhibit a pure perovskite phase without FAI, CsI, or yellow phases of formamidinium lead triiodide ($FAPbI_3$) or $CsPbI_3$ and PbI_2 [481]. No decisive change in peak intensity or significant shift of the main peak positions of the tetragonal perovskite structure is observed when the green solvent system and an annealing temperature of 150 °C were chosen compared to the standard solvent system with 150 °C [413].

From the diffractograms, the author concluded that the crystallographic properties of the perovskite layer fabricated by the green solvent system are similar to those of the perovskite layer fabricated from a DMF:DMSO mixture which confirms the observation from the SEM images (Figure 6.4).

Spectral T and R measurements are conducted on annealed perovskite layers to evaluate the calculated A and compare the absorbing capacity of films fabricated from different solvent systems and annealing temperatures, as illustrated in Figure 6.8 [413].

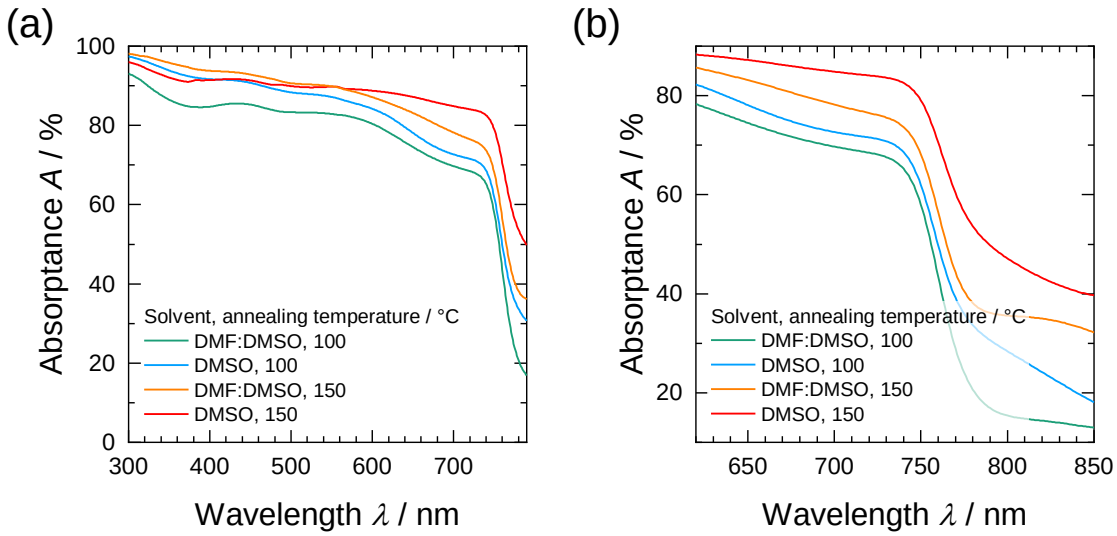

Figure 6.8: Spectral absorptance A of double-cation perovskite layers blade coated on ITO/PTAA/SiO_2 NPs from a precursor solution in different solvent systems both annealed at temperatures of 100 °C or 150 °C as a function of λ. (b) Focus on absorption edge.

Optical A curves indicate in principle relatively similar trends for the different samples. Notably, the typical strong, broad absorption of perovskite is observed also for samples from pure DMSO, indicating no necessity of toxic DMF. Despite the interference effect due to potential perovskite thickness variations, the samples annealed at 150 °C indicate a generally slightly higher absorption in the range from 580 nm to 760 nm than the ones with an annealing temperature of 100 °C. The sample fabricated from the pure DMSO solvent system and 150 °C annealing temperature shows highest A (Figure 6.8a). The absorption edge of the signals of all thin films is formed between 750 nm and 770 nm (Figure 6.8b), which is attributed to the formation of the FACsPbIBr perovskite [460]. This fact correlates to the XRD measurements (Figure 6.7) where the perovskite crystal structure was observed for both solvent systems and annealing temperatures as well [413].

To investigate the chemical properties of the perovskite absorber and the elemental composition of the device stack, TOF-SIMS depth profiles are conducted on PSCs with perovskite layers utilizing both solvent systems and annealing temperatures (Figure 6.9) [413].

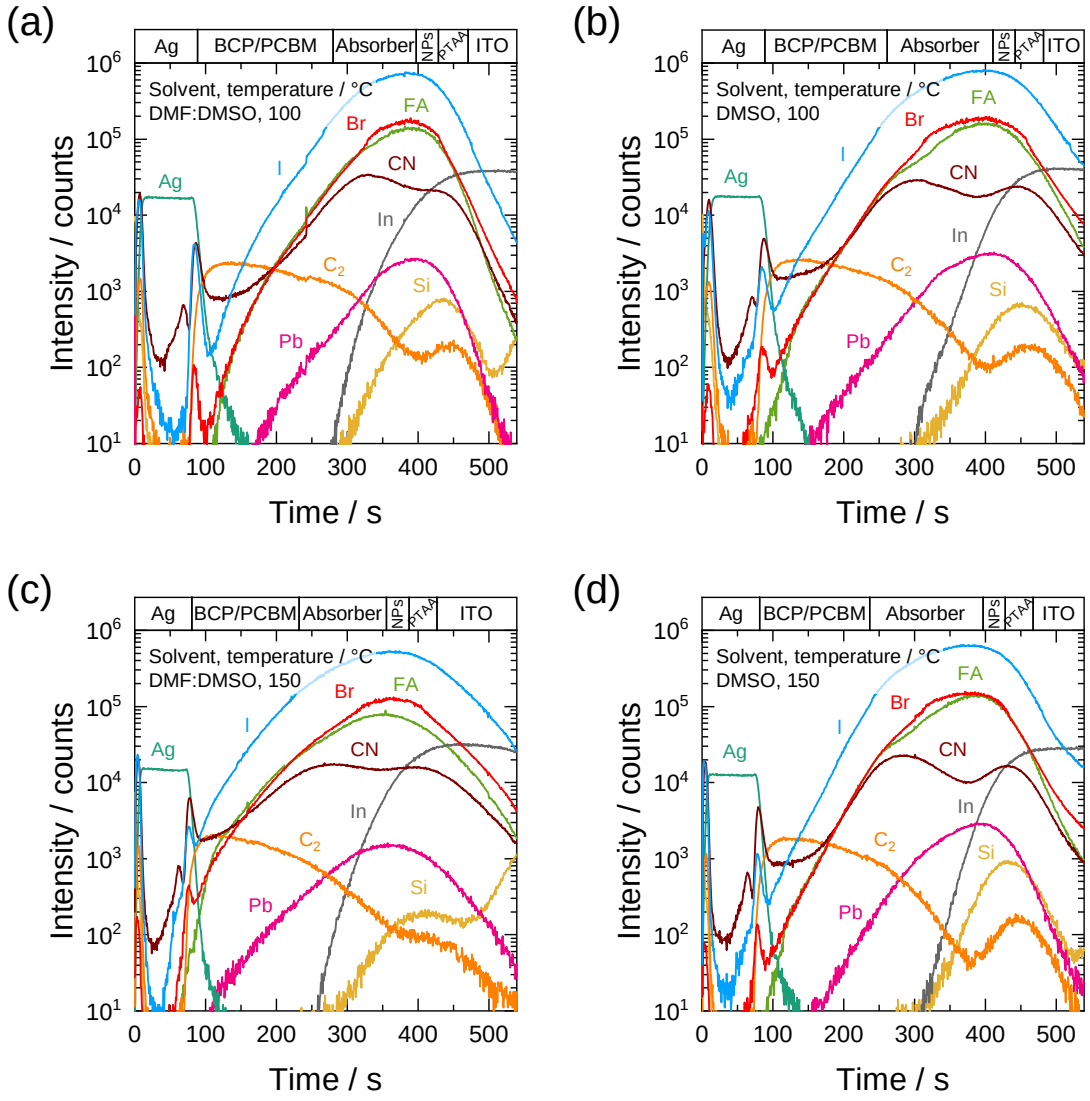

Figure 6.9: TOF-SIMS depth profiles (positive ions) through complete solar cell device stack with a double-cation perovskite absorber blade coated from a precursor solution in different solvent systems and annealed at different temperatures. Slight shifts of the graphs arise from negligible perovskite thickness difference. The labels Ag, C_2, I, Br, FA, Pb, Si, CN and indium (In) represent the signals of $CsAg^+$, $Cs_2C_2^+$, Cs_2I^+, Cs_2Br^+, $CH_5N_2^+$, Pb^+, Si^+, Cs_2CN^+ and In^+, respectively.

The depth profiles reveal an expectable elemental composition through the device stacks. A homogeneous distribution of the main components of the double-cation perovskite, such as halide ions, indicated by the I and Br signals, and FA^+ ions, is identified throughout the perovskite bulk of all samples independent of the solvent system and annealing temperature. The author did not observe a clear indication of any halide ion phase segregation since halide signals run parallel to each other across the perovskite depth [502]. A slightly increased accumulation of the halide signals is observed at the BCP/Ag interface, whereas the signals of FA^+ ions and Pb are not concentrated at this interface. The reason for this fact might be the facile halide ion diffusion [502]. Cs^+ ions in the absorber cannot be detected since a Cs^+ source is utilized as a sputtering ion source to enable the removal of all layers in the complete cell stack. Moreover, negligible shifts of the graphs arise from differences in perovskite and ETL layer thicknesses of the samples, as already presented in Figure 6.6 [413].

Instead of a plateau, the relatively slow increase of characteristic I and Br signals with increasing depth in all samples is caused by the fact that the sputter rate of the organic compounds is much lower than for the inorganic or organic-inorganic compounds when using a Cs^+ sputter source in TOF-SIMS. Consequently, no sharp transition region exists at the PCBM/perovskite interface. The C_2 signal increase between 400 s and 500 s is attributed to the PTAA layer. In addition, the CN signal is ascribed to FA as well as PTAA. The SiO_2 NPs are clearly detectable at the PTAA/absorber interface via the Si signal for all four samples [413].

From the TOF-SIMS study, one can conclude that the chemical properties of the absorber layer and elemental composition in the solar cell are, independent of the annealing temperature, unaltered when choosing green DMSO instead of the standard DMF:DMSO mixture as a perovskite precursor solution solvent.

The perovskite layers deposited by one-step gas stream-assisted BC from a toxic and green solvent system are integrated in PSCs to compare their photovoltaic performance. At this juncture, similar PCEs of up to >16.5 % are reached [413].

Figure 6.10 shows an overview of box charts of all characteristic photovoltaic device parameters of PCE, FF, V_{OC}, and J_{SC} of PSCs blade coated from a precursor solution in 4:1 (vol:vol) DMF:DMSO mixture and pure DMSO and annealed at temperatures of 100 °C and 150 °C evolving over three device batches in which v_{BC} were gradually optimized.

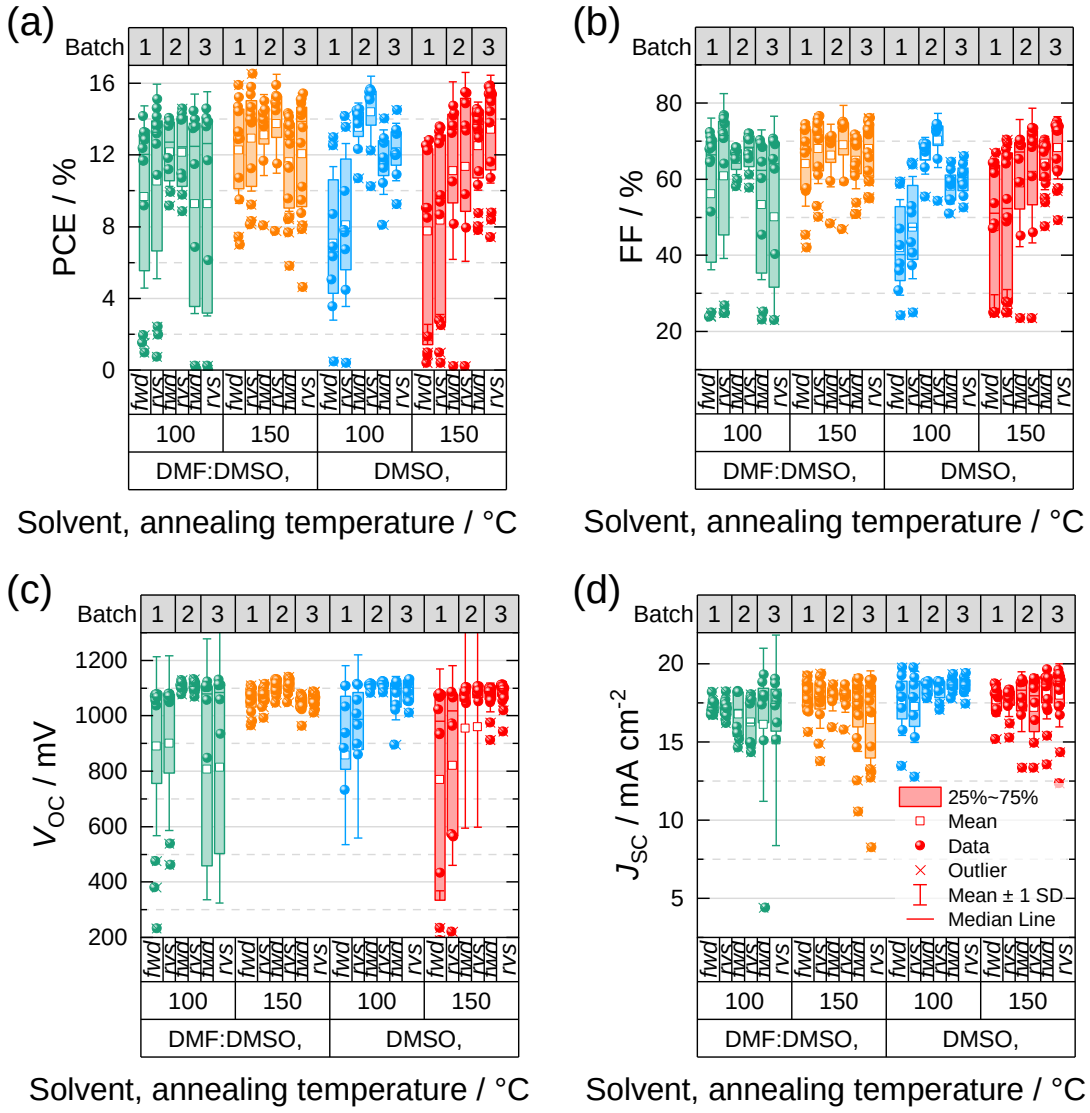

Figure 6.10: Box chart of (a) PCE, (b) FF, (c) V_{OC} and (d) J_{SC} of PSCs with a double-cation perovskite absorber blade coated from a precursor solution in different solvent systems and annealed at different temperatures evolving over three device batches changing v_{BC}: (1) 20 mm s^{-1} (both solvent systems); (2) 20 mm s^{-1}, 10 mm s^{-1} (DMF:DMSO, DMSO); (3) 18 mm s^{-1}, 7.5 mm s^{-1} (DMF:DMSO, DMSO). Shown values were measured in *fwd* and *rvs* scan directions.

Besides the reference of the standard toxic solvent system, Figure 6.10 depicts the evolution of the DMSO recipe until it delivered similar device performances compared to the DMF:DMSO solvent mixture. From the evaluation of device performances with an annealing temperature of 150 °C, the author concludes that with the green DMSO solvent system, similar mean PCEs compared to the standard toxic DMF:DMSO mixture of ~14 % to 16 % can be achieved. Furthermore, an annealing temperature of 150 °C might be more favorable for reaching the highest device performance of >16 % compared to 100 °C (close to 16 %) [413].

The parameter v_{BC} for both solvent systems were consecutively optimized in the three presented device batches. In Batch 1, a v_{BC} of 20 mm s^{-1} were chosen for both solvent systems. In this batch the performance of devices fabricated from pure DMSO were significantly lower compared to devices from the toxic solvent system. The reason for that was a too thick d_{wet} in the case

of pure DMSO and therefore insufficient quenching. Consequently, as mentioned before, v_{BC} of the recipes of both solvent systems were henceforward optimized separately (Batch 2 and 3). This is clearly comprehensible because of the differences in rheology, especially in η and p_{oi} (Table C.1), of both solvent systems [491], requiring slower v_{BC} (and v_{GK}) for pure DMSO by trend to reach d_{wet} values comparable to the case of the solvent mixture and appropriate drying, respectively. Similar PCEs for both solvent systems were reached after optimizing v_{BC} (Figure 6.10) [413].

Moreover, the results of device performance (Batch 3) conform to the measurements of A displayed earlier (Figure 6.8). All devices show moderate hysteresis behavior caused by a small change in an absolute V_{OC} of ~10 mV but mainly due to an alteration in absolute FF of up to 4 %, as illustrated in Figure 6.10b.

The *JV* data in *fwd* and *rvs* scan directions of the champion devices of both solvent systems for this study is illustrated in Figure 6.11 [413].

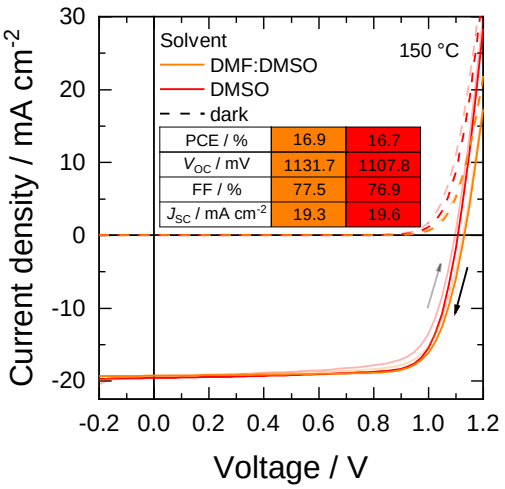

Figure 6.11: *JV* curves in *fwd* and *rvs* scan directions of the champion photovoltaic devices of the two solvent systems (150 °C) in this study.

For the author's study, similar champion PSC PCEs of 16.9 % and 16.7 % were achieved in the *rvs* scan direction for the DMF:DMSO and the DMSO solvent system, respectively, with an annealing temperature of 150 °C and slight hysteresis (Figure 6.11). In the *fwd* scan direction, these devices showed PCEs of 16.3 % and 15.5 % with FF values of 74.5 % and 72.1 %, respectively. The data confirm the successful transfer of one-step double-cation perovskite blade coating from a toxic solvent system to a scalable deposition via a fully green precursor solvent [413].

EQE measurements reveal the relation of the spectral current generation of representative PSCs with perovskite absorber layers blade coated from a precursor solution in different solvent systems and annealed at both temperatures under an additional bias light (Figure C.4).

EQE differences in the range between 580 nm and 760 nm are detected because of differing perovskite absorber thicknesses as illustrated in Figure 6.6, causing in some cases, insufficient absorption of photons due to interference effects as mentioned before. Nevertheless, the inte-

grated photocurrent density obtained by EQE measurement (J_{EQE}) values in Figure C.4 precisely match with the J_{SC} values extracted from the *JV* curves (Figure 6.10d) in this study when a bias light is utilized during the measurement [413].

Figure 6.12 shows the EQE measurements of the same photovoltaic devices without bias light.

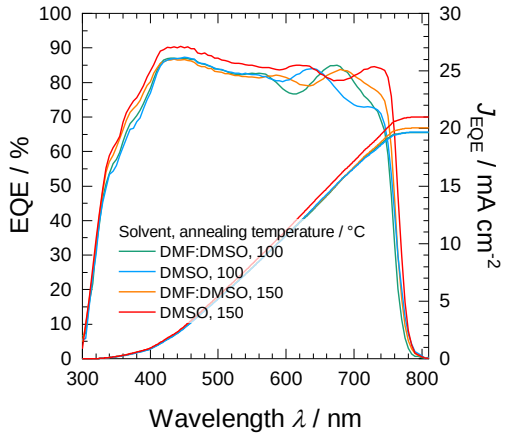

Figure 6.12: Spectral evaluation of EQE of representative PSCs with a double-cation perovskite absorber blade coated from a precursor solution in different solvent systems and annealed at different temperatures measured without a bias light. Figure C.4 presents EQE data measured with a bias light.

The EQE and J_{EQE} values are 5 % to 10 % relatively higher than the results in Figure C.4 in all cases of the four parameter sets. This might be associated with recombination or hysteresis of the photovoltaic devices under light as demonstrated in Figure 6.10 due to ion migration [498, 503]. Without bias light, J_{EQE} values exceed the J_{SC} values obtained from *JV* curves by an absolute value of ~1.5 mA cm^{-2}. Since the parasitic absorption of ITO/PTAA/SiO_2 NPs is expected to be the same for all samples, the differences in EQE might be mainly attributed to discrepancies in average crystal grain sizes (Figure 6.5) and absorber thicknesses (Figure 6.6). The samples annealed at 150 °C exhibit in general larger grain sizes, which could reduce the charge recombination at grain boundaries, leading to a higher EQE [413]. L_c values in the bulk might increase with larger grain sizes as well, thus generally causing a higher quantum efficiency in the range of 400 nm to 600 nm [504].

The FACsPbIBr semiconductor E_g are calculated to be ~1.61 eV for the samples with an annealing temperature of 150 °C and 1.62 eV for cells with perovskite annealed at 100 °C independent from the solvent system, which is in agreement with the measured V_{OC} and J_{SC} relation of corresponding solar cells (Figure 6.10c, d) [413].

Device performances of solar cells fabricated from both solvent systems prove that the concept of blade coating double-cation perovskite from a green precursor solvent, instead of toxic DMF-containing approaches, is extremely promising [413].

6.3 Optimization of slot-die coating with gas-assisted perovskite conversion

This section describes results on the implementation and optimization of slot-die coating with gas-assisted perovskite conversion of multi-cation perovskite thin films incorporated in PSCs.

Establishing slot-die coating with gas-assisted perovskite conversion represents original work of the author of this thesis. The majority of the following studies on additive engineering and defect passivation of slot-die coated perovskite for solar cells were primarily conducted by A. Manu under guidance of the author and the here presented results reflect the main findings of her bachelor thesis [414]. Further information and additional details of the research can be found in the thesis. A. Manu was assisted by J. Hanisch, T. Wahl, J. Zillner, and E. Ahlswede, who carried out TOF-SIMS measurements, conducted SEM images, performed XRD measurements and supervised the work, respectively. All assistants discussed the results with the guide, who reviewed A. Manu's bachelor thesis together with J. Hanisch and E. Ahlswede.

Similar to the utilization of $PbCl_2$ as additive in the precursor solution introduced in Subsection 5.2.2, additive engineering [505] for instance with formamidinium chloride (FACl) is getting increasingly popular in literature. Recently, Tavakoli et al. described the use of FACl as an additive in the perovskite precursor solution and revealed surface defect suppression as well as an improved perovskite absorber layer crystallinity and enlarged average crystal grain size in n-i-p PSCs [506]. Furthermore, similar results have been as well reported by Dagar et al. [507] and others [508–511].

As a staring point for additive engineering by means of FACl in this thesis, blade coating was utilized at first due to its simplicity (Subsection 2.2.1). Figure 6.13 presents an overview of box charts of all characteristic photovoltaic device parameters of PCE, FF, V_{OC} and J_{SC} of PSCs with an absorber blade coated from a precursor solution in a 4:1 (vol:vol) DMF:DMSO mixture with different FACl additive concentrations (3 mol %, 5 mol % and 8 mol %).

Figure 6.13a indicates that the PCE of PSCs gradually increases with increasing the FACl concentration in the perovskite precursor solution from 3 mol % to 5 mol % and 8 mol %. With a concentration of 3, 5 and 8 mol %, the median PCE is ~8.5 %, ~11.0 % and ~12.5 %, respectively, mainly due to a gradual increase in median FF (Figure 6.13b) and J_{SC} (Figure 6.13d), while V_{OC} remains rather constant (Figure 6.13c). These facts might be attributed to an enlarged average crystal grain size as reported later (see Figure 6.16). Similar findings have been reported in literature [506, 508–511]. Since a FACl concentration of 8 mol % shows superior PCE values of PSCs with blade coated double-cation absorbers, it is considered as suitable for the SDC studies below [414].

Furthermore, it should be noted that the utilization of FACl in the perovskite precursor solution retards the nucleation and crystallization rate of the wet film [414, 506] similarly to the case of Cl^- ion addition in the form of $PbCl_2$ [409] as described in Subsection 5.2.2. For further details, the author recommends reference [414].

In order to avoid the d_{wet} and thus the d gradient using blade coating as described in Subsection 5.4.1, the scalable deposition technique was changed to slot-die coating (Subsection 2.2.1). Slot-die coating represents a more industry-relevant deposition technique than blade coating. Additionally, the author continued to utilize the in Subsection 6.1.1 developed dynamic high-pressure gas system for gas stream-assisted perovskite conversion.

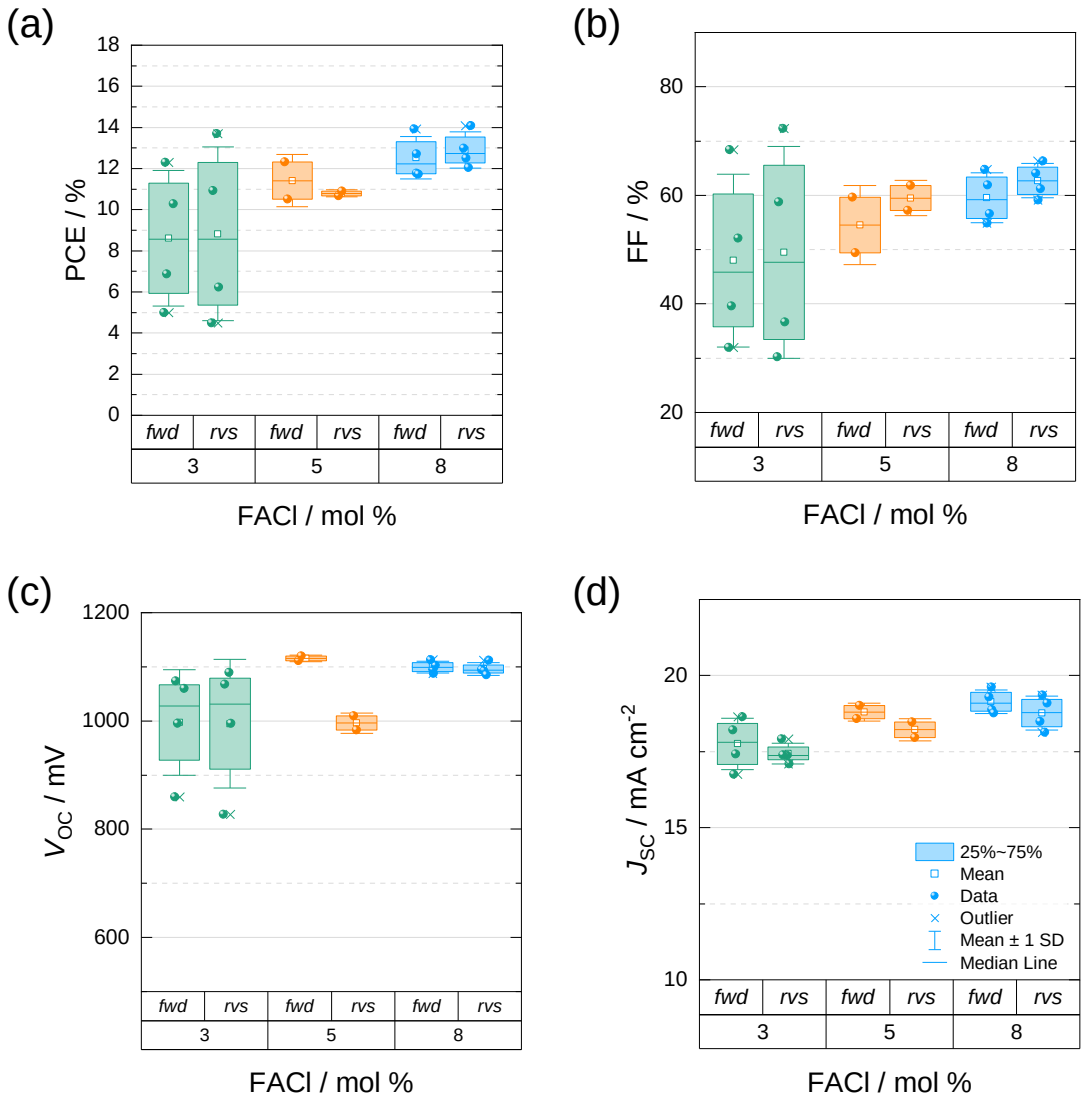

Figure 6.13: Box chart of (a) PCE, (b) FF, (c) V_{OC} and (d) J_{SC} of PSCs with a blade coated double-cation perovskite absorber with 3 mol %, 5 mol % and 8 mol % FACl in the perovskite precursor solution without an additional PEAI passivation layer on top of the absorber (see Figure 6.15) and an annealing temperature of 100 °C for 30 min. Shown values were measured in *fwd* and *rvs* scan directions. Short-circuited devices are omitted.

A photographical image of the experimental setup for slot-die coating perovskite absorber layers with gas-assisted perovskite conversion inside a glovebox is presented in Figure C.5. Details on the procedure are given in Subsection 3.1.4.

Figure 6.14 shows an overview of box charts of all characteristic PV device parameters of PCE, FF, V_{OC} and J_{SC} of PSCs with a double-cation perovskite absorber slot-die coated from a precursor solution in a 4:1 (vol:vol) DMF:DMSO mixture with a FACl additive concentration of 8 mol %. The films were annealed at different annealing temperatures of 100 °C, 130 °C and 150 °C.

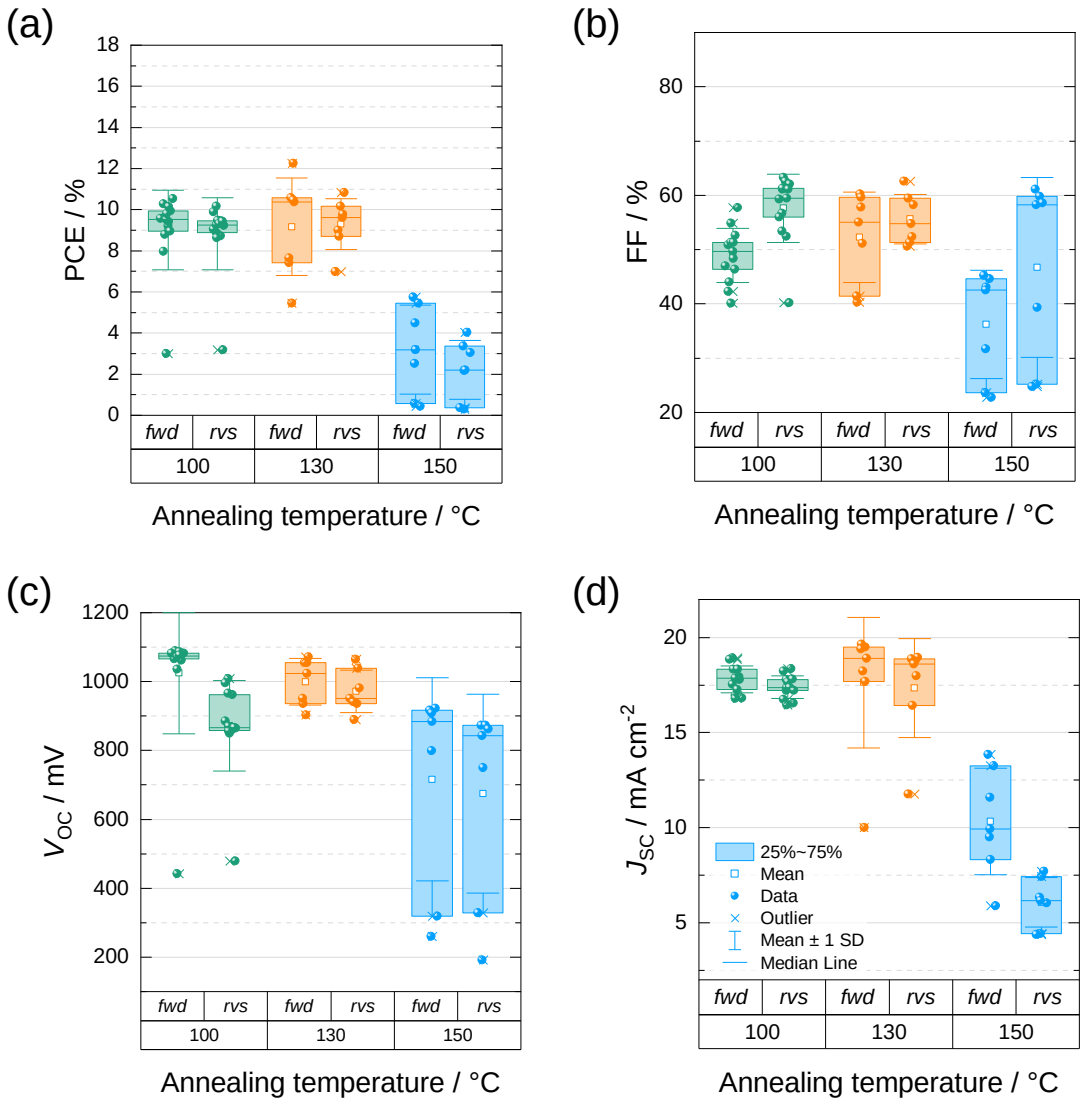

Figure 6.14: Box chart of (a) PCE, (b) FF, (c) V_{OC} and (d) J_{SC} of PSCs combined from two device batches with a slot-die coated double-cation perovskite absorber annealed at 100 °C, 130 °C and 150 °C for 30 min without an additional PEAI passivation layer on top of the absorber (see Figure 6.15) and with FACl (8 mol %) in the perovskite precursor solution. Shown values were measured in *fwd* and *rvs* scan directions. Short-circuited devices are omitted.

When comparing Figure 6.14 with Figure 6.13, a strong difference between the performance of PSCs with slot-die and blade coated perovskite is observed, although only considering results with the same FACl concentration and annealing temperature of 8 mol % and 100 °C, respectively. The PCE is significant lower for slot-die coating (~9.5 %) compared to blade coating (~12.5 %) mainly due to a decreased FF. The large PCE discrepancy between the scalable deposition techniques slot-die and blade coating can not be directly explained since d of the annealed crystallized perovskite layers are similar in both cases (not shown) [414]. Furthermore, perovskite morphology, average grain size and R_q are similar as well (not shown). Differences in the nature of the HTL/perovskite or perovskite/ETL interface could be an option explaining the PCE discrepancy of SDC and BC [414] as supposed further down.

Moreover, Figure 6.14 indicates that an annealing temperature of 130 °C is beneficial for the median PCE of PSCs (~10.0 %) in contrast to 100 °C (~9.5 %) and 150 °C (~2.5 %). Consequently, this annealing temperature has been used in all further SDC studies [414].

Defect passivation [512] is a promising method to enhance device performance of PSCs [350, 513] for instance with phenethylammonium iodide (PEAI) via abundant iodide on the perovskite surface or via formation of a 2D perovskite phase on a 3D perovskite surface and thus filling I^- vacancies on the surface consequently resulting in passivation of the surface halide defects [514].

An overview of box charts of all characteristic device parameters of PSCs with an absorber slot-die coated from a precursor solution in a 4:1 (vol:vol) DMF:DMSO mixture with a FACl additive concentration of 8 mol % without and with an additional PEAI defect passivation layer on top of the double-cation perovskite absorber is presented in Figure 6.15.

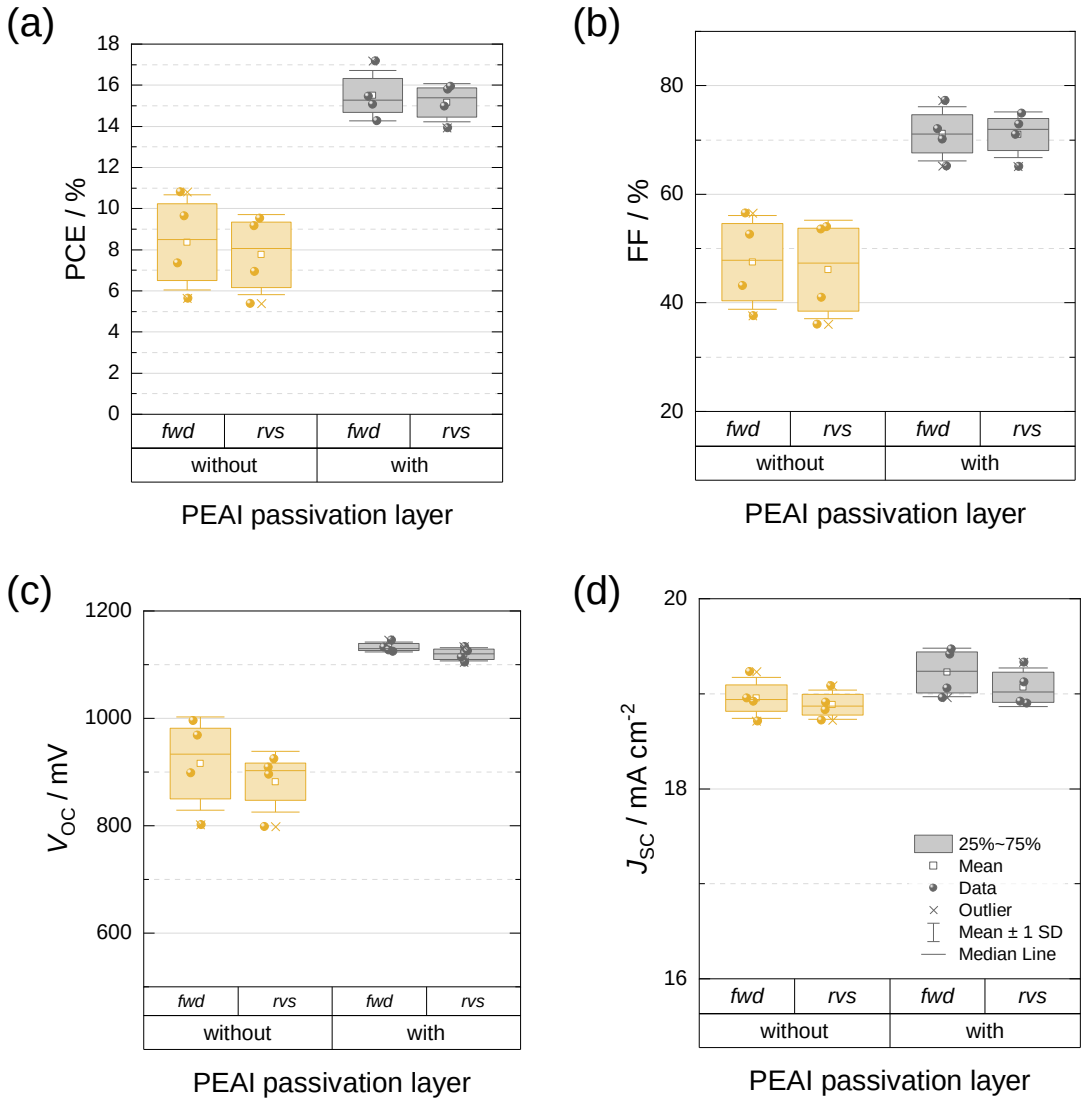

Figure 6.15: Box chart of (a) PCE, (b) FF, (c) V_{OC} and (d) J_{SC} of PSCs with a slot-die coated double-cation perovskite absorber without and with an additional PEAI passivation layer on top of the absorber and with FACl (8 mol %) in the perovskite precursor solution and an perovskite annealing temperature of 130 °C for 30 min. Shown values were measured in *fwd* and *rvs* scan directions.

Figure 6.15 clearly indicates an enormous enhancement of the median PCE from ~8.5 % to ~15.5 % (Figure 6.15a) by the PEAI layer at the perovskite/ETL interface mainly caused by a median FF increase of ~20 % (Figure 6.15b) and a median V_{OC} improvement of >200 mV (Figure 6.15c). However, Figure 6.15d illustrates that the median J_{SC} remains rather constant when utilizing the additional PEAI passivation layer. These improvements, especially of the V_{OC}, can be most likely attributed to the surface defect passivation effect which suppresses nonradiative charge carrier recombination [514].

Xu et al. recently reported a similar drastic increase in average PCE of PSCs with slot-die coated, here MAPI, perovskite absorber layers, from 12.6 % for the case without defect passivation to 20.1 % when utilizing a passivation strategy [359]. This increase is caused by an improvement of all characteristic photovoltaic device parameters [359].

From the SDC study without and with an additional PEAI passivation layer on the absorber surface (Figure 6.15), one can conclude that the prime reason for significant lower PCE values of PSCs with a slot-die coated double-cation perovskite absorber (Figure 6.14) compared to the blade coated counterpart (Figure 6.13) as mentioned before, has to be related to a higher density of surface defects in the case of SDC.

To investigate the different combinations of additive engineering by FACl and defect passivation via PEAI, four parameter sets were examined: (i) without FACl, without PEAI, (ii) with FACl, without PEAI, (iii) without FACl, with PEAI, and (iv) with FACl, with PEAI.

In order to analyze the influence of FACl and PEAI on the perovskite morphology a SEM study is performed. Figure 6.16 presents SEM top-view images of double-cation perovskite layers slot-die coated on ITO/PTAA/SiO_2 NPs without and with 8 mol % FACl in the perovskite precursor solution and without and with an additional PEAI layer on top of the absorber.

It can be observed, that without FACl bright appearing hexagonal flakes exist at the perovskite surface (Figure 6.16a, c), which are most likely PbI_2, although a stoichiometric perovskite precursor solution is utilized. PbI_2 is confirmed by XRD and GIXRD measurements further down (see Figure 6.17). Figure 6.16b, d indicate that, when including FACl in the solution, the PbI_2 flakes disappear. These results are again in excellent agreement with the crystallographic characterization in Figure 6.17. In addition, the average grain size increases with the utilization of FACl (Figure 6.16b, d) as similarly reported for $PbCl_2$ in Subsection 5.2.2 and in literature [506, 507, 511]. Furthermore, Manu's bachelor thesis revealed a slight perovskite surface roughness increase for samples with FACl [414] similarly to the results on incorporation of $PbCl_2$ in the perovskite precursor solution presented in Subsection 5.2.2.
The additional PEAI layer is barely visible in the SEM top-view images (Figure 6.16c-d). The crystal grain size remains unaltered despite the application of a PEAI defect passivation layer [414].

Moreover, a few SiO_2 NPs aggregate on the perovskite surface as illustrated in Figure 6.16a-d. This was the case only on rare occasions when the solution was blade instead of slot-die coated. It was not possible within this thesis to determine, if this NP relocation in the direction of the perovskite/PCBM interface is detrimental to or possibly even beneficial for device performance. The exact reason why NPs aggregate on the perovskite surface is not fully understood till now. The author assumes that the NPs are detached from the PTAA surface and are most likely transported through the precursor wet film due to differing solution adhesion of the perovskite precursor solution to the PTAA/NP surface during ink deposition depending on the different deposition technique itself. The process of NP relocation is enhanced by the drying process

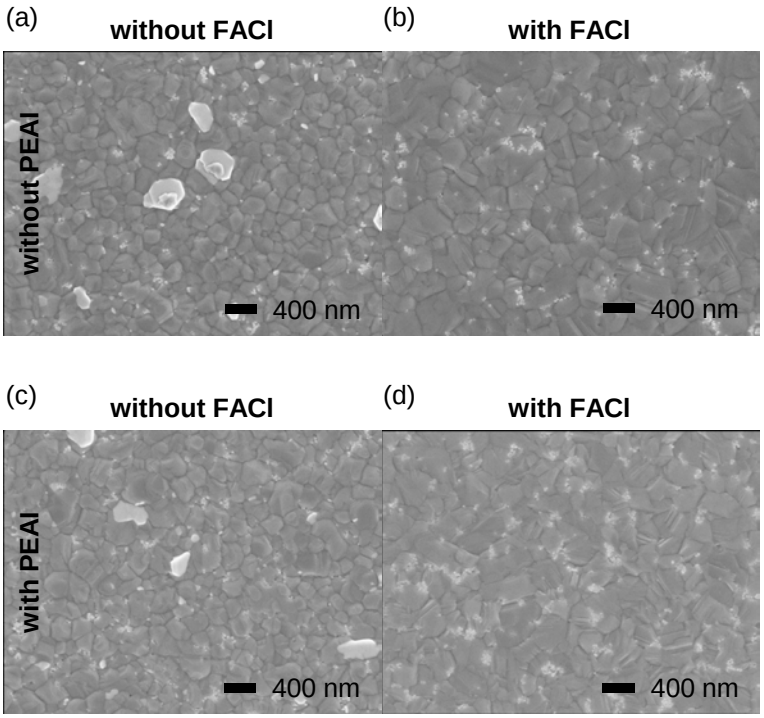

Figure 6.16: SEM top-view images of double-cation perovskite layers slot-die coated on ITO/PTAA/SiO_2 NPs (a, c) without and (b, d) with FACl (8 mol %) in the perovskite precursor solution and (a-b) without and (c-d) with an additional PEAI layer on top of the absorber (perovskite annealing on 130 °C for 30 min).
A few NPs aggregate at the perovskite surface during slot-die coating of the precursor solution.

via the high-pressure gas-assisted perovskite conversion. However, it is highly likely that in particular clusters of NPs detected in the SEM top-view images (Figure 6.16b, d) might decrease solar cell PCE due to their insulating nature (see Figure 6.19) and alter the wetting behavior of the subsequently deposited ETL consisting of PCBM [414].
The relocation of the SiO_2 NPs toward the perovskite/PCBM interface as observed in SEM top-view images in Figure 6.16 is confirmed by TOF-SIMS depth profiles further down (see Figure 6.18).

To analyze the perovskite crystal structure, XRD measurements are conducted on annealed perovskite layers processed via SDC on ITO/PTAA/SiO_2 NPs without and with FACl in the perovskite precursor solution and without and with an additional PEAI layer on top of the absorber (Figure 6.17). Here, diffractograms from XRD measurements are presented in Figure 6.17a, while Figure 6.17b illustrates GIXRD results.

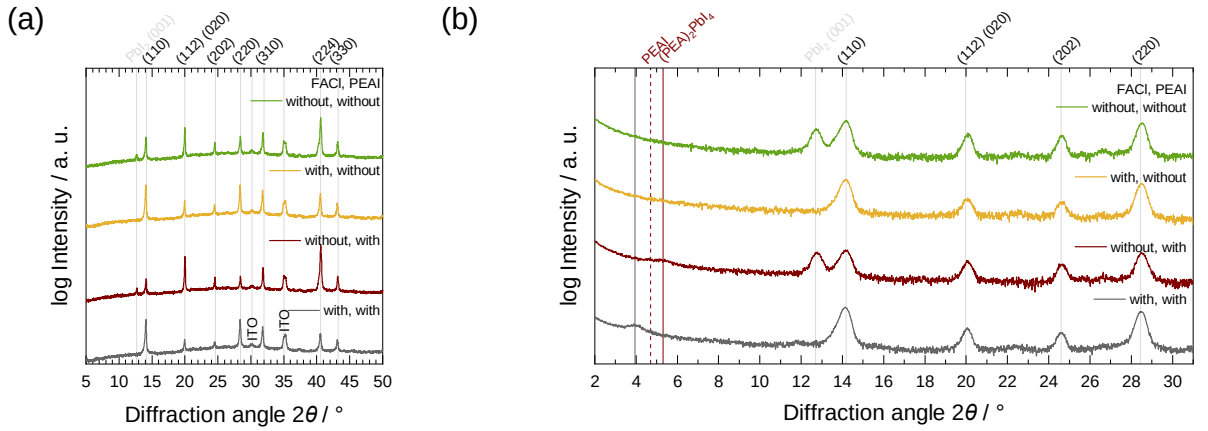

Figure 6.17: (a) XRD and (b) GIXRD patterns of the tetragonal crystal structure of slot-die coated double-cation perovskite layers on top of ITO/PTAA/SiO_2 NPs without and with FACl (8 mol %) in the perovskite precursor solution and without and with an additional PEAI layer on top of the absorber (perovskite annealing on 130 °C for 30 min).

The XRD patterns of the tetragonal perovskite crystal structure in Figure 6.17a reveal three main findings:

(i) No alteration of XRD patterns measured from 5° to 50° is observed when using an additional PEAI passivation layer on the perovskite surface.

(ii) Utilization of FACl in the perovskite precursor solution causes vanishing of the peak at ~12.6°, which indicates detrimental PbI_2 and is in accordance with above mentioned SEM measurements (Figure 6.16), simultaneously increasing the (110) and (220) peaks at ~14.2° and ~28.5°, respectively.

(iii) The (112) and (224) peaks at ~20.0° and ~40.6°, respectively, however, decrease with FACl addition.

To conclude, XRD patterns of samples with FACl suggest an improved perovskite crystallinity as already reported elsewhere [506, 508, 509, 511]. In addition, no additional peaks appear after adding FACl which indicates that the majority of the FACl has evaporated [511] after annealing at 130 °C for 30 min similar to the case of adding $PbCl_2$ to the perovskite precursor solution (Figure 5.14) discussed in Subsection 5.2.2.

Since PEAI films are expected to be thin (few nm) and might form 2D perovskite [514], GIXRD patterns are analyzed. Results from GIXRD measurements (Figure 6.17b) confirm the finding concerning the appearance of a PbI_2 peak at ~12.6° for the samples without FACl in the precursor solution.
Furthermore, the samples with a PEAI layer exhibit additional low angle peaks which might be attributed to the expansion of the perovskite unit cell with increases of the thickness of a 2D perovskite layer in the crystal structure [515]. The peak at ~5.4° for the sample without FACl corresponds to the 2D perovskite $(PEA)_2PbI_4$ with $n = 1$, while n is the number of 2D phases of PbI_6 octahedrons sandwiched between the PEAI spacers [514, 516, 517]. It seems that the addition of FACl prevents the formation of the 2D $(PEA)_2PbI_4$ perovskite (Figure 6.17b) [414]. There is no diffraction peak at 4.7° detectable which would attribute to the diffraction pattern of the pure PEAI phase [514]. However, the reason for the appearance of the peak at ~3.9° in the

case of the sample with FACl is inexplicable till now and its origin is still under investigation. It might result as a consequence of 2D phases with higher n [515, 516, 518, 519].

To examine the distribution of the elemental composition of the device stack ITO/PTAA/SiO_2 NPs/FACsPbIBr/PCBM/BCP/Ag, especially concerning FACl and PEAI, TOF-SIMS depth profiles are conducted on complete stacks of PSCs with the four parameter sets, without and with FACl and without and with an additional PEAI layer, respectively. The results of the analysis are illustrated in Figure 6.18.

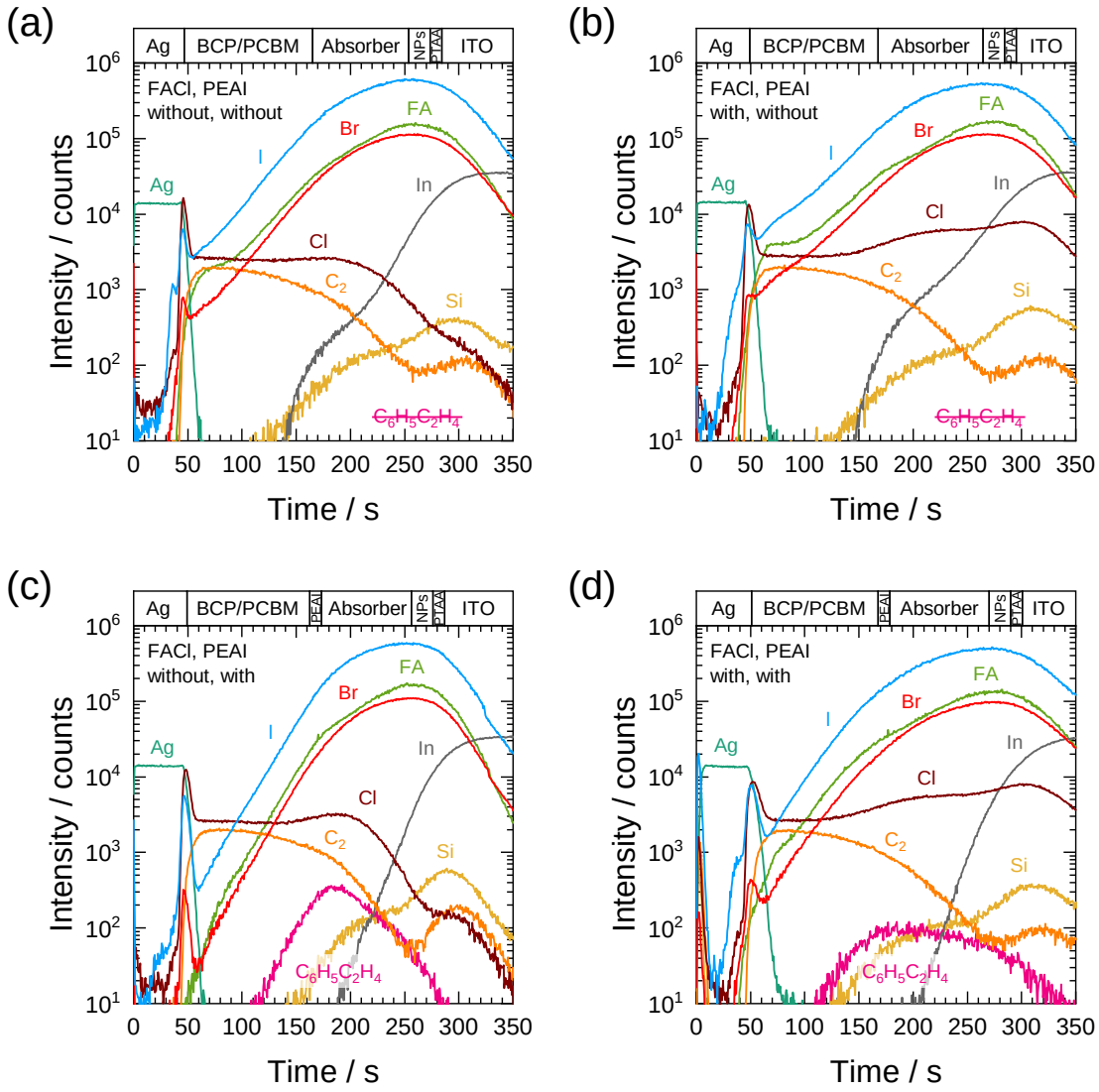

Figure 6.18: TOF-SIMS depth profiles (positive ions) through complete solar cell device stack with a slot-die coated double-cation perovskite absorber (a, c) without and (b, d) with FACl (8 mol %) in the perovskite precursor solution and (a-b) without and (c-d) with an additional PEAI layer on top of the absorber (perovskite annealing on 130 °C for 30 min).
The labels Ag, C_2, I, Br, Cl, FA, $C_6H_5C_2H_4$, Si and In represent the signals of $CsAg^+$, $Cs_2C_2^+$, Cs_2I^+, Cs_2Br^+, Cs_2Cl^+, $CH_5N_2^+$, $C_6H_5C_2H_4^+$, Si^+ and In^+, respectively.

Figure 6.18a-b clearly indicate the absence of the additional PEAI layer on top of the perovskite, since no signals of $C_6H_5C_2H_4$ are detected. However, with the additional passivation layer the signal of $C_6H_5C_2H_4$ is visible at the PCBM/FACsPbIBr perovskite interface (Figure 6.18c-d).

$C_6H_5C_2H_4$ represents a component of PEAI with the chemical formula of $C_8H_{12}IN$. The author assumes that the additional defect passivation layer of PEAI is leveling the perovskite surface roughness due to the observation of a second peak of the In signal from ITO for the samples without PEAI (Figure 6.18a-b) which is absent in the case of corresponding counterparts with PEAI (Figure 6.18c-d).
Furthermore, interesting findings concerning FACl are revealed: For the samples without FACl (Figure 6.18a, c), the Cl signal contribution is only caused by the residuals from the Cl containing solvent used for the PCBM solution. However, on the addition of FACl (Figure 6.18b, d), a second peak of Cl^- ions is observed indicating an accumulation of Cl^- ions toward the PTAA/ITO interface [414]. The findings on the location of Cl^- ions are coherent to the investigations of utilizing $PbCl_2$ as additive in the perovskite precursor solution (Subsection 5.2.2) as presented in Figure 5.15.
All other components are similarly distributed throughout the device stack for the four parameter sets, although slight shifts of the graphs are observed which arise from negligible difference in thickness of the corresponding layers.

As already mentioned in the paragraph discussing the TOF-SIMS depth profiles in Figure 6.9 (Section 6.2), the sputter rate of the inorganic or organic-inorganic compounds is much faster than for pure organic compounds when using a Cs^+ sputter source in TOF-SIMS. Consequently, no sharp transition region exists at the PCBM/perovskite (Figure 6.18a-b) and PCBM/PEAI/perovskite (Figure 6.18c-d) interfaces, respectively.

The author concluded from the TOF-SIMS analysis that PEAI is mainly located at the perovskite surface and does not diffuse deeply in the perovskite bulk thus mainly acting as surface defect passivation layer. Moreover, adding FACl increases the Cl distribution toward the HTL due to accumulation of Cl^- ions at the PTAA/ITO interface and less in the absorber bulk. This might passivate defects at the perovskite crystal grain boundaries [507, 511] toward the HTL.

Furthermore, SiO_2 NPs are clearly detected at the PTAA/perovskite interface by the Si signal in all samples (Figure 6.18a-d). Interestingly, the SiO_2 NPs which relocate at the perovskite surface for the case of slot-die coating the perovskite precursor solution as mentioned before (Figure 6.16) are detected as a second maximum of the characteristic Si signal at the PCBM/perovskite (Figure 6.18a, b) and PEAI/perovskite interfaces (Figure 6.18c, d), respectively, indicates. However, in the case of blade coating the perovskite precursor solution the SiO_2 NPs are not relocated, as mentioned before, which is confirmed by TOF-SIMS depth profiles of PSCs with blade coated absorbers where only one Si signal maximum is observed (Figure 6.9).

To investigate the influence of FACl and PEAI on the PCE of PSCs, the author compared photovoltaic performance of devices comprising slot-die coated double-cation perovskite including FACl and an additional PEAI film on the absorber surface, respectively. In doing so, PCEs of up to >17 % are reached [414].

Figure 6.19 presents an overview of box charts of all characteristic photovoltaic device parameters of PCE, FF, V_{OC} and J_{SC} of PSCs slot-die coated from a double-cation perovskite precursor solution without and with FACl and without and with an additional PEAI layer on top of the perovskite absorber.

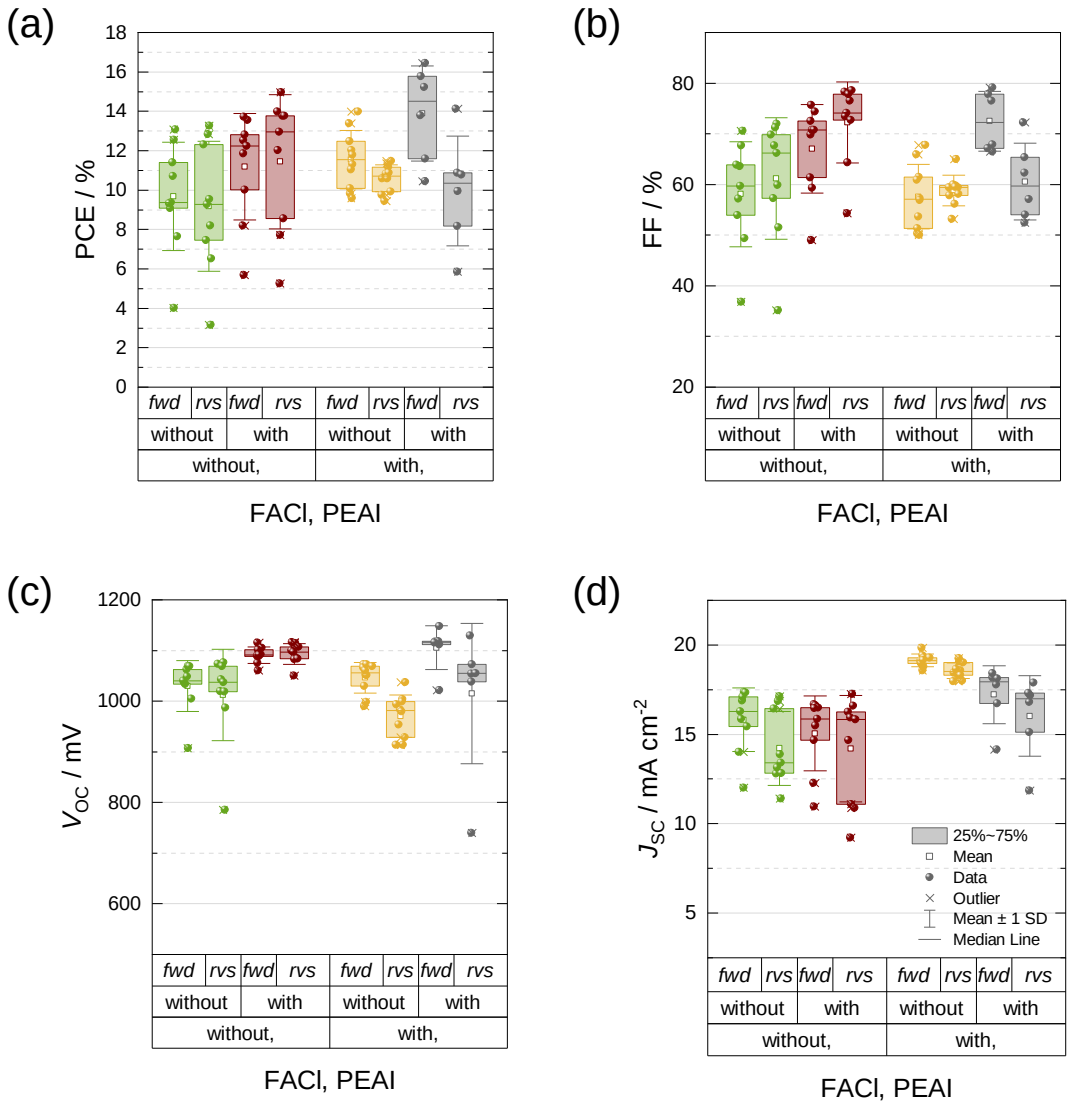

Figure 6.19: Box chart of (a) PCE, (b) FF, (c) V_{OC} and (d) J_{SC} of PSCs with a slot-die coated double-cation perovskite absorber without and with FACl (8 mol %) in the perovskite precursor solution and without and with an additional PEAI layer on top of the absorber (perovskite annealing on 130 °C for 30 min). Shown values were measured in *fwd* and *rvs* scan directions. Short-circuited devices are omitted.

When comparing the PSCs without and with incorporation of FACl, it is observed that the median PCE is increased with FACl by ~2 % (Figure 6.19a). However, with the addition of FACl the hysteresis behavior is in general increased possibly caused by the stronger migration behavior of Cl^- compared to I^- ions as observed in TOF-SIMS depth profiles (Figure 6.18b, d). Moreover, it should be noted that the highest *fwd* and *rvs* scan performances are in the opposite direction in contrast to samples without FACl as similarly observed for the addition of $PbCl_2$ (Figure 5.17) presented in Subsection 5.2.2. Its cause is still under investigation [414]. In addition, J_{SC} values seem to generally increase by FACl incorporation in the perovskite precursor solution (Figure 6.19d), which could be attributed to the larger average perovskite crystal grain size as mentioned before (Figure 6.16b, d) reducing charge recombination [506]. The V_{OC} remains rather unchanged (Figure 6.19c). Figure 6.19b indicates decreased FF values with the use of FACl which might be related to the increased perovskite surface roughness as mentioned before [414].

Adding a PEAI layer at the perovskite/PCBM interface results in a significant FF (Figure 6.19b) and V_{OC} increase (Figure 6.19c), while J_{SC} values remain rather constant (Figure 6.19d) as already mentioned (Figure 6.15). FF values might additionally increase due to a smoothing of the perovskite surface roughness via the deposition of the PEAI defect passivation layer, which was already assumed when evaluating the corresponding TOF-SIMS depth profiles (Figure 6.18). For the record PSCs, the PCE enhances by ~2 % and >2 % for the case without and with FACl, respectively (Figure 6.19a). The reasons for the latter might be the combined favorable effects of the simultaneous utilization of both FACl and PEAI:

(i) Halide vacancies at the perovskite grain boundaries are passivated along with a perovskite crystal grain size increase (Figure 6.16b, d) and suppression of PbI_2 (Figure 6.17) via the Cl^- ions from the FACl in the precursor solution,

(ii) the I^- ions from the additional PEAI layer passivate perovskite surface defects [507, 520], and

(iii) the missing 2D $(PEA)_2PbI_4$ perovskite phase identified by GIXRD measurements (Figure 6.17b) seems to be favorable for device performance.

FACl additive engineering together with the PEAI defect passivation strategy results in the most efficient device performances in *fwd* scan direction of all four parameter combinations (Figure 6.19a) [414].

The *JV* data measured in *fwd* and *rvs* scan directions of the champion solar cell device with slot-die coated double-cation perovskite in this study is illustrated in Figure 6.20.

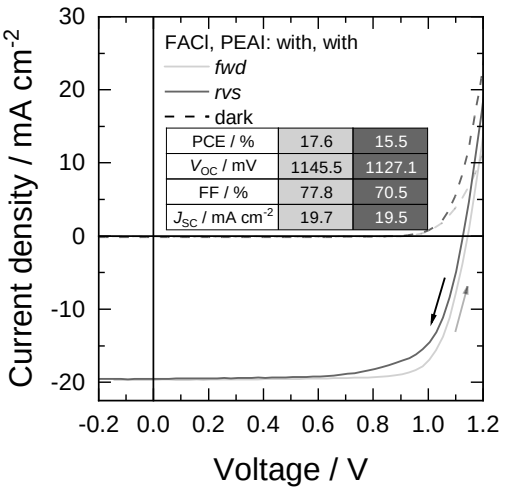

Figure 6.20: *JV* curves in *fwd* and *rvs* scan directions of the champion photovoltaic device with a slot-die coated double-cation perovskite (with FACl, with PEAI) in this study.

In the SDC study of the author, a champion PSC PCE of 17.6 % on an A_{act} of 0.24 cm^2 is achieved in the *fwd* scan direction for a sample including FACl in the perovskite precursor solution and with an additional PEAI defect passivation layer as presented in Figure 6.20. The solar cell exhibits a FF of 77.8 %. In the *rvs* scan direction, this device shows a PCE and FF of

15.5 % and 70.5 %, respectively. These results are reasonable on such an A_{act} (Figure 1.1b) in comparison to reports in literature [244, 479].

The findings from the SDC study indicate that additive engineering with FACl and passivation strategies such as an additional PEAI layer on the perovskite absorber surface are useful tools to drastically improve the performance of slot-die coated PSCs.

6.4 Potential for further optimizations

This section gives examples and discusses the potential for further optimizations.

In Section 6.3, slot-die coating was still optimized with the standard toxic DMF:DMSO solvent mixture. To avoid toxic solvents solely green DMSO should be not only used as solvent system when blade coating (Section 6.2) but also for slot-die coating in future [521]. Due to safety precautions of DMF the transfer to a sustainable solvent like DMSO is required, if producing perovskite layers in ambient conditions without the use of a glovebox and in direct contact with the operator [210]. Fabrication of PSCs in ambient conditions would be the big next step, which will implicate new challenges such as contact of the wet film to humidity and O_2 during deposition and perovskite conversion. Nevertheless, concerning this challenge, the gas-assisted concept is again promising since it can, besides removing solvent molecules during quenching, additionally suppress the accumulation of H_2O and O_2 molecules above the wet film reducing its interaction with these molecules [282].
Furthermore, the toxicity of DCB [522] as solvent to dissolve not only PTAA but also PCBM needs to be addressed in future by replacing DCB with a green solvent such as anisole in both HTL [390] and ETL cases as already presented in literature [523].

As already mentioned, when slot-die coating perovskite precursor solutions, a few SiO_2 NPs were found on top of perovskite surface (Figure 6.16), although the SiO_2 NP wetting agent is utilized at the PTAA/perovskite interface. However, a method to hinder the NP movement was not yet discovered.

To bring gas-assisted perovskite conversion in combination with slot-die coating closer to an industrial process the slot-die coating velocity v_{SD} and the gas knife velocity v_{GK} should be the same in order to enable a R2R process on flexible substrates with a stationary slot-die head and gas knife. First results on harmonizing the coating and gas knife velocity have been already presented by Manu et al. [414], but are not shown in this thesis. In brief, to accomplish the harmonization in general, v_{GK} was increased to match v_{SD}, the blade coater plate and substrate temperature needs to be slightly increased (still <70 °C) [498], and the distance from the gas knife outlet to the blade coater plate was decreased [414] to achieve faster quenching and supersaturation (see Subsection 2.2.2). This is required since the delay time between solution deposition and gas-assisted perovskite conversion is now almost 0 s. Another option would be to utilize a larger Q and v, respectively [282, 498], but these parameter alterations have been avoided in Manu's thesis due to technical limitations [414]. Furthermore, the distance between the slot-die and the gas knife is critical as well. However, v_{SD} and Q_{ink} was left constant resulting in the same d_{wet} as in the case of differing v_{GK} and v_{SD} [414].

In Section 6.3, the PEAI defect passivation strategy was only applied via an additional film on top of the perovskite layer. Literature indicates that it can be applied not only on the perovskite surface but also improves device performance when directly blended in the precursor solution of

the absorber by means of a passivation effect at the grain boundaries additionally to the function of surface passivation [328, 520].

To reach a fully scalable PV device architecture, the deposition of PEAI, PCBM and BCP needs to be transferred from spin coating to blade coating or slot-die coating, which might be an additional challenge in the case of PEAI and BCP since these layers need to be extremely thin (<5 nm) to function sufficiently [520, 524]. It is complex to achieve this by scalable deposition techniques due to an in general thicker wet layer thickness compared to the case of spin coating. For addressing this challenge, diluting and utilizing solutions with very low concentrations might be an option. Recently published results show that a defect passivation layer can be deposited by blade coating [383, 419].

6.5 Conclusion

Chapter 6 depicted the evaluation of scalable perovskite deposition from suitable solvent systems for multi-cation perovskite solar cells via gas-assisted perovskite conversion.

As presented, due to the facts that for a MC precursor solution PbI_2 and $PbBr_2$ and a DMF:DMSO mixture is utilized as Pb sources instead of $PbAc_2$ and the solvent system, respectively, a low-pressure and statically installed gas system (Chapter 5) is not sufficient enough to dry the double-cation wet film as desired. Therefore, a moving high-pressure gas system was established.
Furthermore, the results of Chapter 6 indicate that the author, for the first time, achieved p-i-n MA^+-free double-cation PSCs fabricated by one-step blade coating at low processing temperatures solely from DMSO which represents a green and environmentally safe precursor solvent, avoiding toxic solvent systems with DMF.
By applying the blade coated SiO_2 NP wetting agent developed in Subsection 5.2.1 at the HTL/perovskite interface and realizing sufficient DMSO quenching by gas stream-assisted drying (Subsection 6.1.1), the author addressed and mastered the two major challenges related to DMSO, which explain why it has been rarely used as a pure precursor solvent in the literature for any type of perovskite or coating technique: (i) dewetting of the precursor solution on subjacent layers, especially on the highly hydrophobic PTAA, due to the high σ and η of DMSO, resulting in inhomogeneous perovskite films; and (ii) its complex wet film quenching process due to the low p_{oi} and high BP of DMSO (see Table C.1). Moreover, the author compared trends in perovskite grain size, morphology, crystallinity, and elemental composition of samples fabricated from the toxic and green solvent system, revealing analogous results. Thus, PSCs blade coated from the pure green solvent DMSO achieve a device performance of up to 16.7 % PCE comparable to the ones from the toxic DMF:DMSO mixture (16.9 %). Thereby, the author showed that the use of toxic DMF is unnecessary [413].

In conclusion, the concept of replacing the commonly used toxic DMF as a precursor solution solvent or as a component in solvent mixtures by merely green DMSO discloses a pioneering route for perovskite deposition by scalable printing techniques such as blade coating. Consequently, this study provides a promising pathway to bring environmentally friendly solution processing of PSCs closer to industrial realization and application [413].

In addition, slot-die coating was implemented and optimized for processing MC perovskite layers. Thereby, gas-assisted perovskite conversion was combined with the slot-die coating pro-

cess, however, still using the toxic DMF:DMSO mixture as perovskite precursor solvent system. Nevertheless, by additive engineering and defect passivation strategies a PCE of 17.6 % of a PSC with a slot-die coated absorber was reached.
The presented results indicate that the performance of PSCs based on slot-die coated MC perovskite lag behind the one of their blade coated counterpart. Furthermore, an additional PEAI passivation layer on top of the slot-die coated double-cation perovskite layer is a useful tool to drastically increase the solar cell PCE. This is mainly caused by an increase in FF and V_{OC} highly likely attributed to the defect passivation effect. The PEAI layer can be clearly detected at the perovskite surface via TOF-SIMS measurements [414]. To conclude, the author assumes that PSCs with slot-die coated perovskite can only reach competitive PCE values when utilizing an additional passivation strategy [359, 383, 419].
Moreover, the addition of FACl in the perovskite precursor solution applied in PSCs based on the slot-die coated double-cation perovskite absorber slightly increases J_{SC} values, however, hysteresis, especially in combination with an additional PEAI layer, enhances as well. Furthermore, the average grain size is enlarged by the use of FACl. PSC device stacks with FACl blended in the perovskite precursor solution exhibit an increased Cl^- ion concentration toward the ITO/PTAA interface as TOF-SIMS results indicated [414]. In conclusion, similar to $PbCl_2$ (Subsection 5.2.2), FACl as perovskite precursor solution additive might remain a useful tool in the future in order to increase the in general smaller grain sizes for the gas- compared to the heat-assisted perovskite conversion (Subsection 2.2.2).

In summary, Chapter 6 highlighted that gas-assisted perovskite conversion is suitable for solution processing of double-cation perovskite thin films with well defined morphology and appears to be appropriate to convert green DMSO as pure precursor solvent, which exhibits the lowest p_{oi} of all typical polar precursor solution solvents for PSC production (Table C.1), and to be combined with slot-die coating. Consequently, gas-assisted perovskite conversion is a promising method to upscale solution processing of not only MAPI (Chapter 5) but also MC perovskite by scalable and sustainable techniques for solar cell application.

The following Chapter 7 summarizes this thesis and gives an outlook.

7 Summary and outlook

This chapter summarizes this thesis (Section 7.1) and gives an outlook and perspectives (Section 7.2).

7.1 Summary

To date, hybrid organic-inorganic metal-halide perovskite solar cells (PSCs) achieve a record power conversion efficiency (PCE) of >25 %. Besides their stability and toxicity, upscaling the deposition of homogeneous perovskite absorber layers from small lab scale (~0.1 cm^2) and their fabrication mainly by hardly scalable deposition techniques to large areas (≥100 cm^2) and via industry-relevant processes is one of the major challenges of the PSC technology. In order to enable its commercialization, this challenge needs to be addressed. On this account, this thesis deals with the subject of solution processing of hybrid perovskite layers by scalable and sustainable techniques in order to be applied in solar cells.

In this thesis, a focus was set on the two perovskite conversion methods of heat- and gas-assisted conversion out of the four well-known methods to remove the solvent from the wet film and consequently converting it to a thin dry crystallized layer, since they are identified as the techniques with the largest potential for upscaling.

With the aid of an in-depth study, the heat-assisted conversion method was found to be less suitable for upscaling the perovskite deposition via solution processing for $MAPbI_3$ (MAPI) based solar cells fabricated by means of blade coating (BC) due to wet film fluid dynamics and poor process controllability. Furthermore, it was shown that the use of a surfactant in the perovskite precursor solution improves the morphology of the perovskite film but also results in detrimental consequences during the subsequent processing of the remaining layers in the device stack.

However, gas-assisted conversion after BC via a static low-pressure gas system is found to be superior for controlling the perovskite morphology and for upscaling. The reason for that is the fact that each individual processing step of precursor solution deposition, drying inducing the nucleation, and the crystallization is, in contrast to the heat-assisted conversion method, decoupled from each other. This ensures high process controllability of each processing step and thus improved process reproducibility. Furthermore, it was shown that the MAPI perovskite morphology can be optimized by means of a blade coated nanoparticle (NP) wetting agent and composition engineering of the perovskite precursor solution via utilization of lead chloride ($PbCl_2$). By layer thickness optimizations, a further increase in the PSC champion PCE of up to ~18 % on a standard device area of 0.24 cm^2 was achieved. The author combined all engineering steps to prove the possibility of upscaling to a substrate area of ~80 cm^2. In addition, the thesis presents perovskite solar modules (PSMs) reaching a PCE of ~9 % on an aperture area of up to ~50 cm^2.

Aside from that, the author presented that the gas-assisted conversion is suitable for the scalable deposition of solvent systems to fabricate multi-cation (MC) perovskite layers. It was found that for this purpose a moving high-pressure gas system is required in order to achieve sufficient quenching of the perovskite precursor solution wet film. Therefore, this kind of gas system was established.
Moreover, the green and sustainable perovskite precursor solvent dimethyl sulfoxide (DMSO) is implemented for the first time resulting in comparable performances to the toxic counterpart of ~17 % of PSCs on 0.24 cm^2 device area with a blade coated double-cation absorber. Thus, it is highlighted that the use of toxic solvents such as the widely-used dimethylformamide (DMF) can be avoided.
In addition, gas assisted conversion in combination with the, compared to BC, even more industry-relevant deposition technique of slot-die coating was implemented. Aside from that, this deposition technique is optimized by means of precursor solution additive engineering with formamidinium chloride (FACl) and by a defect passivation strategy via an additional layer of phenethylammonium iodide (PEAI) on top of the absorber. Consequently, this work showed that PSCs with slot-die coated double-cation perovskite exhibit PCE values of >17 % on 0.24 cm^2 device area.

In summary, this thesis overall indicated that the gas-assisted perovskite conversion is a promising method for upscaling solution processing of hybrid perovskite by scalable and sustainable techniques for the application in solar cells.

7.2 Outlook and perspectives

Although this thesis clearly indicated the gas-assisted perovskite conversion as promising method for upscaling PSCs, further general improvements are still possible and should be addressed at the soonest. The outlook below presents a few of various strategic paths for improving solution processing of hybrid perovskite by scalable and sustainable techniques for the application in solar cells in the future.

Future work could be dedicated to replace ITO as TCO with a hydrogen-doped indium oxide (IO:H) front electrode which exhibits lower absorptance in the near-infrared (NIR) region and is expected to increase the transmittance of the PSC [34,35,444]. Furthermore, more cost-effective TCO alternatives should be evaluated in the future [243].

A combination of heat- and gas-assisted perovskite conversion might be a promising option for slot-die coating in the future as presented in literature [448, 498]. Thereby, only a mild temperature of 45 °C to 60 °C is required, which would be still considered as low-temperature processing. As mentioned in Section 6.4, the higher temperature might enable the harmonization of the slot-die coating and gas knife velocity, which is desirable for industrial R2R processing in the near future.

As mentioned in Section 6.4, perovskite solar cell production in ambient conditions with the use of green solvents or at least little use of toxic ones would probably be the ultimate goal for industrial solution processing.

This thesis showed that the module layout needs to be optimized due to a strong performance decrease when upscaling the substrate size (Subsection 5.4.2). The module layout should be altered, so that no etching step is necessary anymore. In the meantime, this new layout has been

already applied at ZSW. Moreover, it is necessary to analyze each of the three patterning steps in an in-depth study as mentioned in Subsection 5.4.2 in order to increase module performance and GFF [23] in the future.

Solvent engineering is of huge importance to develop scalable deposition techniques like blade and slot-die coating because the perovskite nucleation, crystallization, and crystal growth processes are strongly determined by the coordination behavior and ability between the perovskite precursor solvent and the precursor ion itself [42, 406]. The author suggests, that more effort should be made on in-situ investigations to monitor the formation of perovskite during blade and slot-die coating such as in-situ laser reflectometry [423], photoluminescence (PL) [424, 525] or GIXRD [526].
Ex-situ optical imaging for quantifying the large-area perovskite thin film morphology and homogeneity seems promising as well [527].
Such characterizations will provide a comprehensive understanding on the dynamics of each process of solution deposition, drying with nucleation, and crystallization with crystal growth of perovskite wet films with various solvents and compositions. Consequently, this understanding will favor the further development of upscaling the perovskite fabrication via solution processing.

By utilizing co-solvents with a lower BP and higher p_{oi} than DMF or DMSO and thereby a higher volatility, a faster gas-assisted perovskite conversion even at RT can be accomplished [375]. However, the majority of these solvents, such as ACN, 2-ME or tetrahydrofuran (THF), are toxic and exhibit low D_N values (see Table C.1), hence, a weak coordination capability to Pb^{2+} ions. Similar to adding alcohols [236, 237], the poor solubility of perovskite precursors in the mentioned solvents (Table C.1) is another issue [375] which would need to be addressed, if the strategy of these co-solvents is chosen.
In contrast to that, a completely different approach in combination with the gas-assisted perovskite conversion is solvent engineering via the so-called adduct or coordination procedure by adding DMSO, *N*-Methylpyrrolidone (NMP) or dimethylpropyleneurea (DMPU) in the precursor solution [375, 386], which exhibit high D_N values (Table C.1), hence, a strong coordination capability to Pb^{2+} ions. The adduct approach is a powerful technique to improve perovskite film quality by controlling the crystallization via a solid-state intermediate phase formation [299].
To benefit from both advantages, combining the two mentioned approaches seems to be promising for the gas-assisted perovskite conversion as presented by Deng et al. [375].

Although this thesis focuses on solution processing by scalable techniques to upscale hybrid perovskite deposition, the solar cell device A_{act} in this work of $0.24\,cm^2$ is still rather small. A_{act} of single cells need to be increased in future to at least $0.50\,cm^2$ or $1.00\,cm^2$ as first cut to further investigate the loss of device performance through upscaling (see Figure 1.1b). Besides the utilized TCO, this is mainly dependent on the absorber film homogeneity attained by the scalable and sustainable deposition techniques and gas-assisted perovskite conversion developed in this thesis.

Since perovskite layers are not fully homogeneous on $3 \times 9\,cm^2$ substrates after slot-die coating together with the gas-assisted perovskite conversion [414] and the slow or varying formation of the ink meniscus might be the cause for it, the author suggests to additionally blend a surfactant such as LP in the perovskite precursor solution to further improve its wetting on PTAA/SiO_2 NPs and therefore guarantee fast ink meniscus formation [419]. As mentioned in Subsection 4.2.2, the adsorption of the LP molecules at the annealed perovskite layer surface causing the detrimental procedural effects (Subsection 4.2.2) might in general not occur for the gas-assisted perovskite conversion.

In addition, homogeneity via solution processing is in general in need of improvement. Vapor phase deposition techniques under vacuum conditions such as sequential evaporation or co-evaporation are an entire diverse approach and might be more suitable compared to solution processing to achieve homogeneous perovskite films over large areas [23, 241].

Nevertheless, to take advantage of the perovskite thin film technology with low processing temperatures, solution processing of hybrid perovskite by scalable and sustainable techniques via gas-assisted perovskite conversion needs to be transferred from rigid to flexible substrates [375, 389, 390] in the near future.

Since the challenges of the new perovskite technology Pb toxicity and long- or short-term stability were not the focus of this work, they have not been highlighted in this thesis, although short-term stability was regularly tested for instance via performing MPP tracking. However, before a commercial application of perovskite solar cells, besides upscaling, these challenges need to be of course equally addressed in future.

The author expects gas-assisted perovskite conversion to play a significant role in upscaling perovskite solar cells via solution processing in future and thus enabling the quick transition of the photovoltaic technology into the generation of leading electricity source.

Appendices

A Understanding the heat-assisted perovskite conversion for MAPI based solar cells processed by blade coating

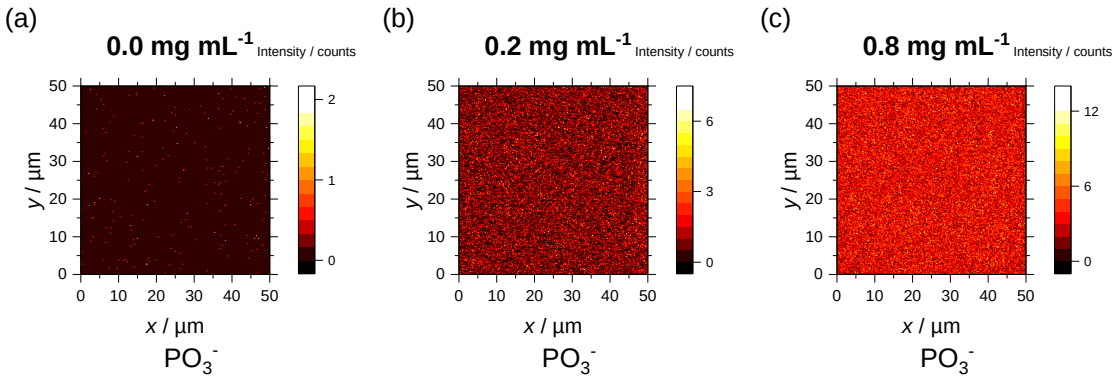

Figure A.1: TOF-SIMS top-view images of annealed perovskite layer spin coated on top of PEDOT:PSS with (a) 0.0 mg mL^{-1}, (b) 0.2 mg mL^{-1}, and (c) 0.8 mg mL^{-1} surfactant: PO_3^- fragment signal, which correspond to the functional group (phosphate) of the LP molecule (Figure 4.5).

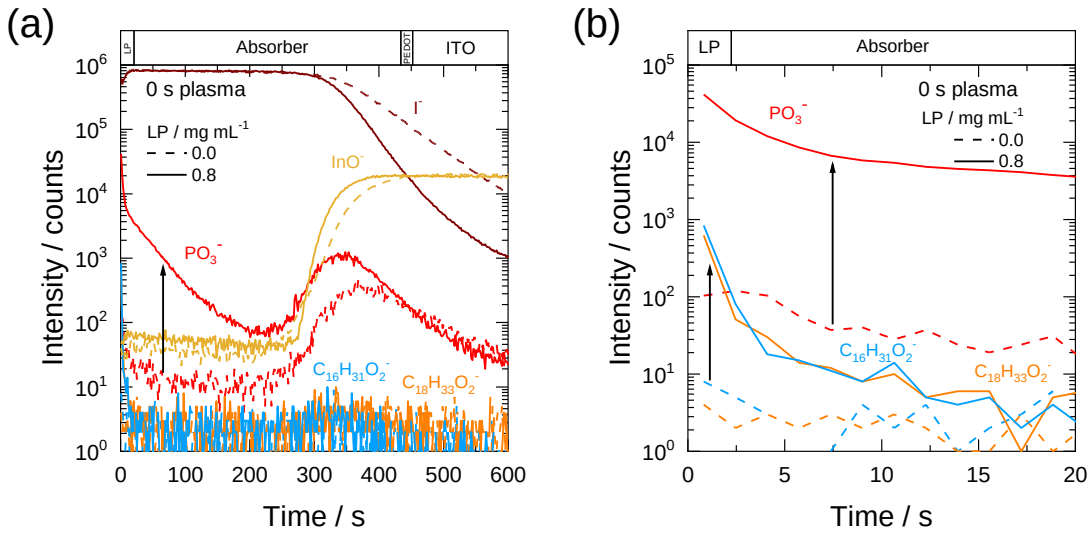

Figure A.2: TOF-SIMS depth profiles through samples of annealed perovskite layer spin coated on top of Glass/ ITO/PEDOT:PSS with and without 0.8 mg mL^{-1} surfactant with 0 s plasma on perovskite. All components in (b) correspond to the functional groups (phosphate, fatty acid tails) of the LP molecule (Figure 4.5).

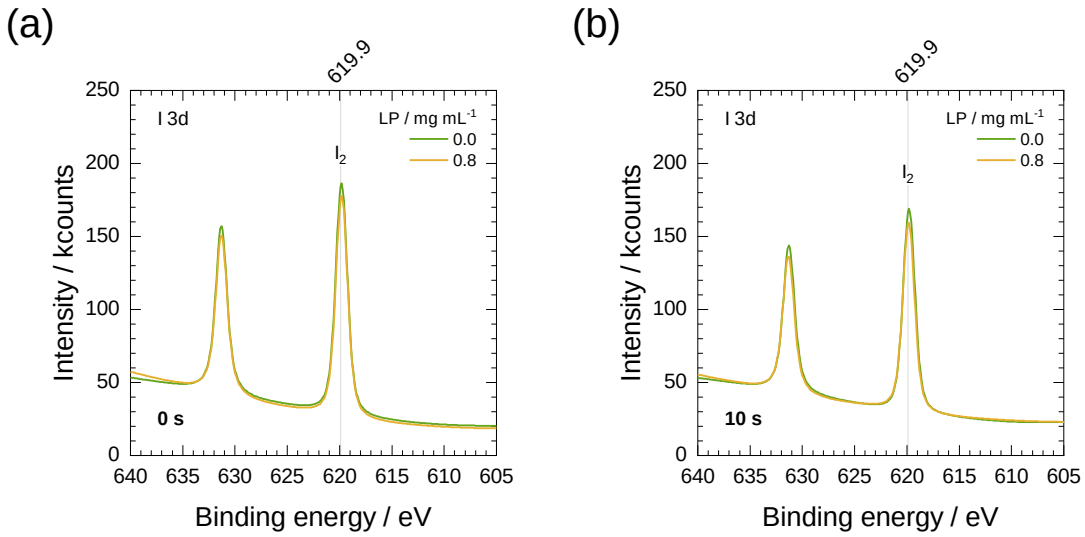

Figure A.3: XPS spectra of annealed perovskite layer spin coated on top of Glass/ITO/PEDOT:PSS (a) without and (b) with 10 s plasma (Ar, 20 W) treatment on the perovskite: Photoelectrons of I 3d.

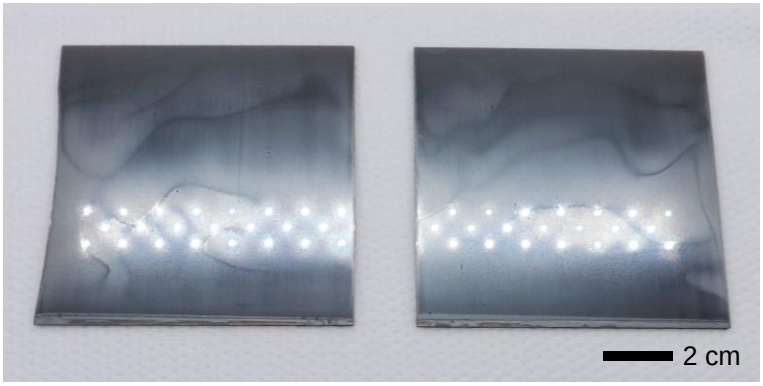

Figure A.4: Photographical image of two examples of annealed MAPI fabricated by blade coating and heat-assisted conversion perovskite films on $9 \times 9\,cm^2$ substrates on Glass/ITO/PEDOT:PSS viewed from top side. The drying features are clearly visible.

B Controlling perovskite morphology for upscaling blade coated MAPI based solar cells and modules

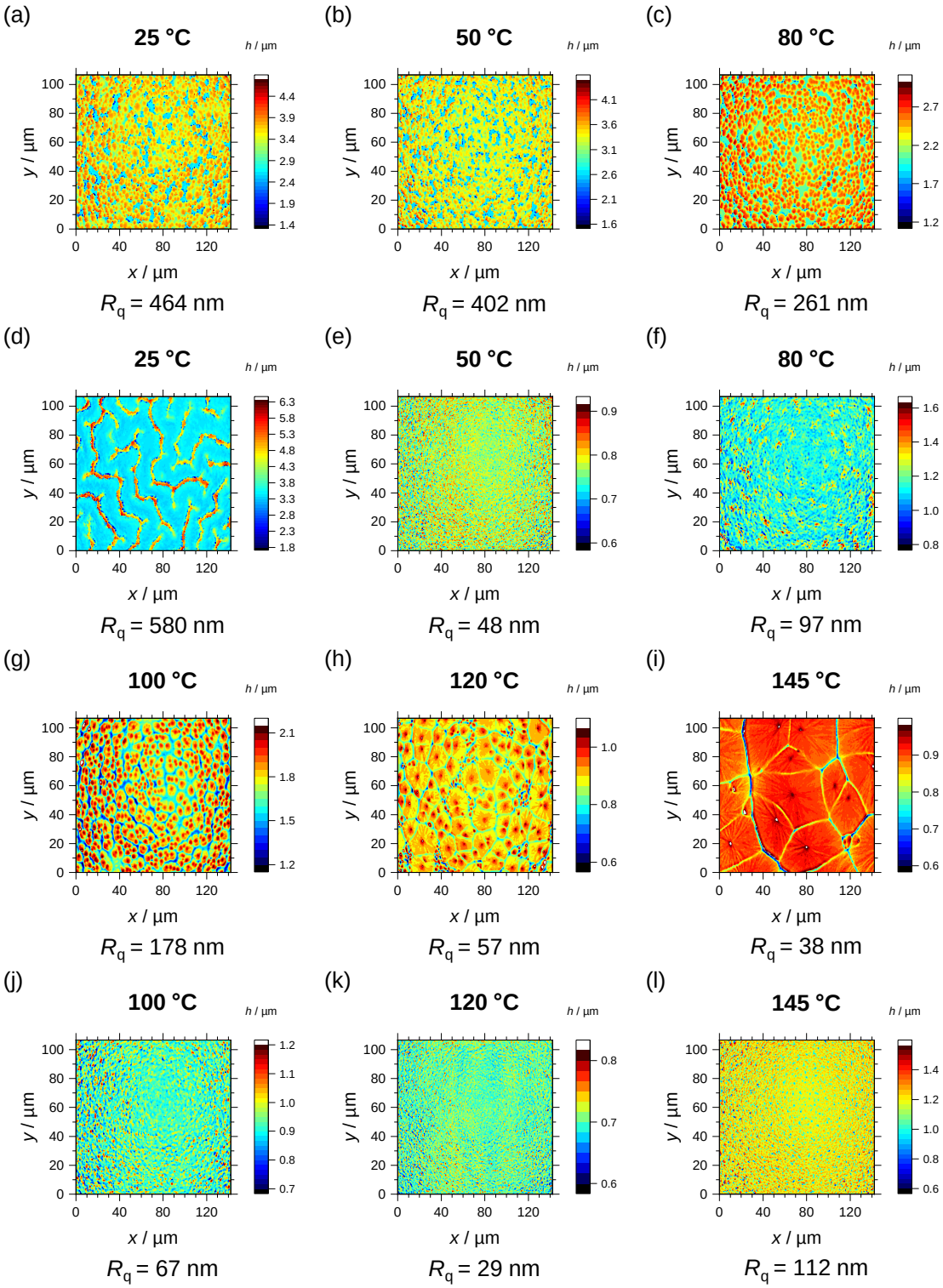

Figure B.1: CLSM top-view height images and R_q analysis of annealed perovskite layer blade coated on top of PEDOT:PSS (a-c, g-i) without and (d-f, j-l) with Q=40 L min^{-1} N_2 stream at different processing temperature with 0.2 mg mL^{-1} surfactant: (a, d) 25 °C, (b, e) 50 °C, (c, f) 80 °C, (g, j) 100 °C, (h, k) 120 °C, (i, l) 145 °C.

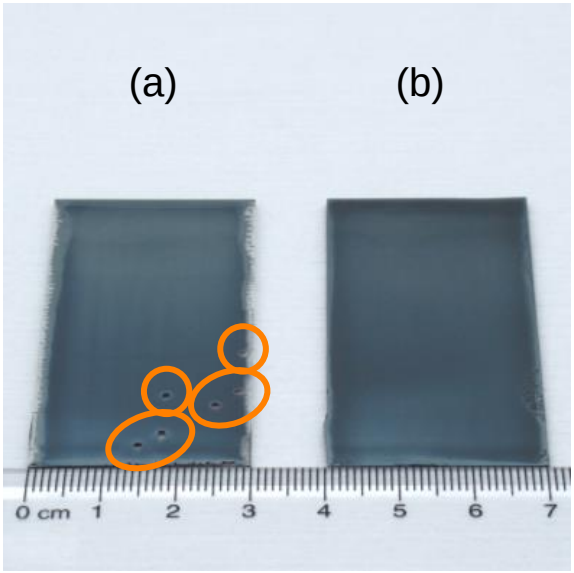

Figure B.2: Photographical image of annealed perovskite films on $3 \times 6\,\mathrm{cm}^2$ substrates on Glass/ITO/PTAA (a) without and (b) with SiO_2 NPs (0.9 wt%) at the PTAA/perovskite interface viewed from top side. Severe dewetting of the perovskite precursor solution causes shrinking of the wet film resulting in inhomogeneous perovskite layer at the edges of the substrate and huge pinholes in the film (circled in orange) as observed in case (a). In case (b), no dewetting and shrinkage occurs and a homogeneous perovskite film without pinholes can be deposited.

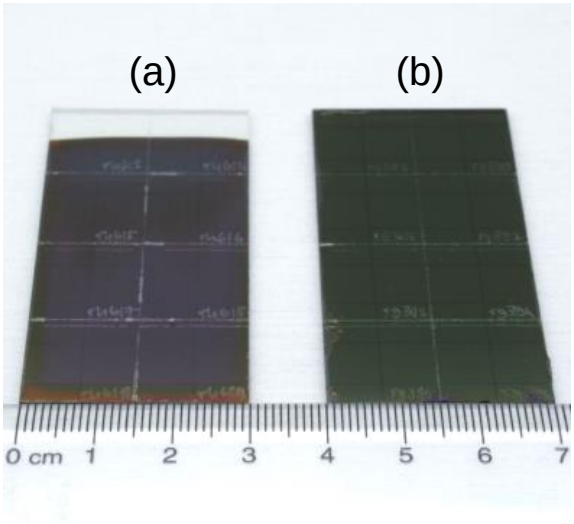

Figure B.3: Photographical image of annealed perovskite films on $3 \times 6\,\mathrm{cm}^2$ substrates on Glass/ITO/PTAA/SiO_2 NPs (a) without and (b) with 5 % $PbCl_2$ of the Pb source in the perovskite precursor solution viewed from the glass side. Void formation at the interface between PTAA/SiO_2 NPs and perovskite is easily observed indicated by a visible milky and grayish appearance in case (a). In case (b), no grayish appearance and therefore no voids are observed. Thus, a homogeneous perovskite layer with excellent contact to the PTAA/SiO_2 NPs is achieved.

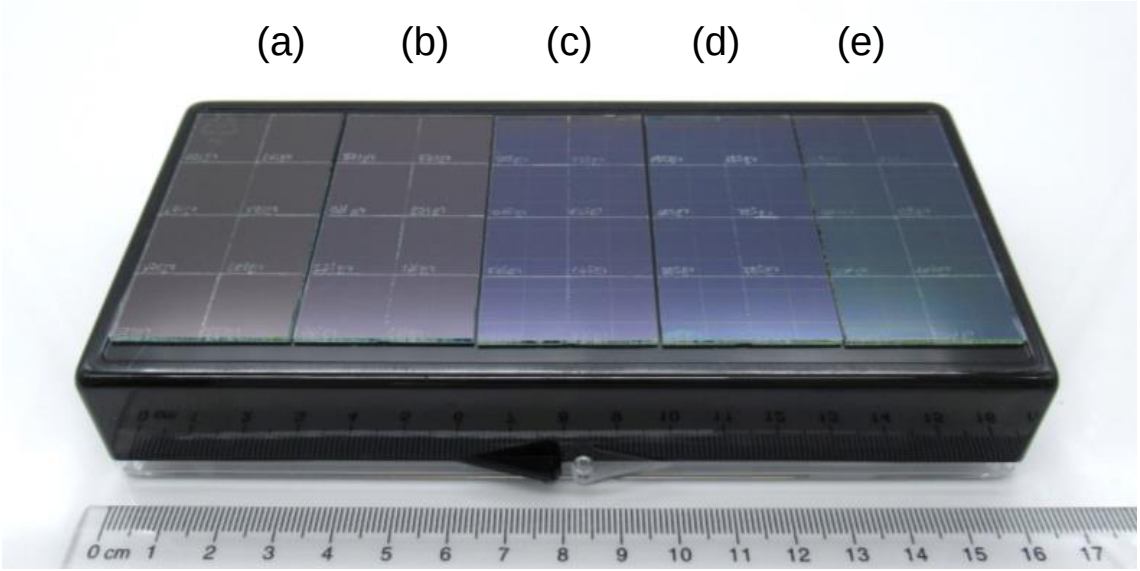

Figure B.4: Photographical image of annealed PTAA films on $3 \times 6\,\mathrm{cm}^2$ substrates blade coated from different concentrations in DCB on top of Glass/ITO at 50 °C substrate temperature viewed from top side. The concentration was tuned from (b) $5\,\mathrm{mg\,mL^{-1}}$ to (c) $10\,\mathrm{mg\,mL^{-1}}$, (d) $15\,\mathrm{mg\,mL^{-1}}$ and (e) $20\,\mathrm{mg\,mL^{-1}}$ correlating to a d of ~8 nm, 20 nm, 30 nm and 75 nm, respectively, while (a) shows pure Glass/ITO. The color appearance changes from (b) thin to (e) thick PTAA layer from purple over blue to green.

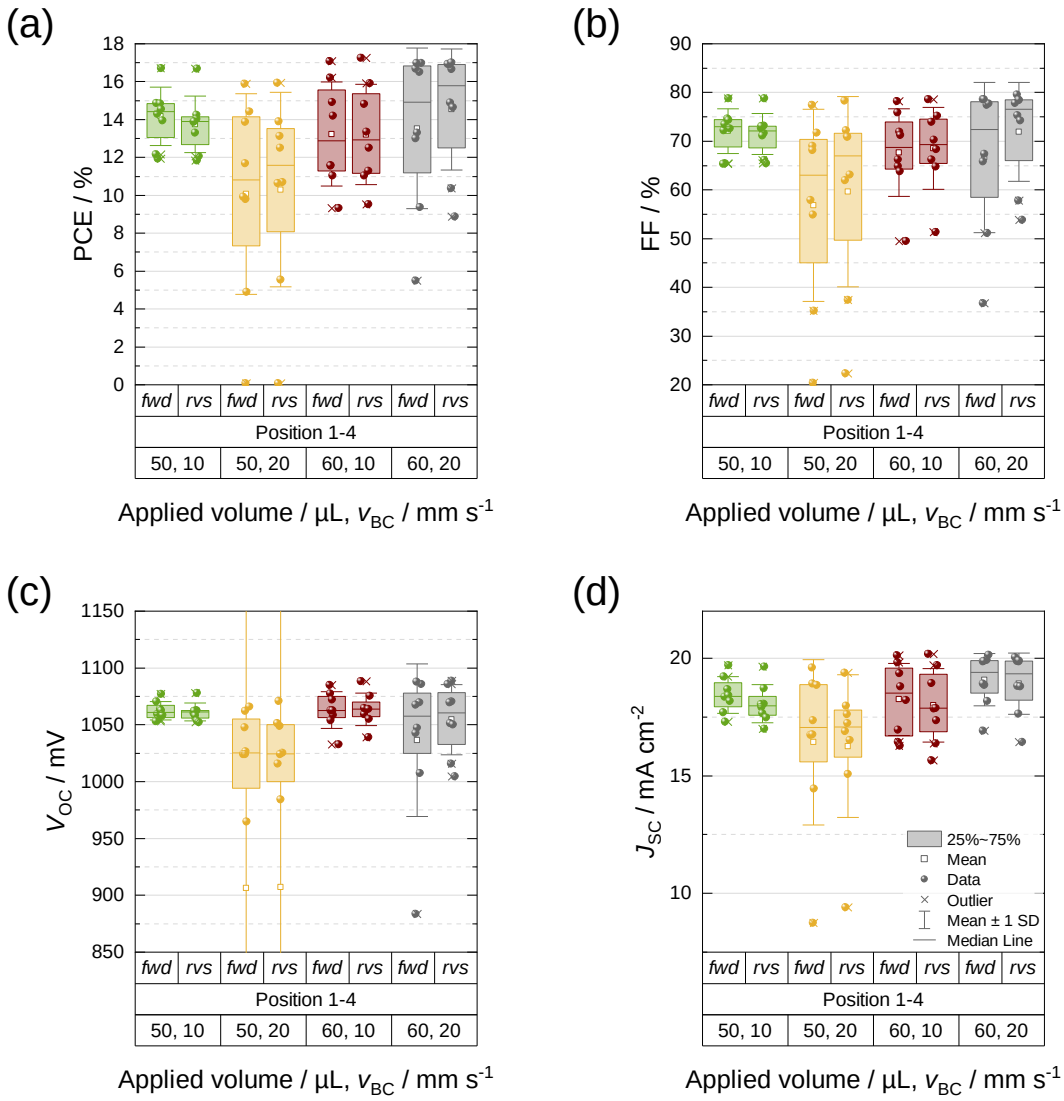

Figure B.5: Homogeneity study on $9 \times 9\,\mathrm{cm}^2$ substrates with four different perovskite coating parameter sets of applied volume and blade coating velocity v_{BC}: Box chart of (a) PCE, (b) FF, (c) V_{OC} and (d) J_{SC} of corresponding devices presented in Figure 5.23 combining all four positions on one $9 \times 9\,\mathrm{cm}^2$ substrate marked in Figure 5.22a. Shown values were measured in *fwd* and *rvs* scan directions.

C Evaluation of scalable perovskite deposition from suitable solvent systems for multi-cation perovskite solar cells

Table C.1: Overview of physical characteristics of typical polar precursor solution solvents for PSC production (ordered by D_N).

Name	BP / °C	p_{oi} / atm (25 °C)	D_N / kcal mol^{-1}	η / cP (25 °C)	ρ / g mL^{-1}	σ / mN m^{-1}	Protic or Aprotic	PbI_2 or MAI dissolution	Toxic
ACN	82	9.58×10^{-2}	14.1	0.34	0.776	28.4	aprotic	no	yes/ no
GBL	204	3.89×10^{-4}	18.0	1.7	1.129	44.6	aprotic	yes	yes
2-ME	124	8.12×10^{-3}	19.8	1.5	0.965	31.8	protic/ aprotic	no	yes
THF	66	2.28×10^{-1}	20.0	0.48	0.888	27.0	aprotic	little	yes
DMF	153	4.63×10^{-3}	26.6	0.92	0.948	35.2	aprotic	yes	yes
NMP	202	4.29×10^{-4}	27.3	1.67	1.028	40.8	aprotic	yes	yes
DMAC	165	2.61×10^{-3}	27.8	0.95	0.937	36.7	aprotic	yes	yes
DMI	225	1.64×10^{-4}	29.0	1.94	1.044	41.0	aprotic	no	yes
DMSO	189	8.18×10^{-4}	29.8	2.00	1.100	42.8	aprotic	yes	no
DEF	176	1.32×10^{-3}	30.9	N/A	0.908	27.8	aprotic	no	no
DMPU	246	1.53×10^{-4}	33.0	2.9	1.060	32.5	aprotic	yes	yes

Acetonitrile (ACN), γ–butyrolactone (GBL), 2-methoxyethanol (2-ME), tetrahydrofuran (THF), dimethylformamide (DMF), *N*-Methylpyrrolidone (NMP), dimethylacetamide (DMAC), dimethylimidazolidinone (DMI), dimethyl sulfoxide (DMSO), diethylformamide (DEF), dimethylpropyleneurea (DMPU).
Data from [22, 210, 235, 236, 238–240, 305, 375, 400, 413, 466, 470, 477, 483, 485, 486, 488, 489, 528–537].

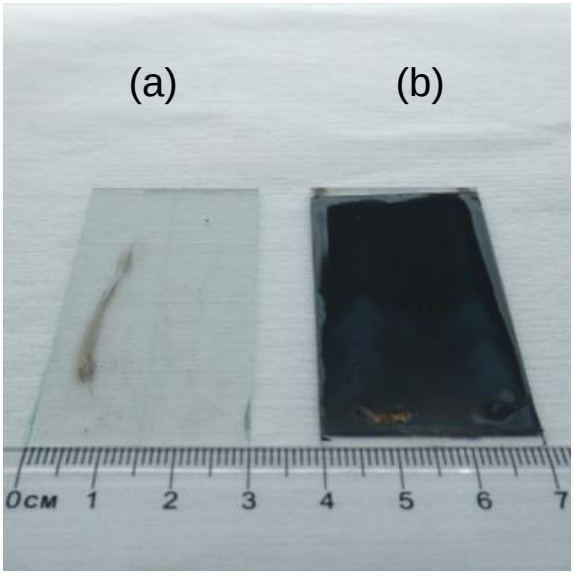

Figure C.1: Photographical image of annealed double-cation perovskite films blade coated from a pure DMSO solvent system on $3 \times 6\,cm^2$ substrates on Glass/ITO/PTAA (a) without and (b) with SiO_2 NPs (0.9 wt%) at the PTAA/perovskite interface viewed from top side. Severe dewetting and shrinking of the precursor solution is observed in case (a) which causes complete removal of the wet film resulting in an uncovered substrate. In case (b), no precursor solution dewetting and shrinkage occurs and a homogeneous perovskite film with full coverage and without pinholes can be deposited.

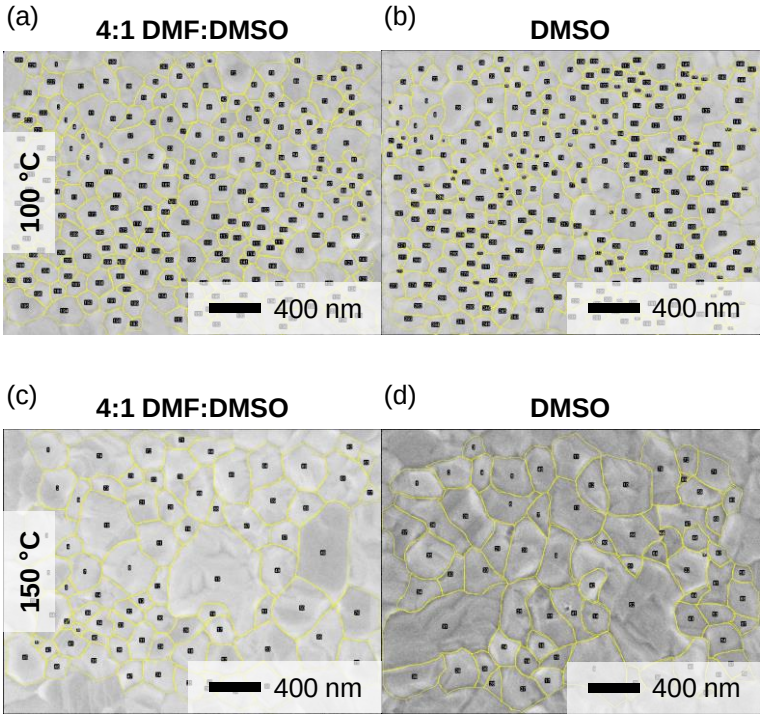

Figure C.2: Analysis of crystal grain size distribution of SEM top-view images of double-cation perovskite layers blade coated on ITO/PTAA/SiO_2 NPs from a precursor solution in different solvent systems and annealed at different temperatures assuming circular grains.

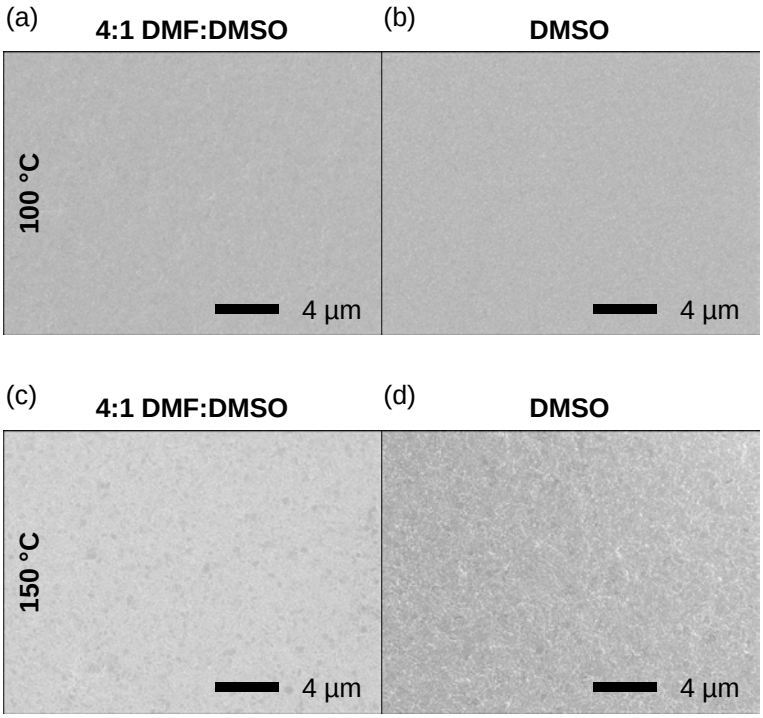

Figure C.3: SEM top-view images of double-cation perovskite layers blade coated on ITO/PTAA/SiO_2 NPs from a precursor solution in different solvent systems and annealed at different temperatures.

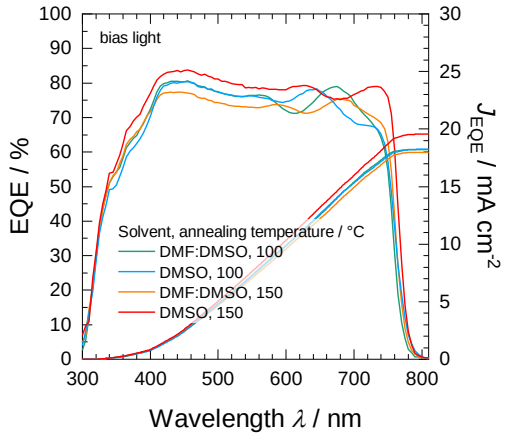

Figure C.4: Spectral evaluation of EQE of PSCs with a double-cation perovskite absorber blade coated from a precursor solution in different solvent systems and annealed at different temperatures (Figure 6.12) measured with a bias light.

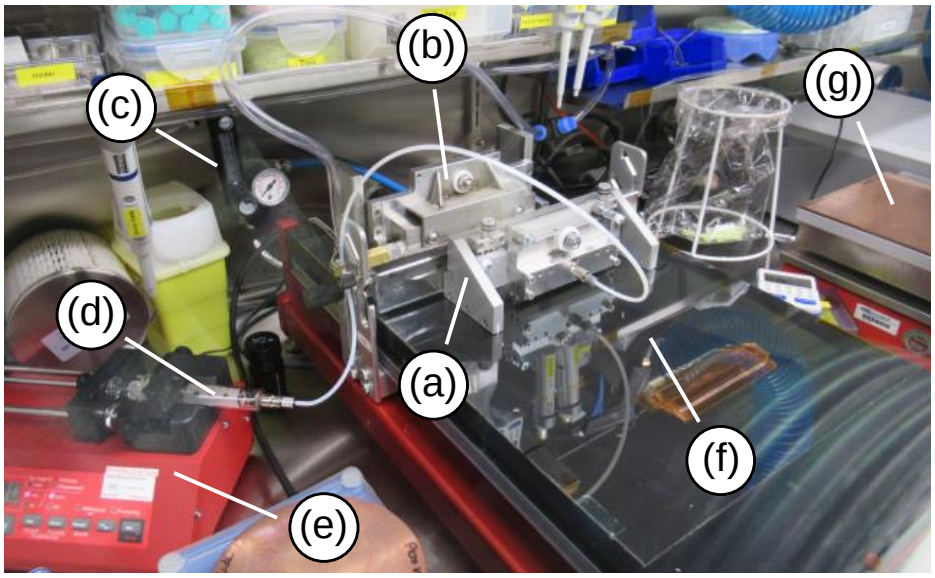

Figure C.5: Photographical image of the experimental setup for slot-die coating with gas-assisted perovskite conversion inside a glovebox: (a) sled with slot-die head, (b) sled with gas knife, (c) controls for p and Q of gas stream, (d) ink supply, (e) solution pumping system to control Q_{ink}, (f) coater plate, and (g) hot plate for annealing.

Bibliography

[1] R. Newell, D. Raimi, S. Villanueva, and B. Prest, "Global Energy Outlook 2021: Pathways from Paris," tech. rep., Resources for the Future (RFF), 2021.

[2] International Energy Agency (IEA), "World Energy Outlook 2020," tech. rep., International Energy Agency (IEA), 2020.

[3] International Renewable Energy Agency (IRENA), "Global energy transformation: A roadmap to 2050 (2019 edition)," tech. rep., International Renewable Energy Agency (IRENA), 2019.

[4] Working Group I Technical Support Unit, "Global warming of 1.5Â°C," tech. rep., Intergovernmental Panel on Climate Change (IPCC), 2019.

[5] Working Group I contribution to the Sixth Assessment Report of the Intergovernmental Panel on Climate Change, "Climate Change 2021 The Physical Science Basis," tech. rep., Intergovernmental Panel on Climate Change (IPCC), 2021.

[6] First Senate of the Federal Constitutional Court, "BVerfG, Order of the First Senate of 24 March 2021 - 1 BvR 2656/18 -, paras. 1-270," 2021.

[7] Conference of the Parties to the United Nations Framework Convention on Climate Change, "Paris Climate Agreement," tech. rep., Conference of the Parties to the United Nations Framework Convention on Climate Change, 2015.

[8] International Renewable Energy Agency (IRENA), "World Energy Transitions Outlook: 1.5Â°C Pathway," tech. rep., International Renewable Energy Agency (IRENA), 2021.

[9] International Renewable Energy Agency (IRENA), "Future of solar photovoltaic," tech. rep., International Renewable Energy Agency (IRENA), 2019.

[10] International Renewable Energy Agency (IRENA), "Global Renewables Outlook: Energy transformation 2050," tech. rep., International Renewable Energy Agency (IRENA), 2020.

[11] Fraunhofer ISE, "Photovoltaics Report 2021," tech. rep., Fraunhofer ISE, 2021.

[12] M. A. Green, E. D. Dunlop, J. Hohl-Ebinger, M. Yoshita, N. Kopidakis, and X. Hao, "Solar cell efficiency tables (Version 58)," *Prog. Photovoltaics Res. Appl.*, vol. 29, pp. 657–667, jul 2021.

[13] S. Kazim, M. K. Nazeeruddin, M. Grätzel, and S. Ahmad, "Perovskite as Light Harvester: A Game Changer in Photovoltaics," *Angew. Chemie Int. Ed.*, vol. 53, pp. 2812–2824, mar 2014.

[14] C. Ma and N.-G. Park, "A Realistic Methodology for 30% Efficient Perovskite Solar Cells," *Chem*, vol. 6, pp. 1254–1264, jun 2020.

[15] T. Wu, Z. Qin, Y. Wang, Y. Wu, W. Chen, S. Zhang, M. Cai, S. Dai, J. Zhang, J. Liu, Z. Zhou, X. Liu, H. Segawa, H. Tan, Q. Tang, J. Fang, Y. Li, L. Ding, Z. Ning, Y. Qi, Y. Zhang, and L. Han, "The Main Progress of Perovskite Solar Cells in 2020-2021," *Nano-Micro Lett.*, vol. 13, p. 152, dec 2021.

[16] NREL, "Best Research-Cell Efficiencies." https://www.nrel.gov/pv/assets/pdfs/best-research-cell-efficiencies-rev210726.pdf. Retrieved 2021-09-15, 2021.

[17] O. Almora, D. Baran, G. C. Bazan, C. Berger, C. I. Cabrera, K. R. Catchpole, S. Erten-Ela, F. Guo, J. Hauch, A. W. Y. Ho-Baillie, T. J. Jacobsson, R. A. J. Janssen, T. Kirchartz, N. Kopidakis, Y. Li, M. A. Loi, R. R. Lunt, X. Mathew, M. D. McGehee, J. Min, D. B. Mitzi, M. K. Nazeeruddin, J. Nelson, A. F. Nogueira, U. W. Paetzold, N. Park, B. P. Rand, U. Rau, H. J. Snaith, E. Unger, L. Vaillant-Roca, H. Yip, and C. J. Brabec, "Device Performance of Emerging Photovoltaic Materials (Version 1)," *Adv. Energy Mater.*, p. 2002774, dec 2020.

[18] O. Almora, D. Baran, G. C. Bazan, C. Berger, C. I. Cabrera, K. R. Catchpole, S. Erten-Ela, F. Guo, J. Hauch, A. W. Y. Ho-Baillie, T. J. Jacobsson, R. A. J. Janssen, T. Kirchartz, N. Kopidakis, Y. Li, M. A. Loi, R. R. Lunt, X. Mathew, M. D. McGehee, J. Min, D. B. Mitzi, M. K. Nazeeruddin, J. Nelson, A. F. Nogueira, U. W. Paetzold, N. Park, B. P. Rand, U. Rau, H. J. Snaith, E. Unger, L. Vaillant-Roca, H. Yip, and C. J. Brabec, "Device Performance of Emerging Photovoltaic Materials (Version 2)," *Adv. Energy Mater.*, p. 2102526, nov 2021.

[19] A. Kojima, K. Teshima, T. Miyasaka, and Y. Shirai, "Novel Photoelectrochemical Cell with Mesoscopic Electrodes Sensitized by Lead-Halide Compounds (2)," *ECS Meet. Abstr.*, 2006.

[20] A. Kojima, K. Teshima, Y. Shirai, and T. Miyasaka, "Organometal Halide Perovskites as Visible-Light Sensitizers for Photovoltaic Cells," *J. Am. Chem. Soc.*, vol. 131, pp. 6050–6051, may 2009.

[21] I. A. Howard, T. Abzieher, I. M. Hossain, H. Eggers, F. Schackmar, S. Ternes, B. S. Richards, U. Lemmer, and U. W. Paetzold, "Coated and Printed Perovskites for Photovoltaic Applications," *Adv. Mater.*, vol. 31, p. 1806702, jun 2019.

[22] R. Swartwout, M. T. Hoerantner, and V. Bulović, "Scalable Deposition Methods for Large-area Production of Perovskite Thin Films," *ENERGY Environ. Mater.*, vol. 2, pp. 119–145, jun 2019.

[23] D. B. Ritzer, T. Abzieher, A. Basibüyük, T. Feeney, F. Laufer, S. Ternes, B. S. Richards, S. Bergfeld, and U. W. Paetzold, "Upscaling of perovskite solar modules: The synergy of fully evaporated layer fabrication and all-laser-scribed interconnections," *Prog. Photovoltaics Res. Appl.*, nov 2021.

[24] Z. Saki, M. M. Byranvand, N. Taghavinia, M. Kedia, and M. Saliba, "Solution-Processed Perovskite Thin-films: The Journey from Lab- to Large-Scale Solar Cells," *Energy Environ. Sci.*, vol. 00, pp. 1–3, 2021.

[25] T. Bu, J. Li, H. Li, C. Tian, J. Su, G. Tong, L. K. Ono, C. Wang, Z. Lin, N. Chai, X.-L. Zhang, J. Chang, J. Lu, J. Zhong, W. Huang, Y. Qi, Y.-B. Cheng, and F. Huang, "Lead halide-templated crystallization of methylamine-free perovskite for efficient photovoltaic modules," *Science (80-.).*, vol. 372, pp. 1327–1332, jun 2021.

[26] J. Feng, Y. Jiao, H. Wang, X. Zhu, Y. Sun, M. Du, Y. Cao, D. Yang, and S. F. Liu, "High-throughput large-area vacuum deposition for high-performance formamidine-based perovskite solar cells," *Energy Environ. Sci.*, vol. 14, pp. 3035–3043, may 2021.

[27] S. M. P. Meroni, C. Worsley, D. Raptis, and T. M. Watson, "Triple-Mesoscopic Carbon Perovskite Solar Cells: Materials, Processing and Applications," *Energies*, vol. 14, p. 386, jan 2021.

[28] X. Xiao, M. Wang, S. Chen, Y. Zhang, H. Gu, Y. Deng, G. Yang, C. Fei, B. Chen, Y. Lin, M. D. Dickey, and J. Huang, "Lead-adsorbing ionogel-based encapsulation for impact-resistant, stable, and lead-safe perovskite modules," *Sci. Adv.*, vol. 7, pp. 8249–8278, oct 2021.

[29] G.-S. Han, H. S. Jung, and N.-G. Park, "Recent Cutting-edge Strategies for Flexible Perovskite Solar Cells Toward Commercialization," *Chem. Commun.*, 2021.

[30] J. F. Benitez-Rodriguez, D. Chen, M. Gao, and R. A. Caruso, "Roll-to-Roll Processes for the Fabrication of Perovskite Solar Cells under Ambient Conditions," *Sol. RRL*, vol. 5, p. 2100341, sep 2021.

[31] T.-Y. Yang, Y. Y. Kim, and J. Seo, "Roll-to-roll manufacturing toward lab-to-fab-translation of perovskite solar cells," *APL Mater.*, vol. 9, p. 110901, nov 2021.

[32] A. W. Y. Ho-Baillie, J. Zheng, M. A. Mahmud, F.-J. Ma, D. R. McKenzie, and M. A. Green, "Recent progress and future prospects of perovskite tandem solar cells," *Appl. Phys. Rev.*, vol. 8, p. 041307, dec 2021.

[33] J. Werner, B. Niesen, and C. Ballif, "Perovskite/Silicon Tandem Solar Cells: Marriage of Convenience or True Love Story? - An Overview," *Adv. Mater. Interfaces*, vol. 1700731, pp. 1–19, 2017.

[34] S. Moghadamzadeh, *Multi-Cation Perovskite Semiconductors for All-Perovskite Tandem Solar Cells*. PhD thesis, Karlsruhe Institute of Technology (KIT), 2021.

[35] M. Schultes, *Four-Terminal Perovskite-CIGS Tandem Solar Cells with Improved Near-Infrared Response*. Phd thesis, Karlsruhe Institute of Technology (KIT), 2019.

[36] G. M. Wilson, M. Al-Jassim, W. K. Metzger, S. W. Glunz, P. Verlinden, G. Xiong, L. M. Mansfield, B. J. Stanbery, K. Zhu, Y. Yan, J. J. Berry, A. J. Ptak, F. Dimroth, B. M. Kayes, A. C. Tamboli, R. Peibst, K. Catchpole, M. O. Reese, C. S. Klinga, P. Denholm, M. Morjaria, M. G. Deceglie, J. M. Freeman, M. A. Mikofski, D. C. Jordan, G. TamizhMani, and D. B. Sulas-Kern, "The 2020 photovoltaic technologies roadmap," *J. Phys. D. Appl. Phys.*, vol. 53, p. 493001, dec 2020.

[37] F. Huang, M. Li, P. Siffalovic, G. Cao, and J. Tian, "From scalable solution fabrication of perovskite films towards commercialization of solar cells," *Energy Environ. Sci.*, 2019.

[38] Y. Rong, Y. Hu, A. Mei, H. Tan, M. I. Saidaminov, S. I. Seok, M. D. McGehee, E. H. Sargent, and H. Han, "Challenges for commercializing perovskite solar cells," *Science (80-.).*, vol. 361, p. eaat8235, sep 2018.

[39] F. Wang, Y. Cao, C. Chen, Q. Chen, X. Wu, X. Li, T. Qin, and W. Huang, "Materials toward the Upscaling of Perovskite Solar Cells: Progress, Challenges, and Strategies," *Adv. Funct. Mater.*, vol. 1803753, p. 1803753, nov 2018.

[40] Z. Li, T. R. Klein, D. H. Kim, M. Yang, J. J. Berry, M. F. A. M. van Hest, and K. Zhu, "Scalable fabrication of perovskite solar cells," *Nat. Rev. Mater.*, vol. 3, p. 18017, apr 2018.

[41] L. Qiu, S. He, L. K. Ono, S. Liu, and Y. Qi, "Scalable Fabrication of Metal Halide Perovskite Solar Cells and Modules," *ACS Energy Lett.*, vol. 4, no. 9, pp. 2147–2167, 2019.

[42] Y. Cheng, Y. Peng, A. K.-Y. Jen, and H.-L. Yip, "Development and Challenges of Metal Halide Perovskite Solar Modules," *Sol. RRL*, p. 2100545, sep 2021.

[43] Z. Yang, Z. Liu, V. Ahmadi, W. Chen, and Y. Qi, "Recent Progress on Metal Halide Perovskite Solar Minimodules," *Sol. RRL*, p. 2100458, aug 2021.

[44] Z. Song, C. L. McElvany, A. B. Phillips, I. Celik, P. W. Krantz, S. C. Watthage, G. K. Liyanage, D. Apul, and M. J. Heben, "A technoeconomic analysis of perovskite solar module manufacturing with low-cost materials and techniques," *Energy Environ. Sci.*, vol. 10, pp. 1297–1305, jun 2017.

[45] Fraunhofer ISE, "Levelized Cost of Electricity Renewable Energy Technologies," tech. rep., Fraunhofer ISE, 2021.

[46] Metalgrass Ltd., "Perovskite companies: the comprehensive list." https://www.perovskite-info.com/companies. Retrieved 2021-09-19.

[47] Ascent Solar Technologies Inc., "Ascent Solar Signs Strategic Partnership and Long Term Supply Agreement with TubeSolar AG." https://www.ascentsolar.com/ir-asti-news-page.html?qmodStoryID=5436435964964320. Retrieved 2021-09-23, 2021.

[48] IEEE Spectrum, "Power From Commercial Perovskite Solar Cells Is Coming Soon." https://spectrum.ieee.org/power-from-commercial-perovskite-solar-cells-is-coming-soon. Retrieved 2021-09-21, 2019.

[49] C. Kamaraki, M. T. Klug, T. Green, L. Miranda Perez, and C. Case, "Perovskite/silicon tandem photovoltaics: Technological disruption without business disruption," *Appl. Phys. Lett.*, vol. 119, p. 070501, aug 2021.

[50] Solar Energy Technologies Office, "Solar Energy Technologies Office Fiscal Year 2020 Perovskite Funding Program," tech. rep., Solar Energy Technologies Office, 2021.

[51] F. C. Krebs, "Fabrication and processing of polymer solar cells: A review of printing and coating techniques," *Sol. Energy Mater. Sol. Cells*, vol. 93, pp. 394–412, apr 2009.

[52] K. Bruening, B. Dou, J. Simonaitis, Y.-Y. Lin, M. F. van Hest, and C. J. Tassone, "Scalable Fabrication of Perovskite Solar Cells to Meet Climate Targets," *Joule*, vol. 2, pp. 2464–2476, nov 2018.

[53] Y. Vaynzof, "The Future of Perovskite Photovoltaics-Thermal Evaporation or Solution Processing?," *Adv. Energy Mater.*, vol. 10, p. 2003073, dec 2020.

[54] G. Rose, "Ueber einige neue Mineralien des Urals," *J. fi¿½r Prakt. Chemie*, vol. 19, pp. 459–468, jan 1840.

[55] P. Wang, Y. Wu, B. Cai, Q. Ma, X. Zheng, and W. Zhang, "Solution-Processable Perovskite Solar Cells toward Commercialization: Progress and Challenges," *Adv. Funct. Mater.*, vol. 1807661, p. 1807661, apr 2019.

[56] J.-P. Correa-Baena, A. Abate, M. Saliba, W. Tress, T. Jesper Jacobsson, M. Grätzel, and A. Hagfeldt, "The rapid evolution of highly efficient perovskite solar cells," *Energy Environ. Sci.*, vol. 10, pp. 710–727, mar 2017.

[57] M. Saliba, "Polyelemental, Multicomponent Perovskite Semiconductor Libraries through Combinatorial Screening," *Adv. Energy Mater.*, vol. 9, p. 1803754, jul 2019.

[58] F. Yang, D. Jang, L. Dong, S. Qiu, A. Distler, N. Li, C. J. Brabec, and H. Egelhaaf, "Upscaling Solution-Processed Perovskite Photovoltaics," *Adv. Energy Mater.*, p. 2101973, oct 2021.

[59] C. Li, X. Lu, W. Ding, L. Feng, Y. Gao, and Z. Guo, "Formability of ABX 3 (X = F, Cl, Br, I) halide perovskites," *Acta Crystallogr. Sect. B Struct. Sci.*, vol. 64, pp. 702–707, dec 2008.

[60] V. M. Goldschmidt, "Die Gesetze der Krystallochemie," *Naturwissenschaften*, vol. 14, pp. 477–485, may 1926.

[61] Q. Xu, D. Yang, J. Lv, Y.-Y. Sun, and L. Zhang, "Perovskite Solar Absorbers: Materials by Design," *Small Methods*, vol. 2, p. 1700316, may 2018.

[62] M. A. Green, A. Ho-Baillie, and H. J. Snaith, "The emergence of perovskite solar cells," *Nat. Photonics*, vol. 8, pp. 506–514, jul 2014.

[63] R. J. Tilley, *Perovskites: Structure-Property Relationships*. John Wiley and Sons, 2016.

[64] K. Korshunova, L. Winterfeld, W. J. D. Beenken, and E. Runge, "Thermodynamic stability of mixed Pb:Sn methyl-ammonium halide perovskites," *Phys. status solidi*, vol. 253, pp. 1907–1915, oct 2016.

[65] R. L. Milot, G. E. Eperon, H. J. Snaith, M. B. Johnston, and L. M. Herz, "Temperature-Dependent Charge-Carrier Dynamics in CH 3 NH 3 PbI 3 Perovskite Thin Films," *Adv. Funct. Mater.*, vol. 25, pp. 6218–6227, oct 2015.

[66] W. Geng, L. Zhang, Y.-N. Zhang, W.-M. Lau, and L.-M. Liu, "First-Principles Study of Lead Iodide Perovskite Tetragonal and Orthorhombic Phases for Photovoltaics," *J. Phys. Chem. C*, vol. 118, pp. 19565–19571, aug 2014.

[67] Z. Li, M. Yang, J.-S. Park, S.-H. Wei, J. J. Berry, and K. Zhu, "Stabilizing Perovskite Structures by Tuning Tolerance Factor: Formation of Formamidinium and Cesium Lead Iodide Solid-State Alloys," *Chem. Mater.*, vol. 28, pp. 284–292, jan 2016.

[68] N. G. Park, "Perovskite solar cells: An emerging photovoltaic technology," *Mater. Today*, vol. 18, no. 2, pp. 65–72, 2015.

[69] W.-J. Yin, J.-H. Yang, J. Kang, Y. Yan, and S.-h. Wei, "Halide perovskite materials for solar cells: a theoretical review," *J. Mater. Chem. A*, vol. 3, no. 17, pp. 8926–8942, 2015.

[70] S. De Wolf, J. Holovsky, S.-J. Moon, P. Löper, B. Niesen, M. Ledinsky, F.-j. Haug, J.-h. Yum, and C. Ballif, "Organometallic Halide Perovskites: Sharp Optical Absorption Edge and Its Relation to Photovoltaic Performance," *J. Phys. Chem. Lett.*, vol. 5, pp. 1035–1039, mar 2014.

[71] E. T. Hoke, D. J. Slotcavage, E. R. Dohner, A. R. Bowring, H. I. Karunadasa, and M. D. McGehee, "Reversible photo-induced trap formation in mixed-halide hybrid perovskites for photovoltaics," *Chem. Sci.*, vol. 6, pp. 613–617, jan 2015.

[72] W.-J. Yin, T. Shi, and Y. Yan, "Unique Properties of Halide Perovskites as Possible Origins of the Superior Solar Cell Performance," *Adv. Mater.*, vol. 26, pp. 4653–4658, jul 2014.

[73] A. Miyata, A. Mitioglu, P. Plochocka, O. Portugall, J. T.-W. Wang, S. D. Stranks, H. J. Snaith, and R. J. Nicholas, "Direct measurement of the exciton binding energy and effective masses for charge carriers in organic-inorganic tri-halide perovskites," *Nat. Phys.*, vol. 11, pp. 582–587, jul 2015.

[74] K. Galkowski, A. Mitioglu, A. Miyata, P. Plochocka, O. Portugall, G. E. Eperon, J. T.-W. Wang, T. Stergiopoulos, S. D. Stranks, H. J. Snaith, and R. J. Nicholas, "Determination of the exciton binding energy and effective masses for methylammonium and formamidinium lead tri-halide perovskite semiconductors," *Energy Environ. Sci.*, vol. 9, pp. 962–970, mar 2016.

[75] Y. Yamada, T. Nakamura, M. Endo, A. Wakamiya, and Y. Kanemitsu, "Photoelectronic Responses in Solution-Processed Perovskite CH3NH3PbI3 Solar Cells Studied by Photoluminescence and Photoabsorption Spectroscopy," *IEEE J. Photovoltaics*, vol. 5, pp. 401–405, jan 2015.

[76] F. Ruf, A. Magin, M. Schultes, E. Ahlswede, H. Kalt, and M. Hetterich, "Excitonic nature of optical transitions in electroabsorption spectra of perovskite solar cells," *Appl. Phys. Lett.*, vol. 112, p. 083902, feb 2018.

[77] D. W. de Quilettes, S. M. Vorpahl, S. D. Stranks, H. Nagaoka, G. E. Eperon, M. E. Ziffer, H. J. Snaith, and D. S. Ginger, "Impact of microstructure on local carrier lifetime in perovskite solar cells," *Science (80-.).*, vol. 348, pp. 683–686, may 2015.

[78] L. M. Herz, "Charge-Carrier Mobilities in Metal Halide Perovskites: Fundamental Mechanisms and Limits," *ACS Energy Lett.*, vol. 2, pp. 1539–1548, jul 2017.

[79] Y. Chen, H. T. Yi, X. Wu, R. Haroldson, Y. N. Gartstein, Y. I. Rodionov, K. S. Tikhonov, A. Zakhidov, X. Y. Zhu, and V. Podzorov, "Extended carrier lifetimes and diffusion in hybrid perovskites revealed by Hall effect and photoconductivity measurements," *Nat. Commun.*, vol. 7, p. 12253, nov 2016.

[80] S. D. Stranks, G. E. Eperon, G. Grancini, C. Menelaou, M. J. P. Alcocer, T. Leijtens, L. M. Herz, A. Petrozza, and H. J. Snaith, "Electron-Hole Diffusion Lengths Exceeding 1 Micrometer in an Organometal Trihalide Perovskite Absorber," *Science (80-.).*, vol. 342, pp. 341–344, oct 2013.

[81] G. Xing, N. Mathews, S. Sun, S. S. Lim, Y. M. Lam, M. Gratzel, S. Mhaisalkar, and T. C. Sum, "Long-Range Balanced Electron- and Hole-Transport Lengths in Organic-Inorganic CH3NH3PbI3," *Science (80-.).*, vol. 342, pp. 344–347, oct 2013.

[82] J. M. Ball, M. M. Lee, A. Hey, and H. J. Snaith, "Low-temperature processed meso-superstructured to thin-film perovskite solar cells," *Energy Environ. Sci.*, vol. 6, p. 1739, jun 2013.

[83] F. Li, C. Ma, H. Wang, W. Hu, W. Yu, A. D. Sheikh, and T. Wu, "Ambipolar solution-processed hybrid perovskite phototransistors," *Nat. Commun.*, vol. 6, p. 8238, nov 2015.

[84] G. Giorgi, J.-I. Fujisawa, H. Segawa, and K. Yamashita, "Small Photocarrier Effective Masses Featuring Ambipolar Transport in Methylammonium Lead Iodide Perovskite: A Density Functional Analysis," *J. Phys. Chem. Lett.*, vol. 4, pp. 4213–4216, dec 2013.

[85] G. E. Eperon, S. D. Stranks, C. Menelaou, M. B. Johnston, L. M. Herz, and H. J. Snaith, "Formamidinium lead trihalide: a broadly tunable perovskite for efficient planar heterojunction solar cells," *Energy Environ. Sci.*, vol. 7, no. 3, p. 982, 2014.

[86] R. Prasanna, A. Gold-Parker, T. Leijtens, B. Conings, A. Babayigit, H.-G. Boyen, M. F. Toney, and M. D. McGehee, "Band Gap Tuning via Lattice Contraction and Octahedral Tilting in Perovskite Materials for Photovoltaics," *J. Am. Chem. Soc.*, vol. 139, pp. 11117–11124, aug 2017.

[87] F. Brivio, A. B. Walker, and A. Walsh, "Structural and electronic properties of hybrid perovskites for high-efficiency thin-film photovoltaics from first-principles," *APL Mater.*, vol. 1, p. 042111, oct 2013.

[88] T. Baikie, Y. Fang, J. M. Kadro, M. Schreyer, F. Wei, S. G. Mhaisalkar, M. Graetzel, and T. J. White, "Synthesis and crystal chemistry of the hybrid perovskite (CH3NH3)PbI3 for solid-state sensitised solar cell applications," *J. Mater. Chem. A*, vol. 1, no. 18, p. 5628, 2013.

[89] V. Sarritzu, N. Sestu, D. Marongiu, X. Chang, Q. Wang, S. Masi, S. Colella, A. Rizzo, A. Gocalinska, E. Pelucchi, M. L. Mercuri, F. Quochi, M. Saba, A. Mura, and G. Bongiovanni, "Direct or Indirect Bandgap in Hybrid Lead Halide Perovskites?," *Adv. Opt. Mater.*, vol. 6, p. 1701254, may 2018.

[90] J. M. Richter, K. Chen, A. Sadhanala, J. Butkus, J. P. H. Rivett, R. H. Friend, B. Monserrat, J. M. Hodgkiss, and F. Deschler, "Direct Bandgap Behavior in Rashba-Type Metal Halide Perovskites," *Adv. Mater.*, vol. 30, p. 1803379, dec 2018.

[91] D. W. DeQuilettes, K. Frohna, D. Emin, T. Kirchartz, V. Bulovic, D. S. Ginger, and S. D. Stranks, "Charge-Carrier Recombination in Halide Perovskites," *Chem. Rev.*, vol. 119, pp. 11007–11019, oct 2019.

[92] T. Wang, B. Daiber, J. M. Frost, S. A. Mann, E. C. Garnett, A. Walsh, and B. Ehrler, "Indirect to direct bandgap transition in methylammonium lead halide perovskite," *Energy Environ. Sci.*, vol. 10, pp. 509–515, feb 2017.

[93] T. Kirchartz and U. Rau, "Decreasing Radiative Recombination Coefficients via an Indirect Band Gap in Lead Halide Perovskites," *J. Phys. Chem. Lett.*, vol. 8, pp. 1265–1271, mar 2017.

[94] E. M. Hutter, M. C. Gélvez-Rueda, A. Osherov, V. Bulović, F. C. Grozema, S. D. Stranks, and T. J. Savenije, "Direct-indirect character of the bandgap in methylammonium lead iodide perovskite," *Nat. Mater.*, vol. 16, pp. 115–120, jan 2017.

[95] X. Ke, J. Yan, A. Zhang, B. Zhang, and Y. Chen, "Optical band gap transition from direct to indirect induced by organic content of CH 3 NH 3 PbI 3 perovskite films," *Appl. Phys. Lett.*, vol. 107, p. 091904, aug 2015.

[96] S. Meloni, G. Palermo, N. Ashari-Astani, M. Grätzel, and U. Rothlisberger, "Valence and conduction band tuning in halide perovskites for solar cell applications," *J. Mater. Chem. A*, vol. 4, pp. 15997–16002, oct 2016.

[97] I. Borriello, G. Cantele, and D. Ninno, "Ab initio investigation of hybrid organic-inorganic perovskites based on tin halides," *Phys. Rev. B*, vol. 77, p. 235214, jun 2008.

[98] F. Chiarella, A. Zappettini, F. Licci, I. Borriello, G. Cantele, D. Ninno, A. Cassinese, and R. Vaglio, "Combined experimental and theoretical investigation of optical, structural, and electronic properties of CH3NH3SnX3 thin films (X=Cl,Br)," *Phys. Rev. B*, vol. 77, p. 045129, jan 2008.

[99] J.-S. Park, S. Choi, Y. Yan, Y. Yang, J. M. Luther, S.-H. Wei, P. Parilla, and K. Zhu, "Electronic Structure and Optical Properties of α-CH 3 NH 3 PbBr 3 Perovskite Single Crystal," *J. Phys. Chem. Lett.*, vol. 6, pp. 4304–4308, nov 2015.

[100] J. H. Noh, S. H. Im, J. H. Heo, T. N. Mandal, and S. I. Seok, "Chemical Management for Colorful, Efficient, and Stable Inorganic-Organic Hybrid Nanostructured Solar Cells," *Nano Lett.*, vol. 13, pp. 1764–1769, apr 2013.

[101] D. M. Jang, K. Park, D. H. Kim, J. Park, F. Shojaei, H. S. Kang, J.-P. Ahn, J. W. Lee, and J. K. Song, "Reversible Halide Exchange Reaction of Organometal Trihalide Perovskite Colloidal Nanocrystals for Full-Range Band Gap Tuning," *Nano Lett.*, vol. 15, pp. 5191–5199, aug 2015.

[102] E. L. Unger, L. Kegelmann, K. Suchan, D. Sörell, L. Korte, and S. Albrecht, "Roadmap and roadblocks for the band gap tunability of metal halide perovskites," *J. Mater. Chem. A*, vol. 5, pp. 11401–11409, jun 2017.

[103] I. M. Hossain, *Semitransparent perovskite solar cells for perovskite-based tandem photovoltaics*. PhD thesis, Karlsruhe Institute of Technology (KIT), 2020.

[104] Y. Yu, D. Zhao, C. R. Grice, W. Meng, C. Wang, W. Liao, A. J. Cimaroli, H. Zhang, K. Zhu, and Y. Yan, "Thermally evaporated methylammonium tin triiodide thin films for lead-free perovskite solar cell fabrication," *RSC Adv.*, vol. 6, pp. 90248–90254, sep 2016.

[105] A. Amat, E. Mosconi, E. Ronca, C. Quarti, P. Umari, M. K. Nazeeruddin, M. Grätzel, and F. De Angelis, "Cation-Induced Band-Gap Tuning in Organohalide Perovskites: Interplay of Spin-Orbit Coupling and Octahedra Tilting," *Nano Lett.*, vol. 14, pp. 3608–3616, jun 2014.

[106] P. Würfel and U. Würfel, *Physics of Solar Cells: From Basic Principles to Advanced Concepts*. Wiley, 3rd ed., 2016.

[107] W. Shockley, "The Theory of p-n Junctions in Semiconductors and p-n Junction Transistors," *Bell Syst. Tech. J.*, vol. 28, pp. 435–489, jul 1949.

[108] D. M. Chapin, C. S. Fuller, and G. L. Pearson, "A New Silicon p-n Junction Photocell for Converting Solar Radiation into Electrical Power," *J. Appl. Phys.*, vol. 25, pp. 676–677, may 1954.

[109] U. Wurfel, A. Cuevas, and P. Wurfel, "Charge Carrier Separation in Solar Cells," *IEEE J. Photovoltaics*, vol. 5, pp. 461–469, jan 2015.

[110] W. Shockley and H. J. Queisser, "Detailed Balance Limit of Efficiency of p-n Junction Solar Cells," *J. Appl. Phys.*, vol. 32, pp. 510–519, mar 1961.

[111] S. Rühle, "Tabulated values of the Shockley-Queisser limit for single junction solar cells," *Sol. Energy*, vol. 130, pp. 139–147, jun 2016.

[112] E. Rodrigues, R. Melício, V. Mendes, and J. Catalão, "Simulation of a solar cell considering single-diode equivalent circuit mode," *Renew. Energy Power Qual. J.*, pp. 369–373, may 2011.

[113] J. Merten, J. Asensi, C. Voz, A. Shah, R. Platz, and J. Andreu, "Improved equivalent circuit and analytical model for amorphous silicon solar cells and modules," *IEEE Trans. Electron Devices*, vol. 45, no. 2, pp. 423–429, 1998.

[114] J. Nelson, *The Physics of Solar Cells*. Imperial College Press, may 2003.

[115] A. Ibrahim, "Analysis of Electrical Characteristics of Photovoltaic Single Crystal Silicon Solar Cells at Outdoor Measurements," *Smart Grid Renew. Energy*, vol. 02, no. 02, pp. 169–175, 2011.

[116] NREL, "Reference Air Mass 1.5 Spectra." https://www.nrel.gov/grid/solar-resource/spectra-am1.5.html. Retrieved 2021-30-04.

[117] C.-c. Chueh, C.-z. Li, and A. K.-Y. Jen, "Recent progress and perspective in solution-processed Interfacial materials for efficient and stable polymer and organometal perovskite solar cells," *Energy Environ. Sci.*, vol. 8, no. 4, pp. 1160–1189, 2015.

[118] M. Ye, C. He, J. Iocozzia, X. Liu, X. Cui, X. Meng, M. Rager, X. Hong, X. Liu, and Z. Lin, "Recent advances in interfacial engineering of perovskite solar cells," *J. Phys. D. Appl. Phys.*, vol. 50, p. 373002, sep 2017.

[119] P. Gao, M. Grätzel, and M. K. Nazeeruddin, "Organohalide lead perovskites for photovoltaic applications," *Energy Environ. Sci.*, vol. 7, p. 2448, jun 2014.

[120] Q. Fu, X. Tang, B. Huang, T. Hu, L. Tan, L. Chen, and Y. Chen, "Recent Progress on the Long-Term Stability of Perovskite Solar Cells," *Adv. Sci.*, vol. 5, p. 1700387, may 2018.

[121] V. Zardetto, B. L. Williams, A. Perrotta, F. Di Giacomo, M. A. Verheijen, R. Andriessen, W. M. M. Kessels, and M. Creatore, "Atomic layer deposition for perovskite solar cells: research status, opportunities and challenges," *Sustain. Energy Fuels*, vol. 1, pp. 30–55, mar 2017.

[122] K. Mahmood, S. Sarwar, and M. T. Mehran, "Current status of electron transport layers in perovskite solar cells: materials and properties," *RSC Adv.*, vol. 7, pp. 17044–17062, mar 2017.

[123] Z. Hu, W. Fu, L. Yan, J. Miao, H. Yu, Y. He, O. Goto, H. Meng, H. Chen, and W. Huang, "Effects of heteroatom substitution in spiro-bifluorene hole transport materials," *Chem. Sci.*, vol. 7, pp. 5007–5012, jul 2016.

[124] W.-C. Lai, K.-W. Lin, T.-F. Guo, P. Chen, and Y.-Y. Liao, "Perovskite-based solar cells with inorganic inverted hybrid planar heterojunction structure," *AIP Adv.*, vol. 8, p. 015109, jan 2018.

[125] P.-H. Huang, Y.-H. Wang, J.-C. Ke, and C.-J. Huang, "Investigation of Various Active Layers for Their Performance on Organic Solar Cells," *Materials (Basel).*, vol. 9, p. 667, aug 2016.

[126] J.-P. Correa-Baena, M. Saliba, T. Buonassisi, M. Grätzel, A. Abate, W. Tress, and A. Hagfeldt, "Promises and challenges of perovskite solar cells," *Science (80-.).*, vol. 358, pp. 739–744, nov 2017.

[127] W. Liu, T. Wu, M. Liu, W. Niu, and Y. Chueh, "Recent Challenges in Perovskite Solar Cells Toward Enhanced Stability, Less Toxicity, and Large-Area Mass Production," *Adv. Mater. Interfaces*, vol. 6, p. 1801758, may 2019.

[128] Y. Galagan, "Perovskite solar cells from lab to fab: the main challenges to access the market," *Oxford Open Mater. Sci.*, vol. 1, nov 2020.

[129] A. Urbina, "The balance between efficiency, stability and environmental impacts in perovskite solar cells: a review," *J. Phys. Energy*, vol. 2, p. 022001, feb 2020.

[130] L. Schmidt-Mende, V. Dyakonov, S. Olthof, F. Ünlü, K. M. T. Lê, S. Mathur, A. D. Karabanov, D. C. Lupascu, L. M. Herz, A. Hinderhofer, F. Schreiber, A. Chernikov, D. A. Egger, O. Shargaieva, C. Cocchi, E. Unger, M. Saliba, M. M. Byranvand, M. Kroll, F. Nehm, K. Leo, A. Redinger, J. Höcker, T. Kirchartz, J. Warby, E. Gutierrez-Partida, D. Neher, M. Stolterfoht, U. Würfel, M. Unmüssig, J. Herterich, C. Baretzky, J. Mohanraj, M. Thelakkat, C. Maheu, W. Jaegermann, T. Mayer, J. Rieger, T. Fauster, D. Niesner, F. Yang, S. Albrecht, T. Riedl, A. Fakharuddin, M. Vasilopoulou, Y. Vaynzof, D. Moia, J. Maier, M. Franckevičius, V. Gulbinas, R. A. Kerner, L. Zhao, B. P. Rand, N. Glück, T. Bein, F. Matteocci, L. A. Castriotta, A. Di Carlo, M. Scheffler, and C. Draxl, "Roadmap on organic-inorganic hybrid perovskite semiconductors and devices," *APL Mater.*, vol. 9, p. 109202, oct 2021.

[131] H. J. Snaith, A. Abate, J. M. Ball, G. E. Eperon, T. Leijtens, N. K. Noel, S. D. Stranks, J. T.-W. Wang, K. Wojciechowski, and W. Zhang, "Anomalous Hysteresis in Perovskite Solar Cells," *J. Phys. Chem. Lett.*, vol. 5, pp. 1511–1515, may 2014.

[132] S. van Reenen, M. Kemerink, and H. J. Snaith, "Modeling Anomalous Hysteresis in Perovskite Solar Cells," *J. Phys. Chem. Lett.*, vol. 6, pp. 3808–3814, oct 2015.

[133] E. L. Unger, E. T. Hoke, C. D. Bailie, W. H. Nguyen, A. R. Bowring, T. Heumüller, M. G. Christoforo, and M. D. McGehee, "Hysteresis and transient behavior in current-voltage measurements of hybrid-perovskite absorber solar cells," *Energy Environ. Sci.*, vol. 7, pp. 3690–3698, aug 2014.

[134] W. Tress, N. Marinova, T. Moehl, S. M. Zakeeruddin, M. K. Nazeeruddin, and M. Grätzel, "Understanding the rate-dependent J-V hysteresis, slow time component, and aging in CH 3 NH 3 PbI 3 perovskite solar cells: the role of a compensated electric field," *Energy Environ. Sci.*, vol. 8, no. 3, pp. 995–1004, 2015.

[135] W. Tress, J. P. Correa Baena, M. Saliba, A. Abate, and M. Graetzel, "Inverted Current-Voltage Hysteresis in Mixed Perovskite Solar Cells: Polarization, Energy Barriers, and Defect Recombination," *Adv. Energy Mater.*, vol. 6, p. 1600396, oct 2016.

[136] S. Meloni, T. Moehl, W. Tress, M. Franckevičius, M. Saliba, Y. H. Lee, P. Gao, M. K. Nazeeruddin, S. M. Zakeeruddin, U. Rothlisberger, and M. Graetzel, "Ionic polarization-induced current-voltage hysteresis in CH3NH3PbX3 perovskite solar cells," *Nat. Commun.*, vol. 7, p. 10334, apr 2016.

[137] H. Zhang, C. Liang, Y. Zhao, M. Sun, H. Liu, J. Liang, D. Li, F. Zhang, and Z. He, "Dynamic interface charge governing the current-voltage hysteresis in perovskite solar cells," *Phys. Chem. Chem. Phys.*, vol. 17, pp. 9613–9618, apr 2015.

[138] C. Liu, J. Fan, X. Zhang, Y. Shen, L. Yang, and Y. Mai, "Hysteretic Behavior upon Light Soaking in Perovskite Solar Cells Prepared via Modified Vapor-Assisted Solution Process," *ACS Appl. Mater. Interfaces*, vol. 7, pp. 9066–9071, may 2015.

[139] L. K. Ono, S. R. Raga, S. Wang, Y. Kato, and Y. Qi, "Temperature-dependent hysteresis effects in perovskite-based solar cells," *J. Mater. Chem. A*, vol. 3, pp. 9074–9080, may 2015.

[140] W. Tress, "Metal Halide Perovskites as Mixed Electronic-Ionic Conductors: Challenges and Opportunities-From Hysteresis to Memristivity," *J. Phys. Chem. Lett.*, vol. 8, pp. 3106–3114, jul 2017.

[141] E. Mosconi and F. De Angelis, "Mobile Ions in Organohalide Perovskites: Interplay of Electronic Structure and Dynamics," *ACS Energy Lett.*, vol. 1, pp. 182–188, jul 2016.

[142] Z. Xiao, Y. Yuan, Y. Shao, Q. Wang, Q. Dong, C. Bi, P. Sharma, A. Gruverman, and J. Huang, "Giant switchable photovoltaic effect in organometal trihalide perovskite devices," *Nat. Mater.*, vol. 14, pp. 193–198, dec 2014.

[143] S. A. L. Weber, I. M. Hermes, S.-H. Turren-Cruz, C. Gort, V. W. Bergmann, L. Gilson, A. Hagfeldt, M. Graetzel, W. Tress, and R. Berger, "How the formation of interfacial charge causes hysteresis in perovskite solar cells," *Energy Environ. Sci.*, vol. 11, no. 9, pp. 2404–2413, 2018.

[144] T. Chen, Z. Sun, M. Liang, and S. Xue, "Correlating hysteresis phenomena with interfacial charge accumulation in perovskite solar cells," *Phys. Chem. Chem. Phys.*, vol. 22, pp. 245–251, dec 2020.

[145] M. Cai, N. Ishida, X. Li, X. Yang, T. Noda, Y. Wu, F. Xie, H. Naito, D. Fujita, and L. Han, "Control of Electrical Potential Distribution for High-Performance Perovskite Solar Cells," *Joule*, vol. 2, pp. 296–306, feb 2018.

[146] V. W. Bergmann, Y. Guo, H. Tanaka, I. M. Hermes, D. Li, A. Klasen, S. A. Bretschneider, E. Nakamura, R. Berger, and S. A. L. Weber, "Local Time-Dependent Charging in a Perovskite Solar Cell," *ACS Appl. Mater. Interfaces*, vol. 8, pp. 19402–19409, aug 2016.

[147] K. Domanski, B. Roose, T. Matsui, M. Saliba, S.-H. Turren-Cruz, J.-P. Correa-Baena, C. R. Carmona, G. Richardson, J. M. Foster, F. De Angelis, J. M. Ball, A. Petrozza, N. Mine, M. K. Nazeeruddin, W. Tress, M. Grätzel, U. Steiner, A. Hagfeldt, and A. Abate, "Migration of cations induces reversible performance losses over day/night cycling in perovskite solar cells," *Energy Environ. Sci.*, vol. 10, no. 2, pp. 604–613, 2017.

[148] A. Guerrero, A. Bou, G. Matt, O. Almora, T. Heumüller, G. Garcia-Belmonte, J. Bisquert, Y. Hou, and C. Brabec, "Switching Off Hysteresis in Perovskite Solar Cells by Fine-Tuning Energy Levels of Extraction Layers," *Adv. Energy Mater.*, vol. 8, p. 1703376, jul 2018.

[149] Y.-C. Wang, X. Li, L. Zhu, X. Liu, W. Zhang, and J. Fang, "Efficient and Hysteresis-Free Perovskite Solar Cells Based on a Solution Processable Polar Fullerene Electron Transport Layer," *Adv. Energy Mater.*, vol. 7, p. 1701144, nov 2017.

[150] Y. Shao, Z. Xiao, C. Bi, Y. Yuan, and J. Huang, "Origin and elimination of photocurrent hysteresis by fullerene passivation in CH3NH3PbI3 planar heterojunction solar cells," *Nat. Commun.*, vol. 5, p. 5784, dec 2014.

[151] D. H. Song, M. H. Jang, M. H. Lee, J. H. Heo, J. K. Park, S.-J. Sung, D.-H. Kim, K.-H. Hong, and S. H. Im, "A discussion on the origin and solutions of hysteresis in perovskite hybrid solar cells," *J. Phys. D. Appl. Phys.*, vol. 49, p. 473001, nov 2016.

[152] M. Wang, X. Jiang, J. Bian, Y. Feng, C. Wang, Y. Huang, Y. Zhang, and Y. Shi, "High-Performance and Stable Mesoporous Perovskite Solar Cells via Well-Crystallized FA 0.85 MA 0.15 Pb(I 0.8 Br 0.2) 3," *ACS Appl. Mater. Interfaces*, vol. 11, pp. 2989–2996, jan 2019.

[153] D. Kang and N. Park, "On the Current-Voltage Hysteresis in Perovskite Solar Cells: Dependence on Perovskite Composition and Methods to Remove Hysteresis," *Adv. Mater.*, vol. 31, p. 1805214, aug 2019.

[154] J.-P. Correa-Baena, M. Anaya, G. Lozano, W. Tress, K. Domanski, M. Saliba, T. Matsui, T. J. Jacobsson, M. E. Calvo, A. Abate, M. Grätzel, H. Míguez, and A. Hagfeldt, "Unbroken Perovskite: Interplay of Morphology, Electro-optical Properties, and Ionic Movement," *Adv. Mater.*, vol. 28, pp. 5031–5037, jul 2016.

[155] S. N. Habisreutinger, N. K. Noel, and H. J. Snaith, "Hysteresis Index: A Figure without Merit for Quantifying Hysteresis in Perovskite Solar Cells," *ACS Energy Lett.*, vol. 3, pp. 2472–2476, oct 2018.

[156] P. Liu, W. Wang, S. Liu, H. Yang, and Z. Shao, "Fundamental Understanding of Photocurrent Hysteresis in Perovskite Solar Cells," *Adv. Energy Mater.*, vol. 9, p. 1803017, apr 2019.

[157] M. Asghar, J. Zhang, H. Wang, and P. Lund, "Device stability of perovskite solar cells - A review," *Renew. Sustain. Energy Rev.*, vol. 77, pp. 131–146, sep 2017.

[158] C. C. Boyd, R. Cheacharoen, T. Leijtens, and M. D. McGehee, "Understanding Degradation Mechanisms and Improving Stability of Perovskite Photovoltaics," *Chem. Rev.*, vol. 119, pp. 3418–3451, mar 2019.

[159] R. Wang, M. Mujahid, Y. Duan, Z. Wang, J. Xue, and Y. Yang, "A Review of Perovskites Solar Cell Stability," *Adv. Funct. Mater.*, vol. 29, p. 1808843, nov 2019.

[160] B. Conings, J. Drijkoningen, N. Gauquelin, A. Babayigit, J. D'Haen, L. D'Olieslaeger, A. Ethirajan, J. Verbeeck, J. Manca, E. Mosconi, F. D. Angelis, and H.-G. Boyen, "Intrinsic Thermal Instability of Methylammonium Lead Trihalide Perovskite," *Adv. Energy Mater.*, vol. 5, p. 1500477, aug 2015.

[161] B. Philippe, B.-W. Park, R. Lindblad, J. Oscarsson, S. Ahmadi, E. M. J. Johansson, and H. Rensmo, "Chemical and Electronic Structure Characterization of Lead Halide Perovskites and Stability Behavior under Different Exposures-A Photoelectron Spectroscopy Investigation," *Chem. Mater.*, vol. 27, pp. 1720–1731, mar 2015.

[162] J. A. Schwenzer, T. Hellmann, B. A. Nejand, H. Hu, T. Abzieher, F. Schackmar, I. M. Hossain, P. Fassl, T. Mayer, W. Jaegermann, U. Lemmer, and U. W. Paetzold, "Thermal Stability and Cation Composition of Hybrid Organic-Inorganic Perovskites," *ACS Appl. Mater. Interfaces*, p. acsami.1c01547, mar 2021.

[163] J. A. Schwenzer, *Thermische Stabilität von Metall-Halogenid-Perowskit-Solarzellen*. Phd thesis, Karlsruhe Institute of Technology (KIT), 2020.

[164] J. A. Schwenzer, L. Rakocevic, R. Gehlhaar, T. Abzieher, S. Gharibzadeh, S. Moghadamzadeh, A. Quintilla, B. S. Richards, U. Lemmer, and U. W. Paetzold, "Temperature Variation-Induced Performance Decline of Perovskite Solar Cells," *ACS Appl. Mater. Interfaces*, vol. 10, pp. 16390–16399, may 2018.

[165] W. Nie, J.-C. Blancon, A. J. Neukirch, K. Appavoo, H. Tsai, M. Chhowalla, M. A. Alam, M. Y. Sfeir, C. Katan, J. Even, S. Tretiak, J. J. Crochet, G. Gupta, and A. D. Mohite, "Light-activated photocurrent degradation and self-healing in perovskite solar cells," *Nat. Commun.*, vol. 7, p. 11574, sep 2016.

[166] S.-W. Lee, S. Kim, S. Bae, K. Cho, T. Chung, L. E. Mundt, S. Lee, S. Park, H. Park, M. C. Schubert, S. W. Glunz, Y. Ko, Y. Jun, Y. Kang, H.-S. Lee, and D. Kim, "UV Degradation and Recovery of Perovskite Solar Cells," *Sci. Rep.*, vol. 6, p. 38150, dec 2016.

[167] N. H. Nickel, F. Lang, V. V. Brus, O. Shargaieva, and J. Rappich, "Unraveling the Light-Induced Degradation Mechanisms of CH 3 NH 3 PbI 3 Perovskite Films," *Adv. Electron. Mater.*, vol. 3, p. 1700158, dec 2017.

[168] S. Ruan, M.-A. Surmiak, Y. Ruan, D. P. McMeekin, H. Ebendorff-Heidepriem, Y.-B. Cheng, J. Lu, and C. R. McNeill, "Light induced degradation in mixed-halide perovskites," *J. Mater. Chem. C*, vol. 7, pp. 9326–9334, aug 2019.

[169] A. Farooq, I. M. Hossain, S. Moghadamzadeh, J. A. Schwenzer, T. Abzieher, B. S. Richards, E. Klampaftis, and U. W. Paetzold, "Spectral Dependence of Degradation under Ultraviolet Light in Perovskite Solar Cells," *ACS Appl. Mater. Interfaces*, vol. 10, pp. 21985–21990, jul 2018.

[170] N. Aristidou, C. Eames, I. Sanchez-Molina, X. Bu, J. Kosco, M. S. Islam, and S. A. Haque, "Fast oxygen diffusion and iodide defects mediate oxygen-induced degradation of perovskite solar cells," *Nat. Commun.*, vol. 8, p. 15218, aug 2017.

[171] A. Senocrate, T. Acartürk, G. Y. Kim, R. Merkle, U. Starke, M. Grätzel, and J. Maier, "Interaction of oxygen with halide perovskites," *J. Mater. Chem. A*, vol. 6, pp. 10847–10855, jun 2018.

[172] D. Bryant, N. Aristidou, S. Pont, I. Sanchez-Molina, T. Chotchunangatchaval, S. Wheeler, J. R. Durrant, and S. A. Haque, "Light and oxygen induced degradation limits the operational stability of methylammonium lead triiodide perovskite solar cells," *Energy Environ. Sci.*, vol. 9, pp. 1655–1660, may 2016.

[173] Q. Sun, P. Fassl, D. Becker-Koch, A. Bausch, B. Rivkin, S. Bai, P. E. Hopkinson, H. J. Snaith, and Y. Vaynzof, "Role of Microstructure in Oxygen Induced Photodegradation of Methylammonium Lead Triiodide Perovskite Films," *Adv. Energy Mater.*, vol. 7, p. 1700977, oct 2017.

[174] A. M. A. Leguy, Y. Hu, M. Campoy-Quiles, M. I. Alonso, O. J. Weber, P. Azarhoosh, M. van Schilfgaarde, M. T. Weller, T. Bein, J. Nelson, P. Docampo, and P. R. F. Barnes, "Reversible Hydration of CH 3 NH 3 PbI 3 in Films, Single Crystals, and Solar Cells," *Chem. Mater.*, vol. 27, pp. 3397–3407, may 2015.

[175] Y.-H. Kye, C.-J. Yu, U.-G. Jong, Y. Chen, and A. Walsh, "Critical Role of Water in Defect Aggregation and Chemical Degradation of Perovskite Solar Cells," *J. Phys. Chem. Lett.*, vol. 9, pp. 2196–2201, may 2018.

[176] C. Aranda, A. Guerrero, and J. Bisquert, "Crystalline Clear or Not: Beneficial and Harmful Effects of Water in Perovskite Solar Cells," *ChemPhysChem*, vol. 20, pp. 2587–2599, oct 2019.

[177] W. Zhang, J. Xiong, J. Li, and W. A. Daoud, "Mechanism of Water Effect on Enhancing the Photovoltaic Performance of Triple-Cation Hybrid Perovskite Solar Cells," *ACS Appl. Mater. Interfaces*, vol. 11, pp. 12699–12708, apr 2019.

[178] Y. C. Kim, T.-Y. Yang, N. J. Jeon, J. Im, S. Jang, T. J. Shin, H.-W. Shin, S. Kim, E. Lee, S. Kim, J. H. Noh, S. I. Seok, and J. Seo, "Engineering interface structures between lead halide perovskite and copper phthalocyanine for efficient and stable perovskite solar cells," *Energy Environ. Sci.*, vol. 10, pp. 2109–2116, oct 2017.

[179] A. K. Jena, Y. Numata, M. Ikegami, and T. Miyasaka, "Role of spiro-OMeTAD in performance deterioration of perovskite solar cells at high temperature and reuse of the perovskite films to avoid Pb-waste," *J. Mater. Chem. A*, vol. 6, no. 5, pp. 2219–2230, 2018.

[180] J. A. Christians, P. Schulz, J. S. Tinkham, T. H. Schloemer, S. P. Harvey, B. J. Tremolet de Villers, A. Sellinger, J. J. Berry, and J. M. Luther, "Tailored interfaces of unencapsulated perovskite solar cells for >1,000 hour operational stability," *Nat. Energy*, vol. 3, pp. 68–74, jan 2018.

[181] Y. Kato, L. K. Ono, M. V. Lee, S. Wang, S. R. Raga, and Y. Qi, "Silver Iodide Formation in Methyl Ammonium Lead Iodide Perovskite Solar Cells with Silver Top Electrodes," *Adv. Mater. Interfaces*, vol. 2, p. 1500195, sep 2015.

[182] K. Domanski, J.-P. Correa-Baena, N. Mine, M. K. Nazeeruddin, A. Abate, M. Saliba, W. Tress, A. Hagfeldt, and M. Grätzel, "Not All That Glitters Is Gold: Metal-Migration-Induced Degradation in Perovskite Solar Cells," *ACS Nano*, vol. 10, pp. 6306–6314, jun 2016.

[183] M. Saliba, T. Matsui, J.-Y. Seo, K. Domanski, J.-P. Correa-Baena, M. K. Nazeeruddin, S. M. Zakeeruddin, W. Tress, A. Abate, A. Hagfeldt, and M. Grätzel, "Cesium-containing triple cation perovskite solar cells: improved stability, reproducibility and high efficiency," *Energy Environ. Sci.*, vol. 9, pp. 1989–1997, jun 2016.

[184] R. E. Beal, D. J. Slotcavage, T. Leijtens, A. R. Bowring, R. A. Belisle, W. H. Nguyen, G. F. Burkhard, E. T. Hoke, and M. D. McGehee, "Cesium Lead Halide Perovskites with Improved Stability for Tandem Solar Cells," *J. Phys. Chem. Lett.*, vol. 7, pp. 746–751, mar 2016.

[185] F. Bella, P. Renzi, C. Cavallo, and C. Gerbaldi, "Caesium for Perovskite Solar Cells: An Overview," *Chem. - A Eur. J.*, vol. 24, pp. 12183–12205, aug 2018.

[186] W. Rehman, D. P. McMeekin, J. B. Patel, R. L. Milot, M. B. Johnston, H. J. Snaith, and L. M. Herz, "Photovoltaic mixed-cation lead mixed-halide perovskites: links between crystallinity, photo-stability and electronic properties," *Energy Environ. Sci.*, vol. 10, pp. 361–369, jan 2017.

[187] K. A. Bush, K. Frohna, R. Prasanna, R. E. Beal, T. Leijtens, S. A. Swifter, and M. D. Mcgehee, "Compositional Engineering for Efficient Wide Band Gap Perovskites with Improved Stability to Photoinduced Phase Segregation," *ACS Energy Lett.*, vol. 3, p. acsenergylett.7b01255, feb 2018.

[188] T. Leijtens, G. E. Eperon, S. Pathak, A. Abate, M. M. Lee, and H. J. Snaith, "Overcoming ultraviolet light instability of sensitized TiO2 with meso-superstructured organometal trihalide perovskite solar cells," *Nat. Commun.*, vol. 4, p. 2885, dec 2013.

[189] S. Ito, S. Tanaka, K. Manabe, and H. Nishino, "Effects of Surface Blocking Layer of Sb 2 S 3 on Nanocrystalline TiO 2 for CH 3 NH 3 PbI 3 Perovskite Solar Cells," *J. Phys. Chem. C*, vol. 118, pp. 16995–17000, jul 2014.

[190] B. Roose, J.-P. C. Baena, K. C. Gödel, M. Graetzel, A. Hagfeldt, U. Steiner, and A. Abate, "Mesoporous SnO2 electron selective contact enables UV-stable perovskite solar cells," *Nano Energy*, vol. 30, pp. 517–522, dec 2016.

[191] T. Abzieher, S. Moghadamzadeh, F. Schackmar, H. Eggers, F. Sutterlüti, A. Farooq, D. Kojda, K. Habicht, R. Schmager, A. Mertens, R. Azmi, L. Klohr, J. A. Schwenzer, M. Hetterich, U. Lemmer, B. S. Richards, M. Powalla, and U. W. Paetzold, "Electron-Beam-Evaporated Nickel Oxide Hole Transport Layers for Perovskite-Based Photovoltaics," *Adv. Energy Mater.*, vol. 9, p. 1802995, mar 2019.

[192] Q. Dong, F. Liu, M. K. Wong, H. W. Tam, A. B. Djurišić, A. Ng, C. Surya, W. K. Chan, and A. M. C. Ng, "Encapsulation of Perovskite Solar Cells for High Humidity Conditions," *ChemSusChem*, vol. 9, pp. 2518–2518, sep 2016.

[193] R. Cheacharoen, C. C. Boyd, G. F. Burkhard, T. Leijtens, J. A. Raiford, K. A. Bush, S. F. Bent, and M. D. McGehee, "Encapsulating perovskite solar cells to withstand damp heat and thermal cycling," *Sustain. Energy Fuels*, vol. 2, pp. 2398–2406, oct 2018.

[194] E. Ramasamy, V. Karthikeyan, K. Rameshkumar, and G. Veerappan, "Glass-to-glass encapsulation with ultraviolet light curable epoxy edge sealing for stable perovskite solar cells," *Mater. Lett.*, vol. 250, pp. 51–54, sep 2019.

[195] S. Emami, J. Martins, D. Ivanou, and A. Mendes, "Advanced hermetic encapsulation of perovskite solar cells: the route to commercialization," *J. Mater. Chem. A*, vol. 8, pp. 2654–2662, feb 2020.

[196] I. C. Smith, E. T. Hoke, D. Solis-Ibarra, M. D. McGehee, and H. I. Karunadasa, "A Layered Hybrid Perovskite Solar-Cell Absorber with Enhanced Moisture Stability," *Angew. Chemie Int. Ed.*, vol. 53, pp. 11232–11235, oct 2014.

[197] H. Tsai, W. Nie, J.-C. Blancon, C. C. Stoumpos, R. Asadpour, B. Harutyunyan, A. J. Neukirch, R. Verduzco, J. J. Crochet, S. Tretiak, L. Pedesseau, J. Even, M. A. Alam, G. Gupta, J. Lou, P. M. Ajayan, M. J. Bedzyk, M. G. Kanatzidis, and A. D. Mohite, "High-efficiency two-dimensional Ruddlesden-Popper perovskite solar cells," *Nature*, vol. 536, pp. 312–316, aug 2016.

[198] G. Grancini, C. Roldán-Carmona, I. Zimmermann, E. Mosconi, X. Lee, D. Martineau, S. Narbey, F. Oswald, F. De Angelis, M. Graetzel, and M. K. Nazeeruddin, "One-Year stable perovskite solar cells by 2D/3D interface engineering," *Nat. Commun.*, vol. 8, p. 15684, jun 2017.

[199] H. Zheng, G. Liu, L. Zhu, J. Ye, X. Zhang, A. Alsaedi, T. Hayat, X. Pan, and S. Dai, "The Effect of Hydrophobicity of Ammonium Salts on Stability of Quasi-2D Perovskite Materials in Moist Condition," *Adv. Energy Mater.*, vol. 8, p. 1800051, jul 2018.

[200] H. Ren, S. Yu, L. Chao, Y. Xia, Y. Sun, S. Zuo, F. Li, T. Niu, Y. Yang, H. Ju, B. Li, H. Du, X. Gao, J. Zhang, J. Wang, L. Zhang, Y. Chen, and W. Huang, "Efficient and stable Ruddlesden-Popper perovskite solar cell with tailored interlayer molecular interaction," *Nat. Photonics*, vol. 14, pp. 154–163, mar 2020.

[201] D. Kim, H. J. Jung, I. J. Park, B. W. Larson, S. P. Dunfield, C. Xiao, J. Kim, J. Tong, P. Boonmongkolras, S. G. Ji, F. Zhang, S. R. Pae, M. Kim, S. B. Kang, V. Dravid, J. J. Berry,

J. Y. Kim, K. Zhu, D. H. Kim, and B. Shin, "Efficient, stable silicon tandem cells enabled by anion-engineered wide-bandgap perovskites," *Science (80-.).*, vol. 368, pp. 155–160, apr 2020.

[202] T. Leijtens, T. Giovenzana, S. N. Habisreutinger, J. S. Tinkham, N. K. Noel, B. A. Kamino, G. Sadoughi, A. Sellinger, and H. J. Snaith, "Hydrophobic Organic Hole Transporters for Improved Moisture Resistance in Metal Halide Perovskite Solar Cells," *ACS Appl. Mater. Interfaces*, vol. 8, pp. 5981–5989, mar 2016.

[203] Y. Liu, S. Akin, L. Pan, R. Uchida, N. Arora, J. V. Milić, A. Hinderhofer, F. Schreiber, A. R. Uhl, S. M. Zakeeruddin, A. Hagfeldt, M. I. Dar, and M. Grätzel, "Ultrahydrophobic 3D/2D fluoroarene bilayer-based water-resistant perovskite solar cells with efficiencies exceeding 22%," *Sci. Adv.*, vol. 5, p. eaaw2543, jun 2019.

[204] P. Holzhey and M. Saliba, "A full overview of international standards assessing the long-term stability of perovskite solar cells," *J. Mater. Chem. A*, vol. 6, pp. 21794–21808, nov 2018.

[205] C. C. Boyd, R. Cheacharoen, K. A. Bush, R. Prasanna, T. Leijtens, and M. D. McGehee, "Barrier Design to Prevent Metal-Induced Degradation and Improve Thermal Stability in Perovskite Solar Cells," *ACS Energy Lett.*, vol. 3, pp. 1772–1778, jul 2018.

[206] K. A. Bush, A. F. Palmstrom, Z. J. Yu, M. Boccard, R. Cheacharoen, J. P. Mailoa, D. P. McMeekin, R. L. Z. Hoye, C. D. Bailie, T. Leijtens, I. M. Peters, M. C. Minichetti, N. Rolston, R. Prasanna, S. Sofia, D. Harwood, W. Ma, F. Moghadam, H. J. Snaith, T. Buonassisi, Z. C. Holman, S. F. Bent, and M. D. McGehee, "23.6%-efficient monolithic perovskite/silicon tandem solar cells with improved stability," *Nat. Energy*, vol. 2, p. 17009, feb 2017.

[207] L. Shi, T. L. Young, J. Kim, Y. Sheng, L. Wang, Y. Chen, Z. Feng, M. J. Keevers, X. Hao, P. J. Verlinden, M. A. Green, and A. W. Ho-Baillie, "Accelerated Lifetime Testing of Organic-Inorganic Perovskite Solar Cells Encapsulated by Polyisobutylene," *ACS Appl. Mater. Interfaces*, vol. 9, pp. 25073–25081, aug 2017.

[208] A. Babayigit, A. Ethirajan, M. Muller, and B. Conings, "Toxicity of organometal halide perovskite solar cells," *Nat. Mater.*, vol. 15, pp. 247–251, mar 2016.

[209] A. Babayigit, D. Duy Thanh, A. Ethirajan, J. Manca, M. Muller, H.-G. Boyen, and B. Conings, "Assessing the toxicity of Pb- and Sn-based perovskite solar cells in model organism Danio rerio," *Sci. Rep.*, vol. 6, p. 18721, may 2016.

[210] R. Vidal, J.-A. Alberola-Borràs, S. N. Habisreutinger, J.-L. Gimeno-Molina, D. T. Moore, T. H. Schloemer, I. Mora-Seró, J. J. Berry, and J. M. Luther, "Assessing health and environmental impacts of solvents for producing perovskite solar cells," *Nat. Sustain.*, vol. 4, pp. 277–285, mar 2021.

[211] N.-G. Park, "Green solvent for perovskite solar cell production," *Nat. Sustain.*, pp. 3–4, dec 2020.

[212] R. Vidal, J. Alberola-Borràs, N. Sánchez-Pantoja, and I. Mora-Seró, "Comparison of Perovskite Solar Cells with other Photovoltaics Technologies from the Point of View of Life Cycle Assessment," *Adv. Energy Sustain. Res.*, p. 2000088, mar 2021.

[213] B. Hailegnaw, S. Kirmayer, E. Edri, G. Hodes, and D. Cahen, "Rain on Methylammonium Lead Iodide Based Perovskites: Possible Environmental Effects of Perovskite Solar Cells," *J. Phys. Chem. Lett.*, vol. 6, pp. 1543–1547, may 2015.

[214] P. Billen, E. Leccisi, S. Dastidar, S. Li, L. Lobaton, S. Spatari, A. T. Fafarman, V. M. Fthenakis, and J. B. Baxter, "Comparative evaluation of lead emissions and toxicity potential in the life cycle of lead halide perovskite photovoltaics," *Energy*, vol. 166, pp. 1089–1096, jan 2019.

[215] J. Li, H.-L. Cao, W.-B. Jiao, Q. Wang, M. Wei, I. Cantone, J. Lü, and A. Abate, "Biological impact of lead from halide perovskites reveals the risk of introducing a safe threshold," *Nat. Commun.*, vol. 11, p. 310, dec 2020.

[216] I. R. Benmessaoud, A.-L. Mahul-Mellier, E. Horváth, B. Maco, M. Spina, H. A. Lashuel, and L. Forró, "Health hazards of methylammonium lead iodide based perovskites: cytotoxicity studies," *Toxicol. Res. (Camb).*, vol. 5, no. 2, pp. 407–419, 2016.

[217] A. Babayigit, H.-G. Boyen, and B. Conings, "Environment versus sustainable energy: The case of lead halide perovskite-based solar cells," *MRS Energy Sustain.*, vol. 5, p. 15, may 2018.

[218] Z. Xiao, Z. Song, and Y. Yan, "From Lead Halide Perovskites to Lead-Free Metal Halide Perovskites and Perovskite Derivatives," *Adv. Mater.*, vol. 31, p. 1803792, nov 2019.

[219] M. Lyu, J.-H. Yun, P. Chen, M. Hao, and L. Wang, "Addressing Toxicity of Lead: Progress and Applications of Low-Toxic Metal Halide Perovskites and Their Derivatives," *Adv. Energy Mater.*, vol. 7, p. 1602512, aug 2017.

[220] H. Hu, B. Dong, and W. Zhang, "Low-toxic metal halide perovskites: opportunities and future challenges," *J. Mater. Chem. A*, vol. 5, pp. 11436–11449, jun 2017.

[221] M. Konstantakou and T. Stergiopoulos, "A critical review on tin halide perovskite solar cells," *J. Mater. Chem. A*, vol. 5, pp. 11518–11549, jun 2017.

[222] S. Shao, J. Liu, G. Portale, H.-H. Fang, G. R. Blake, G. H. ten Brink, L. J. A. Koster, and M. A. Loi, "Highly Reproducible Sn-Based Hybrid Perovskite Solar Cells with 9% Efficiency," *Adv. Energy Mater.*, vol. 8, p. 1702019, feb 2018.

[223] Y. Liao, H. Liu, W. Zhou, D. Yang, Y. Shang, Z. Shi, B. Li, X. Jiang, L. Zhang, L. N. Quan, R. Quintero-Bermudez, B. R. Sutherland, Q. Mi, E. H. Sargent, and Z. Ning, "Highly Oriented Low-Dimensional Tin Halide Perovskites with Enhanced Stability and Photovoltaic Performance," *J. Am. Chem. Soc.*, vol. 139, pp. 6693–6699, may 2017.

[224] Z. Zhu, C. Chueh, N. Li, C. Mao, and A. K. Jen, "Realizing Efficient Lead-Free Formamidinium Tin Triiodide Perovskite Solar Cells via a Sequential Deposition Route," *Adv. Mater.*, vol. 30, p. 1703800, feb 2018.

[225] W. Ke and M. G. Kanatzidis, "Prospects for low-toxicity lead-free perovskite solar cells," *Nat. Commun.*, vol. 10, p. 965, dec 2019.

[226] K. Nishimura, M. A. Kamarudin, D. Hirotani, K. Hamada, Q. Shen, S. Iikubo, T. Minemoto, K. Yoshino, and S. Hayase, "Lead-free tin-halide perovskite solar cells with 13% efficiency," *Nano Energy*, vol. 74, p. 104858, aug 2020.

[227] Y. Takahashi, R. Obara, Z.-Z. Lin, Y. Takahashi, T. Naito, T. Inabe, S. Ishibashi, and K. Terakura, "Charge-transport in tin-iodide perovskite CH3NH3SnI3: origin of high conductivity," *Dalt. Trans.*, vol. 40, p. 5563, may 2011.

[228] T. Leijtens, K. Bush, R. Cheacharoen, R. Beal, A. Bowring, and M. D. McGehee, "Towards enabling stable lead halide perovskite solar cells; interplay between structural, environmental, and thermal stability," *J. Mater. Chem. A*, vol. 5, pp. 11483–11500, jun 2017.

[229] A. Uddin, M. Upama, H. Yi, and L. Duan, "Encapsulation of Organic and Perovskite Solar Cells: A Review," *Coatings*, vol. 9, p. 65, jan 2019.

[230] J. Gong, S. B. Darling, and F. You, "Perovskite Photovoltaics: Life-Cycle Assessment of Energy and Environmental Impacts," *Energy Environ. Sci.*, vol. 8, no. 7, pp. 1953–1968, 2015.

[231] N. Espinosa, L. Serrano-Luján, A. Urbina, and F. C. Krebs, "Solution and vapour deposited lead perovskite solar cells: Ecotoxicity from a life cycle assessment perspective," *Sol. Energy Mater. Sol. Cells*, vol. 137, pp. 303–310, jun 2015.

[232] A. Binek, M. L. Petrus, N. Huber, H. Bristow, Y. Hu, T. Bein, and P. Docampo, "Recycling Perovskite Solar Cells To Avoid Lead Waste," *ACS Appl. Mater. Interfaces*, vol. 8, pp. 12881–12886, may 2016.

[233] J. M. Kadro, N. Pellet, F. Giordano, A. Ulianov, O. Müntener, J. Maier, M. Grätzel, and A. Hagfeldt, "Proof-of-concept for facile perovskite solar cell recycling," *Energy Environ. Sci.*, vol. 9, pp. 3172–3179, oct 2016.

[234] M. Monteiro Lunardi, A. Wing Yi Ho-Baillie, J. P. Alvarez-Gaitan, S. Moore, and R. Corkish, "A life cycle assessment of perovskite/silicon tandem solar cells," *Prog. Photovoltaics Res. Appl.*, vol. 25, pp. 679–695, aug 2017.

[235] A. J. Doolin, R. G. Charles, C. S. P. De Castro, R. G. Rodriguez, E. V. Péan, R. Patidar, T. Dunlop, C. Charbonneau, T. Watson, and M. L. Davies, "Sustainable solvent selection for the manufacture of methylammonium lead triiodide (MAPbI 3) perovskite solar cells," *Green Chem.*, vol. 23, no. 6, pp. 2471–2486, 2021.

[236] J. Wang, F. Di Giacomo, J. Brüls, H. Gorter, I. Katsouras, P. Groen, R. A. J. Janssen, R. Andriessen, and Y. Galagan, "Highly Efficient Perovskite Solar Cells Using Non-Toxic Industry Compatible Solvent System," *Sol. RRL*, vol. 1, p. 1700091, nov 2017.

[237] K. L. Gardner, J. G. Tait, T. Merckx, W. Qiu, U. W. Paetzold, L. Kootstra, M. Jaysankar, R. Gehlhaar, D. Cheyns, P. Heremans, and J. Poortmans, "Nonhazardous Solvent Systems for Processing Perovskite Photovoltaics," *Adv. Energy Mater.*, vol. 6, p. 1600386, jul 2016.

[238] N. K. Noel, S. N. Habisreutinger, B. Wenger, M. T. Klug, M. T. Hörantner, M. B. Johnston, R. J. Nicholas, D. T. Moore, and H. J. Snaith, "A low viscosity, low boiling point, clean solvent system for the rapid crystallisation of highly specular perovskite films," *Energy Environ. Sci.*, vol. 10, no. 1, pp. 145–152, 2017.

[239] S.-H. Huang, K.-y. Tian, H.-C. Huang, C.-f. Li, W.-c. Chu, K.-m. Lee, Y.-c. Huang, and W.-F. Su, "Controlling the Morphology and Interface of the Perovskite Layer for Scalable High-Efficiency Solar Cells Fabricated Using Green Solvents and Blade Coating in an Ambient Environment," *ACS Appl. Mater. Interfaces*, vol. 12, pp. 26041–26049, jun 2020.

[240] Y. Galagan, F. Di Giacomo, H. Gorter, G. Kirchner, I. de Vries, R. Andriessen, and P. Groen, "Roll-to-Roll Slot Die Coated Perovskite for Efficient Flexible Solar Cells," *Adv. Energy Mater.*, vol. 8, p. 1801935, nov 2018.

[241] T. Abzieher, *Thermische Koverdampfung von hybriden Perowskit-Halbleitern für den Einsatz in Solarzellen*. Phd thesis, Karlsruhe Institute of Technology (KIT), 2019.

[242] NREL, "Champion Module Efficiencies." https://www.nrel.gov/pv/assets/pdfs/champion-module-efficiencies.pdf. Retrieved 2021-09-20, 2021.

[243] M. Cai, Y. Wu, H. Chen, X. Yang, Y. Qiang, and L. Han, "Cost-Performance Analysis of Perovskite Solar Modules," *Adv. Sci.*, vol. 4, p. 1600269, jan 2017.

[244] B. Dou, J. B. Whitaker, K. Bruening, D. T. Moore, L. M. Wheeler, J. Ryter, N. J. Breslin, J. J. Berry, S. M. Garner, F. S. Barnes, S. E. Shaheen, C. J. Tassone, K. Zhu, and M. F. A. M. van Hest, "Roll-to-Roll Printing of Perovskite Solar Cells," *ACS Energy Lett.*, vol. 3, pp. 2558–2565, oct 2018.

[245] C. Zuo, D. Vak, D. Angmo, L. Ding, and M. Gao, "One-step roll-to-roll air processed high efficiency perovskite solar cells," *Nano Energy*, vol. 46, pp. 185–192, apr 2018.

[246] N. L. Chang, A. W. Y. Ho-Baillie, D. Vak, M. Gao, M. A. Green, and R. J. Egan, "Manufacturing cost and market potential analysis of demonstrated roll-to-roll perovskite photovoltaic cell processes," *Sol. Energy Mater. Sol. Cells*, vol. 174, pp. 314–324, jan 2018.

[247] D. Angmo, G. DeLuca, A. D. Scully, A. S. Chesman, A. Seeber, C. Zuo, D. Vak, U. Bach, and M. Gao, "A Lab-to-Fab Study toward Roll-to-Roll Fabrication of Reproducible Perovskite Solar Cells under Ambient Room Conditions," *Cell Reports Phys. Sci.*, p. 100293, jan 2021.

[248] Toshiba Corporation, "Toshiba's Polymer Film-Based Perovskite Large-Area Photovoltaic Module Reaches Record Power Conversion Efficiency of 15.1%." https://www.global.toshiba/ww/technology/corporate/rdc/rd/topics/21/2109-01.html. Retrieved 2021-09-20, 2021.

[249] T. Abzieher, T. Feeney, F. Schackmar, Y. J. Donie, I. M. Hossain, J. A. Schwenzer, T. Hellmann, T. Mayer, M. Powalla, and U. W. Paetzold, "From Groundwork to Efficient Solar Cells: On the Importance of the Substrate Material in Co-Evaporated Perovskite Solar Cells," *Adv. Funct. Mater.*, p. 2104482, jul 2021.

[250] Y. Xiao, C. Zuo, J. Zhong, W. Wu, L. Shen, and L. Ding, "Large-Area Blade-Coated Solar Cells: Advances and Perspectives," *Adv. Energy Mater.*, p. 2100378, apr 2021.

[251] J. Cheng, F. Liu, Z. Tang, and Y. Li, "Scalable Blade Coating: A Technique Accelerating the Commercialization of Perovskite-Based Photovoltaics," *Energy Technol.*, vol. 9, p. 2100204, aug 2021.

[252] R. Patidar, D. Burkitt, K. Hooper, D. Richards, and T. Watson, "Slot-Die Coating of Perovskite Solar Cells: An Overview," *Mater. Today Commun.*, vol. 22, p. 100808, dec 2019.

[253] N.-G. Park and K. Zhu, "Scalable fabrication and coating methods for perovskite solar cells and solar modules," *Nat. Rev. Mater.*, feb 2020.

[254] S. Razza, S. Castro-Hermosa, A. Di Carlo, and T. M. Brown, "Research Update: Large-area deposition, coating, printing, and processing techniques for the upscaling of perovskite solar cell technology," *APL Mater.*, vol. 4, p. 091508, sep 2016.

[255] Y.-S. Jung, K. Hwang, Y.-J. Heo, J.-E. Kim, D. Vak, and D.-Y. Kim, "Progress in Scalable Coating and Roll-to-Roll Compatible Printing Processes of Perovskite Solar Cells toward Realization of Commercialization," *Adv. Opt. Mater.*, p. 1701182, mar 2018.

[256] Y. Wang, C. Duan, P. Lv, Z. Ku, J. Lu, F. Huang, and Y.-B. Cheng, "Printing strategies for scaling-up perovskite solar cells," *Natl. Sci. Rev.*, vol. 8, p. 2021, apr 2021.

[257] J. E. Bishop, T. J. Routledge, and D. G. Lidzey, "Advances in Spray-Cast Perovskite Solar Cells," *J. Phys. Chem. Lett.*, vol. 9, pp. 1977–1984, apr 2018.

[258] J. E. Bishop, J. A. Smith, and D. G. Lidzey, "Development of Spray-Coated Perovskite Solar Cells," *ACS Appl. Mater. Interfaces*, vol. 12, pp. 48237–48245, oct 2020.

[259] H. Cai, X. Liang, X. Ye, J. Su, J. Guan, J. Yang, Y. Liu, X. Zhou, R. Han, J. Ni, J. Li, and J. Zhang, "High Efficiency over 20% of Perovskite Solar Cells by Spray Coating via a Simple Process," *ACS Appl. Energy Mater.*, vol. 0, p. acsaem.0c01129, oct 2020.

[260] F. Mathies, H. Eggers, B. S. Richards, G. Hernandez-Sosa, U. Lemmer, and U. W. Paetzold, "Inkjet-Printed Triple Cation Perovskite Solar Cells," *ACS Appl. Energy Mater.*, vol. 1, pp. 1834–1839, may 2018.

[261] F. Mathies, E. J. List-Kratochvil, and E. L. Unger, "Advances in Inkjet-Printed Metal-Halide Perovskite Photovoltaic and Optoelectronic Devices," *Energy Technol.*, vol. 81, p. ente.201900991, nov 2019.

[262] F. Mathies, *Inkjet-gedruckte Metallhalogenid-Perowskite für optoelektronische Bauelemente*. PhD thesis, Karlsruhe Institute of Technology (KIT), 2018.

[263] Q. Hu, H. Wu, J. Sun, D. Yan, Y. Gao, and J. Yang, "Large-area perovskite nanowire arrays fabricated by large-scale roll-to-roll micro-gravure printing and doctor blading," *Nanoscale*, vol. 8, no. 9, pp. 5350–5357, 2016.

[264] Y. Y. Kim, T.-Y. Yang, R. Suhonen, A. Kemppainen, K. Hwang, N. J. Jeon, and J. Seo, "Roll-to-roll gravure-printed flexible perovskite solar cells using eco-friendly antisolvent bathing with wide processing window," *Nat. Commun.*, vol. 11, p. 5146, dec 2020.

[265] Y. Hu, S. Si, A. Mei, Y. Rong, H. Liu, X. Li, and H. Han, "Stable Large-Area (10 x 10 cm 2) Printable Mesoscopic Perovskite Module Exceeding 10% Efficiency," *Sol. RRL*, vol. 1, p. 1600019, feb 2017.

[266] Y. Hu, Z. Zhang, A. Mei, Y. Jiang, X. Hou, Q. Wang, K. Du, Y. Rong, Y. Zhou, G. Xu, and H. Han, "Improved Performance of Printable Perovskite Solar Cells with Bifunctional Conjugated Organic Molecule," *Adv. Mater.*, vol. 30, p. 1705786, mar 2018.

[267] Z. Ku, Y. Rong, M. Xu, T. Liu, and H. Han, "Full Printable Processed Mesoscopic CH3NH3PbI3/TiO2 Heterojunction Solar Cells with Carbon Counter Electrode," *Sci. Rep.*, vol. 3, p. 3132, nov 2013.

[268] A. Mei, X. Li, L. Liu, Z. Ku, T. Liu, Y. Rong, M. Xu, M. Hu, J. Chen, Y. Yang, M. Gratzel, and H. Han, "A hole-conductor-free, fully printable mesoscopic perovskite solar cell with high stability," *Science (80-.).*, vol. 345, pp. 295–298, jul 2014.

[269] Q. Wang, W. Zhang, Z. Zhang, S. Liu, J. Wu, Y. Guan, A. Mei, Y. Rong, Y. Hu, and H. Han, "Crystallization Control of Ternary-Cation Perovskite Absorber in Triple-Mesoscopic Layer for Efficient Solar Cells," *Adv. Energy Mater.*, vol. 10, p. 1903092, feb 2020.

[270] M. Xu, W. Ji, Y. Sheng, Y. Wu, H. Cheng, J. Meng, Z. Yan, J. Xu, A. Mei, Y. Hu, Y. Rong, and H. Han, "Efficient triple-mesoscopic perovskite solar mini-modules fabricated with slot-die coating," *Nano Energy*, vol. 74, p. 104842, aug 2020.

[271] S. Siegrist, S.-C. Yang, E. Gilshtein, X. Sun, A. N. Tiwari, and F. Fu, "Triple-cation perovskite solar cells fabricated by a hybrid PVD/blade coating process using green solvents," *J. Mater. Chem. A*, aug 2021.

[272] M. Ernst, J.-P. Herterich, C. Margenfeld, M. Kohlstädt, and U. Würfel, "Multi-Layer Blade Coating Fabrication of Methylammonium-Free Perovskite Photovoltaic Modules with 66 cm2 Active Area," *Sol. RRL*, p. solr.202100535, aug 2021.

[273] L. Landau and B. Levich, "Dragging of a Liquid by a Moving Plate," in *Dyn. Curved Front.*, vol. XVII, pp. 141–153, Elsevier, 1988.

[274] Y. Deng, X. Zheng, Y. Bai, Q. Wang, J. Zhao, and J. Huang, "Surfactant-controlled ink drying enables high-speed deposition of perovskite films for efficient photovoltaic modules," *Nat. Energy*, vol. 3, pp. 560–566, jul 2018.

[275] L. Ke, S. Luo, X. Ren, and Y. Yuan, "Factors influencing the nucleation and crystal growth of solution-processed organic lead halide perovskites: a review," *J. Phys. D. Appl. Phys.*, vol. 54, p. 163001, apr 2021.

[276] X. Dai, Y. Deng, C. H. Van Brackle, and J. Huang, "Meniscus fabrication of halide perovskite thin films at high throughput for large area and low-cost solar panels," *Int. J. Extrem. Manuf.*, vol. 1, p. 022004, jun 2019.

[277] M. Le Berre, Y. Chen, and D. Baigl, "From Convective Assembly to Landau-Levich Deposition of Multilayered Phospholipid Films of Controlled Thickness," *Langmuir*, vol. 25, pp. 2554–2557, mar 2009.

[278] X. Ding, J. Liu, and T. A. L. Harris, "A review of the operating limits in slot die coating processes," *AIChE J.*, vol. 62, pp. 2508–2524, jul 2016.

[279] S. Lee and J. Nam, "Analysis of slot coating flow under tilted die," *AIChE J.*, vol. 61, pp. 1745–1758, may 2015.

[280] H. Hu, Z. Ren, P. W. K. Fong, M. Qin, D. Liu, D. Lei, X. Lu, and G. Li, "Room-Temperature Meniscus Coating of >20% Perovskite Solar Cells: A Film Formation Mechanism Investigation," *Adv. Funct. Mater.*, vol. 29, p. 1900092, jun 2019.

[281] A. R. Pascoe, Q. Gu, M. U. Rothmann, W. Li, Y. Zhang, A. D. Scully, X. Lin, L. Spiccia, U. Bach, and Y.-B. B. Cheng, "Directing nucleation and growth kinetics in solution-processed hybrid perovskite thin-films," *Sci. China Mater.*, vol. 60, pp. 617–628, jul 2017.

[282] P. W. Fong, H. Hu, Z. Ren, K. Liu, L. Cui, T. Bi, Q. Liang, Z. Wu, J. Hao, and G. Li, "Printing High-Efficiency Perovskite Solar Cells in High-Humidity Ambient Environment-An In Situ Guided Investigation," *Adv. Sci.*, p. 2003359, jan 2021.

[283] H. Hu, M. Singh, X. Wan, J. Tang, C.-W. Chu, and G. Li, "Nucleation and crystal growth control for scalable solution-processed organic-inorganic hybrid perovskite solar cells," *J. Mater. Chem. A*, 2020.

[284] Y. Yang, Z. Xue, L. Chen, C. F. J. Lau, and Z. Wang, "Large-area perovskite films for PV applications: A perspective from nucleation and crystallization," *J. Energy Chem.*, vol. 59, pp. 626–641, aug 2021.

[285] V. K. LaMer and R. H. Dinegar, "Theory, Production and Mechanism of Formation of Monodispersed Hydrosols," *J. Am. Chem. Soc.*, 1950.

[286] L. Zeng, S. Chen, K. Forberich, C. J. Brabec, Y. Mai, and F. Guo, "Controlling the crystallization dynamics of photovoltaic perovskite layers on larger-area coatings," *Energy Environ. Sci.*, vol. 13, no. 12, pp. 4666–4690, 2020.

[287] J.-W. Lee, D.-K. Lee, D.-N. Jeong, and N.-G. Park, "Control of Crystal Growth toward Scalable Fabrication of Perovskite Solar Cells," *Adv. Funct. Mater.*, p. 1807047, dec 2018.

[288] P. P. von Weimarn, "The Precipitation Laws.," *Chem. Rev.*, vol. 2, pp. 217–242, jul 1925.

[289] J. Nývlt, "Kinetics of nucleation in solutions," *J. Cryst. Growth*, vol. 3-4, pp. 377–383, jan 1968.

[290] W. K. Burton, N. Cabrera, and F. C. Frank, "The growth of crystals and the equilibrium structure of their surfaces," *Philos. Trans. R. Soc. London. Ser. A, Math. Phys. Sci.*, vol. 243, pp. 299–358, jun 1951.

[291] D. Liu, W. Zhou, H. Tang, P. Fu, and Z. Ning, "Supersaturation controlled growth of MAFAPbI3 perovskite film for high efficiency solar cells," *Sci. China Chem.*, vol. 61, pp. 1278–1284, oct 2018.

[292] C. Liu, Y.-B. Cheng, and Z. Ge, "Understanding of perovskite crystal growth and film formation in scalable deposition processes.," *Chem. Soc. Rev.*, vol. 49, pp. 1653–1687, mar 2020.

[293] N. T. K. Thanh, N. Maclean, and S. Mahiddine, "Mechanisms of Nucleation and Growth of Nanoparticles in Solution," *Chem. Rev.*, vol. 114, pp. 7610–7630, aug 2014.

[294] Z. Wu, W. Li, Y. Ye, X. Li, and H. Lin, "Recent progress in meniscus coating for large-area perovskite solar cells and solar modules," *Sustain. Energy Fuels*, vol. 5, pp. 1926–1951, apr 2021.

[295] N. J. Jeon, J. H. Noh, Y. C. Kim, W. S. Yang, S. Ryu, and S. I. Seok, "Solvent engineering for high-performance inorganic-organic hybrid perovskite solar cells," *Nat. Mater.*, vol. 13, pp. 897–903, sep 2014.

[296] A. D. Taylor, Q. Sun, K. P. Goetz, Q. An, T. Schramm, Y. Hofstetter, M. Litterst, F. Paulus, and Y. Vaynzof, "A general approach to high-efficiency perovskite solar cells by any antisolvent," *Nat. Commun.*, vol. 12, p. 1878, dec 2021.

[297] M. Xiao, L. Zhao, M. Geng, Y. Li, B. Dong, Z. Xu, L. Wan, W. Li, and S. Wang, "Selection of an anti-solvent for efficient and stable cesium-containing triple cation planar perovskite solar cells," *Nanoscale*, vol. 10, no. 25, pp. 12141–12148, 2018.

[298] J. Kim, J. S. Yun, Y. Cho, D. S. Lee, B. Wilkinson, A. M. Soufiani, X. Deng, J. Zheng, A. Shi, S. Lim, S. Chen, Z. Hameiri, M. Zhang, C. F. J. Lau, S. Huang, M. A. Green, A. W. Y. Ho-Baillie, S. L. Da, B. Wilkinson, A. M. Soufiani, X. Deng, J. Zheng, A. Shi, S. Lim, S. Chen, Z. Hameiri, M. Zhang, C. F. J. Lau, S. Huang, M. A. Green, and A. W. Y. Ho-Baillie, "Overcoming the challenges of large-area high-efficiency perovskite solar cells," *ACS Energy Lett.*, vol. 2, pp. 1978–1984, sep 2017.

[299] D.-K. Lee and N.-G. Park, "Materials and Methods for High-Efficiency Perovskite Solar Modules," *Sol. RRL*, p. solr.202100455, sep 2021.

[300] Y. Zhou, M. Yang, W. Wu, A. L. Vasiliev, K. Zhu, and N. P. Padture, "Room-temperature crystallization of hybrid-perovskite thin films via solvent-solvent extraction for high-performance solar cells," *J. Mater. Chem. A*, vol. 3, no. 15, pp. 8178–8184, 2015.

[301] G. E. Eperon, T. Leijtens, K. A. Bush, R. Prasanna, T. Green, J. T.-W. Wang, D. P. McMeekin, G. Volonakis, R. L. Milot, R. May, A. Palmstrom, D. J. Slotcavage, R. A. Belisle, J. B. Patel, E. S. Parrott, R. J. Sutton, W. Ma, F. Moghadam, B. Conings, A. Babayigit, H.-G. Boyen, S. Bent, F. Giustino, L. M. Herz, M. B. Johnston, M. D. McGehee, and H. J. Snaith, "Perovskite-perovskite tandem photovoltaics with optimized band gaps," *Science (80-.).*, vol. 354, pp. 861–865, nov 2016.

[302] C. O. Ramírez Quiroz, I. Levchuk, C. Bronnbauer, M. Salvador, K. Forberich, T. Huemueller, Y. Hou, P. Schweizer, E. Spiecker, C. J. Brabec, T. Heumüller, Y. Hou, P. Schweizer, E. Spiecker, C. J. Brabec, T. Huemueller, Y. Hou, P. Schweizer, E. Spiecker, and C. J. Brabec, "Pushing Efficiency Limits for Semitransparent Perovskite Solar Cells," *J. Mater. Chem. A*, vol. 3, no. 47, pp. 24071–24081, 2015.

[303] H.-H. Huang, Q.-H. Liu, H. Tsai, S. Shrestha, L.-Y. Su, P.-T. Chen, Y.-T. Chen, T.-A. Yang, H. Lu, C.-H. Chuang, K.-F. Lin, S.-P. Rwei, W. Nie, and L. Wang, "A simple one-step

method with wide processing window for high-quality perovskite mini-module fabrication," *Joule*, mar 2021.

[304] G. Jang, S. Ma, H.-C. Kwon, S. Goh, H. Ban, J. Lee, C. Uk Lee, and J. Moon, "Binary antisolvent bathing enabled highly efficient and uniform large-area perovskite solar cells," *Chem. Eng. J.*, vol. 423, p. 130078, nov 2021.

[305] M. Yang, Z. Li, M. O. Reese, O. G. Reid, D. H. Kim, S. Siol, T. R. Klein, Y. Yan, J. J. Berry, M. F. A. M. van Hest, K. Zhu, and S. Information, "Perovskite ink with wide processing window for scalable high-efficiency solar cells," *Nat. Energy*, vol. 2, p. 17038, may 2017.

[306] M. Yang, D. H. Kim, T. R. Klein, Z. Li, M. O. Reese, B. J. Tremolet de Villers, J. J. Berry, M. F. A. M. van Hest, and K. Zhu, "Highly Efficient Perovskite Solar Modules by Scalable Fabrication and Interconnection Optimization," *ACS Energy Lett.*, vol. 3, pp. 322–328, feb 2018.

[307] L. Vesce, M. Stefanelli, J. P. Herterich, L. A. Castriotta, M. Kohlstädt, U. Würfel, and A. Di Carlo, "Ambient Air Blade-coating Fabrication of Stable Triple Cation Perovskite Solar Modules by Green Solvent Quenching," *Sol. RRL*, p. solr.202100073, may 2021.

[308] J. B. Whitaker, D. H. Kim, B. W. Larson, F. Zhang, J. J. Berry, M. F. A. M. van Hest, and K. Zhu, "Scalable slot-die coating of high performance perovskite solar cells," *Sustain. Energy Fuels*, vol. 2, no. 11, pp. 2442–2449, 2018.

[309] Z. Yang, W. Zhang, S. Wu, H. Zhu, Z. Liu, Z. Liu, Z. Jiang, R. Chen, J. Zhou, Q. Lu, Z. Xiao, L. Shi, H. Chen, L. K. Ono, S. Zhang, Y. Zhang, Y. Qi, L. Han, and W. Chen, "Slot-die coating large-area formamidinium-cesium perovskite film for efficient and stable parallel solar module," *Sci. Adv.*, vol. 7, p. eabg3749, apr 2021.

[310] B. Ding, Y. Li, S.-Y. Huang, Q.-Q. Chu, C.-J. C.-X. Li, C.-J. C.-X. Li, and G.-J. Yang, "Material nucleation/growth competition tuning towards highly reproducible planar perovskite solar cells with efficiency exceeding 20%," *J. Mater. Chem. A*, vol. 5, pp. 6840–6848, apr 2017.

[311] F. X. Xie, D. Zhang, H. Su, X. Ren, K. S. Wong, M. Grätzel, and W. C. H. Choy, "Vacuum-Assisted Thermal Annealing of CH 3 NH 3 PbI 3 for Highly Stable and Efficient Perovskite Solar Cells," *ACS Nano*, vol. 9, pp. 639–646, jan 2015.

[312] M. Liu, Z. Chen, Q. Xue, S. H. Cheung, S. K. So, H.-L. Yip, and Y. Cao, "High performance low-bandgap perovskite solar cells based on a high-quality mixed Sn-Pb perovskite film prepared by vacuum-assisted thermal annealing," *J. Mater. Chem. A*, vol. 6, pp. 16347–16354, aug 2018.

[313] C. Liang, P. Li, H. Gu, Y. Zhang, F. Li, Y. Song, G. Shao, N. Mathews, and G. Xing, "One-Step Inkjet Printed Perovskite in Air for Efficient Light Harvesting," *Sol. RRL*, vol. 2, p. 1700217, feb 2018.

[314] X. Li, D. Bi, C. Yi, J.-D. Decoppet, J. Luo, S. M. Zakeeruddin, A. Hagfeldt, and M. Gratzel, "A vacuum flash-assisted solution process for high-efficiency large-area perovskite solar cells," *Science (80-.).*, vol. 353, pp. 58–62, jul 2016.

[315] B. Ding, L. Gao, L. Liang, Q. Chu, X. Song, Y. Li, G. Yang, B. Fan, M. Wang, C. Li, and C. Li, "Facile and Scalable Fabrication of Highly Efficient Lead Iodide Perovskite Thin-Film Solar Cells in Air Using Gas Pump Method," *ACS Appl. Mater. Interfaces*, vol. 8, pp. 20067–20073, aug 2016.

[316] C. Wu, D. Wang, Y. Zhang, F. Gu, G. Liu, N. Zhu, W. Luo, D. Han, X. Guo, B. Qu, S. Wang, Z. Bian, Z. Chen, and L. Xiao, "FAPbI 3 Flexible Solar Cells with a Record Efficiency of 19.38% Fabricated in Air via Ligand and Additive Synergetic Process," *Adv. Funct. Mater.*, vol. 29, p. 1902974, aug 2019.

[317] B. Abdollahi Nejand, I. M. Hossain, M. Jakoby, S. Moghadamzadeh, T. Abzieher, S. Gharibzadeh, J. A. Schwenzer, P. Nazari, F. Schackmar, D. Hauschild, L. Weinhardt, U. Lemmer, B. S. Richards, I. A. Howard, and U. W. Paetzold, "Vacuum-Assisted Growth of Low-Bandgap Thin Films (FA 0.8 MA 0.2 Sn 0.5 Pb 0.5 I 3) for All-Perovskite Tandem Solar Cells," *Adv. Energy Mater.*, vol. 10, p. 1902583, feb 2020.

[318] F. Guo, W. He, S. Qiu, C. Wang, X. Liu, K. Forberich, C. J. Brabec, and Y. Mai, "Sequential Deposition of High-Quality Photovoltaic Perovskite Layers via Scalable Printing Methods," *Adv. Funct. Mater.*, vol. 29, p. 1900964, jun 2019.

[319] F. Guo, S. Qiu, J. Hu, H. Wang, B. Cai, J. Li, X. Yuan, X. Liu, K. Forberich, C. J. Brabec, and Y. Mai, "A Generalized Crystallization Protocol for Scalable Deposition of High-Quality Perovskite Thin Films for Photovoltaic Applications," *Adv. Sci.*, vol. 6, p. 1901067, sep 2019.

[320] C. Li, J. Yin, R. Chen, X. Lv, X. Feng, Y. Wu, and J. Cao, "Monoammonium Porphyrin for Blade-Coating Stable Large-Area Perovskite Solar Cells with >18% Efficiency," *J. Am. Chem. Soc.*, vol. 141, pp. 6345–6351, apr 2019.

[321] Z. Xu, R. Chen, Y. Wu, R. He, J. Yin, W. Lin, B. Wu, J. Li, and N. Zheng, "Br-containing alkyl ammonium salt-enabled scalable fabrication of high-quality perovskite films for efficient and stable perovskite modules," *J. Mater. Chem. A*, vol. 7, pp. 26849–26857, dec 2019.

[322] L. Zeng, Z. Chen, S. Qiu, J. Hu, C. Li, X. Liu, G. Liang, C. J. Brabec, Y. Mai, and F. Guo, "2D-3D heterostructure enables scalable coating of efficient low-bandgap Sn-Pb mixed perovskite solar cells," *Nano Energy*, vol. 66, p. 104099, dec 2019.

[323] Z. Wang, L. Zeng, C. Zhang, Y. Lu, S. Qiu, C. Wang, C. Liu, L. Pan, S. Wu, J. Hu, G. Liang, P. Fan, H. Egelhaaf, C. J. Brabec, F. Guo, and Y. Mai, "Rational Interface Design and Morphology Control for Blade-Coating Efficient Flexible Perovskite Solar Cells with a Record Fill Factor of 81%," *Adv. Funct. Mater.*, vol. 30, p. 2001240, aug 2020.

[324] C. Li, Y. Pan, J. Hu, S. Qiu, C. Zhang, Y. Yang, S. Chen, X. Liu, C. J. Brabec, M. K. Nazeeruddin, Y. Mai, and F. Guo, "Vertically Aligned 2D/3D Pb-Sn Perovskites with Enhanced Charge Extraction and Suppressed Phase Segregation for Efficient Printable Solar Cells," *ACS Energy Lett.*, pp. 1386–1395, apr 2020.

[325] J. Hu, C. Wang, S. Qiu, Y. Zhao, E. Gu, L. Zeng, Y. Yang, C. Li, X. Liu, K. Forberich, C. J. Brabec, M. K. Nazeeruddin, Y. Mai, and F. Guo, "Spontaneously Self-Assembly of a 2D/3D Heterostructure Enhances the Efficiency and Stability in Printed Perovskite Solar Cells," *Adv. Energy Mater.*, vol. 10, p. 2000173, may 2020.

[326] F. Yang, L. Dong, D. Jang, K. C. Tam, K. Zhang, N. Li, F. Guo, C. Li, C. Arrive, M. Bertrand, C. J. Brabec, and H. Egelhaaf, "Fully Solution Processed Pure α-Phase Formamidinium Lead Iodide Perovskite Solar Cells for Scalable Production in Ambient Condition," *Adv. Energy Mater.*, vol. 10, p. 2001869, nov 2020.

[327] Z. Huang, X. Hu, Z. Xing, X. Meng, X. Duan, J. Long, T. Hu, L. Tan, and Y. Chen, "Stabilized and Operational PbI 2 Precursor Ink for Large-Scale Perovskite Solar Cells via Two-Step Blade-Coating," *J. Phys. Chem. C*, vol. 124, pp. 8129–8139, apr 2020.

[328] M. Abbas, B. Cai, J. Hu, F. Guo, Y. Mai, and X.-C. Yuan, "Improving the Photovoltage of Blade-Coated MAPbI 3 Perovskite Solar Cells via Surface and Grain Boundary Passivation with π-Conjugated Phenyl Boronic Acids," *ACS Appl. Mater. Interfaces*, p. acsami.1c11335, sep 2021.

[329] I. Zimmermann, M. Al Atem, O. Fournier, S. Bernard, S. Jutteau, L. Lombez, and J. Rousset, "Sequentially Slot-Die-Coated Perovskite for Efficient and Scalable Solar Cells," *Adv. Mater. Interfaces*, p. 2100743, aug 2021.

[330] S. Bernard, S. Jutteau, S. Mejaouri, S. Cacovich, I. Zimmermann, A. Yaiche, S. Gbegnon, D. Loisnard, S. Collin, A. Duchatelet, F. Sauvage, and J. Rousset, "One-Step Slot-Die Coating Deposition of Wide-Bandgap Perovskite Absorber for Highly Efficient Solar Cells," *Sol. RRL*, vol. 5, p. 2100391, sep 2021.

[331] J. E. Bishop, J. A. Smith, C. Greenland, V. Kumar, N. Vaenas, O. S. Game, T. J. Routledge, M. Wong-Stringer, C. Rodenburg, and D. G. Lidzey, "High-Efficiency Spray-Coated Perovskite Solar Cells Utilizing Vacuum-Assisted Solution Processing," *ACS Appl. Mater. Interfaces*, vol. 10, pp. 39428–39434, nov 2018.

[332] H. Eggers, F. Schackmar, T. Abzieher, Q. Sun, U. Lemmer, Y. Vaynzof, B. S. Richards, G. Hernandez-Sosa, and U. W. Paetzold, "Inkjet-Printed Micrometer-Thick Perovskite Solar Cells with Large Columnar Grains," *Adv. Energy Mater.*, vol. 10, p. 1903184, feb 2020.

[333] F. Schackmar, H. Eggers, M. Frericks, B. S. Richards, U. Lemmer, G. Hernandez-Sosa, and U. W. Paetzold, "Perovskite Solar Cells with All-Inkjet-Printed Absorber and Charge Transport Layers," *Adv. Mater. Technol.*, p. 2000271, jul 2020.

[334] Z. Li, P. Li, G. Chen, Y. Cheng, X. Pi, X. Yu, D. Yang, L. Han, Y. Zhang, and Y. Song, "Ink Engineering of Inkjet Printing Perovskite," *ACS Appl. Mater. Interfaces*, vol. 12, pp. 39082–39091, sep 2020.

[335] Z. Xing, S. Lin, X. Meng, T. Hu, D. Li, B. Fan, Y. Cui, F. Li, X. Hu, and Y. Chen, "A Highly Tolerant Printing for Scalable and Flexible Perovskite Solar Cells," *Adv. Funct. Mater.*, p. 2107726, sep 2021.

[336] Z. Wang, Y. Lu, Z. Xu, J. Hu, Y. Chen, C. Zhang, Y. Wang, F. Guo, and Y. Mai, "An Embedding 2D/3D Heterostructure Enables High-Performance FA-Alloyed Flexible Perovskite Solar Cells with Efficiency over 20%," *Adv. Sci.*, p. 2101856, oct 2021.

[337] K. Liao, C. Li, L. Xie, Y. Yuan, S. Wang, Z. Cao, L. Ding, and F. Hao, "Hot-Casting Large-Grain Perovskite Film for Efficient Solar Cells: Film Formation and Device Performance," *Nano-Micro Lett.*, vol. 12, p. 156, dec 2020.

[338] J. Zhong, W. Wu, L. Ding, and D. Kuang, "Blade-coating Perovskite Films with Diverse Compositions for Efficient Photovoltaics," *ENERGY Environ. Mater.*, p. eem2.12118, sep 2020.

[339] W. Nie, H. Tsai, R. Asadpour, J.-C. J.-C. Blancon, A. J. Neukirch, G. Gupta, J. J. Crochet, M. Chhowalla, S. Tretiak, M. A. Alam, H.-L. H.-L. Wang, and A. D. Mohite, "High-efficiency solution-processed perovskite solar cells with millimeter-scale grains," *Science (80-.).*, vol. 347, pp. 522–525, jan 2015.

[340] Y. Deng, E. Peng, Y. Shao, Z. Xiao, Q. Dong, and J. Huang, "Scalable fabrication of efficient organolead trihalide perovskite solar cells with doctor-bladed active layers," *Energy Environ. Sci.*, vol. 8, no. 5, pp. 1544–1550, 2015.

[341] Z. Yang, C.-C. Chueh, F. Zuo, J. H. Kim, P.-W. Liang, and A. K.-Y. Jen, "High-Performance Fully Printable Perovskite Solar Cells via Blade-Coating Technique under the Ambient Condition," *Adv. Energy Mater.*, vol. 5, p. 1500328, jul 2015.

[342] Y. Deng, Q. Dong, C. Bi, Y. Yuan, and J. Huang, "Air-Stable, Efficient Mixed-Cation Perovskite Solar Cells with Cu Electrode by Scalable Fabrication of Active Layer," *Adv. Energy Mater.*, vol. 6, p. 1600372, jun 2016.

[343] H. Back, J. Kim, G. Kim, T. Kyun Kim, H. Kang, J. Kong, S. Ho Lee, and K. Lee, "Interfacial modification of hole transport layers for efficient large-area perovskite solar cells achieved via blade-coating," *Sol. Energy Mater. Sol. Cells*, vol. 144, pp. 309–315, 2016.

[344] S. Tang, Y. Deng, X. Zheng, Y. Bai, Y. Fang, Q. Dong, H. Wei, and J. Huang, "Composition Engineering in Doctor-Blading of Perovskite Solar Cells," *Adv. Energy Mater.*, vol. 7, p. 1700302, sep 2017.

[345] W.-Q. Wu, Q. Wang, Y. Fang, Y. Shao, S. Tang, Y. Deng, H. Lu, Y. Liu, T. Li, Z. Yang, A. Gruverman, and J. Huang, "Molecular doping enabled scalable blading of efficient hole-transport-layer-free perovskite solar cells," *Nat. Commun.*, vol. 9, p. 1625, dec 2018.

[346] W. Kong, G. Wang, J. Zheng, H. Hu, H. Chen, Y. Li, M. Hu, X. Zhou, C. Liu, B. N. Chandrashekar, A. Amini, J. Wang, B. Xu, and C. Cheng, "Fabricating High-Efficient Blade-Coated Perovskite Solar Cells under Ambient Condition Using Lead Acetate Trihydrate," *Sol. RRL*, vol. 2, p. 1700214, mar 2018.

[347] Q. Wang, M. Eslamian, T. Zhao, and A. K.-Y. Jen, "Achieving Fully Blade-Coated Ambient-Processed Perovskite Solar Cells by Controlling the Blade-Coater Temperature," *IEEE J. Photovoltaics*, vol. 8, pp. 1662–1669, nov 2018.

[348] J. Li, R. Munir, Y. Fan, T. Niu, Y. Liu, Y. Zhong, Z. Yang, Y. Tian, B. Liu, J. Sun, D.-M. Smilgies, S. Thoroddsen, A. Amassian, K. Zhao, and S. F. Liu, "Phase Transition Control for High-Performance Blade-Coated Perovskite Solar Cells," *Joule*, vol. 2, pp. 1313–1330, jul 2018.

[349] Y. Zhong, R. Munir, J. Li, M.-C. Tang, M. R. Niazi, D.-M. Smilgies, K. Zhao, and A. Amassian, "Blade-Coated Hybrid Perovskite Solar Cells with Efficiency > 17%: An In Situ Investigation," *ACS Energy Lett.*, vol. 3, pp. 1078–1085, may 2018.

[350] W.-q. Wu, Z. Yang, P. N. Rudd, Y. Shao, X. Dai, H. Wei, J. Zhao, Y. Fang, Q. Wang, Y. Liu, Y. Deng, X. Xiao, Y. Feng, and J. Huang, "Bilateral alkylamine for suppressing charge recombination and improving stability in blade-coated perovskite solar cells," *Sci. Adv.*, vol. 5, p. eaav8925, mar 2019.

[351] Y. Fan, J. Fang, X. Chang, M.-C. Tang, D. Barrit, Z. Xu, Z. Jiang, J. Wen, H. Zhao, T. Niu, D.-M. Smilgies, S. Jin, Z. Liu, E. Q. Li, A. Amassian, S. F. Liu, and K. Zhao, "Scalable Ambient Fabrication of High-Performance CsPbI2Br Solar Cells," *Joule*, vol. 3, pp. 2485–2502, oct 2019.

[352] W.-q. Wu, P. N. Rudd, Q. Wang, Z. Yang, and J. Huang, "Blading Phase-Pure Formamidinium-Alloyed Perovskites for High-Efficiency Solar Cells with Low Photovoltage Deficit and Improved Stability," *Adv. Mater.*, vol. 32, p. 2000995, jul 2020.

[353] M. He, B. Li, X. Cui, B. Jiang, Y. He, Y. Chen, D. O'Neil, P. Szymanski, M. A. EI-Sayed, J. Huang, and Z. Lin, "Meniscus-assisted solution printing of large-grained perovskite films for high-efficiency solar cells," *Nat. Commun.*, vol. 8, p. 16045, dec 2017.

[354] M. K. Kim, H. S. Lee, S. R. Pae, D.-J. Kim, J.-Y. Lee, I. Gereige, S. Park, and B. Shin, "Effects of temperature and coating speed on the morphology of solution-sheared halide perovskite thin-films," *J. Mater. Chem. A*, vol. 6, no. 48, pp. 24911–24919, 2018.

[355] G. B. Adugna, S. Y. Abate, W.-T. Wu, and Y.-T. Tao, "Toward Large-Area and Fully Solution-Sheared Perovskite Solar Cells," *ACS Appl. Mater. Interfaces*, vol. 13, pp. 25926–25936, jun 2021.

[356] J. Kim, S. Kim, C. Zuo, M. Gao, D. Vak, and D. Kim, "Humidity-Tolerant Roll-to-Roll Fabrication of Perovskite Solar Cells via Polymer-Additive-Assisted Hot Slot Die Deposition," *Adv. Funct. Mater.*, vol. 1809194, p. 1809194, may 2019.

[357] Q. Hu, L. Zhao, J. Wu, K. Gao, D. Luo, Y. Jiang, Z. Zhang, C. Zhu, E. Schaible, A. Hexemer, C. Wang, Y. Liu, W. Zhang, M. Grätzel, F. Liu, T. P. Russell, R. Zhu, and Q. Gong, "In situ dynamic observations of perovskite crystallisation and microstructure evolution intermediated from [PbI6]4-cage nanoparticles," *Nat. Commun.*, vol. 8, p. 15688, jun 2017.

[358] C. Zuo, A. D. Scully, D. Vak, W. Tan, X. Jiao, C. R. McNeill, D. Angmo, L. Ding, and M. Gao, "Self-Assembled 2D Perovskite Layers for Efficient Printable Solar Cells," *Adv. Energy Mater.*, vol. 9, p. 1803258, jan 2019.

[359] F. Xu, J. Liu, A. S. Subbiah, W. Liu, J. Kang, G. T. Harrison, X. Yang, F. H. Isikgor, E. Aydin, M. De Bastiani, and S. De Wolf, "Potassium Thiocyanate-Assisted Enhancement of Slot-Die-Coated Perovskite Films for High-Performance Solar Cells," *Small Sci.*, p. 2000044, feb 2021.

[360] A. Vijayan, M. B. Johansson, S. Svanström, U. B. Cappel, H. Rensmo, and G. Boschloo, "Simple Method for Efficient Slot-Die Coating of MAPbI 3 Perovskite Thin Films in Ambient Air Conditions," *ACS Appl. Energy Mater.*, vol. 3, pp. 4331–4337, may 2020.

[361] L. Gao, K. Huang, C. Long, F. Zeng, B. Liu, and J. Yang, "Fully slot-die-coated perovskite solar cells in ambient condition," *Appl. Phys. A*, vol. 126, p. 452, jun 2020.

[362] W.-C. Chang, D.-H. Lan, K.-M. Lee, X.-F. Wang, and C.-L. Liu, "Controlled Deposition and Performance Optimization of Perovskite Solar Cells Using Ultrasonic Spray-Coating of Photoactive Layers," *ChemSusChem*, vol. 10, pp. 1405–1412, apr 2017.

[363] J. H. Heo, M. H. Lee, M. H. Jang, and S. H. Im, "Highly efficient CH 3 NH 3 PbI 3-x Cl x mixed halide perovskite solar cells prepared by re-dissolution and crystal grain growth via spray coating," *J. Mater. Chem. A*, vol. 4, no. 45, pp. 17636–17642, 2016.

[364] C. Gao, P. Wang, H. Wang, C. Yu, B. Du, H. Zhang, T. Li, D. Liu, and T. Wang, "Binary Additive Engineering Enables Efficient Perovskite Solar Cells via Spray-Coating in Air," *ACS Appl. Energy Mater.*, p. acsaem.1c02235, sep 2021.

[365] N. Rolston, W. J. Scheideler, A. C. Flick, J. P. Chen, H. Elmaraghi, A. Sleugh, O. Zhao, M. Woodhouse, and R. H. Dauskardt, "Rapid Open-Air Fabrication of Perovskite Solar Modules," *Joule*, vol. 4, pp. 2675–2692, dec 2020.

[366] L. Huang, C. Li, X. Sun, R. Xu, Y. Du, J. Ni, H. Cai, J. Li, Z. Hu, and J. Zhang, "Efficient and hysteresis-less pseudo-planar heterojunction perovskite solar cells fabricated by a facile and solution-saving one-step dip-coating method," *Org. Electron.*, vol. 40, pp. 13–23, jan 2017.

[367] P. Li, C. Liang, B. Bao, Y. Li, X. Hu, Y. Wang, Y. Zhang, F. Li, G. Shao, and Y. Song, "Inkjet manipulated homogeneous large size perovskite grains for efficient and large-area perovskite solar cells," *Nano Energy*, vol. 46, pp. 203–211, apr 2018.

[368] Y. Yu, F. Zhang, T. Hou, X. Sun, H. Yu, and M. Zhang, "A Review on Gas-Quenching Technique for Efficient Perovskite Solar Cells," *Sol. RRL*, p. 2100386, aug 2021.

[369] F. Huang, Y. Dkhissi, W. Huang, M. Xiao, I. Benesperi, S. Rubanov, Y. Zhu, X. Lin, L. Jiang, Y. Zhou, A. Gray-Weale, J. Etheridge, C. R. McNeill, R. A. Caruso, U. Bach, L. Spiccia, and Y.-B. Cheng, "Gas-assisted preparation of lead iodide perovskite films consisting of a monolayer of single crystalline grains for high efficiency planar solar cells," *Nano Energy*, vol. 10, pp. 10–18, nov 2014.

[370] B. Conings, A. Babayigit, M. T. Klug, S. Bai, N. Gauquelin, N. Sakai, J. T. W. Wang, J. Verbeeck, H.-G. G. Boyen, H. J. Snaith, J. Tse, W. Wang, J. Verbeeck, H.-G. G. Boyen, and H. J. Snaith, "A Universal Deposition Protocol for Planar Heterojunction Solar Cells with High Efficiency Based on Hybrid Lead Halide Perovskite Families," *Adv. Mater.*, vol. 28, no. 48, pp. 10701–10709, 2016.

[371] L.-L. Gao, C.-X. C.-J. Li, C.-X. C.-J. Li, and G.-J. Yang, "Large-area high-efficiency perovskite solar cells based on perovskite films dried by the multi-flow air knife method in air," *J. Mater. Chem. A*, vol. 5, no. 4, pp. 1548–1557, 2017.

[372] K. O. Brinkmann, J. He, F. Schubert, J. Malerczyk, C. Kreusel, F. van gen Hassend, S. Weber, J. Song, J. Qu, and T. Riedl, "Extremely Robust Gas-Quenching Deposition of Halide Perovskites on Top of Hydrophobic Hole Transport Materials for Inverted (p-i-n) Solar Cells by Targeting the Precursor Wetting Issue," *ACS Appl. Mater. Interfaces*, vol. 11, pp. 40172–40179, oct 2019.

[373] S. Razza, F. Di Giacomo, F. Matteocci, L. Cinà, A. L. Palma, S. Casaluci, P. Cameron, A. D'Epifanio, S. Licoccia, A. Reale, T. M. Brown, and A. Di Carlo, "Perovskite solar cells and large area modules (100 cm 2) based on an air flow-assisted PbI 2 blade coating deposition process," *J. Power Sources*, vol. 277, pp. 286–291, mar 2015.

[374] M. Kohlstädt, M. A. Yakoob, and U. Würfel, "A Matter of Drying: Blade-Coating of Lead Acetate Sourced Planar Inverted Perovskite Solar Cells on Active Areas >1 cm 2," *Phys. status solidi*, vol. 215, p. 1800419, nov 2018.

[375] Y. Deng, C. H. Van Brackle, X. Dai, J. Zhao, B. Chen, and J. Huang, "Tailoring solvent coordination for high-speed, room-temperature blading of perovskite photovoltaic films," *Sci. Adv.*, vol. 5, p. eaax7537, dec 2019.

[376] Z. Ouyang, M. Yang, J. B. Whitaker, D. Li, and M. F. A. M. van Hest, "Toward Scalable Perovskite Solar Modules Using Blade Coating and Rapid Thermal Processing," *ACS Appl. Energy Mater.*, p. acsaem.0c00180, apr 2020.

[377] S. Chen, X. Xiao, B. Chen, L. L. Kelly, J. Zhao, Y. Lin, M. F. Toney, and J. Huang, "Crystallization in one-step solution deposition of perovskite films: Upward or downward?," *Sci. Adv.*, vol. 7, p. eabb2412, jan 2021.

[378] S. Chen, X. Dai, S. Xu, H. Jiao, L. Zhao, and J. Huang, "Stabilizing perovskite-substrate interfaces for high-performance perovskite modules," *Science (80-.).*, vol. 373, pp. 902–907, aug 2021.

[379] F. Yang, L. Dong, D. Jang, B. Saparov, K. C. Tam, K. Zhang, N. Li, C. J. Brabec, and H. Egelhaaf, "Low Temperature Processed Fully Printed Efficient Planar Structure Carbon Electrode Perovskite Solar Cells and Modules," *Adv. Energy Mater.*, p. 2101219, jun 2021.

[380] A. S. Marques, R. M. Faria, J. N. Freitas, and A. F. Nogueira, "Low-Temperature Blade-Coated Perovskite Solar Cells," *Ind. Eng. Chem. Res.*, p. acs.iecr.1c00789, may 2021.

[381] K. Hwang, Y.-S. Jung, Y.-J. Heo, F. H. Scholes, S. E. Watkins, J. Subbiah, D. J. Jones, D.-Y. Kim, and D. Vak, "Toward Large Scale Roll-to-Roll Production of Fully Printed Perovskite Solar Cells," *Adv. Mater.*, vol. 27, pp. 1241–1247, feb 2015.

[382] G. Cotella, J. Baker, D. Worsley, F. De Rossi, C. Pleydell-Pearce, M. Carnie, and T. Watson, "One-step deposition by slot-die coating of mixed lead halide perovskite for photovoltaic applications," *Sol. Energy Mater. Sol. Cells*, vol. 159, pp. 362–369, jan 2017.

[383] M. Du, X. Zhu, L. Wang, H. Wang, J. Feng, X. Jiang, Y. Cao, Y. Sun, L. Duan, Y. Jiao, K. Wang, X. Ren, Z. Yan, S. Pang, and S. F. Liu, "High-Pressure Nitrogen-Extraction and Effective Passivation to Attain Highest Large-Area Perovskite Solar Module Efficiency," *Adv. Mater.*, vol. 2004979, p. 2004979, oct 2020.

[384] D.-K. Lee, D.-N. Jeong, T. K. Ahn, and N.-G. Park, "Precursor Engineering for a Large-Area Perovskite Solar Cell with >19% Efficiency," *ACS Energy Lett.*, vol. 4, pp. 2393–2401, oct 2019.

[385] K.-S. Lim, D.-K. Lee, J.-W. Lee, and N.-G. Park, "17% efficient perovskite solar mini-module via hexamethylphosphoramide (HMPA)-adduct-based large-area D-bar coating," *J. Mater. Chem. A*, vol. 8, no. 18, pp. 9345–9354, 2020.

[386] D.-K. Lee, K.-S. Lim, J.-W. Lee, and N.-G. Park, "Scalable perovskite coating via anti-solvent-free Lewis acid-base adduct engineering for efficient perovskite solar modules," *J. Mater. Chem. A*, vol. 9, no. 5, pp. 3018–3028, 2021.

[387] J. W. Yoo, J. Jang, U. Kim, Y. Lee, S.-G. Ji, E. Noh, S. Hong, M. Choi, and S. I. Seok, "Efficient perovskite solar mini-modules fabricated via bar-coating using 2-methoxyethanol-based formamidinium lead tri-iodide precursor solution," *Joule*, sep 2021.

[388] J. Ding, Q. Han, Q.-Q. Ge, D.-J. Xue, J.-Y. Ma, B.-Y. Zhao, Y.-X. Chen, J. Liu, D. B. Mitzi, and J.-S. Hu, "Fully Air-Bladed High-Efficiency Perovskite Photovoltaics," *Joule*, vol. 3, pp. 402–416, feb 2019.

[389] X. Dai, Y. Deng, C. H. Van Brackle, S. Chen, P. N. Rudd, X. Xiao, Y. Lin, B. Chen, and J. Huang, "Scalable Fabrication of Efficient Perovskite Solar Modules on Flexible Glass Substrates," *Adv. Energy Mater.*, vol. 10, p. 1903108, jan 2020.

[390] L. A. Castriotta, R. Fuentes Pineda, V. Babu, P. Spinelli, B. Taheri, F. Matteocci, F. Brunetti, K. Wojciechowski, and A. Di Carlo, "Light-Stable Methylammonium-Free Inverted Flexible Perovskite Solar Modules on PET Exceeding 10.5% on a 15.7 cm 2 Active Area," *ACS Appl. Mater. Interfaces*, p. acsami.1c05506, jun 2021.

[391] A. Babayigit, J. D'Haen, H.-G. Boyen, and B. Conings, "Gas Quenching for Perovskite Thin Film Deposition," *Joule*, vol. 2, pp. 1205–1209, jul 2018.

[392] J.-E. Kim, Y.-S. Jung, Y.-J. Heo, K. Hwang, T. Qin, D.-Y. Kim, and D. Vak, "Slot die coated planar perovskite solar cells via blowing and heating assisted one step deposition," *Sol. Energy Mater. Sol. Cells*, vol. 179, pp. 80–86, jun 2018.

[393] F. Mathies, E. R. Nandayapa, G. Paramasivam, M. F. Al Rayes, V. R. F. Schröder, C. Rehermann, E. J. W. List-Kratochvil, and E. L. Unger, "Gas flow-assisted vacuum drying: identification of a novel process for attaining high-quality perovskite films," *Mater. Adv.*, 2021.

[394] M.-R. Ahmadian-Yazdi and M. Eslamian, "Effect of Marangoni Convection on the Perovskite Thin Liquid Film Deposition," *Langmuir*, vol. 37, pp. 2596–2606, mar 2021.

[395] R. A. Kraenkel, S. M. Kurcbart, J. G. Pereira, and M. A. Manna, "Dissipative Boussinesq system of equations in the Bénard-Marangoni phenomenon," *Phys. Rev. E*, vol. 49, pp. 1759–1762, feb 1994.

[396] A. V. Getling, "Formation of spatial structures in Rayleigh-Bénard convection," *Sov. Phys. Uspekhi*, vol. 34, pp. 737–776, sep 1991.

[397] F. Ye, W. Tang, F. Xie, M. Yin, J. He, Y. Wang, H. Chen, Y. Qiang, X. Yang, and L. Han, "Low-Temperature Soft-Cover Deposition of Uniform Large-Scale Perovskite Films for High-Performance Solar Cells," *Adv. Mater.*, vol. 29, p. 1701440, sep 2017.

[398] J. R. A. Pearson, "On convection cells induced by surface tension," *J. Fluid Mech.*, vol. 4, pp. 489–500, sep 1958.

[399] J. Anand and H. Karam, "Surface deformation of thin coatings caused by evaporative convection," *J. Colloid Interface Sci.*, vol. 31, pp. 208–215, oct 1969.

[400] M.-R. Ahmadian-Yazdi, A. Rahimzadeh, Z. Chouqi, Y. Miao, and M. Eslamian, "Viscosity, surface tension, density and contact angle of selected PbI 2 , PbCl 2 and methylammonium lead halide perovskite solutions used in perovskite solar cells," *AIP Adv.*, vol. 8, p. 025109, feb 2018.

[401] Y. Deng, Q. Wang, Y. Yuan, and J. Huang, "Vividly colorful hybrid perovskite solar cells by doctor-blade coating with perovskite photonic nanostructures," *Mater. Horiz.*, vol. 2, no. 6, pp. 578–583, 2015.

[402] R. Krechetnikov and G. M. Homsy, "Surfactant effects in the Landau-Levich problem," *J. Fluid Mech.*, vol. 559, p. 429, jul 2006.

[403] E. Parvazian, A. Abdollah-zadeh, M. M. Dehghani, and N. Taghavinia, "Photovoltaic Performance Improvement in Vacuum-Assisted Meniscus Printed Triple-Cation Mixed-Halide Perovskite Films by Surfactant Engineering," *ACS Appl. Energy Mater.*, vol. 2, pp. 6209–6217, aug 2019.

[404] J. Erz, *In-situ Visualisierung von Oberflächendeformationen aufgrund von Marangoni-Konvektion während der Filmtrocknung*. Phd thesis, Karlsruhe Institute of Technology (KIT), 2013.

[405] H.-S. H.-J. Kim, H.-S. H.-J. Kim, and N.-G. Park, "Progress of Perovskite Solar Modules," *Adv. Energy Sustain. Res.*, vol. 2, p. 2000051, jun 2021.

[406] C. Yang, R. Zhi, M. U. Rothmann, F. Huang, Y.-B. Cheng, and W. Li, "Towards commercialization of efficient and stable perovskite solar modules," *Sol. RRL*, sep 2021.

[407] M. Powalla, S. Paetel, E. Ahlswede, R. Wuerz, C. D. Wessendorf, and T. Magorian Friedlmeier, "Thin-film solar cells exceeding 22% solar cell efficiency: An overview on CdTe-, Cu(In,Ga)Se 2 -, and perovskite-based materials," *Appl. Phys. Rev.*, vol. 5, p. 041602, dec 2018.

[408] F. Di Giacomo, L. A. Castriotta, F. U. Kosasih, D. Di Girolamo, C. Ducati, and A. Di Carlo, "Upscaling Inverted Perovskite Solar Cells: Optimization of Laser Scribing for Highly Efficient Mini-Modules," *Micromachines*, vol. 11, p. 1127, dec 2020.

[409] J. Küffner, T. Wahl, M. Schultes, J. Hanisch, J. Zillner, E. Ahlswede, and M. Powalla, "Nanoparticle Wetting Agent for Gas Stream-Assisted Blade-Coated Inverted Perovskite Solar Cells and Modules," *ACS Appl. Mater. Interfaces*, vol. 12, pp. 52678–52690, nov 2020.

[410] G. Bogush, M. Tracy, and C. Zukoski, "Preparation of monodisperse silica particles: Control of size and mass fraction," *J. Non. Cryst. Solids*, vol. 104, pp. 95–106, aug 1988.

[411] M. Schultes, N. Giesbrecht, J. Küffner, E. Ahlswede, P. Docampo, T. Bein, and M. Powalla, "Universal Nanoparticle Wetting Agent for Upscaling Perovskite Solar Cells," *ACS Appl. Mater. Interfaces*, vol. 11, pp. 12948–12957, apr 2019.

[412] J. Küffner, T. Wahl, J. Hanisch, W. Hempel, E. Ahlswede, and M. Powalla, "Blade Coating Perovskite Solar Cells: Impacts of Surfactant in Absorber Layer," in *Proc. Int. Conf. Hybrid Org. Photovoltaics*, 2019.

[413] J. Küffner, J. Hanisch, T. Wahl, J. Zillner, E. Ahlswede, and M. Powalla, "One-Step Blade Coating of Inverted Double-Cation Perovskite Solar Cells from a Green Precursor Solvent," *ACS Appl. Energy Mater.*, p. acsaem.1c02425, sep 2021.

[414] A. V. Manu, *Additive Engineering of Slot-die Coated Perovskite for Solar Cells*. Bachelor thesis, Hochschule Düsseldorf, 2021.

[415] L. Tian, W. Zhang, Y. Huang, F. Wen, H. Yu, Y. Li, Q. Wang, C. Peng, Z. Ma, T. Hu, L. Du, and M. Zhang, "Effects of Annealing Time on Triple Cation Perovskite Films and Their Solar Cells," *ACS Appl. Mater. Interfaces*, vol. 12, p. acsami.0c06558, jun 2020.

[416] C. A. Schneider, W. S. Rasband, and K. W. Eliceiri, "NIH Image to ImageJ: 25 years of image analysis," *Nat. Methods*, vol. 9, pp. 671–675, jul 2012.

[417] X. Zheng, B. Chen, J. Dai, Y. Fang, Y. Bai, Y. Lin, H. Wei, X. C. Zeng, and J. Huang, "Defect passivation in hybrid perovskite solar cells using quaternary ammonium halide anions and cations," *Nat. Energy*, vol. 2, p. 17102, jul 2017.

[418] W.-Q. Wu, P. N. Rudd, Z. Ni, C. H. Van Brackle, H. Wei, Q. Wang, B. R. Ecker, Y. Gao, and J. Huang, "Reducing Surface Halide Deficiency for Efficient and Stable Iodide-Based Perovskite Solar Cells," *J. Am. Chem. Soc.*, vol. 142, pp. 3989–3996, feb 2020.

[419] A. S. Subbiah, F. H. Isikgor, C. T. Howells, M. De Bastiani, J. Liu, E. Aydin, F. Furlan, T. G. Allen, F. Xu, S. Zhumagali, S. Hoogland, E. H. Sargent, I. McCulloch, and S. De Wolf, "High-Performance Perovskite Single-Junction and Textured Perovskite/Silicon Tandem Solar Cells via Slot-Die-Coating," *ACS Energy Lett.*, vol. 5, no. 9, pp. 3034–3040, 2020.

[420] S. M. Hira and C. K. Payne, "Protein-mediated synthesis of the conducting polymer PEDOT:PSS," *Synth. Met.*, vol. 176, pp. 104–107, jul 2013.

[421] A. Banerji, S. Kirchmeyer, K. Meerholz, and F. Scharinger, "Teaching Organic Electronics - Part II: Quick & Easy Synthesis of the (Semi-)Conductive Polymer PEDOT: PSS in a Snap-Cap Vial," *World J. Chem. Educ.*, vol. 7, pp. 166–171, apr 2019.

[422] M.-c. Tang, Y. Fan, D. Barrit, X. Chang, H. X. Dang, R. Li, K. Wang, D.-m. Smilgies, S. F. Liu, S. De Wolf, T. D. Anthopoulos, K. Zhao, and A. Amassian, "Ambient blade coating of mixed cation, mixed halide perovskites without dripping: in situ investigation and highly efficient solar cells," *J. Mater. Chem. A*, vol. 8, no. 3, pp. 1095–1104, 2020.

[423] S. Ternes, T. Börnhorst, J. A. Schwenzer, I. M. Hossain, T. Abzieher, W. Mehlmann, U. Lemmer, P. Scharfer, W. Schabel, B. S. Richards, and U. W. Paetzold, "Drying Dynamics of Solution-Processed Perovskite Thin-Film Photovoltaics: In Situ Characterization, Modeling, and Process Control," *Adv. Energy Mater.*, vol. 9, p. 1901581, oct 2019.

[424] S. Ternes, F. Laufer, P. Scharfer, W. Schabel, B. S. Richards, I. A. Howard, and U. W. Paetzold, "Correlative in situ multi-channel imaging for large-area monitoring of morphology formation in solution processed perovskite layers," *Sol. RRL*, sep 2021.

[425] J. Qing, H.-T. Chandran, Y.-H. Cheng, X.-K. Liu, H.-W. Li, S.-W. Tsang, M.-F. Lo, and C.-S. Lee, "Chlorine Incorporation for Enhanced Performance of Planar Perovskite Solar Cell Based on Lead Acetate Precursor," *ACS Appl. Mater. Interfaces*, vol. 7, pp. 23110–23116, oct 2015.

[426] W. Zhang, M. Saliba, D. T. Moore, S. K. Pathak, M. T. Hörantner, T. Stergiopoulos, S. D. Stranks, G. E. Eperon, J. A. Alexander-Webber, A. Abate, A. Sadhanala, S. Yao, Y. Chen, R. H. Friend, L. A. Estroff, U. Wiesner, and H. J. Snaith, "Ultrasmooth organic-inorganic perovskite thin-film formation and crystallization for efficient planar heterojunction solar cells," *Nat. Commun.*, vol. 6, p. 6142, may 2015.

[427] Y. Xia, C. Ran, Y. Chen, Q. Li, N. Jiang, C. Li, Y. Pan, T. Li, J. P. Wang, and W. Huang, "Management of perovskite intermediates for highly efficient inverted planar heterojunction perovskite solar cells," *J. Mater. Chem. A*, vol. 5, no. 7, pp. 3193–3202, 2017.

[428] K.-m. Lee, C.-h. Lai, W.-c. Chu, S.-h. Chan, and V. Suryanarayanan, "Thermal assisted blade coating methylammonium lead iodide films with non-toxic solvent precursors for efficient perovskite solar cells and sub-module," *Sol. Energy*, vol. 204, pp. 337–345, jul 2020.

[429] Y. Yao, W.-L. Hsu, and M. Dagenais, "High-Efficiency Perovskite Solar Cell Based on Sequential Doping of PTAA," *IEEE J. Photovoltaics*, vol. 9, pp. 1025–1030, jul 2019.

[430] D. B. Khadka, Y. Shirai, M. Yanagida, and K. Miyano, "Unraveling the Impacts Induced by Organic and Inorganic Hole Transport Layers in Inverted Halide Perovskite Solar Cells," *ACS Appl. Mater. Interfaces*, vol. 11, pp. 7055–7065, feb 2019.

[431] D. B. Khadka, Y. Shirai, M. Yanagida, J. W. Ryan, and K. Miyano, "Exploring the effects of interfacial carrier transport layers on device performance and optoelectronic properties of planar perovskite solar cells," *J. Mater. Chem. C*, vol. 5, no. 34, pp. 8819–8827, 2017.

[432] M. Stolterfoht, P. Caprioglio, C. M. Wolff, J. A. Márquez, J. Nordmann, S. Zhang, D. Rothhardt, U. Hörmann, Y. Amir, A. Redinger, L. Kegelmann, F. Zu, S. Albrecht, N. Koch, T. Kirchartz, M. Saliba, T. Unold, and D. Neher, "The impact of energy alignment and interfacial recombination on the internal and external open-circuit voltage of perovskite solar cells," *Energy Environ. Sci.*, vol. 12, no. 9, pp. 2778–2788, 2019.

[433] X. Liu, Y. Cheng, C. Liu, T. Zhang, N. Zhang, S. Zhang, J. Chen, Q. Xu, J. Ouyang, and H. Gong, "20.7% highly reproducible inverted planar perovskite solar cells with enhanced fill factor and eliminated hysteresis," *Energy Environ. Sci.*, vol. 12, pp. 1622–1633, may 2019.

[434] D. Luo, W. Yang, Z. Wang, A. Sadhanala, Q. Hu, R. Su, R. Shivanna, G. F. Trindade, J. F. Watts, Z. Xu, T. Liu, K. Chen, F. Ye, P. Wu, L. Zhao, J. Wu, Y. Tu, Y. Zhang, X. Yang, W. Zhang, R. H. Friend, Q. Gong, H. J. Snaith, and R. Zhu, "Enhanced photovoltage for inverted planar heterojunction perovskite solar cells," *Science (80-.).*, vol. 360, pp. 1442–1446, jun 2018.

[435] Z. Liu, L. Krückemeier, B. Krogmeier, B. Klingebiel, J. A. Márquez, S. Levcenko, S. Öz, S. Mathur, U. Rau, T. Unold, and T. Kirchartz, "Open-Circuit Voltages Exceeding 1.26 V in Planar Methylammonium Lead Iodide Perovskite Solar Cells," *ACS Energy Lett.*, vol. 4, pp. 110–117, jan 2019.

[436] T. Liu, F. Jiang, F. Qin, W. Meng, Y. Jiang, S. Xiong, J. Tong, Z. Li, Y. Liu, and Y. Zhou, "Nonreduction-Active Hole-Transporting Layers Enhancing Open-Circuit Voltage and Efficiency of Planar Perovskite Solar Cells," *ACS Appl. Mater. Interfaces*, vol. 8, pp. 33899–33906, dec 2016.

[437] C. Xu, Z. Liu, and E.-C. Lee, "High-performance metal oxide-free inverted perovskite solar cells using poly(bis(4-phenyl)(2,4,6-trimethylphenyl)amine) as the hole transport layer," *J. Mater. Chem. C*, vol. 6, no. 26, pp. 6975–6981, 2018.

[438] C. Bi, Q. Wang, Y. Shao, Y. Yuan, Z. Xiao, and J. Huang, "Non-wetting surface-driven high-aspect-ratio crystalline grain growth for efficient hybrid perovskite solar cells," *Nat. Commun.*, vol. 6, p. 7747, nov 2015.

[439] F. H. Isikgor, A. S. Subbiah, M. K. Eswaran, C. T. Howells, A. Babayigit, M. De Bastiani, E. Yengel, J. Liu, F. Furlan, G. T. Harrison, S. Zhumagali, J. I. Khan, F. Laquai, T. D. Anthopoulos, I. McCulloch, U. Schwingenschlögl, and S. De Wolf, "Scaling-up perovskite solar cells on hydrophobic surfaces," *Nano Energy*, p. 105633, nov 2020.

[440] X. Xu, C. Ma, Y. Cheng, Y.-M. Xie, X. Yi, B. Gautam, S. Chen, H.-W. Li, C.-S. Lee, F. So, and S.-W. Tsang, "Ultraviolet-ozone surface modification for non-wetting hole transport materials based inverted planar perovskite solar cells with efficiency exceeding 18%," *J. Power Sources*, vol. 360, pp. 157–165, aug 2017.

[441] S. Zhang, M. Stolterfoht, A. Armin, Q. Lin, F. Zu, J. Sobus, H. Jin, N. Koch, P. Meredith, P. L. Burn, and D. Neher, "Interface Engineering of Solution-Processed Hybrid Organohalide Perovskite Solar Cells," *ACS Appl. Mater. Interfaces*, vol. 10, pp. 21681–21687, jun 2018.

[442] Q. Wang, C. Bi, and J. Huang, "Doped hole transport layer for efficiency enhancement in planar heterojunction organolead trihalide perovskite solar cells," *Nano Energy*, vol. 15, pp. 275–280, 2015.

[443] C. M. Wolff, F. Zu, A. Paulke, L. P. Toro, N. Koch, and D. Neher, "Reduced Interface-Mediated Recombination for High Open-Circuit Voltages in CH3NH3PbI3 Solar Cells," *Adv. Mater.*, vol. 29, no. 28, pp. 1–8, 2017.

[444] M. Schultes, T. Helder, E. Ahlswede, M. F. Aygüler, P. Jackson, S. Paetel, J. A. Schwenzer, I. M. Hossain, U. W. Paetzold, and M. Powalla, "Sputtered Transparent Electrodes (IO:H and IZO) with Low Parasitic Near-Infrared Absorption for Perovskite-Cu(In,Ga)Se 2 Tandem Solar Cells," *ACS Appl. Energy Mater.*, vol. 2, pp. 7823–7831, nov 2019.

[445] B. Thomas Young and M. D. For Sec, "III. An essay on the cohesion of fluids," *Philos. Trans. R. Soc. London*, vol. 95, pp. 65–87, dec 1805.

[446] J. You, F. Guo, S. Qiu, W. He, C. Wang, X. Liu, W. Xu, and Y. Mai, "The fabrication of homogeneous perovskite films on non-wetting interfaces enabled by physical modification," *J. Energy Chem.*, vol. 38, pp. 192–198, nov 2019.

[447] J. Hu, J. You, C. Peng, S. Qiu, W. He, C. Li, X. Liu, Y. Mai, and F. Guo, "Polyfluorene Copolymers as High-Performance Hole-Transport Materials for Inverted Perovskite Solar Cells," *Sol. RRL*, vol. 4, p. 1900384, mar 2020.

[448] D. Lee, Y.-S. Jung, Y.-J. Heo, S. Lee, K. Hwang, Y.-J. Jeon, J.-E. Kim, J. Park, G. Y. Jung, and D.-Y. Kim, "Slot-Die Coated Perovskite Films Using Mixed Lead Precursors for Highly Reproducible and Large-Area Solar Cells," *ACS Appl. Mater. Interfaces*, vol. 10, pp. 16133–16139, may 2018.

[449] Q. Dong, Y. Yuan, Y. Shao, Y. Fang, Q. Wang, and J. Huang, "Abnormal crystal growth in CH 3 NH 3 PbI 3-x Cl x using a multi-cycle solution coating process," *Energy Environ. Sci.*, vol. 8, no. 8, pp. 2464–2470, 2015.

[450] B. Chen, Z. J. Yu, S. Manzoor, S. Wang, W. Weigand, Z. Yu, G. Yang, Z. Ni, X. Dai, Z. C. Holman, and J. Huang, "Blade-Coated Perovskites on Textured Silicon for 26%-Efficient Monolithic Perovskite/Silicon Tandem Solar Cells," *Joule*, vol. 4, pp. 850–864, apr 2020.

[451] H. Yu, F. Wang, F. Xie, W. Li, J. Chen, and N. Zhao, "The Role of Chlorine in the Formation Process of CH 3 NH 3 PbI 3-x Cl x Perovskite," *Adv. Funct. Mater.*, vol. 24, pp. n/a–n/a, sep 2014.

[452] C. M. M. Soe, C. C. Stoumpos, B. Harutyunyan, E. F. Manley, L. X. Chen, M. J. Bedzyk, T. J. Marks, and M. G. Kanatzidis, "Room Temperature Phase Transition in Methylammonium Lead Iodide Perovskite Thin Films Induced by Hydrohalic Acid Additives," *ChemSusChem*, vol. 9, pp. 2656–2665, sep 2016.

[453] F. Matteocci, Y. Busby, J.-J. Pireaux, G. Divitini, S. Cacovich, C. Ducati, and A. Di Carlo, "Interface and Composition Analysis on Perovskite Solar Cells," *ACS Appl. Mater. Interfaces*, vol. 7, pp. 26176–26183, dec 2015.

[454] H. Min, M. Kim, S.-U. Lee, H. Kim, G. Kim, K. Choi, J. H. Lee, and S. I. Seok, "Efficient, stable solar cells by using inherent bandgap of α-phase formamidinium lead iodide," *Science (80-.).*, vol. 366, pp. 749–753, nov 2019.

[455] S. Bai, P. Da, C. Li, Z. Wang, Z. Yuan, F. Fu, M. Kawecki, X. Liu, N. Sakai, J. T.-W. Wang, S. Huettner, S. Buecheler, M. Fahlman, F. Gao, and H. J. Snaith, "Planar perovskite solar cells with long-term stability using ionic liquid additives," *Nature*, vol. 571, pp. 245–250, jul 2019.

[456] M. Ralaiarisoa, Y. Busby, J. Frisch, I. Salzmann, J.-J. Pireaux, and N. Koch, "Correlation of annealing time with crystal structure, composition, and electronic properties of CH 3 NH 3 PbI 3-x Cl x mixed-halide perovskite films," *Phys. Chem. Chem. Phys.*, vol. 19, no. 1, pp. 828–836, 2017.

[457] H.-Y. Lin, G.-S. Liou, W.-Y. Lee, and W.-C. Chen, "Poly(triarylamine): Its synthesis, properties, and blend with polyfluorene for white-light electroluminescence," *J. Polym. Sci. Part A Polym. Chem.*, vol. 45, pp. 1727–1736, may 2007.

[458] M. Saliba, J.-P. Correa-Baena, C. M. Wolff, M. Stolterfoht, N. Phung, S. Albrecht, D. Neher, and A. Abate, "How to Make over 20% Efficient Perovskite Solar Cells in Regular (n-i-p) and Inverted (p-i-n) Architectures," *Chem. Mater.*, vol. 30, pp. 4193–4201, jul 2018.

[459] M. Saliba, T. Matsui, K. Domanski, J.-Y. Seo, A. Ummadisingu, S. M. Zakeeruddin, J.-P. Correa-Baena, W. R. Tress, A. Abate, A. Hagfeldt, and M. Gratzel, "Incorporation of rubidium cations into perovskite solar cells improves photovoltaic performance," *Science (80-.).*, vol. 354, pp. 206–209, oct 2016.

[460] D. P. McMeekin, G. Sadoughi, W. Rehman, G. E. Eperon, M. Saliba, M. T. Horantner, A. Haghighirad, N. Sakai, L. Korte, B. Rech, M. B. Johnston, L. M. Herz, and H. J. Snaith, "A mixed-cation lead mixed-halide perovskite absorber for tandem solar cells," *Science (80-.).*, vol. 351, pp. 151–155, jan 2016.

[461] D. Luo, L. Zhao, J. Wu, Q. Hu, Y. Zhang, Z. Xu, Y. Liu, T. Liu, K. Chen, W. Yang, W. Zhang, R. Zhu, and Q. Gong, "Dual-Source Precursor Approach for Highly Efficient Inverted Planar Heterojunction Perovskite Solar Cells," *Adv. Mater.*, vol. 29, p. 1604758, may 2017.

[462] S. Gharibzadeh, B. Abdollahi Nejand, M. Jakoby, T. Abzieher, D. Hauschild, S. Moghadamzadeh, J. A. Schwenzer, P. Brenner, R. Schmager, A. A. Haghighirad, L. Weinhardt, U. Lemmer, B. S. Richards, I. A. Howard, and U. W. Paetzold, "Record Open-Circuit Voltage Wide-Bandgap Perovskite Solar Cells Utilizing 2D/3D Perovskite Heterostructure," *Adv. Energy Mater.*, vol. 9, p. 1803699, jun 2019.

[463] D. Prochowicz, P. Yadav, M. Saliba, D. J. Kubicki, M. M. Tavakoli, S. M. Zakeeruddin, J. Lewiński, L. Emsley, and M. Grätzel, "One-step mechanochemical incorporation of an insoluble cesium additive for high performance planar heterojunction solar cells," *Nano Energy*, vol. 49, pp. 523–528, jul 2018.

[464] M. Aamir, T. Adhikari, M. Sher, N. Revaprasadu, W. Khalid, J. Akhtar, and J.-M. Nunzi, "Fabrication of planar heterojunction CsPbBr 2 I perovskite solar cells using ZnO as an electron transport layer and improved solar energy conversion efficiency," *New J. Chem.*, vol. 42, pp. 14104–14110, aug 2018.

[465] L. K. Ono, N.-G. Park, K. Zhu, W. Huang, and Y. Qi, "Perovskite Solar Cells-Towards Commercialization," *ACS Energy Lett.*, vol. 2, pp. 1749–1751, aug 2017.

[466] R. Swartwout, R. Patidir, E. Belliveau, B. Dou, D. Beynon, P. Greenwood, N. Moody, D. W. DeQuilettes, M. Bawendi, T. M. Watson, and V. Bulovic, "Predicting Low Toxicity and Scalable Solvent Systems for High Speed Roll-to-Roll Perovskite Manufacturing," *ChemRxiv*, nov 2020.

[467] M. Zhang, D. Xin, X. Zheng, Q. Chen, and W.-H. Zhang, "Toward Greener Solution Processing of Perovskite Solar Cells," *ACS Sustain. Chem. Eng.*, vol. 8, pp. 13126–13138, sep 2020.

[468] C. Capello, U. Fischer, and K. Hungerbühler, "What is a green solvent? A comprehensive framework for the environmental assessment of solvents," *Green Chem.*, vol. 9, p. 927, aug 2007.

[469] A. Babaei, L. Albero-Blanquer, A. M. Igual-Muñoz, D. Pérez-Del-Rey, M. Sessolo, H. J. Bolink, and R. Tadmouri, "Hansen theory applied to the identification of nonhazardous solvents for hybrid perovskite thin-films processing," *Polyhedron*, vol. 147, pp. 9–14, jun 2018.

[470] S. Huang, C. Guan, P. Lee, H. Huang, C. Li, Y. Huang, and W. Su, "Toward All Slot-Die Fabricated High Efficiency Large Area Perovskite Solar Cell Using Rapid Near Infrared Heating in Ambient Air," *Adv. Energy Mater.*, vol. 2001567, p. 2001567, jul 2020.

[471] S. Öz, J. Burschka, E. Jung, R. Bhattacharjee, T. Fischer, A. Mettenbörger, H. Wang, and S. Mathur, "Protic ionic liquid assisted solution processing of lead halide perovskites with water, alcohols and acetonitrile," *Nano Energy*, vol. 51, pp. 632–638, sep 2018.

[472] Z. Bi, X. Rodríguez-Martínez, C. Aranda, E. Pascual-San-José, A. R. Goñi, M. Campoy-Quiles, X. Xu, and A. Guerrero, "Defect tolerant perovskite solar cells from blade coated non-toxic solvents," *J. Mater. Chem. A*, vol. 6, no. 39, pp. 19085–19093, 2018.

[473] C. Worsley, D. Raptis, S. Meroni, A. Doolin, R. Garcia-Rodriguez, M. Davies, and T. Watson, "γ-Valerolactone: A Nontoxic Green Solvent for Highly Stable Printed Mesoporous Perovskite Solar Cells," *Energy Technol.*, p. 2100312, may 2021.

[474] L. A. Castriotta, F. Matteocci, L. Vesce, L. Cinà, A. Agresti, S. Pescetelli, A. Ronconi, M. Löffler, M. M. Stylianakis, F. Di Giacomo, P. Mariani, M. Stefanelli, E. M. Speller, A. Alfano, B. Paci, A. Generosi, F. Di Fonzo, A. Petrozza, B. Rellinghaus, E. Kymakis, and

A. Di Carlo, "Air-Processed Infrared-Annealed Printed Methylammonium-Free Perovskite Solar Cells and Modules Incorporating Potassium-Doped Graphene Oxide as an Interlayer," *ACS Appl. Mater. Interfaces*, p. acsami.0c18920, mar 2021.

[475] H. Li, T. Bu, J. Li, Z. Lin, J. Pan, Q. Li, X.-L. Zhang, Z. Ku, Y.-B. Cheng, and F. Huang, "Ink Engineering for Blade Coating FA-Dominated Perovskites in Ambient Air for Efficient Solar Cells and Modules," *ACS Appl. Mater. Interfaces*, p. acsami.1c00900, apr 2021.

[476] N. Li, J. Liu, C. Li, Y. Li, J. Jia, Y. Wu, H. Yu, B. Yuan, and B. Cao, "Zwitterion-Stabilizing Scalable Bladed α-Phase Cs 0.1 FA 0.9 PbI 3 Films for Efficient Inverted Planar Perovskite Solar Cells," *ACS Sustain. Chem. Eng.*, vol. 8, pp. 7020–7030, may 2020.

[477] D. Burkitt, R. Swartwout, J. McGettrick, P. Greenwood, D. Beynon, R. Brenes, V. Bulović, and T. Watson, "Acetonitrile based single step slot-die compatible perovskite ink for flexible photovoltaics," *RSC Adv.*, vol. 9, no. 64, pp. 37415–37423, 2019.

[478] D. Burkitt, R. Patidar, P. Greenwood, K. Hooper, J. McGettrick, S. Dimitrov, M. Colombo, V. Stoichkov, D. Richards, D. Beynon, M. Davies, and T. Watson, "Roll-to-roll slot-die coated P-I-N perovskite solar cells using acetonitrile based single step perovskite solvent system," *Sustain. Energy Fuels*, no. c, pp. 1–5, 2020.

[479] J. Li, J. Dagar, O. Shargaieva, M. A. Flatken, H. Köbler, M. Fenske, C. Schultz, B. Stegemann, J. Just, D. M. Többens, A. Abate, R. Munir, and E. Unger, "20.8% Slot-Die Coated MAPbI 3 Perovskite Solar Cells by Optimal DMSO-Content and Age of 2-ME Based Precursor Inks," *Adv. Energy Mater.*, vol. 11, p. 2003460, mar 2021.

[480] N. Park, "Research Direction toward Scalable, Stable, and High Efficiency Perovskite Solar Cells," *Adv. Energy Mater.*, vol. 10, p. 1903106, apr 2020.

[481] Y. Deng, S. Xu, S. Chen, X. Xiao, J. Zhao, and J. Huang, "Defect compensation in formamidinium-caesium perovskites for highly efficient solar mini-modules with improved photostability," *Nat. Energy*, pp. 1–9, may 2021.

[482] B. Wilk, S. Öz, E. Radicchi, F. Ünlü, T. Ahmad, A. P. Herman, F. Nunzi, S. Mathur, R. Kudrawiec, and K. Wojciechowski, "Green Solvent-Based Perovskite Precursor Development for Ink-Jet Printed Flexible Solar Cells," *ACS Sustain. Chem. Eng.*, p. acssuschemeng.0c09208, mar 2021.

[483] F. P. Byrne, S. Jin, G. Paggiola, T. H. M. Petchey, J. H. Clark, T. J. Farmer, A. J. Hunt, C. Robert McElroy, and J. Sherwood, "Tools and techniques for solvent selection: green solvent selection guides," *Sustain. Chem. Process.*, vol. 4, p. 7, dec 2016.

[484] E. Gu, X. Tang, S. Langner, P. Duchstein, Y. Zhao, I. Levchuk, V. Kalancha, T. Stubhan, J. Hauch, H. J. Egelhaaf, D. Zahn, A. Osvet, and C. J. Brabec, "Robot-Based High-Throughput Screening of Antisolvents for Lead Halide Perovskites," *Joule*, vol. 4, pp. 1806–1822, aug 2020.

[485] J. C. Hamill, J. Schwartz, and Y.-L. Loo, "Influence of Solvent Coordination on Hybrid Organic-Inorganic Perovskite Formation," *ACS Energy Lett.*, vol. 3, pp. 92–97, jan 2018.

[486] M. Geppert-Rybczyńska, J. K. Lehmann, J. Safarov, and A. Heintz, "Thermodynamic surface properties of [BMIm][NTf2] or [EMIm][NTf2] binary mixtures with tetrahydrofuran, acetonitrile or dimethylsulfoxide," *J. Chem. Thermodyn.*, vol. 62, pp. 104–110, jul 2013.

[487] K. Liu, Q. Liang, M. Qin, D. Shen, H. Yin, Z. Ren, Y. Zhang, H. Zhang, P. W. Fong, Z. Wu, J. Huang, J. Hao, Z. Zheng, S. K. So, C.-s. Lee, X. Lu, and G. Li, "Zwitterionic-Surfactant-Assisted Room-Temperature Coating of Efficient Perovskite Solar Cells," *Joule*, pp. 1–22, oct 2020.

[488] D.-N. Jeong, D.-K. Lee, S. Seo, S. Y. Lim, Y. Zhang, H. Shin, H. Cheong, and N.-G. Park, "Perovskite Cluster-Containing Solution for Scalable D-Bar Coating toward High-Throughput Perovskite Solar Cells," *ACS Energy Lett.*, vol. 4, pp. 1189–1195, may 2019.

[489] O. Shargaieva, H. Näsström, J. A. Smith, D. Többens, R. Munir, and E. Unger, "Hybrid perovskite crystallization from binary solvent mixtures: interplay of evaporation rate and binding strength of solvents," *Mater. Adv.*, vol. 1, no. 9, pp. 3314–3321, 2020.

[490] M. Ozaki, A. Shimazaki, M. Jung, Y. Nakaike, N. Maruyama, S. Yakumaru, A. I. Rafieh, T. Sasamori, N. Tokitoh, P. Ekanayake, Y. Murata, R. Murdey, and A. Wakamiya, "A Purified, Solvent-Intercalated Precursor Complex for Wide-Process-Window Fabrication of Efficient Perovskite Solar Cells and Modules," *Angew. Chemie*, vol. 131, pp. 9489–9493, jul 2019.

[491] D. Burkitt, J. Searle, D. Worsley, and T. Watson, "Sequential Slot-Die Deposition of Perovskite Solar Cells Using Dimethylsulfoxide Lead Iodide Ink," *Materials (Basel).*, vol. 11, p. 2106, oct 2018.

[492] S. Masi, C. Echeverría-Arrondo, K. M. M. Salim, T. T. Ngo, P. F. Mendez, E. López-Fraguas, D. F. Macias-Pinilla, J. Planelles, J. I. Climente, and I. Mora-Seró, "Chemi-Structural Stabilization of Formamidinium Lead Iodide Perovskite by Using Embedded Quantum Dots," *ACS Energy Lett.*, vol. 5, pp. 418–427, feb 2020.

[493] Y.-H. Seo, E.-C. Kim, S.-P. Cho, S.-S. Kim, and S.-I. Na, "High-performance planar perovskite solar cells: Influence of solvent upon performance," *Appl. Mater. Today*, vol. 9, pp. 598–604, dec 2017.

[494] A. Giuri, S. Masi, A. Listorti, G. Gigli, S. Colella, C. Esposito Corcione, and A. Rizzo, "Polymeric rheology modifier allows single-step coating of perovskite ink for highly efficient and stable solar cells," *Nano Energy*, vol. 54, pp. 400–408, dec 2018.

[495] Y. Zhang, M. Chen, Y. Zhou, W. Li, Y. Lee, H. Kanda, X. Gao, R. Hu, K. G. Brooks, R. Zia, S. Kinge, N. P. Padture, and M. K. Nazeeruddin, "The Synergism of DMSO and Diethyl Ether for Highly Reproducible and Efficient MA 0.5 FA 0.5 PbI 3 Perovskite Solar Cells," *Adv. Energy Mater.*, vol. 10, p. 2001300, aug 2020.

[496] A. Al-Ashouri, E. Köhnen, B. Li, A. Magomedov, H. Hempel, P. Caprioglio, J. A. Márquez, A. B. Morales Vilches, E. Kasparavicius, J. A. Smith, N. Phung, D. Menzel, M. Grischek, L. Kegelmann, D. Skroblin, C. Gollwitzer, T. Malinauskas, M. Jošt, G. Matič, B. Rech, R. Schlatmann, M. Topič, L. Korte, A. Abate, B. Stannowski, D. Neher, M. Stolterfoht, T. Unold, V. Getautis, and S. Albrecht, "Monolithic perovskite/silicon tandem solar cell with >29% efficiency by enhanced hole extraction," *Science (80-.).*, vol. 370, pp. 1300–1309, dec 2020.

[497] H. Ying, Y. Liu, Y. Dou, J. Zhang, Z. Wu, Q. Zhang, Y.-B. Cheng, and J. Zhong, "Surfactant-assisted doctor-blading-printed FAPbBr3 films for efficient semitransparent perovskite solar cells," *Front. Optoelectron.*, pp. 1–10, jul 2020.

[498] M. Fievez, P. J. Singh Rana, T. M. Koh, M. Manceau, J. H. Lew, N. F. Jamaludin, B. Ghosh, A. Bruno, S. Cros, S. Berson, S. G. Mhaisalkar, and W. L. Leong, "Slot-die coated methylammonium-free perovskite solar cells with 18% efficiency," *Sol. Energy Mater. Sol. Cells*, vol. 230, p. 111189, sep 2021.

[499] M. Jaysankar, W. Qiu, J. Bastos, J. G. Tait, M. Debucquoy, U. W. Paetzold, D. Cheyns, and J. Poortmans, "Crystallisation dynamics in wide-bandgap perovskite films," *J. Mater. Chem. A*, vol. 4, no. 27, pp. 10524–10531, 2016.

[500] X. Ren, Z. Yang, D. Yang, X. Zhang, D. Cui, Y. Liu, Q. Wei, H. Fan, and S. F. Liu, "Modulating crystal grain size and optoelectronic properties of perovskite films for solar cells by reaction temperature," *Nanoscale*, vol. 8, pp. 3816–3822, feb 2016.

[501] X. Cao, L. Zhi, Y. Jia, Y. Li, X. Cui, K. Zhao, L. Ci, K. Ding, and J. Wei, "High annealing temperature induced rapid grain coarsening for efficient perovskite solar cells," *J. Colloid Interface Sci.*, vol. 524, pp. 483–489, aug 2018.

[502] J. Xu, C. C. Boyd, Z. J. Yu, A. F. Palmstrom, D. J. Witter, B. W. Larson, R. M. France, J. Werner, S. P. Harvey, E. J. Wolf, W. Weigand, S. Manzoor, M. F. A. M. van Hest, J. J. Berry, J. M. Luther, Z. C. Holman, and M. D. McGehee, "Triple-halide wide-band gap perovskites with suppressed phase segregation for efficient tandems," *Science (80-.).*, vol. 367, pp. 1097–1104, mar 2020.

[503] M. Saliba and L. Etgar, "Current Density Mismatch in Perovskite Solar Cells," *ACS Energy Lett.*, vol. 5, pp. 2886–2888, sep 2020.

[504] B. Chen, Z. Yu, K. Liu, X. Zheng, Y. Liu, J. Shi, D. Spronk, P. N. Rudd, Z. Holman, and J. Huang, "Grain Engineering for Perovskite/Silicon Monolithic Tandem Solar Cells with Efficiency of 25.4%," *Joule*, vol. 3, pp. 177–190, jan 2019.

[505] M. Mangrulkar and K. J. Stevenson, "The Progress of Additive Engineering for CH3NH3PbI3 Photo-Active Layer in the Context of Perovskite Solar Cells," *Crystals*, vol. 11, p. 814, jul 2021.

[506] M. M. Tavakoli, P. Yadav, D. Prochowicz, M. Sponseller, A. Osherov, V. Bulović, and J. Kong, "Controllable Perovskite Crystallization via Antisolvent Technique Using Chloride Additives for Highly Efficient Planar Perovskite Solar Cells," *Adv. Energy Mater.*, vol. 9, p. 1803587, may 2019.

[507] J. Dagar, M. Fenske, A. Al-Ashouri, C. Schultz, B. Li, H. Köbler, R. Munir, G. Parmasivam, J. Li, I. Levine, A. Merdasa, L. Kegelmann, H. Näsström, J. A. Marquez, T. Unold, D. M. Többens, R. Schlatmann, B. Stegemann, A. Abate, S. Albrecht, and E. Unger, "Compositional and Interfacial Engineering Yield High-Performance and Stable p-i-n Perovskite Solar Cells and Mini-Modules," *ACS Appl. Mater. Interfaces*, vol. 13, pp. 13022–13033, mar 2021.

[508] M. Lyu and N.-G. Park, "Effect of Additives AX (A = FA, MA, Cs, Rb, NH 4 , X = Cl, Br, I) in FAPbI 3 on Photovoltaic Parameters of Perovskite Solar Cells," *Sol. RRL*, vol. 4, p. 2000331, oct 2020.

[509] A. Suzuki, M. Kato, N. Ueoka, and T. Oku, "Additive Effect of Formamidinium Chloride in Methylammonium Lead Halide Compound-Based Perovskite Solar Cells," *J. Electron. Mater.*, vol. 48, pp. 3900–3907, jun 2019.

[510] Y. Wu, X. Li, S. Fu, L. Wan, and J. Fang, "Efficient methylammonium lead trihalide perovskite solar cells with chloroformamidinium chloride (Cl-FACl) as an additive," *J. Mater. Chem. A*, vol. 7, pp. 8078–8084, apr 2019.

[511] S. You, X. Xi, X. Zhang, H. Wang, P. Gao, X. Ma, S. Bi, J. Zhang, H. Zhou, and Z. Wei, "Long-term stable and highly efficient perovskite solar cells with a formamidinium chloride (FACl) additive," *J. Mater. Chem. A*, vol. 8, no. 34, pp. 17756–17764, 2020.

[512] M. M. Byranvand and M. Saliba, "Defect Passivation of Perovskite Films for Highly Efficient and Stable Solar Cells," *Sol. RRL*, vol. 5, p. 2100295, aug 2021.

[513] X. Zheng, Y. Hou, C. Bao, J. Yin, F. Yuan, Z. Huang, K. Song, J. Liu, J. Troughton, N. Gasparini, C. Zhou, Y. Lin, D.-j. Xue, B. Chen, A. K. Johnston, N. Wei, M. N. Hedhili, M. Wei, A. Y. Alsalloum, P. Maity, B. Turedi, C. Yang, D. Baran, T. D. Anthopoulos, Y. Han, Z.-h. Lu, O. F. Mohammed, F. Gao, E. H. Sargent, and O. M. Bakr, "Managing grains and interfaces via ligand anchoring enables 22.3%-efficiency inverted perovskite solar cells," *Nat. Energy*, vol. 5, pp. 131–140, feb 2020.

[514] Q. Jiang, Y. Zhao, X. Zhang, X. Yang, Y. Chen, Z. Chu, Q. Ye, X. Li, Z. Yin, and J. You, "Surface passivation of perovskite film for efficient solar cells," *Nat. Photonics*, vol. 13, pp. 460–466, jul 2019.

[515] Y.-H. Chang, J.-C. Lin, Y.-C. Chen, T.-R. Kuo, and D.-Y. Wang, "Facile synthesis of two-dimensional Ruddlesden-Popper perovskite quantum dots with fine-tunable optical properties," *Nanoscale Res. Lett.*, vol. 13, p. 247, dec 2018.

[516] Y. Tong, E. Bladt, M. F. Aygüler, A. Manzi, K. Z. Milowska, V. A. Hintermayr, P. Docampo, S. Bals, A. S. Urban, L. Polavarapu, and J. Feldmann, "Highly Luminescent Cesium Lead Halide Perovskite Nanocrystals with Tunable Composition and Thickness by Ultrasonication," *Angew. Chemie Int. Ed.*, vol. 55, pp. 13887–13892, oct 2016.

[517] J. Hu, I. W. H. Oswald, S. J. Stuard, M. M. Nahid, N. Zhou, O. F. Williams, Z. Guo, L. Yan, H. Hu, Z. Chen, X. Xiao, Y. Lin, Z. Yang, J. Huang, A. M. Moran, H. Ade, J. R. Neilson, and W. You, "Synthetic control over orientational degeneracy of spacer cations enhances solar cell efficiency in two-dimensional perovskites.," *Nat. Commun.*, vol. 10, p. 1276, dec 2019.

[518] X. Yang, X. Zhang, J. Deng, Z. Chu, Q. Jiang, J. Meng, P. Wang, L. Zhang, Z. Yin, and J. You, "Efficient green light-emitting diodes based on quasi-two-dimensional composition and phase engineered perovskite with surface passivation," *Nat. Commun.*, vol. 9, p. 570, dec 2018.

[519] K. T. Cho, G. Grancini, Y. Lee, E. Oveisi, J. Ryu, O. Almora, M. Tschumi, P. A. Schouwink, G. Seo, S. Heo, J. Park, J. Jang, S. Paek, G. Garcia-Belmonte, and M. K. Nazeeruddin, "Selective growth of layered perovskites for stable and efficient photovoltaics," *Energy Environ. Sci.*, vol. 11, no. 4, pp. 952–959, 2018.

[520] S. Gharibzadeh, P. Fassl, I. Hossain, P. N. Rohrbeck, M. Frericks, M. Schmidt, T. Duong, M. R. Khan, T. Abzieher, B. Abdollahi Nejand, F. Schackmar, O. Almora, T. Feeney, R. Singh, D. Fuchs, U. Lemmer, J. P. Hofmann, S. Weber, and U. W. Paetzold, "Two Birds with One Stones: Dual Grain-Boundary and Interface Passivation Enables > 22% Efficient Inverted Methylammonium-Free Perovskite Solar Cells," *Energy Environ. Sci.*, 2021.

[521] F. Bisconti, A. Giuri, G. Marra, A. Savoini, P. Fumo, R. Marrazzo, S. Zanardi, G. Corso, R. Po, P. Biagini, E. Quadrivi, R. Suhonen, T. M. Kraft, M. Ylikunnari, A. Listorti, C. Esposito Corcione, S. Colella, and A. Rizzo, "Polymer-Assisted Single-Step Slot-Die Coating of Flexible Perovskite Solar Cells at Mild Temperature from Dimethyl Sulfoxide," *Chempluschem*, vol. 86, pp. 1442–1450, oct 2021.

[522] J.-A. Alberola-Borràs, R. Vidal, and I. Mora-Seró, "Evaluation of multiple cation/anion perovskite solar cells through life cycle assessment," *Sustain. Energy Fuels*, vol. 2, no. 7, pp. 1600–1609, 2018.

[523] M. Wang, Q. Fu, L. Yan, J. Huang, Q. Ma, M. Humayun, W. Pi, X. Chen, Z. Zheng, and W. Luo, "Systematic optimization of perovskite solar cells via green solvent systems," *Chem. Eng. J.*, vol. 387, p. 123966, may 2020.

[524] T. Wahl, J. Hanisch, S. Meier, M. Schultes, and E. Ahlswede, "Sputtered indium zinc oxide rear electrodes for inverted semitransparent perovskite solar cells without using a protective buffer layer," *Org. Electron.*, vol. 54, pp. 48–53, mar 2018.

[525] Y. Xie, Z. Zeng, X. Xu, C. Ma, Y. Ma, M. Li, C. Lee, and S. Tsang, "FA-Assistant Iodide Coordination in Organic-Inorganic Wide-Bandgap Perovskite with Mixed Halides," *Small*, vol. 16, p. 1907226, mar 2020.

[526] M. Qin, K. Tse, T. Lau, Y. Li, C. Su, G. Yang, J. Chen, J. Zhu, U. Jeng, G. Li, H. Chen, and X. Lu, "Manipulating the Mixed-Perovskite Crystallization Pathway Unveiled by In Situ GIWAXS," *Adv. Mater.*, vol. 31, p. 1901284, jun 2019.

[527] N. Taherimakhsousi, M. Fievez, B. P. MacLeod, E. P. Booker, E. Fayard, M. Matheron, M. Manceau, S. Cros, S. Berson, and C. P. Berlinguette, "A machine vision tool for facilitating the optimization of large-area perovskite photovoltaics," *npj Comput. Mater.*, vol. 7, p. 190, dec 2021.

[528] J. Lopez, S. Pletscher, A. Aemissegger, C. Bucher, and F. Gallou, "N -Butylpyrrolidinone as Alternative Solvent for Solid-Phase Peptide Synthesis," *Org. Process Res. Dev.*, vol. 22, pp. 494–503, apr 2018.

[529] K. H. Hendriks, J. J. van Franeker, B. J. Bruijnaers, J. A. Anta, M. M. Wienk, and R. A. J. Janssen, "2-Methoxyethanol as a new solvent for processing methylammonium lead halide perovskite solar cells," *J. Mater. Chem. A*, vol. 5, no. 5, pp. 2346–2354, 2017.

[530] J.-W. Lee, Z. Dai, C. Lee, H. M. Lee, T.-H. Han, N. De Marco, O. Lin, C. S. Choi, B. Dunn, J. Koh, D. Di Carlo, J. H. Ko, H. D. Maynard, and Y. Yang, "Tuning Molecular Interactions for Highly Reproducible and Efficient Formamidinium Perovskite Solar Cells via Adduct Approach," *J. Am. Chem. Soc.*, vol. 140, pp. 6317–6324, may 2018.

[531] Z. S. Baird, P. Uusi-Kyyny, J.-P. Pokki, E. Pedegert, and V. Alopaeus, "Vapor Pressures, Densities, and PC-SAFT Parameters for 11 Bio-compounds," *Int. J. Thermophys.*, vol. 40, p. 102, nov 2019.

[532] M. Del Carmen Grande, M. García, and C. M. Marschoff, "Density and viscosity of anhydrous mixtures of dimethylsulfoxide with acetonitrile in the range (298.15 to 318.15) K," *J. Chem. Eng. Data*, vol. 54, pp. 652–658, feb 2009.

[533] M. M. Kiaee, T. Maeder, and J. Brugger, "Inkjet-Printing Polymer Nanocomposite for Detecting VOCs," *Proceedings*, vol. 2, p. 882, dec 2018.

[534] L. Zhi, Y. Li, X. Cao, Y. Li, X. Cui, L. Ci, and J. Wei, "Perovskite Solar Cells Fabricated by Using an Environmental Friendly Aprotic Polar Additive of 1,3-Dimethyl-2-imidazolidinone," *Nanoscale Res. Lett.*, vol. 12, p. 632, dec 2017.

[535] B. Febriansyah, T. M. Koh, P. J. S. Rana, T. J. N. Hooper, Z. Z. Ang, Y. Li, A. Bruno, M. Grätzel, J. England, S. G. Mhaisalkar, and N. Mathews, "Hybrid 2D [Pb(CH3NH2)I2]n coordination polymer precursor for scalable perovskite deposition," *ACS Energy Lett.*, vol. 69166, p. acsenergylett.0c00781, jun 2020.

[536] L. Xie, A.-N. Cho, N.-G. Park, and K. Kim, "Efficient and Reproducible CH 3 NH 3 PbI 3 Perovskite Layer Prepared Using a Binary Solvent Containing a Cyclic Urea Additive," *ACS Appl. Mater. Interfaces*, vol. 10, pp. 9390–9397, mar 2018.

[537] B. Chaudhary, A. Kulkarni, A. K. Jena, M. Ikegami, and T. Miyasaka, "Tetrahydrofuran as an Oxygen Donor Additive to Enhance Stability and Reproducibility of Perovskite Solar Cells Fabricated in High Relative Humidity (50%) Atmosphere," *Energy Technol.*, vol. 8, p. 1900990, mar 2020.

List of scientific publications

Peer-reviewed paper

J. **Küffner**, T. Wahl, M. Schultes, J. Hanisch, J. Zillner, E. Ahlswede, and M. Powalla, "Nanoparticle Wetting Agent for Gas Stream-Assisted Blade-Coated Inverted Perovskite Solar Cells and Modules," *ACS Appl. Mater. Interfaces*, vol. 12, pp. 52678–52690, nov 2020.

J. **Küffner**, J. Hanisch, T. Wahl, J. Zillner, E. Ahlswede, and M. Powalla, "One-Step Blade Coating of Inverted Double-Cation Perovskite Solar Cells from a Green Precursor Solvent," *ACS Appl. Energy Mater.*, p. acsaem.1c02425, sep 2021.

M. Schultes, N. Giesbrecht, **J**. **Küffner**, E. Ahlswede, P. Docampo, T. Bein, and M. Powalla, "Universal Nanoparticle Wetting Agent for Upscaling Perovskite Solar Cells," *ACS Appl. Mater. Interfaces*, vol. 11, pp. 12948–12957, apr 2019.

J. Zillner, H.-G. Boyen, P. Schulz, J. Hanisch, **J**. **Küffner**, D. Desta, L. Eisele, E. Ahlswede, and M. Powalla, "The Role of SnF_2 Additives on Interface and Film Formation in All Lead-Free $FASnI_3$ Perovskite Solar Cells," *In Submission*, 2021.

J. Zillner, H.-G. Boyen, G. Delport, P. Schulz, J. Hanisch, **J**. **Küffner**, E. Ahlswede, and M. Powalla, "Optimization of Charge Transport Layer Interfaces in $FASnI_3$ Perovskite Solar Cells," *In Preparation*, 2021.

Conference contributions

J. **Küffner**, T. Wahl, J. Hanisch, W. Hempel, E. Ahlswede, and M. Powalla. *Blade Coating Perovskite Solar Cells: Impacts of Surfactant in Absorber Layer*. Poster presentation, International Conference on Hybrid and Organic Photovoltaics (HOPV19), 2019.

J. **Küffner**, T. Wahl, M. Schultes, J. Hanisch, J. Zillner, E. Ahlswede, and M. Powalla. *Nanoparticle Wetting Agent for Gas Stream-Assisted Blade Coated Inverted Perovskite Solar Cells and Modules*. Oral presentation, NanoGe Fall Meeting (NFM20), 2020.

J. **Küffner**, J. Hanisch, T. Wahl, J. Zillner, E. Ahlswede, and M. Powalla. *One-Step Blade Coating of Inverted Double-Cation Perovskite Solar Cells from a Green Precursor Solvent*. Oral presentation, International Conference on Hybrid and Organic Photovoltaics (HOPV21), 2021.

Acknowledgment

I would like to take the opportunity to express my deepest appreciation to all the people who contributed to this work and supported me on my journey to this thesis.

I am deeply grateful to Prof. Dr. Michael Powalla for providing me the opportunity to do my Ph.D. at ZSW and supervising this thesis. I would like to extend my deep gratitude to Prof. Dr. Christoph Brabec in Erlangen for introducing me to the subject of thin film solar cells and for spending the time and effort to act as second referee.

I would like to share my special appreciation with my colleagues during my Ph.D. at ZSW Julia Zillner, Moritz Loy, Tina Wahl, Jonas Hanisch, Erik Ahlswede, Alexander Eslam, Tim Helder, Mario Zinßer, Thomas Schnabel, Daniela Müller, Meltem Aygüler, Cordula Wessendorf, Wolfram Hempel and all the other colleagues I could count on.

I am particularly grateful to Simon Ternes and David Ritzer at the Karlsruher Institut für Technologie (KIT) for numerous fruitful discussions during the Ph.D.

A very special thanks is directed to Andreas Köhnke and Eberhard Jocher in the workshop of ZSW who did a great job in helping me constructing experimental setups.

Furthermore, I would like to thank my trainee and student Aradhana Manu.

I also wish to thank Karlsruhe School of Optics and Photonics (KSOP) for providing a graduate program and for the great organization of many scientific and social events and my KSOP mentor Franco Weth for his assistance and support.

Moreover, thanks go to the board gamer Frank, Dominik and Julia and to my former flatmates and current ones Rici, Mirjam, Jan, Jojo and Jo who became supportive friends.

Last but not least, I would like to express my deepest gratitude to Laura, my family especially my brothers Moritz, Kiwi and my sister Mareike, and my back-to-the-roots friends, teammates and club members in my hometown. This milestone would have never been possible without the support from you. Finally, I thank my parents for paving me the way to my academic studies and this thesis.

And, I want to thank me for not giving up on me.